Magnetic Helicity and Force-Free Properties of Astrophysical Magnetic Fields

THESIS

Submitted

In partial fulfillment of the requirement for the degree of

Doctor of Philosophy

To

INDIRA GANDHI NATIONAL OPEN UNIVERSITY

By

Avijeet Prasad

School of Inter-Disciplinary and
Trans-Disciplinary Studies,
Indira Gandhi National Open University,
New Delhi – 110 068

May, 2015

DECLARATION

I, Avijeet Prasad, do hereby solemnly declare that the Thesis entitled “Magnetic Helicity and Force-Free Properties of Astrophysical Magnetic Fields ” is a faithful record of the work carried out by me under the supervision of Professor Arun Mangalam of Indian Institute of Astrophysics, Bangalore. I further declare that I have not submitted any part of this Thesis for the award of any other degree of the Indira Gandhi National Open University, New Delhi or any other university in India or abroad.

(Avijeet Prasad)
Place: New Delhi
Date: 21 May, 2015

CERTIFICATE

This is to certify that the Thesis entitled “Magnetic helicity and force-free properties of astrophysical magnetic fields ” submitted for the award of the degree of Doctor of Philosophy in Astrophysics of Indira Gandhi National Open University, is actual record of bona fide work carried out by Mr. Avijeet Prasad under our guidance and supervision. To the best of our knowledge the Thesis is an original work and it has not been submitted for the award of any other degree or diploma in any institution in India or abroad. The Thesis is worthy of consideration for the award of the degree of Doctor of Philosophy (PhD.) in Astrophysics.

(Prof. Arun Mangalam)
Supervisor,
Indian Institute of Astrophysics
2nd Block, Koramangala
Bangalore, Karnataka

(Dr. Nandini Sinha Kapur)
Director,
School of Inter-Disciplinary and
Trans-Disciplinary Studies
(SOITS),
IGNOU, New Delhi

(Dr. C. K. Ghosh)
Program Coordinator and Nodal Officer,
IGNOU-IIA Int. M.Sc.-PhD. in
Physics and Astrophysics
IGNOU, New Delhi

List of Publications:

In Refereed Journals:

1. *Models of force-free spheres and applications to solar active regions.*[a]
   Prasad, A., and Mangalam, A. (2013), eds. Gopalswamy, N., Hasan, S. S., Rao, P. B., & Subramanian, P 2013, ASI Conf. Ser. 10, 53.

2. *Separable solutions of force-free spheres and applications to solar active regions.*[a]
   Prasad, A., Mangalam, A. and Ravindra, B., 2014, ApJ, 786, 81.

Submitted:

3. *Galactic dynamo with helicity and coronal fields.*[b]

   Prasad, A., and Mangalam, A., 2015, ApJ (under review).

Under Preparation:

4. *Topological properties of coronal fields derived from nonlinear force-free field solutions.*[c]
   Prasad, A., and Mangalam, A.

5. *Formulation of relative helicity in generalized toroidal-poloidal representation.*[d]
   Mangalam, A., and **Prasad, A.**

---

a. Presented in Chapter 6.

b. Presented in Chapter 8.

c. Presented in part in Chapter 7.

d. Presented in part in Section 2.4

Acknowledgements

I thank my guide from Indian Institute of Astrophysics (IIA), Prof. Arun Mangalam for helping me with the work in this thesis. I would like to thank Dr. B. Ravindra for helping me with the analysis of HINODE data. I am thankful to IIA for providing the hostel, library, computing facilities and an academic environment as well as its administrative staff for their succour and co-operation during my tenure.

I would like to thank Prof. Vijayshri (Director, SOS, IGNOU), Dr. Nandini Sinha Kapur (Director, SOITS, IGNOU), Prof. B. P. Das (IIA) for helping me with various academic procedures and Dr. C. K. Ghosh (Program Coordinator and Nodal Officer, IGNOU-IIA Integrated M.Sc.-PhD. in Physics and Astrophysics Programme) who in addition to carrying out his duties taught me several Physics courses during my MSc. I would also like to thank CSIR for the SPM Fellowship and DST for providing international and domestic travel support for attending conferences.

I thank my parents, my sister, my extended family and my teachers for being a constant source of encouragement in my academic pursuits, supportive of the most important decisions I have made. I also thank all my friends and fellow students at IIA for their constant support and encouragement.

Abstract

Magnetic fields are ubiquitous in the universe and play an important role in variety of astrophysical phenomenon. It is thus very important to understand the origin, structure and strength of these astrophysical magnetic fields. In this Thesis, we use the concept of magnetic helicity conservation and properties of force-free magnetic fields to investigate the topological properties of magnetic fields in the solar corona and the amplification and nonlinear saturation of dynamo generated field in disc galaxies.

For the case of solar corona, we solve the linear and nonlinear force-free field equation using photospheric boundary conditions to obtain simple axisymmetric magnetic field configurations in spherical geometry. We show that the condition of separability of solutions in the radial and angular variables leads to two classes of solutions: linear and nonlinear force-free fields (NLFF). We extended the set of NLFF solutions with radial power law index $n = p/q$, for all cases of odd p and cases of $q > p$ for even p. We apply these solutions to simulate photospheric vector magnetograms obtained using the spectro-polarimeter on board Hinode and search for best-fit configurations. The effectiveness of our search strategy is demonstrated on test inputs of dipolar, axisymmetric, and non axisymmetric linear force-free fields. Using the best fit, we build three- dimensional axisymmetric field configurations and calculate the energy and relative helicity with two independent meth-

ods. The magnetic helicity and free energy content of these fields are useful indicators of energy available for release during eruptive events like solar flares. We analyze five magnetograms for active regions (AR) 10930 spanning a period of three days during which two X-class flares occurred and calculate the free energy and relative helicity of the active region before and after the flare. Our analysis indicates a peak in these quantities before the flare events, which is consistent with the previous results. We also analyze single-polarity regions AR 10923 and 10933, which showed very good fits to potential fields. This method provides useful reconstruction of NLFF and input fields for other numerical techniques. We also apply the NLFF solutions to calculate the amount of braiding in coronal magnetic fields using the concept of mean crossing number. This is then used to estimate the free energy content in solar active regions. We find that the free energy estimates obtained from calculation of magnetic braiding is in good agreement with those obtained by exact calculations of NLFF fields. We then apply the model of self-organized criticality (SOC) to these braided field lines and calculate the distribution of coherent braid sequences and flare energies. We find find good agreement in the flare energy distributions obtained using SOC model and NLFFF extrapolation. These results provide useful information on the coronal loop structure and also imply that the coronal heating can be supplied by the braiding in the case of the active sun.

We provide a new formulation for relative helicity in arbitrary geometries using the toroidal-poloidal representation of the magnetic field iand discuss the special cases of planar and spherical geometry. In a general astrophysical application, the fields penetrate the generation region and extend to a surrounding corona. It is important to develop gauge-free form for Helicity that can be readily used in different geometries without involving integrals over

external volumes. The further extension of the ideas here can be formalized through use of differential geometry.

Magnetic fields correlated on kiloparsec scales are seen in disc galaxies. The origin could be due to amplification of small scale seed fields by a turbulent dynamo. Helicity conservation imposes constraints on dynamo action and one can study the minimal field strength of the large scale magnetic field that could arise despite the constraint. The calculation of helicity is technically complicated because of open boundaries and the usual form for the magneto-hydrodynamic (MHD) invariant needs to be modified to take this into account. We then present a global semi-analytic axisymmetric model for a turbulent dynamo operating in a galaxy with a corona. Here, we show that the supernovae (SNe) and magneto-rotational instability (MRI) driven turbulence parameters have nearly the same radial dependence and can be treated in a common formalism; however we assume the main contribution from SNe. The general toroidal-poloidal representation is then used to calculate the global gauge invariant relative magnetic helicity in cylindrical geometry. We present the analytic steady-state solutions within the disc that are matched to force-free fields in the corona. A dynamical solution for the dynamo is then obtained by expanding the time-dependent field in the basis obtained using the steady-state solutions. The non-linear quenching of the dynamo is alleviated by inclusion of small-scale advective and diffusive magnetic helicity fluxes, which allow the helicity to be transferred outside the disc and consequently build up a corona during the course of dynamo action. We find quadrupolar solutions for in the galactic disc that extend out into the corona and show oscillations radially. The mean field is found to reach saturation within a timescale of 1 Gyr with a strength which is of the order of equipartition magnetic energy ($\sim B_{eq}$).

The following is the arrangement of the Thesis. Chapter 1 gives an overview of astrophysical magnetic fields with special focus on observations of solar and galactic magnetic fields. Chapter 2 outlines the basics concepts of MHD and describes the processes relating to magnetic field generation and dissipation. We also discuss the topological properties of magnetic field using magnetic helicity and provide a novel prescription for calculating magnetic helicity in arbitrary geometries. Chapter 3 presents a description of potential and force-free fields and outlines their important properties. We then discuss analytical and numerical techniques for solving potential and force-free fields equations for determining coronal magnetic fields. In Chapter 4, we present an overview of various coronal heating mechanisms and discuss the statistical properties of solar flares. We then discuss braiding in coronal magnetic fields and calculate the free energy in these configurations due to braiding. Chapter 5 gives an introduction to large-scale turbulent dynamos and discusses various closure approximations used in mean field MHD. We then present its application to disc galaxies, discuss the basic analytic solutions and give an overview of current problems in dynamo theory. In Chapter 6, we present new solutions to the nonlinear force-free field equation and discuss its application for determining the topological properties of coronal magnetic fields, such as their free-energy and relative helicity. We then apply the solutions to a time sequence of vector magnetograms to estimate the energy released in a solar flare due to change in magnetic field configuration. In Chapter 7, we use the NLFF field solutions obtained in Chapter 6 and estimate the amount of free-energy due to braiding in these configurations. We then apply a model of SOC to this field and calculate the power-law distribution of flare energies which is then compared with observations. In Chapter 8, we present a model of nonlinear turbulent dynamo applied to a disc galaxy having a force-free

corona. We discuss the significance of small-scale magnetic helicity fluxes with regards nonlinear saturation of the dynamo. Chapter 9 then presents a summary of the results from all chapters, highlight the novel aspects of this Thesis with its impact. Then, we present future work which includes papers under preparation.

Abbreviations

AC Alternating Current.

AR Active Region.

CME Coronal Mass Ejection.

DC Direct Current.

DNS Direct Numerical Simulations.

EDQNM Eddy Damped Quasi-Normal Markovian.

emf electromotive force.

EUV Extreme Ultraviolet.

FOSA First-Order Smoothing Approximation.

HXR Hard X-rays.

ISM Interstellar Medium.

MFD Mean Field Dynamo.

MHD Magnetohydrodynamics.

MRI Magneto-rotational Instability.

MTA Minimal-τ Approximation.

NLFFF Nonlinear Force-Free Field.

PIL Polarity Inversion Line.

RM Faraday Rotation Measure.

SNe Supernovae.

SOC Self-Organized Criticality.

SOCA Second Order Correlation Approximation.

SOHO Solar and Heliospheric Observatory.

SP Spectro-Polarimeter.

SXR Soft X-rays.

TRACE Transition Region And Coronal Explorer.

UV Ultraviolet.

Nomenclature

B_{eq} Equipartition magnetic field.

H' Mean small-scale magnetic helicity.

R_m Magnetic Reynolds number.

α_k Kinetic α effect.

α_m Magnetic α effect.

$\boldsymbol{\mathcal{E}}$ Mean turbulent emf.

η Magnetic diffusivity.

η_t Turbulent diffusivity.

$\mathbf{A}$ Magnetic vector potential.

$\mathbf{B}$ Total magnetic field.

$\mathbf{E}$ Electric field intensity.

$\mathbf{J}$ Current density.

$\mathbf{U}$ Velocity of plasma.

$\mathbf{b}$ Small-scale magnetic field.

$\mathcal{M}$ Mach number of turbulence.

μ_0 Magnetic permeability.

ν Kinematic viscosity.

$\overline{H}$ Large-scale magnetic helicity.

$\overline{\mathbf{B}}$ Mean magnetic field.

ρ Mass density.

σ Electrical conductivity.

Contents

List of Figures

List of Tables

Chapter 1

Introduction

1.1 Astrophysical magnetic fields

Magnetic fields are ubiquitous in the universe and play an important role in variety of astrophysical phenomenon. It is thus very important to understand the origin, structure and strength of these astrophysical magnetic fields. Magnetic field of Sun was first discovered by Hale (1908), a few hundred years after the discovery of magnetic fields on Earth. The magnetic fields on other stars were detected half a century later by Babcock (1947). There is a large variation in strength of magnetic field as observed in different astrophysical objects (presented in Table 1.1 along with the corresponding observational technique). The first theory to explain the origin of magnetic field in the Earth and the Sun was proposed by Larmor (1919). According to this theory, known as the hydromagnetic dynamo theory, the magnetic fields are maintained and amplified by fluid motion in a conducting plasma. Cowling (1933), in an anti dynamo theorem proved the impossibility of maintaining an axisymmetric magnetic field by fluid motions. Steenbeck, Krause, and Rädler (1966) proposed a practical and convenient approach called the

mean field electrodynamics, which simplified the study of large scale magnetic fields. Parker (1955) proposed a hydrodynamic dynamo model associated with the helicity of the flow. A topological approaches to the hydromagnetic dynamo problem was proposed by Moffatt (Moffatt, 1969) which led to further progress of the dynamo theory. Along with the large-scale fields, the role played by small-scale, fluctuating magnetic field is particularly important, especially with regards to the back reaction of the field on the fluid motion (the nonlinear dynamo problem). A self-consistent treatment of the back reaction of the magnetic field on the turbulence or rotation is required to explain the saturation strength of the mean magnetic field (Zeldovich, Ruzmaikin, and Sokolov, 1983; Gruzinov and Diamond, 1994; Brandenburg and Subramanian, 2005a). This thesis focuses on the magnetic fields in the solar corona and the large-scale fields observed in disc galaxies. We first begin by giving below, a short description of the properties of magnetic fields in the Sun and disc galaxies.

Object	Field strength	Observational technique
Intergalactic medium	10^{-9} G	Faraday rotation
Galaxy	10^{-6} G	Faraday rotation
Interstellar clouds	10^{-5} G	Zeeman effect in 21 cm
Quasars	100 G	Intrinsic Faraday rotation
Sun	1 G	Zeeman effect, Hanle effect, Faraday rotation
White dwarfs	10^{6} G	Polarized synchrotron emission
Neutron stars	10^{12} G	Polarized synchrotron emission

Table 1.1: The magnetic field strength observed for different astrophysical objects with the corresponding observational technique.

1.2 Solar magnetic fields

1.2.1 Overview of the solar interior and atmosphere

Our nearest star, Sun is a typical star in our galaxy, of spectral type G2-V having a radius of $R_{\odot}= 7 \times 10^{10}$ cm and a mass of $M_{\odot} = 2 \times 10^{33}$ g. The Sun is of particular significance to us as it the ultimate source of energy for the entire solar system. The Sun has been an object of fascination and has been studied with interest for thousands of years. It is the closest laboratory for studying various astrophysical plasma processes in great detail. The basic structure of the Sun is sketched in Figure 1.1.

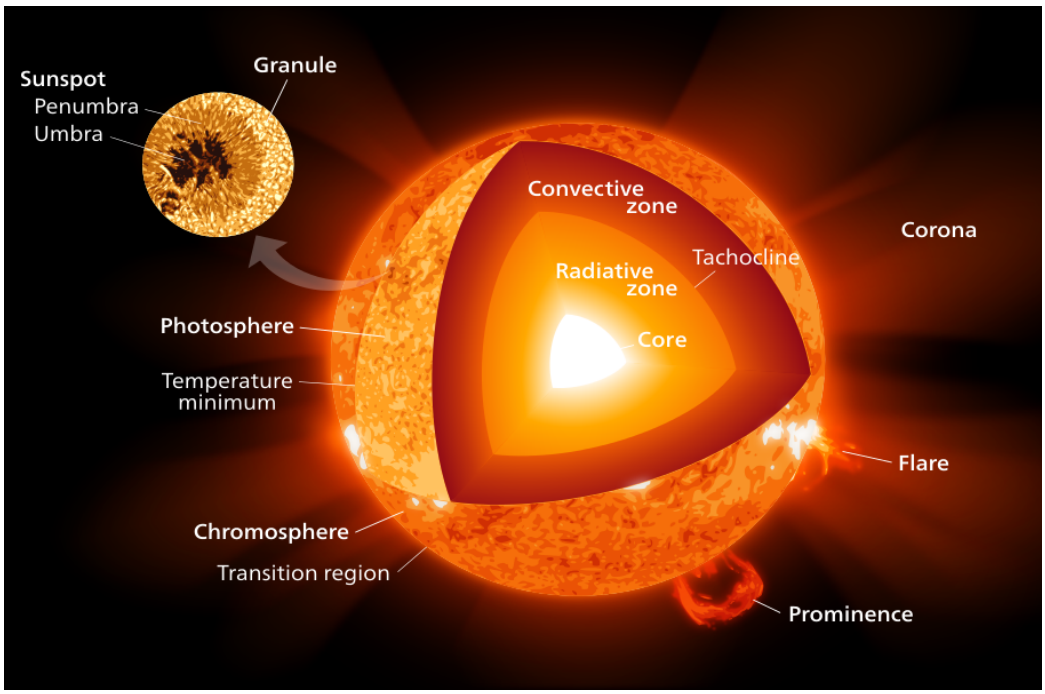

Figure 1.1: The interior of the Sun. Figure courtesy: Kelvinsong (Wikipedia)[1]

The Sun was formed from a contracting and rotating interstellar cloud

[1]Licensed under CC BY-SA 3.0 via Wikimedia Commons - http://commons.wikimedia.org/wiki/File:Sun_poster.svg#/media/File:Sun_poster.svg.

around 5 billion years ago. After gravitational contraction and subsequent collapse, the central object became the Sun when the core temperature was hot enough to ignite thermonuclear reactions. The central core has a temperature of $\sim$ 15 million K and a density of $\sim$ 160 g cm^{-3}. The fusion of hydrogen nuclei (H) into helium nucleus (He) takes place mainly by the proton-proton (PP) chain and partly by the CNO cycle. During this process four protons (^{1}H) fuse to form one Helium nucleus (^{4}He) releasing 27.6 MeV of energy along with two positrons (e^+) and two electron neutrinos (ν)

$$4^1\mathrm{H} \rightarrow^4 \mathrm{He} + 2e^+ + 2\nu + 27.6 \text{ MeV}.$$

The radiative zone extends out from the core to about 0.7 solar radii, where energy is transported mainly by radiative diffusion. The ions of hydrogen and helium emit hard X-ray photons, which travel only a brief distance before getting scattered, absorbed and remitted by other ions during a period of random walk for $10^5 - 10^6$ years. In the Sun's outer layer, from $\sim 0.7R_\odot$ to its surface, the temperature is lower than the interior so the heavier atoms are not fully ionized. As a result, the heat transport through radiation is not very effective and thermal convection becomes the dominant mode of energy transport. Material at the base of the convection zone heats up, expands (which reduces its density) and rises till the base of photosphere where it releases energy through diffusion and radiation. As the material cools off, its density increases and it sinks back to the base of the convection zone, where it again picks up heat from the top of the radiative zone, thus continuing the convective cycle. These thermal columns in the convection zone leave an imprint on the photosphere as the solar granulation and supergranulation patterns. At the photosphere (the solar surface that is observed in white light), the temperature drops to $\sim$ 5,700 K and the photons leave the Sun in optical wavelengths which is about a factor of 10^5 lower than the original

hard X-ray photons generated in the nuclear core. The solar surface radiates most of the its energy in the optical wavelengths, whereas in the solar corona, which contains ionized plasma in the temperature range of $\sim 1 - 2$ million K, the emission in EUV is most dominant.

1.2.2 The solar dynamo and sunspots

The Sun possess a strong magnetic field (compared to the planets in the solar system), which is generated with a magnetic field strength of $B \sim 10^5$ G in the tachocline, which is a transition layer between the radiative zone and the convective zone. In this region, there is a sharp change between the uniform rotation of the radiative zone and the differential rotation of the convection zone, which results in a large shear generation in this region. Magnetic flux tubes can become buoyant and rise through the convection zone and emerge at the solar surface in active regions, which leads to the formation sunspots with magnetic field strengths of $B \sim 10^3$ G. This is often in the form of a leading sunspot, followed by groups of opposite magnetic polarity. The coronal loops are seen with field strengths of $B \sim 10^2$ G. The differential rotation on the solar surface winds up the surface magnetic field, which is carried to the poles through meridional circulation. This process re-orients the toroidal component of the magnetic field line (which is oriented in the east-west direction) at solar maximum into a poloidal field (which connects the magnetic North Pole to the South Pole) in the solar minimum (see Figure 1.2). This process which changes the direction of magnetic field of the Sun almost every 11 years is called the solar dynamo. The initial magnetic configuration is assumed every ~ 22 years. This is known as the solar cycle. During the maximum of the solar cycle, there is a peak in the solar activity which is inferred from the sunspot number and occurrence of

events like flares and coronal mass ejections (CMEs).

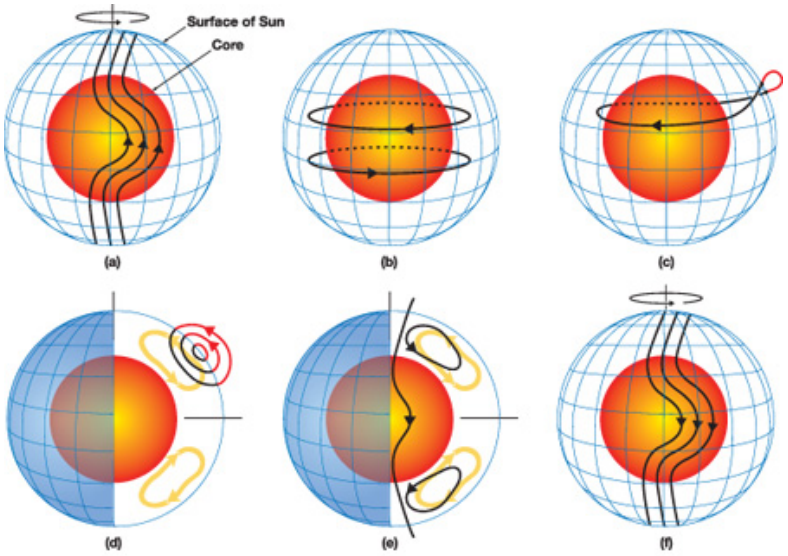

Figure 1.2: Illustration showing how magnetic fields are recycled to produce sunspots within the solar convection zone (the top 30% of the solar interior, shown in white, surrounding the radiative core, in orange). As the sun rotates faster at the equator than the poles, the north-south (poloidal) magnetic field (a) gets twisted into an east-west (toroidal) field (b). Regions of enhanced toroidal field become buoyant and rise to the surface. These field lines get twisted in the process due to the rotation of the Sun and emerge as sunspots on the photosphere(c, upper right). Panels (d) and (e) show the solar dynamo, the meridional circulation of the plasma (shown in yellow) carries the surface magnetic flux toward the poles. This process reverses the direction of the polar field which eventually move back toward the equator. The new sunspots that are formed now from the poloidal field (f), will have opposite polarity to those that in (a). Figure courtesy: M. Dikpati, NCAR[2]

The solar magnetic fields can be directly inferred from observations of the photospheric field, from splitting of spectral lines in visible wavelengths

[2]http://www.ucar.edu/communications/quarterly/spring06/images/dikpati.jpg

(e.g. Fe 5250 Å) due to the Zeeman effect. The two-dimensional (2D) maps of the photospheric magnetic field strength are called magnetograms. An example of a magnetogram depicting the line of site magnetic field obtained through Solar and Heliospheric Observatory (SOHO) is depicted in Figure 1.3. Maps of three-component photospheric magnetic field are called vector magnetograms which can be obtained using instruments like the Spectro-Polarimeter (SP) on board *HINODE*. The coronal magnetic field is reconstructed using extrapolation techniques from magnetograms at the lower boundary, where the magnetic field is assumed to be following a potential field or force-free field equation of state. The extrapolation of magnetic field through the chromosphere and transition region is largely uncertain because of the unknown currents and non force-free conditions. The coronal loops generally exhibit much less expansion with height than predicted by potential field models, so non-linear force-free models are more favored. Direct measurements of the magnetic field in coronal heights are yet to be established.

Sunspots are the regions with the strongest magnetic fields on the photosphere. Sunspots appear dark because they are regions of lower temperature than the areas surrounding them. Large sunspots typically have temperatures of about 4,000 K which is much lower than the temperature of 5,700 K in the photosphere, that surrounds the sunspots. Sunspots are good indicators of solar activity. The appearance of sunspots are usually confined to an equatorial belt ranging between -35 degrees south and +35 degrees north in latitude. When a new solar cycle begins, sunspots tend to appear at high latitudes, but as the cycle progresses towards its maximum (marked by large numbers of sunspots), the sunspots appear at lower latitudes. During the

[3]http://solar-center.stanford.edu/solar-images/magnetograms.html

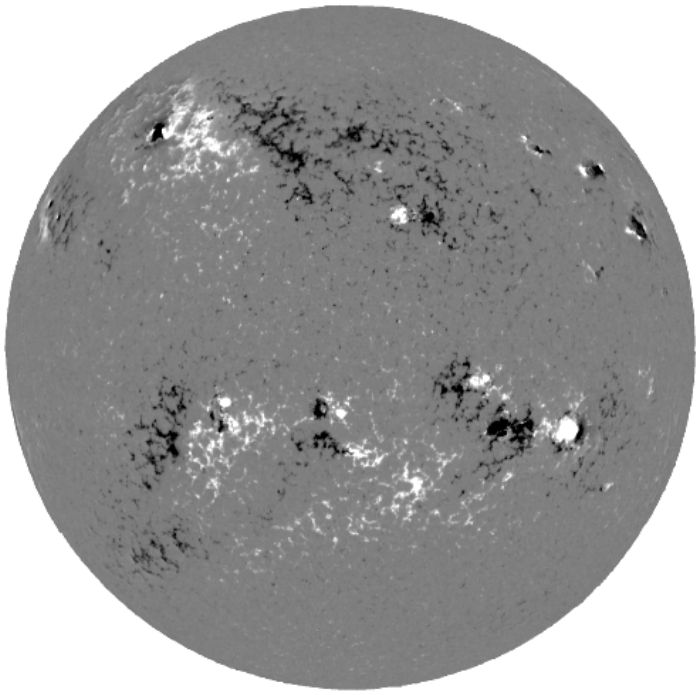

Figure 1.3: Line-of sight magnetogram of the Sun. Here white represents the north polarity (outward directed) while black represents the south polarity (inward directed) of the magnetic field. The gray color represents regions of weak magnetic field. Figure courtesy: SOHO[3]

minimum of the cycle, sunspots appear very close to the equator, and as a new cycle begins, sunspots again form at high latitudes. This recurrent behavior of sunspots shows a "butterfly" pattern when the number of sunspots are plotted as a function of latitude and time (Figure 1.4). This feature was first discovered by Edward Maunder in the year 1904. All solar activity phenomena such as the flare rate, active region area, global soft X-ray brightness, and radio emission, which are controlled by the magnetic field have a similar solar cycle dependence as sunspots. The total luminosity of the Sun lowers by $\sim 0.15\%$ during the sunspot maximum due to appearance

of dark sunspots.

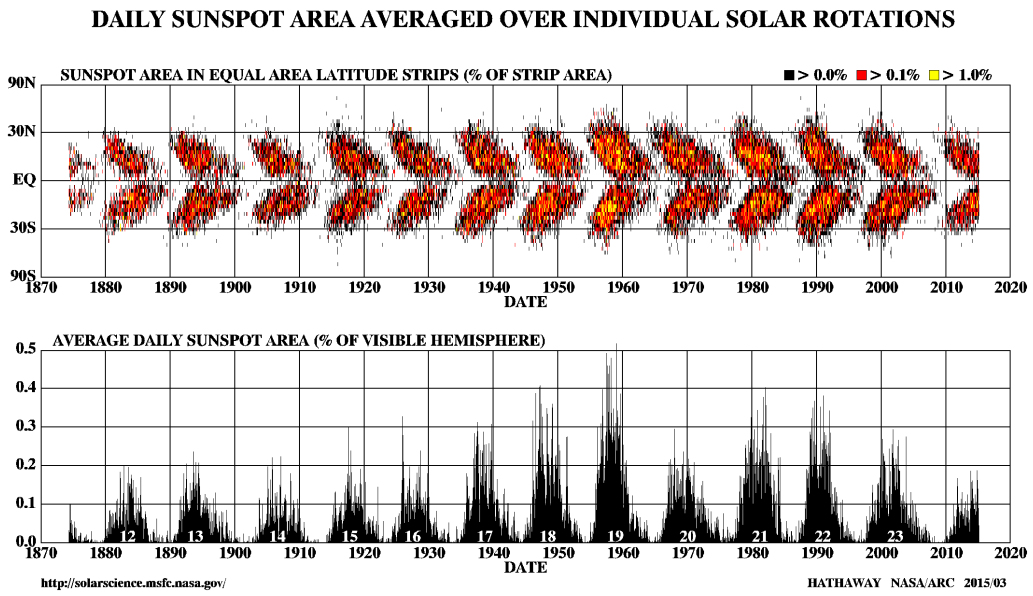

Figure 1.4: Top: The butterfly diagram of sunspot appearance marks the latitude of sunspot locations as a function of time, during the solar cycles 12-23 (covering the years 1880-2000). Bottom: Sunspot area plotted as a function of time. Figure courtesy: D. Hathaway, NASA/MSFC[4]

1.2.3 Coronal magnetic fields

The hot plasma can can only propagate along these field lines (the cross-field diffusion is strongly inhibited), so the magnetic field controls the dynamics and topology of all coronal phenomena. The coronal loops are nothing but conduits filled with heated plasma whose geometry is shaped by that of the coronal magnetic field. The solar corona is generally divided into three zones, namely : (1) active regions, (2) quiet-Sun regions, and (3) coronal holes.

[4]http://solarscience.msfc.nasa.gov/images/bfly.gif

1. Active regions: Active regions areas of strong magnetic field concentrations visible as sunspot groups in optical wavelengths or magnetograms. Active regions are mainly made up of closed magnetic field lines of bipolar nature. Typically sunspots appear in a strongly concentrated leading magnetic polarity which is followed by a weaker trailing group, having the opposite polarity. Magnetic activities like magnetic flux emergence, flux cancellation and magnetic reconnection processes occur in active regions which leads to events like flares and CMEs. These processes lead to heating of the plasma in the chromosphere which causes up flows hot plasma into coronal loops, which produce bright emission in soft X-rays and EUV wavelengths. The closed-field lines also produce a slow solar wind component of ~ 400 km/s. Active regions comprise a larger area around sunspots, with average photospheric fields of $B \approx 100 - 300$ G, containing small-scale pores with typical fields of $B \approx 1000$ G.

2. Quiet-Sun Regions: The areas outside of active regions are generally referred to as quiet-Sun regions. Small-scale dynamic processes in the quiet Sun include network heating events, nanoflares, bright points and soft X-ray jets.

3. Coronal holes: The polar regions of the Sun are dominated by open magnetic field lines. Since open field lines are efficient conduits for transporting energy (fed by chromospheric upflows), from the corona into the solar wind, they are generally darker than the equatorial zones. Open-field lines connect the solar surface with the interplanetary field and are the source of the fast solar wind ($\sim$800 km/s). The quiet Sun and the coronal holes have a net background magnetic field of

$B \approx 0.1 - 0.5$ G.

1.2.4 Solar flares and CMEs

Flares and CMEs are eruptive phenomena in the solar corona which result from a loss of equilibrium in the magnetic field configuration, driven by magnetic reconnection. New magnetic flux generated by the solar dynamo is constantly added into the corona, which rises due to buoyancy from the bottom of the convection zone through the photosphere into the corona. Also the differential rotation and the motion at the solar surface continuously twist and tangle the coronal fields. These dynamic boundary conditions constantly stress the coronal magnetic field which has to adjust its topology by restructuring the large-scale magnetic field through the magnetic reconnection processes. These topological changes in the magnetic field configuration liberate the free (non potential) energy of the system, which is released into the heating of plasma and the acceleration of particles. When the magnetic reconnection processes happens suddenly with a large release in energy, they are manifested as flares and CMEs. During these eruptive events, there is emission of radiation in almost all wavelengths: radio, white light, EUV, soft X-rays, hard X-rays, and even gamma rays during large flares. The energy released in flares extend over many orders of magnitude; a large flare can be of the order of 10^{33} ergs. Smaller flares that have an energy content of 10^{-6} to 10^{-9} times that of the largest flares are categorized as microflares and nanoflares, and are observed not only in active as well as the quiet-Sun regions of the corona.

1.2.5 The coronal heating problem

Spectroscopic observations of the solar corona by Grotrian in 1930s revealed some unusual absorption lines (Grotrian, 1934) which were identified as Fe IX and Ca XIV by Edlén (Edlén, 1943). These highly ionized lines correspond to a coronal temperature of $T \sim 1$ MK. When this is compared to the temperature of the underlying photosphere, which is close to 6000 K (see Fig.1.5), we are confronted with the puzzle of how the coronal temperature is maintained at several hundred times that of the photosphere. This is known as the coronal heating problem.

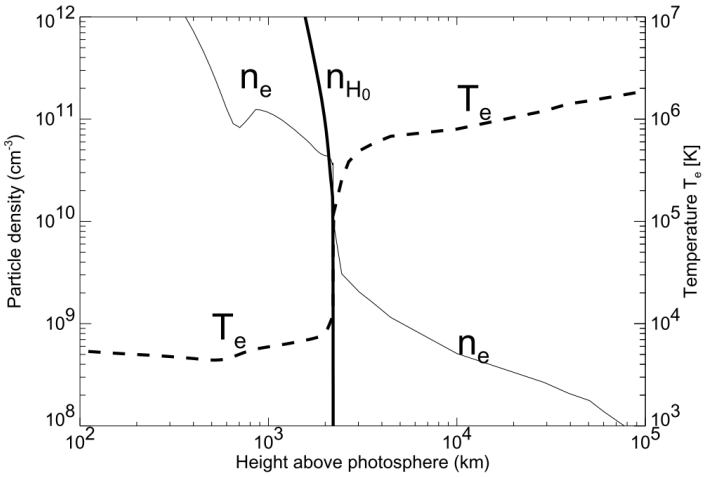

Figure 1.5: Electron density and temperature model of the chromosphere (Fontenla, Avrett, and Loeser (1990); Model FAL-C) and lower corona (Gabriel, 1976). Figure courtesy: Aschwanden (2004).

If we consider only thermal conduction, then the temperature in the corona should steadily drop down from the chromospheric value with increasing distance. Moreover, due to radiative losses through EUV emission (as seen in the TRACE[5] images, Fig. 1.6), the corona would cool off within

[5]TRACE is a NASA Small Explorer Project, built and operated by Lockheed Martin

a timescale of few hours to days unless energy is constantly supplied to it through some heating mechanisms. An overview of these heating mechanisms is presented in §4.1.

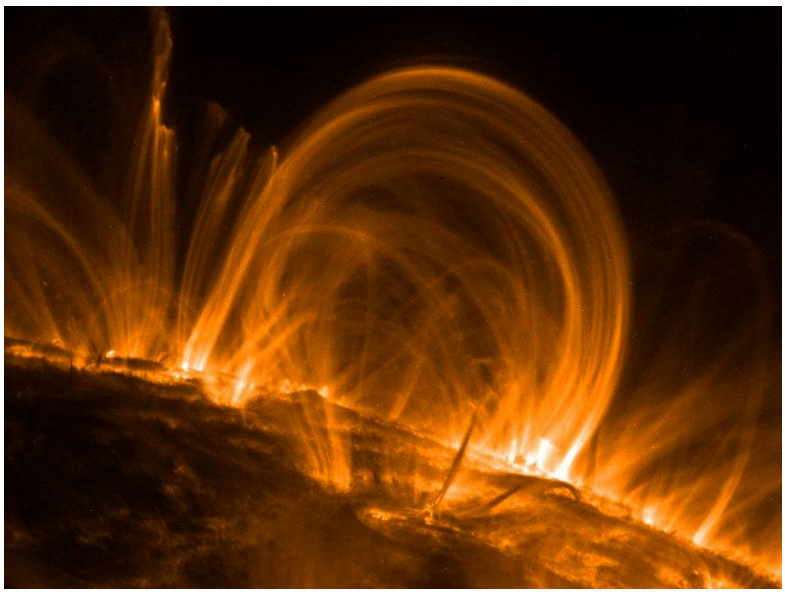

Figure 1.6: EUV emissions from hot coronal loops taken from TRACE in the 171Å passband which has a characteristic plasma temperature of 1 MK.

1.3 Galactic magnetic fields

The total magnetic fields observed in spiral galaxies is typically of strength $B \sim 10\mu$G, which is comparable to the equipartition field strength $Beq = \sqrt{\mu_0 \rho} u_T$ of the Interstellar Medium (ISM) turbulence. For a density of order 10^{-24} g/cm^3 and a turbulence velocity of about 10 km/s, $B_{eq} \approx 3.5\mu$G. The energy budgets for various components like ISM, magnetic fields, cosmic rays, turbulence and gas rotation for NGC 6946 are shown in Table 1.2. We can see that the turbulence and the magnetic fields are roughly in energy

Solar and Astrophysics Lab

equipartition, which is one magnitude higher than the thermal energy of the gas.

Warm medium	Magnetic field	Cosmic ray	Turbulence	Gas rotation
1	13	13	10	5000

Table 1.2: Average energy densities in 10^{12} erg/cm^3 in the inner disc of NGC 6946 (Beck, 2002)

The total magnetic field $\mathbf{B}$ can be divided into a mean large-scale component $\overline{\mathbf{B}}$ with a coherent scale approaching the radius of the disc ($\sim$ 10 kpc) and a small-scale random component $\mathbf{b}$ which is coherent over the outer scale of interstellar turbulence ($\sim$ 100) pc. Thus we can write

$$\mathbf{B} = \overline{\mathbf{B}} + \mathbf{b} \tag{1.1}$$

where $\overline{\overline{\mathbf{B}}} = \overline{\mathbf{B}}$, $\overline{\mathbf{b}} = 0$ and $\langle B^2 \rangle = \overline{B}^2 + \langle b^2 \rangle$. The overbar formally denotes ensemble averaging, but for all practical purposes can be thought of as spatial averaging over scales greater than the turbulent scale and less than the scale of the system (Germano, 1992; Gent *et al.*, 2013). The galactic magnetic fields can be observed in the optical range through the polarization induced in starlight, when it is scattered by interstellar dust grains present in the foreground. These grains are elongated in shape and often get aligned by the magnetic fields (such that the major axis of the grain becomes perpendicular to the magnetic field lines). These aligned dust grains show polarized infrared emission, which help us determine the magnetic fields in dust clouds in the Milky Way. Relatively strong fields in the nearby dense gas clouds of the Milky Way can be observed through the Zeeman splitting of radio spectral lines. The most powerful technique for measuring magnetic fields across Milky Way and nearby galaxies is through the observation of polarized syn-

chrotron radio emission. The total magnetic field strength in the plane of the sky can be inferred from the total synchrotron intensity, provided we know the cosmic ray electron density, n_{cr}. The polarized synchrotron emission is produced only by magnetic fields with a preferred orientation. The amount of Faraday Rotation Measure (RM) of the polarized synchrotron emission along a given line of sight, which is produced only by large-scale magnetic fields is determined by the magnetic field along the line of sight and the thermal electron density, n_e. The total I, polarized P synchrotron intensities and the RM are calculated as weighted integrals of magnetic field over the line of sight L as (Shukurov, 2004)

$$\begin{aligned} I &= K \int_L n_{cr} B_\perp^2 \mathrm{d}l \\ P &= K \int_L n_{cr} \overline{B}_\perp^2 \mathrm{d}l \end{aligned} \tag{1.2}$$

$$RM = K_1 \int_L n_e B_\parallel^2 \mathrm{d}l \tag{1.3}$$

where subscripts $\perp$ and $\parallel$ refer to the perpendicular and parallel components of the magnetic field taken with respect to the line of sight, and K and $K_1 = e^3/(2\pi m_e^2 c^4) = 0.81$ rad m^{-2} cm^3 μG^{-1} pc^{-1} are certain dimensional constants (with e and m_e the electron charge and mass and c the speed of light). The degree of polarization p is related to the ratio $\langle b^2 \rangle / \overline{B}^2$ as (Shukurov, 2004),

$$p \equiv \frac{P}{I} \approx p_0 \frac{\overline{B}_\perp^2}{B_\perp^2} = p_0 \frac{\overline{B}_\perp^2}{\overline{B}_\perp^2 + \frac{2}{3}\langle b^2 \rangle} \tag{1.4}$$

where the random field $\mathbf{b}$ has been assumed to be isotropic, n_{cr} has been assumed to be constant and $p_0 \sim 0.75$. This widely used relation is only approximate as it does not allow for any anisotropy of the random magnetic

field or the dependence of n_{cr} on B (Sokoloff *et al.*, 1998). The intensity of synchrotron emission is a measure of the density of cosmic-ray electrons and of the strength of the total magnetic field component in the sky plane. The degree of linear polarization of synchrotron emission for a completely ordered field can be as high as 75%. Anisotropic turbulent fields (with random orientations), which are generated from isotropic turbulent fields can give polarized emission on scales smaller than the telescope beam while isotropic turbulent fields that have been generated by turbulent gas flows give rise to unpolarized synchrotron emission. Thus three components of the total field namely: regular, anisotropic turbulent and isotropic turbulent fields, can be distinguished by observations. The Faraday rotation measure, RM, is sensitive to the direction of **B** (the sign of $\overline{B}_{\parallel}$) and this allows one to determine the orientation as well as the direction of B. Thus, the measurement of Faraday rotation helps us in revealing the three-dimensional structure of the magnetic field (Beck *et al.*, 1996; Berkhuijsen *et al.*, 1997).

In many cases, a quadrupolar symmetry of the magnetic fields is found to be dominant along with symmetry with respect to the rotation axis (Figure 1.7). Krause and Beck (1998) mention the difference of dipolar and quadrupolar field symmetry whereby, if the magnetic field amplitudes averaged over the whole sky is zero, then the galactic magnetic fields have dipolar symmetry; otherwise the symmetry is quadrupolar.

The pitch angle, defined as $p = \arctan(B_r/B_\phi)$ gives the ratio of the radial (B_r) and the azimuthal (B_ϕ) component of the magnetic field. For galaxies pitch angles of in the range 10-40° have been reported which decrease with the radial distance (Rüdiger and Hollerbach, 2004). Such observed values indicate that the differential rotation does not play a dominant role

[6]http://www.scholarpedia.org/article/File:N5775.jpg

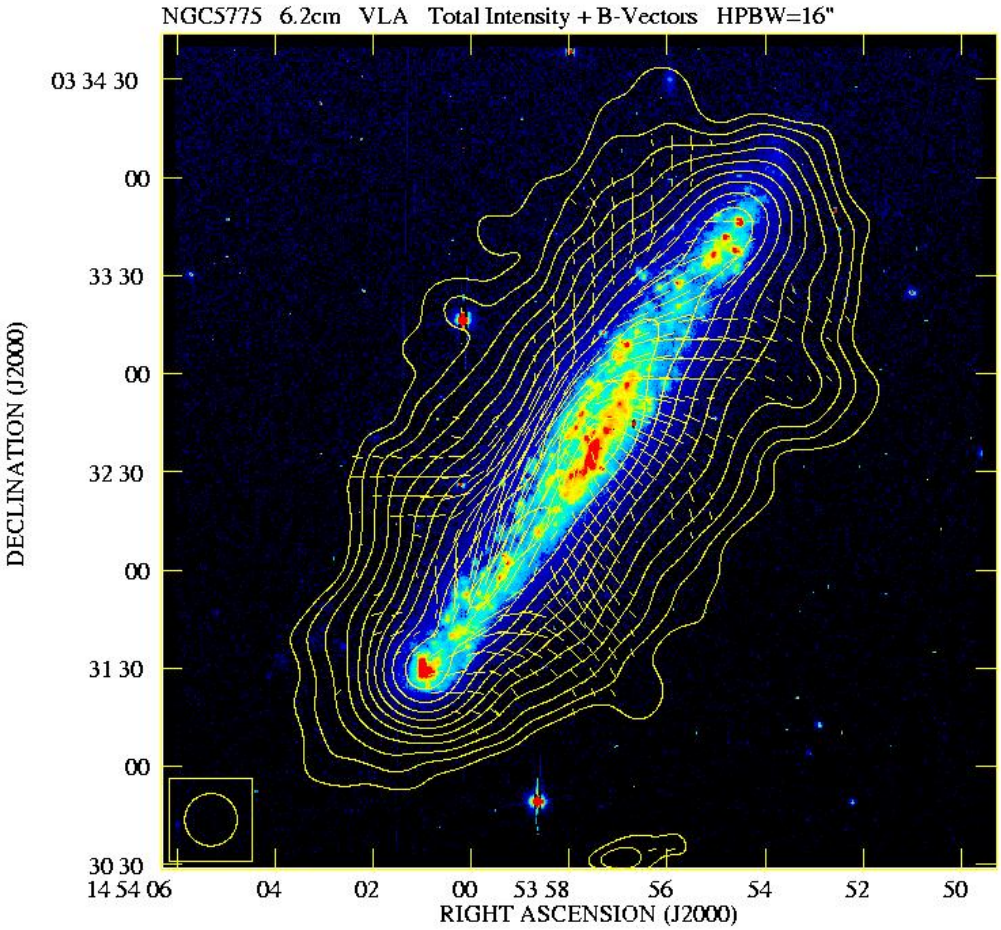

Figure 1.7: Optical image of the spiral galaxy NGC 5775 seen almost edge-on in the Hα line overlaid by contours of the total radio emission intensity at 6cm wavelength and polarization vectors, observed with the VLA (Tüllmann *et al.*, 2000). We can notice that the field lines are parallel to the disk near the plane, but orient vertically above and below the disc. Figure courtesy: Cracow Observatory[6]

in magnetic field generation in galaxies. The frozen-in magnetic fields which are wound up by differential rotation (due to small magnetic diffusivity), are expected to show small pitch angles. Only when the diffusivity is large,

does one expect to observe large pitch angles. In NGC 4414, pitch angles up to 45° have been found. In the case of NGC 6946 pitch angles have been observed between 20° and 30°. Here, the large-scale magnetic fields are concentrated between the optical spiral arms as seen in Figure 1.8 with axisymmetric orientation for the azimuthal field (Beck and Hoernes, 1996). The turbulent component of the magnetic field in the spiral arm is observed to have a strength of 15 μG, while the regular field located in the inter arm region is around 10 μG .

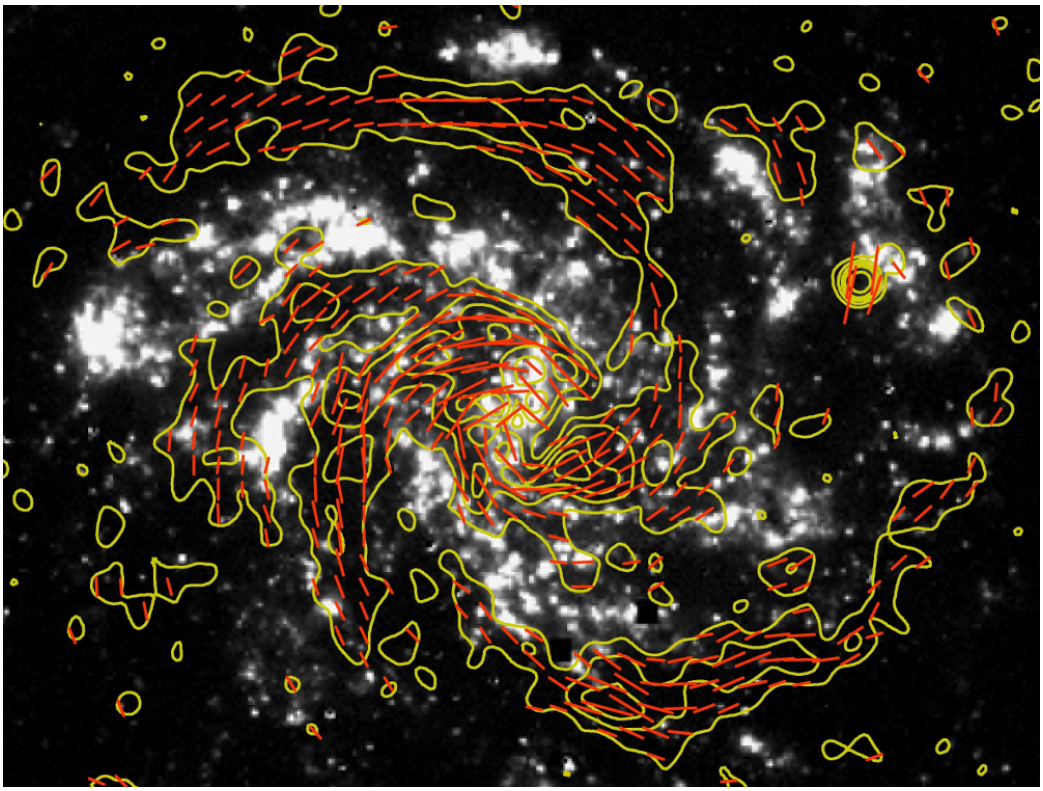

Figure 1.8: Polarized radio emission (contours) and B-vectors of NGC 6946, combined from observations at 6 cm wavelength with the VLA and Effelsberg telescopes (Beck, 2007), overlaid onto an H image. Figure courtesy: MPIfR, Bonn

1.4 Aims of this thesis

- To obtain new solutions to the nonlinear force-free field equation and applying them observed vector magnetograms of photospheric magnetic fields. To use the full three-dimensional solutions to determine topological properties, like free-energy and relative helicity of the coronal magnetic fields, and estimate the energy released in solar flares due to changes in magnetic field topology.

- To estimate the amount of braiding in corona magnetic fields and apply models of Self-Organized Criticality (SOC) to obtain the power-law distribution for peak-flare energies.

- To study gauge invariant forms of magnetic helicity in arbitrary geometries and apply them to the specific cases of solar corona and disc galaxies.

- To apply magnetic helicity conservation and study the nonlinear saturation of dynamo for a disc galaxy in the presence of a force-free corona. We also study the dependence of saturated field strength on the small-scale helicity fluxes.

The thesis aims at using the magnetic helicity conservation and properties of force-free magnetic fields in different astrophysical context. We solve the linear and nonlinear force-free field equation for the case of solar corona through photospheric boundary conditions and use magnetic helicity to estimate the free energy content in these fields, available for release during eruptive events like solar flares. The magnetic helicity conservation is then used as a constraint on the action of turbulent dynamos in disc galaxies, which leads to

[7] http://www3.mpifr-bonn.mpg.de/staff/rbeck/MKSP/Pictures/n6946.jpg

nonlinear saturation of the large-scale field strength. The magnetic helicity flux from the galactic disc forms a corona surrounding the disc during the course of dynamo action, which in its relaxed state, is assumed to follow the linear force-free equation.

1.5 Thesis constituents

The structure of this thesis is arranged into the next eight chapters. Chapter 2 outlines the basics concepts of MHD and describes the processes relating to magnetic field generation and dissipation. We also discuss the topological properties of magnetic field using magnetic helicity and provide a novel prescription for calculating magnetic helicity in arbitrary geometries. Chapter 3 presents a description of potential and force-free fields and outlines their important properties. We then discuss analytical and numerical techniques for solving potential and force-free fields equations for determining coronal magnetic fields. In Chapter 4, we present an overview of various coronal heating mechanisms and discuss the statistical properties of solar flares. We then discuss braiding in coronal magnetic fields and calculate the free energy in these configurations due to braiding. Chapter 5 gives an introduction to large-scale turbulent dynamos and discusses various closure approximations used in mean field MHD. We then present its application to disc galaxies, discuss the basic analytic solutions and give an overview of current problems in dynamo theory. In Chapter 6, we present new solutions to the nonlinear force-free field equation and discuss its application for determining the topological properties of coronal magnetic fields, such as their free-energy and relative helicity. We then apply the solutions to a time sequence of vector magnetograms to estimate the energy released in a solar flare due to change

in magnetic field configuration. In Chapter 7, we use the NLFF field solutions obtained in Chapter 6 and estimate the amount of free-energy due to braiding in these configurations. We then apply a model of SOC to this field and calculate the power-law distribution of flare energies which is then compared with observations. In Chapter 8, we present a model of nonlinear turbulent dynamo applied to a disc galaxy having a force-free corona. We discuss the significance of small-scale magnetic helicity fluxes with regards nonlinear saturation of the dynamo. Chapter 9 then presents a summary of the results from all chapters, highlight the novel aspects of this Thesis with its impact. Then, we present future work which includes papers under preparation.

Chapter 2

Basics of MHD and magnetic helicity

2.1 General principles

In this chapter we develop from basic principles, some useful concepts such as the induction equation, flux freezing of magnetic fields and obtain expressions for magnetic energy and dissipation. We also introduce the basic concepts of magnetic topology and relative helicity. These ideas are important to understand various plasma processes and explain the generation, amplification and dissipation of magnetic fields. In this thesis our aim is to investigate the structure and strength of magnetic fields in two astrophysical settings: the Sun and disc galaxies. In §2.5 [1] , we also provide a new formulation for relative helicity in arbitrary geometries using the toroidal-poloidal representation of the magnetic field and discuss its utility for specific cases of planar and spherical geometry.

The equations of Magnetohydrodynamics (MHD) are the usual electro-

[1] *The work presented in part in §2.5 is in preparation for submission.*

magnetic and hydrodynamic equations, modified to take account of the interaction between the motion and the magnetic field (Cowling, 1976). If $\mathbf{J}$ is the current density, and $\mathbf{B}$ the magnetic field, then from Maxwell's equations (written in SI unites), we get,

$$\nabla \times \mathbf{B} = \mu_0 \mathbf{J}; \quad \nabla \cdot \mathbf{J} = 0. \tag{2.1}$$

where μ_0 is the magnetic permeability. Also if $\mathbf{E}$ is the electric field intensity

$$\nabla \times \mathbf{E} = -\frac{\partial \mathbf{B}}{\partial t}, \quad \nabla \cdot \mathbf{B} = 0. \tag{2.2}$$

If a material in the plasma moves with a velocity $\mathbf{U}$, it is subjected to a total electric field of $\mathbf{E} + \mathbf{U} \times \mathbf{B}$. Thus if σ is the electrical conductivity then

$$\mathbf{J} = \sigma(\mathbf{E} + \mathbf{U} \times \mathbf{B}). \tag{2.3}$$

For a mass density ρ, the hydrodynamic equation of continuity is given by

$$\frac{\partial \rho}{\partial t} + \nabla \cdot (\rho \mathbf{U}) = 0. \tag{2.4}$$

The Euler equation of motion in the presence of force due to gravity $\mathbf{F}$ is given by

$$\rho \frac{\mathrm{d}\mathbf{U}}{\mathrm{d}t} = -\nabla p + \mathbf{F} + \mathbf{F}_{vis} + \mathbf{J} \times \mathbf{B}, \tag{2.5}$$

where p is the pressure, $\mathbf{F}_{vis}$ is the viscous force per unit volume and

$$\frac{\mathrm{d}}{\mathrm{d}t} = \frac{\partial}{\partial t} + \mathbf{U} \cdot \nabla \tag{2.6}$$

In a liquid $\mathbf{F}_{vis}$ is given by

$$\mathbf{F}_{vis} = \rho \nu \nabla^2 \mathbf{U} \tag{2.7}$$

where ν is the kinematic viscosity. If Q is the heat loss per unit volume the heat equation is

$$\rho \frac{\mathrm{d}Q}{\mathrm{d}t} = \frac{p}{\rho} \frac{\mathrm{d}\rho}{\mathrm{d}t} + \varepsilon, \tag{2.8}$$

where ε is the heating effect per unit volume due to viscosity, heat conduction and the flow of electric currents. In uniform liquids

$$\varepsilon = \rho\nu|\nabla \times \mathbf{U}|^2 + \lambda\nabla^2 T + \frac{\mathbf{J}^2}{\sigma}, \tag{2.9}$$

where T is the temperature and λ the thermal conductivity.

2.2 Electromagnetic effects

An equation for the evolution of the magnetic field can be derived by combining Ohm's law and Faraday's law. Assuming σ to be spatially uniform, the Ohm's law is given by equation (2.3). Rearranging the terms in equation (2.3), we get the following expression for the electric field

$$\mathbf{E} = -\mathbf{U} \times \mathbf{B} + \frac{\mathbf{J}}{\sigma}. \tag{2.10}$$

Taking a curl of equation (2.10) we obtain

$$\nabla \times \mathbf{E} = -\nabla \times (\mathbf{U} \times \mathbf{B}) + \frac{1}{\mu_0 \sigma}\nabla \times \nabla \times \mathbf{B}. \tag{2.11}$$

Combining equations (2.2) & (2.11), we get

$$\frac{\partial \mathbf{B}}{\partial t} = \nabla \times (\mathbf{U} \times \mathbf{B}) + \eta\nabla^2 \mathbf{B}, \tag{2.12}$$

where $\eta{=}(\mu_0\sigma)^{-1}$, is called the magnetic diffusivity. Equation (2.12) is known as the induction equation. If the material is at rest, equation (2.12) reduces to the diffusion equation:

$$\frac{\partial \mathbf{B}}{\partial t} = \eta\nabla^2 \mathbf{B}. \tag{2.13}$$

The equation indicates that the field leaks through the material from point to point and decays as oppositely directed fields initially at different points leak together and neutralize each other. Dimensional arguments indicate a

time of decay of order: $\tau = L^2/\eta = \mu_0 \sigma L^2$. For lab conductors, the time of decay is short, say 10 s for a Copper sphere of radius 1 m. For the Sun, $\tau \sim 10^9$years. Thus, magnetic field lines in a large conducting mass leak very slowly. Suppose the material is in motion, and has negligible electrical resistance, then

$$\frac{\partial \mathbf{B}}{\partial t} = \nabla \times (\mathbf{U} \times \mathbf{B}) \,. \tag{2.14}$$

This implies that the field changes are the same as if the magnetic field lines were constrained to move with the material. The ratio of the right hand side (RHS), of equations (2.13) & (2.14) gives us a dimensionless number called the magnetic Reynolds number, R_m, given by:

$$R_m = \frac{vB/L}{\eta B/L^2} = \frac{Lv}{\eta}. \tag{2.15}$$

The transport effects are weak if $Lv >> \eta$ i.e. $R_m >> 1$, which is readily satisfied in astrophysical scenarios.

2.2.1 Frozen in fields

For a medium with infinite conductivity, $\sigma = \infty$, equation (2.10) becomes $\mathbf{E} + \mathbf{U} \times \mathbf{B} = 0$. Under this condition, equation (2.12) reduces to equation (2.14). If we consider any loop S in the plasma, there are two contributions to the change in $\mathbf{B}$ with time. First, there may be changes in magnetic field due to external causes and second, there is a change in flux due to motion of the loop. The first contribution is $\int \frac{\partial \mathbf{B}}{\partial t} \cdot \mathrm{d}\mathbf{S}$. The second component which is due to induced emf produced by the motion of loop given by

$$\int \mathbf{B} \cdot \frac{\partial \mathbf{S}}{\partial t} = \int \mathbf{B} \cdot \frac{\partial}{\partial t} (\mathbf{U} \mathrm{d}t \times \mathrm{d}l) = - \oint (\mathbf{U} \times \mathbf{B}) \cdot \mathrm{d}l = - \int \nabla \times (\mathbf{U} \times \mathbf{B}) \cdot \mathrm{d}\mathbf{S} \tag{2.16}$$

Adding, together both contributions, we obtain

$$\begin{aligned}\frac{\mathrm{d}}{\mathrm{d}t}\int \mathbf{B}\cdot\mathrm{d}\mathbf{S} &= \int \frac{\partial \mathbf{B}}{\partial t}\cdot\mathrm{d}\mathbf{S} - \int \nabla\times(\mathbf{U}\times\mathbf{B})\cdot\mathrm{d}\mathbf{S} \\ &= \int\left(\frac{\partial \mathbf{B}}{\partial t} - \nabla\times(\mathbf{U}\times\mathbf{B})\right)\cdot\mathrm{d}\mathbf{S} = 0. \qquad (2.17)\end{aligned}$$

i.e. the magnetic flux through the loop is constant. In this situation the behavior of field is controlled completely by the motion of fluid. One usually says that the magnetic field is frozen into the medium. If $\mathrm{d}S$ is the normal cross-section of a magnetic flux tube, the strength $B\mathrm{d}S$ of the tube must remain constant as it is carried about with the material. If $\mathrm{d}l$ is the distance along the tube between two neighboring cross-sections, the mass $\rho\mathrm{d}l\mathrm{d}S$ between these sections also remain constant as the tube is carried about. Hence during the motion $B \propto \rho\mathrm{d}l$; i.e. if the motion extends the field lines, it increases B/ρ in the same ratio. Using equations (2.2), (2.4) & (2.14), we can work out the following steps

$$\begin{aligned}&\frac{\partial}{\partial t}\left(\frac{\mathbf{B}}{\rho}\right) + \mathbf{U}\cdot\nabla\left(\frac{\mathbf{B}}{\rho}\right) \\ =\ & \mathbf{B}\frac{\partial}{\partial t}\left(\frac{1}{\rho}\right) + \frac{1}{\rho}\frac{\partial \mathbf{B}}{\partial t} + \frac{1}{\rho}(\mathbf{U}\cdot\nabla)\mathbf{B} + \mathbf{B}(\mathbf{U}\cdot\nabla)\frac{1}{\rho} \\ =\ & -\frac{\mathbf{B}}{\rho^2}\frac{\partial \rho}{\partial t} + \frac{1}{\rho}\nabla\times(\mathbf{U}\times\mathbf{B}) + \frac{1}{\rho}(\mathbf{U}\cdot\nabla)\mathbf{B} + \mathbf{B}(\mathbf{U}\cdot\nabla)\frac{1}{\rho} \\ =\ & \frac{\mathbf{B}}{\rho^2}\nabla\cdot(\rho\mathbf{U}) + \frac{1}{\rho}(\mathbf{B}\cdot\nabla)\mathbf{U} - \frac{1}{\rho}(\mathbf{U}\cdot\nabla)\mathbf{B} + \frac{\mathbf{U}}{\rho}(\nabla\cdot\mathbf{B}) - \frac{\mathbf{B}}{\rho}(\nabla\cdot\mathbf{U}) \\ &+\frac{1}{\rho}(\mathbf{U}\cdot\nabla)\mathbf{B} + \mathbf{B}(\mathbf{U}\cdot\nabla)\frac{1}{\rho} \\ =\ & \frac{\mathbf{B}}{\rho}(\nabla\cdot\mathbf{U}) + \frac{\mathbf{B}}{\rho^2}\mathbf{U}\cdot(\nabla\rho) + \mathbf{B}(\mathbf{U}\cdot\nabla)\frac{1}{\rho} + \frac{1}{\rho}(\mathbf{B}\cdot\nabla)\mathbf{U} - \frac{\mathbf{B}}{\rho}(\nabla\cdot\mathbf{U}) \\ =\ & \frac{\mathbf{B}}{\rho^2}\mathbf{U}\cdot(\nabla\rho) + \mathbf{B}(\mathbf{U}\cdot\nabla)\frac{1}{\rho} + \frac{1}{\rho}(\mathbf{B}\cdot\nabla)\mathbf{U} \\ =\ & \frac{1}{\rho}(\mathbf{B}\cdot\nabla)\mathbf{U} \qquad (2.18)\end{aligned}$$

Equation (2.18) can be integrated to indicate how the field is modified by a given internal displacement of the fluid (Zeldovich, Ruzmaikin, and Sokolov,

1983). If, after a finite time, the position vector $\mathbf{r}$ of a material point has altered to $\mathbf{r}'$; suppose that the field and density at this material point have altered from $\mathbf{B}$ and ρ to $\mathbf{B}'$ and ρ'. Then $\mathbf{B}'/\rho$ is the increment in $\mathbf{r}'$ which corresponds to the initial increment $\mathbf{B}/\rho$ in $\mathbf{r}$. Integrating equation (2.18) we obtain

$$\frac{\mathbf{B}'}{\rho'} - \frac{\mathbf{B}}{\rho} = \int \frac{\mathbf{B}}{\rho} \cdot \nabla \left(\frac{\mathrm{d}\mathbf{r}}{\mathrm{d}t} \right) \mathrm{d}t = \left[\frac{\mathbf{B}}{\rho} \cdot \nabla \mathbf{r}(t) \right]_{t=0}^{t=t'} = \left(\frac{\mathbf{B}}{\rho} \cdot \nabla \right) \mathbf{r}' - \frac{\mathbf{B}}{\rho} \quad (2.19)$$

This gives

$$\frac{\mathbf{B}'}{\rho'} = \left(\frac{\mathbf{B}}{\rho} \cdot \nabla \right) \mathbf{r}'. \quad (2.20)$$

2.2.2 Magnetic Energy and Stresses

The energy density of a magnetic field is given by $\mathbf{B}^2/2\mu_0$ and the total energy W_M, is

$$W = \int \frac{\mathbf{B}^2}{2\mu_0} \mathrm{d}V, \quad (2.21)$$

the integration being over the volume occupied by the field.

The rate of change of energy is given by

$$\begin{aligned} \frac{\mathrm{d}W}{\mathrm{d}t} &= \frac{\mathrm{d}}{\mathrm{d}t} \int \frac{\mathbf{B}^2}{2\mu_0} \mathrm{d}V = \frac{1}{2\mu_0} \int \frac{\partial}{\partial t} (\mathbf{B}^2) \mathrm{d}V = \frac{1}{\mu_0} \int \mathbf{B} \cdot \frac{\partial \mathbf{B}}{\partial t} \mathrm{d}V \\ &= \frac{1}{\mu_0} \int \mathbf{B} \cdot \{ \nabla \times (\mathbf{U} \times \mathbf{B}) + \eta \nabla^2 \mathbf{B} \} \mathrm{d}V. \end{aligned} \quad (2.22)$$

Now

$$\begin{aligned} \mu_0^{-1} \int \eta \mathbf{B} \cdot \nabla^2 \mathbf{B} \mathrm{d}V &= -\mu_0^{-1} \int \eta \mathbf{B} \cdot \nabla \times (\nabla \times \mathbf{B}) \mathrm{d}V \\ &= -\int \eta \mathbf{B} \cdot (\nabla \times \mathbf{J}) \mathrm{d}V \\ &= -\int \eta [\nabla \cdot (\mathbf{J} \times \mathbf{B}) + \mathbf{J} \cdot (\nabla \times \mathbf{B})] \mathrm{d}V \\ &= -\eta \oint (\mathbf{J} \times \mathbf{B}) \cdot \mathrm{d}S - \eta \int \mathbf{J} \cdot (\nabla \times \mathbf{B}) \mathrm{d}V \\ &= -\int \frac{\mathbf{J}^2}{\sigma} \mathrm{d}V. \end{aligned} \quad (2.23)$$

If the volume occupied by the field is infinite, the use of the divergence theorem leads to a surface integral over an infinite sphere. To ensure that this surface integral vanishes, it is sufficient to assume that the current density $\mathbf{J}$ vanishes outside an appropriate finite volume. Thus the η term on the right of equation (2.23) represents the conversion of magnetic energy into Joule heating at the rate $\mathbf{J}^2/\sigma$ per unit volume. Again the $\mathbf{U}$ term on the right of equation (2.22) is

$$\begin{aligned} & \mu_0^{-1} \int \mathbf{B} \cdot [\nabla \times (\mathbf{U} \times \mathbf{B})] \mathrm{d}V \\ = \; & \mu_0^{-1} \int [\nabla \cdot [(\mathbf{U} \times \mathbf{B}) \times \mathbf{B}] + (\mathbf{U} \times \mathbf{B}) \cdot (\nabla \times \mathbf{B})] \mathrm{d}V \\ = \; & \mu_0^{-1} \oint (\mathbf{U} \times \mathbf{B}) \times \mathbf{B} \mathrm{d}s + \mu_0^{-1} \int (\mathbf{U} \times \mathbf{B}) \cdot (\nabla \times \mathbf{B}) \mathrm{d}V \\ = \; & \int (\mathbf{U} \times \mathbf{B}) \cdot \mathbf{J} \mathrm{d}V = - \int \mathbf{U} \cdot (\mathbf{J} \times \mathbf{B}) \mathrm{d}V. \end{aligned} \tag{2.24}$$

Thus this term represents the decrease of magnetic energy because of work done by the magnetic force $\mathbf{J} \times \mathbf{B}$ on the material. This term can be interpreted in terms of Maxwell's stresses. Since $\nabla \times \mathbf{B} = \mu_0 \mathbf{J}$ and $\nabla \cdot \mathbf{B} = 0$,

$$\begin{aligned} \mathbf{J} \times \mathbf{B} &= -\mu_0^{-1} \mathbf{B} \times (\nabla \times \mathbf{B}) = \mu_0^{-1} \left(\frac{1}{2} \nabla \mathbf{B}^2 \right) + (\mathbf{B} \cdot \nabla) \mathbf{B} \\ &= -\nabla \left(\frac{\mathbf{B}^2}{2\mu_0} \right) + \nabla \cdot \left(\frac{\mathbf{B}\mathbf{B}}{\mu_0} \right), \end{aligned} \tag{2.25}$$

where the last term is a dyadic. This equation implies that the force $\mathbf{J} \times \mathbf{B}$ is equivalent to a hydrostatic pressure $B^2/2\mu_0$, together with a tension B^2/μ_0 per unit area along the magnetic flux tubes. If the motion produces no density changes, a hydrostatic pressure does no work. Thus, changes in magnetic energy result solely from work done against the tension B^2/μ_0 along the field lines; any extension of the field lines increases the magnetic energy.

2.3 Magnetic helicity

2.3.1 Introduction

The magnetic helicity of a magnetic-field configuration is defined as:

$$H = \int \mathrm{d}V \ (\mathbf{B} \cdot \mathbf{A}), \quad \mathbf{B} = \nabla \times \mathbf{A}. \tag{2.26}$$

where $\mathbf{A}$ is the vector potential. For a given magnetic field configuration, the vector potential is defined only to within a gauge transformation,

$$\mathbf{A} \rightarrow \mathbf{A}' + \nabla\chi, \tag{2.27}$$

where χ is an arbitrary scalar function of position. The corresponding change in helicity is given by

$$\begin{aligned} H \rightarrow H' &= H + \int \mathrm{d}V \ (\mathbf{B} \cdot \nabla\chi) \\ H' - H &= \int \mathrm{d}V \ \nabla \cdot (\chi\mathbf{B}) = \oint \hat{n} \cdot \mathbf{B}\chi. \end{aligned} \tag{2.28}$$

where the surface integration is taken over the boundary containing the region over which helicity is calculated. The helicity integral is well defined if the field extends over all of space and if $\mathbf{B}$ decreases rapidly with distance. For a magnetic field configuration of finite dimensions, we see that magnetic helicity is well defined if and only if $\hat{n} \cdot \mathbf{B} = 0$ on the boundary surface.

2.3.2 Helicity conservation

The helicity of a magnetic-field configuration is conserved if

1. the field is confined within a closed surface S,

2. $\hat{n} \cdot \mathbf{B} = 0$ at the surface and

3. the field permeates a perfectly conducting medium, that moves in such a way that $\hat{n} \cdot \mathbf{U} = 0$ on S.

From induction equation (2.12):

$$\begin{aligned} \frac{\partial \mathbf{B}}{\partial t} &= \nabla \times (\mathbf{U} \times \mathbf{B}) \\ \nabla \times \frac{\partial \mathbf{A}}{\partial t} &= \nabla \times (\mathbf{U} \times \mathbf{B}) \\ \frac{\partial \mathbf{A}}{\partial t} &= (\mathbf{U} \times \mathbf{B}) + \nabla \chi \end{aligned} \tag{2.29}$$

To calculate the time derivative of the magnetic helicity we write

$$\begin{aligned} \frac{\mathrm{d}H}{\mathrm{d}t} &= \int \mathrm{d}V \left[\frac{\partial \mathbf{A}}{\partial t} \cdot \mathbf{B} + \mathbf{A} \cdot \frac{\partial \mathbf{B}}{\partial t} \right] \\ &= \int \mathrm{d}V \left[\frac{\partial \mathbf{A}}{\partial t} \cdot (\nabla \times \mathbf{A}) + \mathbf{A} \cdot \frac{\partial}{\partial t} (\nabla \times \mathbf{A}) \right]. \end{aligned}$$

The first term in the integral is

$$\int \mathrm{d}V (\mathbf{U} \times \mathbf{B}) \cdot \mathbf{B} + \int \nabla \chi \cdot \mathbf{B} \mathrm{d}V = \int \mathbf{B} \cdot \hat{n} \chi \mathrm{d}S = 0, \tag{2.30}$$

so we can change its sign without affecting the value of the integral. Then

$$\begin{aligned} \frac{\mathrm{d}H}{\mathrm{d}t} &= \int \mathrm{d}V \, \nabla \cdot \left(\frac{\partial \mathbf{A}}{\partial t} \times \mathbf{A} \right) = \hat{n} \cdot \left(\frac{\partial \mathbf{A}}{\partial t} \times \mathbf{A} \right) \\ &= \int \mathrm{d}S \left[\frac{\partial \mathbf{A}}{\partial t} \cdot (\mathbf{A} \times \hat{n}) \right]. \end{aligned}$$

According to our assumptions $\mathbf{B} (= \nabla \times \mathbf{A})$ is perpendicular to $\hat{n}$. So, $\mathbf{A}$ is parallel to $\hat{n}$. Then $\mathbf{A} \times \hat{n} = 0$. Therefore

$$\frac{\mathrm{d}H}{\mathrm{d}t} = 0; \quad H = \text{const.} \tag{2.31}$$

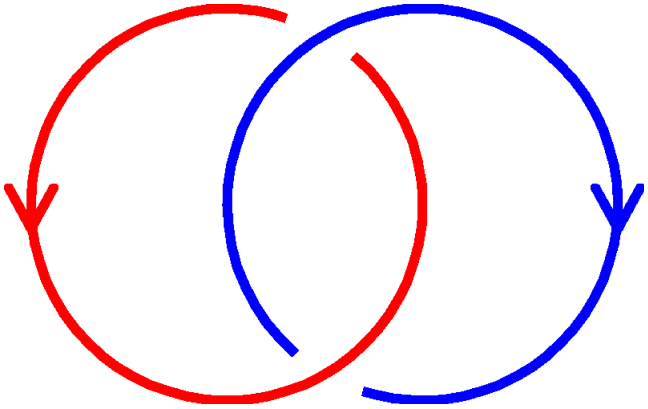

Figure 2.1: Two linked flux tubes.

2.3.3 Self helicity and mutual helicity

Suppose that **B** is identically zero except in two flux-tubes occupying volumes V_1 and V_2 of infinitesimal cross-section following curves C_1 and C_2 fig.(2.1) and let Φ_1 and Φ_2 be the respective fluxes (Moffatt, 1978),

$$H_m = \int_{\mathrm{V_m}} \mathrm{d}V \ \mathbf{A} \cdot \mathbf{B} \quad (m = 1, 2) \tag{2.32}$$

For the configuration drawn, evidently $\mathbf{B}\mathrm{d}V$ may be replaced by $\Phi_1 \mathrm{dx}$ on C_1 and $\Phi_2 \mathrm{dx}$ on C_2 with the result that

$$H_1 = \Phi_1 \oint_{C_1} \mathbf{A} \cdot \mathrm{d}\mathbf{x} = \Phi_1 \Phi_2 \tag{2.33}$$

and similarly

$$H_2 = \Phi_2 \oint_{C_2} \mathbf{A} \cdot \mathrm{d}\mathbf{x} = \Phi_1 \Phi_2 \tag{2.34}$$

More generally, if the tubes link round each other L times (i.e. L is the linking number of C_1 relative to C_2) then $H_1 = H_2 = \pm L \Phi_1 \Phi_2$. The + or - being chosen according to the relative orientation of the curves which may be right- or left-handed. For closed magnetic tubes with $i \neq j, H_{ij} = L_{ij} \Phi_1 \Phi 2$ can be called the mutual helicity. For $i = j$, the term H_{ii} is called the self helicity.

2.3.4 Dissipation of magnetic helicity

In order to estimate the rate of dissipation of magnetic helicity, we first calculate the time-derivative of its density, given by

$$\frac{\partial}{\partial t}(\mathbf{A}\cdot\mathbf{B}) = \frac{\partial \mathbf{A}}{\partial t}\cdot\mathbf{B} + \mathbf{A}\cdot\frac{\partial \mathbf{B}}{\partial t} \tag{2.35}$$

In the presence of resistivity, the induction equation, (2.12) can be rewritten as

$$\nabla\times\frac{\partial \mathbf{A}}{\partial t} = \nabla\times(\mathbf{U}\times\mathbf{B} - \eta\nabla\times\mathbf{B}) \tag{2.36}$$

Uncurling the above equation, we get (using units with $\mu_0 = 1$ for clarity)

$$\frac{\partial \mathbf{A}}{\partial t} = (\mathbf{U}\times\mathbf{B}) - \eta\mathbf{J} + \nabla\chi. \tag{2.37}$$

Taking a dot product of equation (2.37) with $\mathbf{B}$, we get

$$\frac{\partial \mathbf{A}}{\partial t}\cdot\mathbf{B} = \mathbf{U}\times\mathbf{B}\cdot\mathbf{B} - \eta\nabla\times\mathbf{B}\cdot\mathbf{B} + \nabla\chi\cdot\mathbf{B} = -\eta\mathbf{J}\cdot\mathbf{B} + \nabla\cdot(\chi\mathbf{B}). \tag{2.38}$$

Also taking the dot product of equation (2.12) with $\mathbf{A}$, we get

$$\begin{aligned}\mathbf{A}\cdot\frac{\partial \mathbf{B}}{\partial t} &= \mathbf{A}\cdot\frac{\partial}{\partial t}(\nabla\times\mathbf{A}) = \mathbf{A}\cdot\nabla\times\frac{\partial \mathbf{A}}{\partial t} = \nabla\cdot\left(\frac{\partial \mathbf{A}}{\partial t}\times\mathbf{A}\right) + \frac{\partial \mathbf{A}}{\partial t}\cdot\mathbf{B}\\ &= \nabla\cdot\left(\frac{\partial \mathbf{A}}{\partial t}\times\mathbf{A}\right) - \eta\mathbf{J}\cdot\mathbf{B} + \nabla\times(\chi\mathbf{B}).\end{aligned} \tag{2.39}$$

Combining equations (2.35), (2.37) & (2.39), we obtain

$$\frac{\partial}{\partial t}(\mathbf{A}\cdot\mathbf{B}) = \nabla\cdot\left(\frac{\partial \mathbf{A}}{\partial t}\times\mathbf{A}\right) + 2\nabla\cdot(\chi\mathbf{B}) - 2\eta\mathbf{J}\cdot\mathbf{B}. \tag{2.40}$$

Thus, the rate of change of relative helicity is given by (cf. Mangalam, 2008)

$$\frac{\mathrm{d}H}{\mathrm{d}t} = -2\int_V \eta\mathbf{J}\cdot\mathbf{B}\mathrm{d}V + 2\oint_S \chi\mathbf{B}\cdot\hat{n}\mathrm{d}S + \oint_S\left(\frac{\partial \mathbf{A}}{\partial t}\times\mathbf{A}\right)\cdot\hat{n}\mathrm{d}S \tag{2.41}$$

where S is the surface bounding volume V having a normal $\hat{n}$. In absence of helicity transfer across boundaries, the derivative of helicity can then be written as

$$\frac{\mathrm{d}H}{\mathrm{d}t} = -2\int_V \eta\mathbf{J}\cdot\mathbf{B}\mathrm{d}V. \tag{2.42}$$

Let $W = \int \mathbf{B}^2 \mathrm{d}V$ measure the magnetic energy. From equation (2.23), the Ohmic dissipation rate is given by $\left|\frac{\mathrm{dW}}{\mathrm{d}t}\right| = 2\int \eta \mathbf{J}^2 \mathrm{d}V$. The integrals are related by Schwartz inequality (Berger, 1999; Berger, 2013)

$$\begin{aligned} & \frac{1}{2\eta}\left|-\int 2\eta \mathbf{J}\cdot\mathbf{B}\mathrm{d}V\right|^2 \leq \left|\int \mathbf{B}^2\mathrm{d}V\right|\left|\int 2\eta\mathbf{J}^2\mathrm{d}V\right| \\ \Rightarrow \quad & \left|\frac{\mathrm{d}H}{\mathrm{d}t}\right| \leq \sqrt{2\eta \mathrm{W}\left|\frac{\mathrm{dW}}{\mathrm{d}t}\right|} \end{aligned} \tag{2.43}$$

We define a length scale $L \equiv \left|\frac{H}{\mathrm{W}}\right|$, which measures the effective size of helical field structure and a dissipation time scale $\tau_d = \frac{L^2}{\eta}$. Consider an arbitrary reconnection or dissipating process occurring over a time Δt.

$$\begin{aligned} \left(\frac{\mathrm{d}H}{\mathrm{d}t}\right)^2 &\leq 2\eta \frac{H}{L}\frac{1}{L}\frac{\mathrm{d}H}{\mathrm{d}t} \\ \Rightarrow \dot{H}^2 &\leq \frac{1}{\tau_d} 2H\dot{H} \\ \Rightarrow \dot{H}^2 &\leq \frac{1}{\tau_d}\frac{\mathrm{d}H^2}{\mathrm{d}t}. \end{aligned} \tag{2.44}$$

Integrating over time Δt

$$\begin{aligned} \left(\frac{\Delta H}{\Delta \mathrm{t}}\right)^2 &\leq \frac{1}{\tau_d}\frac{H^2}{\Delta \mathrm{t}} \\ \Rightarrow \left(\frac{\Delta H}{H}\right)^2 &\leq \frac{\Delta \mathrm{t}}{\tau_d} \\ \Rightarrow \left(\frac{\Delta H}{H}\right) &\leq \sqrt{\frac{\Delta \mathrm{t}}{\tau_d}}. \end{aligned} \tag{2.45}$$

This inequality shows that ΔH is negligible for any fast reconnection event, where $\Delta \mathrm{t} << \tau_d$. For example, consider a solar flare, where $\Delta \mathrm{t} \approx 1000$ s, $L \approx 10^3$ km and $\eta = 10^{-6}\mathrm{km}^2\mathrm{s}^{-1}$. With these values $\tau_d \approx 10^{12}$ s and $\left|\frac{\Delta H}{H}\right| < 3 \times 10^{-5}$.

2.4 Relative Helicity

The helicity is gauge invariant only if $\mathbf{B} \cdot \hat{n} = 0$ everywhere on the surface. This condition is not satisfied in the case of open field lines. This leads to ambiguity in counting the linkage outside the volume of interest. This is resolved by defining a gauge invariant relative helicity which depends only on the quantities defined within V, relative to an external volume (Berger and Field, 1984), and is hence a physically meaningful quantity. We define a volume external to the volume of interest ($\mathrm{V_a}$) and call it $\mathrm{V_b}$, such that volume $\mathrm{V} = \mathrm{V_a} + \mathrm{V_b}$ has no open field lines i.e. $\mathbf{B} \cdot \hat{n}\mathrm{d}S = 0$ on the surface of V. We construct a hypothetical reference magnetic field $\mathbf{B}_{ref}$ which

1. Equals $\mathbf{B}$ in $\mathrm{V_b}$ but differs in $\mathrm{V_a}$,

2. Has the same normal component on $\mathrm{S_{int}}$ (interface between a and b) as does $\mathbf{B}$ and,

3. Is easily calculated inside $\mathrm{V_a}$.

The simplest magnetic field prescribed by normal boundary condition on the surface is the vacuum magnetic field $\mathbf{B}_{vac}$. The vacuum field satisfies the current-free condition $\nabla \times \mathbf{B}_{vac} = 0 \Rightarrow \mathbf{B}_{vac} = \nabla\chi_{vac}$. Also $\nabla \cdot \mathbf{B}_{vac} = 0$ $\Rightarrow \nabla^2\chi_{vac} = 0$. So, except for a constant, χ_{vac} is completely determined by its normal derivative on the boundary surface (Neumann boundary condition). Also the vacuum field has the minimum energy for a given boundary flux $\mathbf{B} \cdot \hat{n}|_s$.

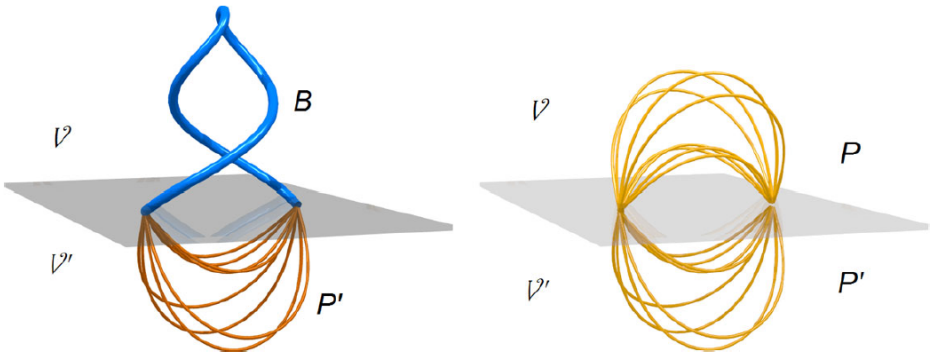

Figure 2.2: The left diagram shows a magnetic field on either side of a boundary. the total helicity of this field is H_{total}. In the right diagram, a vacuum field has replaced the true field in the upper volume. The helicity of this field is H_{ref}; $H_{total} - H_{ref}$ provides a well defined helicity for the upper volume. Figure courtesy: Pevtsov *et al.* (2014).

So, the reference field is constructed as (Bellan, 2013)

$$\mathbf{B}_{ref} = \begin{cases} \mathbf{B}_{vac} & \text{in} \mathrm{V_a} \\ \mathbf{B} & \text{in} \mathrm{V_b} \end{cases}$$
$$\mathbf{A_{ref}} = \begin{cases} \mathbf{A}_{vac} & \text{in} \mathrm{V_a} \\ \mathbf{A} + \nabla \mathrm{h} & \text{in} \mathrm{V_b} \end{cases} \tag{2.46}$$

where $\nabla \times \mathbf{A}_{vac} = \mathbf{B}_{vac}$ in $\mathrm{V_a}$, $\nabla \times \mathbf{A} = \mathbf{B}$ in $\mathrm{V_b}$, $\hat{n_a} \cdot \mathbf{B} = \hat{n_a} \cdot \mathbf{B}_{vac}$ on S and $\nabla \mathrm{h}$ characterizes any allowed difference between $\mathbf{A}$ and $\mathbf{A}_{vac}$ in $\mathrm{V_b}$. An integral over V will have no ambiguities as V has no open field lines. Thus both $H = \int_V \mathbf{A} \cdot \mathbf{B} \mathrm{d}V$ and $H_{ref} = \int_V \mathbf{A_{ref}} \cdot \mathbf{B}_{ref} \mathrm{d}V$ are gauge invariant.

So $H_{rel} = H - H_{ref}$ is also gauge invariant. Therefore,

$$\begin{aligned} H_{rel} &= \int_{V_a} (\mathbf{A}\cdot\mathbf{B} - \mathbf{A_{ref}}\cdot\mathbf{B}_{ref})\,\mathrm{d}V + \int_{V_b} (\mathbf{A} - \mathbf{A_{ref}})\cdot\mathbf{B}\mathrm{d}V \\ &= \int_{V_a} (\mathbf{A}\cdot\mathbf{B} - \mathbf{A}_{vac}\cdot\mathbf{B}_{vac})\,\mathrm{d}V + \int_{V_b} \nabla\mathrm{h}\cdot\mathbf{B}\mathrm{d}V \\ &= \int_{V_a} (\mathbf{A}\cdot\mathbf{B} - \mathbf{A}_{vac}\cdot\mathbf{B}_{vac})\,\mathrm{d}V - \oint_{S_{int}} \mathrm{h}\mathbf{B}\cdot\hat{n_a}\mathrm{dS} \end{aligned} \tag{2.47}$$

Finn and Antonsen (1983) defined the relative helicity as:

$$\begin{aligned} H_{rel}^{FA} &= \int_{V_a} (\mathbf{A} + \mathbf{A}_{vac})\cdot(\mathbf{B} - \mathbf{B}_{vac})\mathrm{d}V \\ &= \int_{V_a} (\mathbf{A}\cdot\mathbf{B} - \mathbf{A}_{vac}\cdot\mathbf{B}_{vac})\mathrm{d}V + \int_{V_a} (\mathbf{A}_{vac}\cdot\mathbf{B} - \mathbf{A}\cdot\mathbf{B}_{vac})\mathrm{d}V \end{aligned} \tag{2.48}$$

now $\quad \mathbf{A}_{vac}\cdot\mathbf{B} - \mathbf{A}\cdot\mathbf{B}_{vac} = \mathbf{A}_{vac}\cdot\nabla\times\mathbf{A} - \mathbf{A}\cdot\nabla\times\mathbf{A}_{vac} = \nabla\cdot(\mathbf{A}\times\mathbf{A}_{vac})$

$$H_{rel}^{FA} = \int_{V_a} (\mathbf{A}\cdot\mathbf{B} - \mathbf{A}_{vac}\cdot\mathbf{B}_{vac})\mathrm{d}V + \int_{V_a} \nabla\cdot(\mathbf{A}\times\mathbf{A}_{vac})\mathrm{d}V \tag{2.49}$$

The last term in the r.h.s. can be written as:

$$\int_V \nabla\cdot(\mathbf{A}\times\mathbf{A}_{vac})\mathrm{d}V = \oint_S (\mathbf{A}\times\mathbf{A}_{vac})\cdot\hat{n}\mathrm{dS} = 0.$$
$$\because \quad \mathbf{B}\cdot\hat{n}\mid_S = \mathbf{B}_{vac}\cdot\hat{n}\mid_S = 0.$$

Since both $\mathbf{A}$ and $\mathbf{A}_{vac}$ are parallel to $\hat{n}$, $\mathbf{A}\times\mathbf{A}_{vac}$ is perpendicular to $\hat{n}$. The surface integral is calculated on a remote surface surrounding $(V_a + V_b)$.

$$\begin{aligned} &\int_{V_a} \nabla\cdot(\mathbf{A}\times\mathbf{A}_{vac})\mathrm{d}V \\ =\ & -\int_{V_b} \nabla\cdot(\mathbf{A}\times\mathbf{A}_{vac})\mathrm{d}V = -\int_{V_b} \nabla\cdot\{(\mathbf{A}_{vac} + \nabla\mathrm{h})\times\mathbf{A}_{vac}\}\,\mathrm{d}V \\ =\ & -\int_{V_b} \nabla\cdot(\nabla\mathrm{h}\times\mathbf{A}_{vac})\mathrm{d}V = \int_{V_b} \nabla\mathrm{h}\cdot\mathbf{B}_{vac}\mathrm{d}V \\ =\ & \oint_{S_{int}} \mathrm{h}\mathbf{B}\cdot\hat{n_b}\mathrm{dS} = -\oint_{S_{int}} \mathrm{h}\mathbf{B}\cdot\hat{n_a}\mathrm{dS}. \end{aligned} \tag{2.50}$$

This form is equivalent to equation (2.47). The advantage of H_{rel}^{FA} is that it involves integration over the volume of interest V_a only.

2.4.1 Relative helicity in different gauges

In section (2.4), we calculated the relative helicity H_R which is both gauge invariant and independent of external field given by Finn and Antonsen (1983). Let $\mathbf{B_v}$ be the vacuum field ($\nabla \times \mathbf{B_v} = 0$) associated with $\mathbf{B}$, i.e. $\mathbf{B_v} \cdot \hat{n}|_S = \mathbf{B} \cdot \hat{n}|_S$.

$$H_R = \int_V (\mathbf{A} + \mathbf{A_v}) \cdot (\mathbf{B} - \mathbf{B_v}) \mathrm{d}V$$

where V is the volume of interest and S being its bounding surface (Mangalam, 2008). If a gauge potential $\nabla\phi$ is added to $\mathbf{A}$ and $\nabla\phi_v$ is added to $\mathbf{A_v}$ then the change in H_R is

$$\int_V \nabla(\phi + \phi_v) \cdot (\mathbf{B} - \mathbf{B_v}) \mathrm{d}V = \oint_S (\phi + \phi_v)(\mathbf{B} - \mathbf{B_v}) \cdot \hat{n} \mathrm{d}S = 0.$$

The boundary conditions on $\mathbf{B_v}$ can be satisfied by choosing the gauges of $\mathbf{A}$ and $\mathbf{A_v}$ so that $\mathbf{A} \times \hat{n}|_S = \mathbf{A_v} \times \hat{n}|_S$. The helicity (Jensen and Chu, 1984) can be written as

$$\begin{aligned} H_R &= \int_V (\mathbf{A} \cdot \mathbf{B} - \mathbf{A_v} \cdot \mathbf{B_v}) \mathrm{d}V + \int_V (\mathbf{A_v} \cdot \mathbf{B} - \mathbf{A} \cdot \mathbf{B_v}) \mathrm{d}V \\ &= \int_V (\mathbf{A} \cdot \mathbf{B} - \mathbf{A_v} \cdot \mathbf{B_v}) \mathrm{d}V + \oint_S \nabla \cdot (\mathbf{A} \times \mathbf{A_v}) \cdot \hat{n} \mathrm{d}S \\ &= \int_V (\mathbf{A} \cdot \mathbf{B} - \mathbf{A_v} \cdot \mathbf{B_v}) \mathrm{d}V \end{aligned} \tag{2.51}$$

on a remote boundary $(\mathbf{A} \times \mathbf{A_v}) \cdot \hat{n} = \mathbf{A_v} \cdot (\hat{n} \times \mathbf{A}) = \mathbf{A_v} \cdot (\hat{n} \times \mathbf{A_v}) = 0$.

We define another set of vector potentials $\mathbf{C_R}$ and $\mathbf{C_v}$ (Berger, 1988) which satisfy the boundary conditions

$$\begin{aligned} \nabla \times \mathbf{C_v} &= \mathbf{B_v} & \nabla \times \mathbf{C_R} &= \mathbf{B} \\ \nabla \cdot \mathbf{C_v} &= 0 & \nabla \cdot \mathbf{C_R} &= 0 \\ \mathbf{C_v} \cdot \hat{n}|_S &= 0 & \mathbf{C_R} \times \hat{n}|_S &= \mathbf{C_v} \times \hat{n}|_S. \end{aligned} \tag{2.52}$$

Furthermore, if V extends to infinity, then $\mathbf{C_R}$ and $\mathbf{C_v}$ must vanish at infinity. To show that these conditions uniquely define $\mathbf{C_v}$, we suppose a different field $\mathbf{C'_v} = \mathbf{C_v} + \nabla\phi$ satisfying the same boundary conditions. Taking the divergence shows that ϕ satisfies the Laplace equation$\nabla^2\phi = 0$. Also $\nabla\phi \cdot \hat{n}|_S = 0$. The only solution possible is $\nabla\phi = 0$ throughout V. Thus $\mathbf{C'_v} = \mathbf{C_v}$. Next suppose $\mathbf{C'_R} = \mathbf{C_R} + \nabla\phi$ satisfies the same boundary conditions as $\mathbf{C_R}$. Again $\nabla^2\phi = 0$ and $\nabla\phi \times \hat{n}|_S = 0$. Thus ϕ is a constant on S implying $\nabla\phi = 0$ in V. Now using eqn (2.51) with $\mathbf{A}$ and $\mathbf{A_v}$ replaced by $\mathbf{C_R}$ and $\mathbf{C_v}$. We write the vacuum field $\mathbf{B_v} = \nabla\psi$ for some scalar ψ. By Gauss theorem,

$$\begin{aligned}\int_V \mathbf{C_v} \cdot \mathbf{B_v} \mathrm{d}V &= \int_V \mathbf{C_v} \cdot \nabla\psi \mathrm{d}V \\ &= \int_V \nabla \cdot (\psi \mathbf{C_v}) \mathrm{d}V - \int_V \psi(\nabla \cdot \mathbf{C_v}) \mathrm{d}V \\ &= \oint_S \psi \mathbf{C_v} \cdot \hat{n} \mathrm{d}S = 0\end{aligned}$$

Thus the relative helicity can now be expressed as

$$H_R = \int_V \mathbf{C_R} \cdot \mathbf{B} \mathrm{d}V \tag{2.53}$$

Thus the gauge invariant H_R can be calculated in the same way as the non invariant ordinary helicity H, but with a special (unique and gauge invariant) vector potential.

2.5 Magnetic helicity in arbitrary geometries

We define the poloidal and toroidal components of magnetic fields as

$$\mathbf{B} = \mathbf{B}_P + \mathbf{B}_T, \quad \mathbf{B}_P = \nabla \times \nabla \times (P\nabla\chi), \quad \mathbf{B}_T = \nabla \times (T\nabla\chi) \tag{2.54}$$

and an operator $\mathbf{L} = -\nabla\chi \times \nabla$, we get $\mathbf{L}P = \nabla P \times \nabla\chi = \nabla \times (P\nabla\chi)$ and

$$\begin{aligned}\mathbf{B}_P &= \nabla \times (\nabla P \times \nabla\chi + P\nabla \times \nabla\chi) = \nabla \times (\nabla P \times \nabla\chi) = \nabla \times \mathbf{L}P \\ \mathbf{B}_T &= \nabla \times (T\nabla\chi) = \nabla T \times \nabla\chi + T\nabla \times \nabla\chi = \mathbf{L}T\end{aligned} \tag{2.55}$$

Combining equations (2.54) & (2.55), we get

$$\mathbf{B} = \nabla \times \mathbf{L}P + \mathbf{L}T = \nabla \times \mathbf{L}P + \nabla \times (T\nabla\chi). \tag{2.56}$$

Uncurling equation (2.56), we get the expression for the vector potential of the magnetic field as

$$\mathbf{A} = \mathbf{L}P + T\nabla\chi + \nabla\psi \tag{2.57}$$

where ψ is an arbitrary gauge function. Now the magnetic helicity density is defined as

$$\begin{aligned} \mathbf{A}\cdot\mathbf{B} &= (\mathbf{L}P + T\nabla\chi + \nabla\psi)\cdot(\nabla\times\mathbf{L}P + \mathbf{L}T) \\ &= \mathbf{L}P\cdot(\nabla\times\mathbf{L}P) + \mathbf{L}P\cdot\mathbf{L}T + T\nabla\psi\cdot(\nabla\times\mathbf{L}P) \\ &+ T\nabla\psi\cdot\mathbf{L}T + \nabla\psi\cdot(\nabla\times\mathbf{L}P) + \nabla\psi\cdot\mathbf{L}T \end{aligned} \tag{2.58}$$

Now $T\nabla\chi\cdot\mathbf{L}T = (T\nabla\chi\cdot\nabla T)\times\nabla\chi = 0$, thus equation (2.58) can be rewritten as

$$\mathbf{A}\cdot\mathbf{B} = \mathbf{L}P\cdot(\nabla\times\mathbf{L}P) + \mathbf{L}P\cdot\mathbf{L}T + T\nabla\psi\cdot(\nabla\times\mathbf{L}P) + \nabla\psi\cdot\mathbf{B}. \tag{2.59}$$

Now, we will evaluate each term in the RHS in equation (2.59) separately. First, we evaluate the following

$$\begin{aligned} &\nabla\times\mathbf{L}P = \nabla\times[\nabla\times(P\nabla\chi)] = \nabla(\nabla\cdot P\nabla\chi) - \nabla^2(P\nabla\chi) \\ &= \nabla(P\nabla^2\chi + \nabla\chi\cdot\nabla P) - \nabla\chi\nabla^2 P - 2(\nabla P\cdot\nabla)\nabla\chi - (P\nabla^2)\nabla\chi \end{aligned} \tag{2.60}$$

and the first term in the RHS in equation (2.59) as

$$\begin{aligned} \mathbf{L}P\cdot\nabla\times\mathbf{L}P &= \nabla P\times\nabla\chi\cdot[\nabla(P\nabla^2\chi + \nabla\chi\cdot\nabla P) \\ &- \nabla\chi\nabla^2 P - (2\nabla P\cdot\nabla)\nabla\chi - P\nabla^2(\nabla\chi)]. \end{aligned} \tag{2.61}$$

Noting that $(\nabla P\times\nabla\chi)\cdot(\nabla\chi\nabla^2 P) = 0$ and $(\nabla P\times\nabla\chi)\cdot P\nabla^2(\nabla\chi) = (\nabla P\times\nabla\chi)\cdot\nabla(P\nabla^2\chi)$. We get the following expression for equation (2.61)

$$\mathbf{L}P\cdot(\nabla\times\mathbf{L}P) = \mathbf{L}P\cdot[\nabla(\nabla\chi\cdot\nabla P) - 2(\nabla P\cdot\nabla)\nabla\chi] \tag{2.62}$$

The first term in the RHS of equation (2.62) can be evaluated as

$$\mathbf{L}P\cdot\nabla(\nabla\chi\cdot\nabla P)=\nabla\cdot[\mathbf{L}P(\nabla\chi\cdot\nabla P)]-(\nabla\chi\cdot\nabla P)\nabla\cdot\mathbf{L}P=\nabla\cdot[\mathbf{L}P(\nabla\chi\cdot\nabla P)] \tag{2.63}$$

as $\nabla\cdot\mathbf{L}P=0$. Thus equation (2.62) can be rewritten as

$$\mathbf{L}P\cdot(\nabla\times\mathbf{L}P)=\nabla\cdot[\mathbf{L}P(\nabla\chi\cdot\nabla P)]-2\mathbf{L}P\cdot(\nabla P\cdot\nabla)\nabla\chi. \tag{2.64}$$

The third term in the RHS of equation (2.59) can be written as

$$T\nabla\chi\cdot(\nabla\times\mathbf{L}P)=\nabla\cdot(\mathbf{L}P\times T\nabla\chi)+\mathbf{L}P\cdot\mathbf{L}T \tag{2.65}$$

Combing equations (2.59), (2.64) & (2.65), we get the following expression for the helicity density

$$\mathbf{A}\cdot\mathbf{B}=\nabla\cdot[\mathbf{L}P(\nabla\chi\cdot\nabla P)]+\nabla\cdot(\mathbf{L}P\times T\nabla\chi)+2\mathbf{L}P\cdot\mathbf{L}T-2\mathbf{L}P\cdot(\nabla P\cdot\nabla)\nabla\chi+\nabla\psi\cdot\mathbf{B}. \tag{2.66}$$

The magnetic helicity is then given by the volume integral of equation (2.66).

2.5.1 Magnetic helicity in planar geometry

The analysis for magnetic helicity given in §2.5 can be followed for the special case of planar geometry by substituting $\nabla\chi=\hat{z}$, where $\hat{z}$ represents the unit vector along the z axis. So, for the planar geometry, we write (cf. Berger, 1985)

$$\mathbf{B}=\mathbf{B}_P+\mathbf{B}_T,\quad \mathbf{B}_P=\nabla\times\nabla\times P\hat{z},\quad \mathbf{B}_T=\nabla\times T\hat{z} \tag{2.67}$$

and $\mathbf{L}=-\hat{z}\times\nabla$. The poloidal and toroidal components of the magnetic field are then given by

$$\mathbf{B}_P = \nabla\times\nabla\times(P\hat{z})=\nabla\times(P\nabla\times\hat{z}+\nabla P\times\hat{z})=\nabla\times\mathbf{L}P \tag{2.68}$$

$$\mathbf{B}_T = \nabla\times(T\hat{z})=\nabla T\times\hat{z}+T\nabla\times\hat{z}=\mathbf{L}T \tag{2.69}$$

Thus the expression for the magnetic field $\mathbf{B}$ and its vector potential $\mathbf{A}$ are given by

$$\mathbf{B} = \nabla \times \mathbf{L}P + \mathbf{L}T, \quad \mathbf{A} = \mathbf{L}P + \hat{z}T + \nabla\psi. \tag{2.70}$$

Thus the expression for the helicity density can now be obtained by substituting $\nabla\chi = \hat{z}$ in equation (2.66) and noting that $(\nabla P \cdot \nabla)\hat{z} = 0$. We then get the magnetic helicity density in planar geometry as

$$\mathbf{A} \cdot \mathbf{B} = \nabla \cdot [(\hat{z} \cdot \nabla P)\mathbf{L}P] + \nabla \cdot (\mathbf{L}P \times \hat{z}T) + 2\mathbf{L}P \cdot \mathbf{L}T + \nabla\psi \cdot \mathbf{B} \tag{2.71}$$

The divergence terms in equation (2.71) vanish upon volume integration, as shown below

$$\int_V \nabla \cdot [(\hat{z} \cdot \nabla P)\mathbf{L}P]\mathrm{d}V = \int_S (\hat{z} \cdot \nabla P)\nabla P \times \hat{z} \cdot \hat{z}\mathrm{d}S = 0 \tag{2.72}$$

$$\int_V \nabla \cdot (\mathbf{L}P \times \hat{z}T)\mathrm{d}V = \int_S \mathbf{L}P \times \hat{z}T \cdot \mathrm{d}S = 0. \tag{2.73}$$

Thus the final expression for magnetic helicity H in planar geometry is given by

$$H = \int_V \mathbf{A} \cdot \mathbf{B}\mathrm{d}V = 2\int_V \mathbf{L}P \cdot \mathbf{L}T\mathrm{d}V + \int_S \psi\mathbf{B} \cdot \hat{z}\mathrm{d}S. \tag{2.74}$$

2.5.2 Magnetic helicity in spherical geometry

For calculating the magnetic helicity in spherical geometry we follow steps similar to that given in §2.5 & §2.5.1 with $\nabla\chi = \mathbf{r}$ (cf. Berger, 1985). The main results are mentioned as follows.

$$\mathbf{B} = \mathbf{B}_P + \mathbf{B}_T, \quad \mathbf{B}_P = \nabla \times \nabla \times (P\mathbf{r}) = \nabla \times \mathbf{L}P, \quad \mathbf{B}_T = \nabla \times (T\mathbf{r}) = \mathbf{L}T. \tag{2.75}$$

with $\mathbf{L} = -\mathbf{r} \times \nabla$. The helicity density is given by substituting $\nabla\chi = \mathbf{r}$ in equation (2.66) as

$$\mathbf{A}\cdot\mathbf{B} = \nabla\cdot[(\mathbf{r}\cdot\nabla P)\mathbf{L}P] + \nabla\cdot(\mathbf{L}P\times\mathbf{r}T) + 2\mathbf{L}P\cdot\mathbf{L}T - 2\mathbf{L}P\cdot(\nabla P\cdot\nabla)\mathbf{r} + \nabla\psi\cdot\mathbf{B}. \tag{2.76}$$

Now we can write

$$(\nabla P \cdot \nabla)\mathbf{r} = (\nabla \mathbf{r} \cdot \nabla P) - \nabla P \times (\nabla \times \mathbf{r}) = \nabla P \cdot \mathbf{1} = \nabla P \tag{2.77}$$

where $\mathbf{1}$ is the unit dyadic. Thus the second last term in RHS of equation (2.76) becomes

$$\mathbf{L}P \cdot (\nabla P \cdot \nabla)\mathbf{r} = (\nabla P \times \mathbf{r}) \cdot \nabla P = 0, \tag{2.78}$$

since in this case $\mathbf{L}P = \nabla P \times \mathbf{r}$. Equation (2.76) now reduces to

$$\mathbf{A} \cdot \mathbf{B} = \nabla \cdot [(\mathbf{r} \cdot \nabla P)\mathbf{L}P] + \nabla \cdot (\mathbf{L}P \times \mathbf{r}T) + 2\mathbf{L}P \cdot \mathbf{L}T + \nabla\psi \cdot \mathbf{B}. \tag{2.79}$$

The divergence terms in the RHS of equation (2.79) vanish upon volume integration as shown below

$$\int_V \nabla \cdot [(\mathbf{r} \cdot \nabla P)\mathbf{L}P]\mathrm{d}V = \int_S (\mathbf{r} \cdot \nabla P)(\nabla P \times \mathbf{r}) \cdot \hat{r}\mathrm{d}S = 0 \tag{2.80}$$

$$\int_V \nabla \cdot (\mathbf{L}P \times \mathbf{r}T)\mathrm{d}V = \int_S \mathbf{L}P \times \mathbf{r}T \cdot \hat{r}\mathrm{d}S = 0. \tag{2.81}$$

Thus the final expression for magnetic helicity for spherical geometry is given by

$$H = \int_V \mathbf{A} \cdot \mathbf{B}\mathrm{d}V = 2\int_V \mathbf{L}P \cdot \mathbf{L}T\mathrm{d}V + \int_S \psi\mathbf{B} \cdot \hat{r}\mathrm{d}S. \tag{2.82}$$

The gauge-invariant expression for magnetic helicity for planar and spherical geometry corresponding to equations (2.74) & (2.83)

$$H = \int_V \mathbf{A} \cdot \mathbf{B}\mathrm{d}V = 2\int_V \mathbf{L}P \cdot \mathbf{L}T\mathrm{d}V. \tag{2.83}$$

was previously obtained in Berger (1985). In the context of constant-α force-free fields (discussed in Chapter 3), it is shown that if the volume of a spherical shell region is increased indefinitely holding the helicity constant, then α tends to zero. This means that the magnetic field asymptotically relaxes to

a potential field while conserving the helicity, which is possible only if reconnection is allowed over a large volume. It is also found that even though for a given boundary condition and helicity, there may exist several α eigenvalues, but only the lowest α state, having the minimum energy for the given helicity, is stable against all helicity-preserving fixed-boundary perturbations.

2.5.3 Absolute magnetic helicity in cylindrical coordinates

Low (2006) present a primitive form of magnetic helicity that is based on a general partitioning of an ideal hydromagnetic fluid into disjoint, infinitesimally thin, toroidal sub volumes using a two-flux description of the embedded magnetic field. Here each of these toroidal sub volumes of fluid is endowed with a gauge-independent magnetic helicity conserved during its ideal Lagrangian evolution. The magnetic field is represented using the Chandrasekhar-Kendall (C-K) representation in cylindrical coordinates as (Low, 2011)

$$\mathbf{B} = \mathbf{B}_\phi + \mathbf{B}_\psi, \tag{2.84}$$

where $\mathbf{B}_\phi$ and $\mathbf{B}_\psi$ are given by

$$\mathbf{B}_\phi = \nabla \times \phi\hat{z} = \frac{1}{R}\frac{\partial \phi}{\partial \varphi}\hat{R} - \frac{\partial \phi}{\partial R}\hat{\varphi}, \tag{2.85}$$

$$\begin{aligned}\mathbf{B}_\psi &= \nabla \times (\nabla \times \psi\hat{z}) = -(\nabla_\perp \psi)\hat{z} + \frac{\partial^2 \psi}{\partial z \partial R}\hat{R} + \frac{1}{R}\frac{\partial^2 \psi}{\partial z \partial \varphi}\hat{\varphi} \\ &= -(\nabla^2 \psi)\hat{z} + \nabla \frac{\partial \psi}{\partial z},\end{aligned} \tag{2.86}$$

for the scalar functions ϕ and ψ. The subscript $\perp$ denotes derivatives in the $R - \varphi$ plane. The induction equation (2.12) takes the form (Low, 2011)

$$\nabla \times \left(\nabla \times \frac{\partial \psi}{\partial t}\hat{z}\right) + \nabla \times \frac{\partial \phi}{\partial t}\hat{z} = \nabla \times (\mathbf{U} \times [\nabla \times (\nabla \times \psi\hat{z}) + (\nabla \times \phi\hat{z})]). \tag{2.87}$$

Considering the domain $V(L_0) : |z| < L_0;\ 0 < R < R_0$, a cylinder of length $2L_0$ and radius R_0. The boundaries are taken as rigid, perfect electrical conductors. Assuming the field is tangential on $R = R_0$ and threads across $z = \pm L_0$, the variables ψ, ϕ and $\mathbf{U}$ are subject to the following boundary conditions

$$\begin{aligned} U_R|_{R=R_0} &= 0, \quad \phi|_{R=R_0} = 0, && (2.88)\\ \frac{\partial\psi}{\partial R}|_{R=R_0} &= -\frac{F_0}{2\pi R_0}, \quad \psi|_{z=\pm L_0} = \psi_\pm(R,\varphi), && (2.89)\\ \mathbf{U}|_{z=\pm L_0} &= 0, && (2.90) \end{aligned}$$

where $\psi_\pm$ is the solution of

$$\nabla_\perp^2 \psi = -B_z(R,\varphi,z), \tag{2.91}$$

with the prescribed B_z at $z = \pm L_0$. The absolute helicity for this system is then defined as

$$H_{abs}[\mathbf{B};V] = \int_V (\nabla\times\psi\hat{z})\cdot[\nabla\times(\nabla\times\psi\hat{z}) + 2(\nabla\times\phi\hat{z})\mathrm{d}V. \tag{2.92}$$

The absolute helicity, H_{abs} can be shown to be a constant of motion. There is no issue of gauge dependence because ϕ and ψ are uniquely defined in the helicity density

$$h_{abs}(\psi,\phi) = (\nabla\times\psi\hat{z})\cdot[\nabla\times(\nabla\times\psi\hat{z}) + 2(\nabla\times\phi\hat{z})]. \tag{2.93}$$

Similarly, the magnetic vector potential defined as

$$\mathbf{A} = \nabla\times\psi\hat{z} + \phi\hat{z} \tag{2.94}$$

is a physically well defined quantity. The rate of change of the absolute helicity can be shown to be written in terms of surface integrals as (Low, 2011)

$$\frac{\mathrm{d}H_{abs}}{\mathrm{d}t} = S_1 + S_2 + S_3, \tag{2.95}$$

where the expressions for S_1, S_2 and S_3 are defined below.

$$\begin{aligned} S_1 &= 2\int_{\partial V}[(\mathbf{U}\times\mathbf{B})\times\mathbf{A}]\cdot\mathrm{d}\mathbf{S} \\ &= 2\int_{\partial V}[(\mathbf{A}\cdot\mathbf{U})\mathbf{B}-(\mathbf{A}\cdot\mathbf{B})\mathbf{U}]\cdot\mathrm{d}\mathbf{S}, \end{aligned} \tag{2.96}$$

where ∂V denotes the rigid boundaries $R = R_0$ and $z = \pm L_0$. On $R = R_0$, the normal components of $\mathbf{B}$ and $\mathbf{U}$ vanish. On $z = \pm L_0$, the normal component of $\mathbf{U}$ vanish by the rigid boundary condition. But the tangential components of $\mathbf{U}$ must also vanish for the continuity of the tangential electric field since the normal component of $\mathbf{B}$ is nonzero. Thus, $S_1 = 0$. The second integral is given by

$$S_2 = -\int_{\partial V}\left[\left(\nabla\times\frac{\partial\psi}{\partial t}\hat{z}\right)\times(\nabla\times\psi\hat{z})\right]\cdot\mathrm{d}\mathbf{S}. \tag{2.97}$$

The contribution from $R = R_0$ vanishes because $\hat{z}\cdot\mathrm{d}\mathbf{S} = 0$ on that surface. On $z \pm L_0$, the boundary value of ψ is independent of time and $\nabla\dfrac{\partial\psi}{\partial t}\times\hat{z}$ evaluated on that boundary has only derivatives in R and φ. Hence, $S_2 = 0$. Finally, we have

$$S_3 = 2\int_{\partial V}\left[\left(\nabla\times\frac{\partial\psi}{\partial t}\hat{z}\right)\times\phi\hat{z}\right]\cdot\mathrm{d}\mathbf{S} = 0, \tag{2.98}$$

because $\phi = 0$ on $R = R_0$ and the integral vanishes on $z = \pm L_0$ by the property that $\mathrm{d}\mathbf{S}$ is parallel to $\hat{z}$ on that boundary. Hence,

$$\frac{\mathrm{d}H_{abs}}{\mathrm{d}t} = 0, \tag{2.99}$$

and hence H_{abs} is a constant. We use the gauge invariant helicity density given in equation (2.93) in Chapter 8 to calculate the magnetic helicity for linear force-free fields present in the corona of a disc galaxy. In the following chapter, we know give a description of force-free fields and its properties.

Chapter 3

Force free fields

In this chapter, we discuss the simplest possible configurations of coronal fields, namely: potential and force-free fields, that can be derived from photospheric fields (in the case of the Sun) or from the fields specified at the disc surface (in case of a galaxy).

3.1 Potential magnetic fields

We start with a description of the potential fields, which are the simplest. If the current density vanishes everywhere, then from equation (2.1), we get $\nabla \times \mathbf{B} = 0$. We can thus express the magnetic field as

$$\mathbf{B} = \nabla\Psi, \tag{3.1}$$

where Ψ is the scalar magnetic potential. Applying the condition $\nabla \cdot \mathbf{B} = 0$, we get

$$\nabla^2\Psi = 0. \tag{3.2}$$

Such fields are called potential magnetic fields. The solutions of equation (3.2), Ψ can be uniquely determined within a closed volume if the normal

component of the magnetic field ($\partial\Psi/\partial n \equiv B_n$) are specified on the boundary. Potential fields are of particular interest in solar physics. For a semi-infinite region such as the solar atmosphere above the photosphere (which can be taken as plane or a spherical surface with large radius), for a specified normal field at the photosphere, the potential fields contain the smallest amount of magnetic energy (given by equation 2.21) provided that there are no sources at infinity and the field falls of faster than R^{-2} at large distances R. The basic proof for this theorem is given as follows (Priest, 2014).

We start with a potential field $\mathbf{B}_0$ and write any other arbitrary magnetic field with the same normal boundary conditions at a surface S as $\mathbf{B} = \mathbf{B}_0 + \mathbf{B}_1$, such that $B_n = B_{0n}$ and $B_{1n} = 0$. The magnetic energy of this field using equation (2.21) can be written as

$$W = \int \frac{B^2}{2\mu_0} \mathrm{d}V = \int \frac{(\mathbf{B}_0 + \mathbf{B}_1) \cdot (\mathbf{B}_0 + \mathbf{B}_1)}{2\mu_0} \mathrm{d}V = \int \frac{B_0^2 + 2\mathbf{B}_0 \cdot \mathbf{B}_1 + B_1^2}{2\mu_0} \mathrm{d}V. \tag{3.3}$$

Using equation (3.1), we can write

$$\begin{aligned} \int \mathbf{B}_0 \cdot \mathbf{B}_1 \mathrm{d}V &= \int (\nabla\Psi_0) \cdot \mathbf{B}_1 \mathrm{d}V = \int \nabla \cdot (\Psi_0 \mathbf{B}_1) - \Psi_0 (\nabla \cdot \mathbf{B}_1) \mathrm{d}V \\ &= \int \hat{\mathbf{n}} \cdot (\Psi_0 \mathbf{B}_1) \mathrm{d}S = \int \Psi_0 B_{1n} \mathrm{d}S = 0 \end{aligned} \tag{3.4}$$

as $B_{1n} = 0$ on S. Thus equation (3.3) now reduces to

$$W = \int \frac{B^2}{2\mu_0} \mathrm{d}V = \int \frac{B_0^2 + B_1^2}{2\mu_0} \mathrm{d}V. \tag{3.5}$$

Since $B_1^2 > 0$, the energy of the magnetic field given in equation (3.5) will always be greater than that of a potential field $\left(= \int \frac{B_0^2}{2\mu_0} \mathrm{d}V \right)$.

Below we present the standard solutions to equation (3.2) obtained using the method of separation of variables for different coordinate systems (Priest, 2014).

1. *Cartesian coordinates (x, y, z)*: For a solution above the $x-y$ plane that decays for large values of z, we can write

$$\Psi(x,y,z) = a\exp(ik_x x + ik_y y - kz), \tag{3.6}$$

where $k_x,\ k_y,\ k\ > 0$ are real and $k^2 = k_x^2 + k_y^2$. If the field is periodic and vanishes on the sides $x = 0$, $y = 0$, $x = a$ and $y = b$, the general solution can be written as

$$\Psi = \sum_{n=0}^{\infty}\sum_{m=0}^{\infty} a_{nm}\sin\left(\frac{2n\pi x}{a}\right)\sin\left(\frac{2m\pi y}{b}\right)\exp(k_{nm}z), \tag{3.7}$$

where $k_{nm}^2 = (2n\pi/a)^2 + (2m\pi/a)^2$ and the coefficients a_{nm} can be written in terms of B_z prescribed at $z = 0$.

2. *Spherical polar coordinates (r, θ, φ)*: The general solution is given by

$$\Psi(r,\theta,\phi) = \sum_{l=0}^{\infty}\sum_{m=-l}^{l}\left[a_{lm}r^l + b_{lm}r^{-(l+1)}\right]P_l^m(cos\theta)\exp(im\phi), \tag{3.8}$$

where P_l^m are the associated Legendre polynomials. For axisymmetric fields, the solutions are independent of ϕ and can be written as

$$\Psi(r,\theta) = \sum_{l=0}^{\infty}\left[a_l r^l + b_l r^{-(l+1)}\right]P_l(cos\theta), \tag{3.9}$$

where P_l represents the Legendre polynomials.

3. *Cylindrical coordinates (R, φ, z)*: The general solution can be written as

$$\Psi(R,\phi,z) = \sum_{n=-\infty}^{\infty}\left[c_n J_n(kR) + d_n Y_n(kR)\right]\exp(in\phi \pm kz), \tag{3.10}$$

where J_n and Y_n are Bessel functions.

The magnetic field in the solar corona can be expected to be potential if the following conditions are satisfied: magnetic pressure dominates over plasma pressure, the region contains no magnetic helicity, and photospheric perturbations are small enough that the field can reduce to its minimum energy configuration. Several techniques have been used to find potential fields, either for a local part of the corona (treated as a plane) or for the global corona (treated as a sphere). There are two main techniques for calculating potential fields, when treating the coronal base as a plane. The first, called the *Green's function* method (Schmidt, 1964), places a series of monopoles on the lower boundary at points $(x', y', 0)$, each having a magnetic flux $B_n \mathrm{d}x'\mathrm{d}y'$. As the magnetic potential from a single source of half-flux F_m at a distance r is $-F_m/(\pi r)$, the resulting potential at (x, y, z) due to the normal magnetic field $B_n(x', y')$ on $z = 0$ is (Priest, 2014)

$$\Psi(x, y, z) = \int B_n(x', y') G_n(x, y, z, x', y') \mathrm{d}x'\mathrm{d}y', \tag{3.11}$$

where $G_n(x, y, z, x', y') = -1/(\pi|\mathbf{r} - \mathbf{r}'|)$ is the Green's function and $|\mathbf{r} - \mathbf{r}'|$ is the distance between (x, y, z) and $(x', y', 0)$.

The second technique, called the *Fourier expansion* method is to expand the boundary value in its Fourier components over appropriate values of k_x and k_y as

$$B_n(x, y) = B_0 + \sum_{\mathbf{k}} B_{\mathbf{k}} \exp(ik_x x + ik_y y), \tag{3.12}$$

whose solution obtained using equation (3.6) is given by (Priest, 2014)

$$\Psi(x, y, z) = B_0 z - \sum_{\mathbf{k}} \frac{B_{\mathbf{k}}}{k} \exp(ik_x x + ik_y y - kz). \tag{3.13}$$

Sakurai (1982) adapted the Green's function technique for a spherical surface while treating the coronal base as a sphere. Altschuler and Newkirk (1969) on the other hand, approximate the global magnetic field line by a

series (equation 3.8) whose coefficients are determined by matching it with the photospheric field. More detailed global MHD models have been used in Mikić *et al.* (2007), Linker *et al.* (2011) and Riley, Linker, and Mikič (2013).

3.2 Force-free magnetic field

The Lorentz force dominates the pressure gradient and gravitational force in equation (2.5) in systems having low plasma beta, defined as the ratio of plasma pressure p_0 and magnetic pressure, $\beta = (2\mu_0 p_0)/B_0^2$, the systems achieves equilibrium under the condition

$$\mathbf{J} \times \mathbf{B} = 0. \tag{3.14}$$

This implies that the electric current density has a direction parallel to the magnetic field. Using equation (2.1), we can write

$$\nabla \times \mathbf{B} = \alpha \mathbf{B}, \tag{3.15}$$

where α is a scalar function of space. Taking a divergence of equation (3.15) and using $\nabla \cdot \mathbf{B} = 0$, we get

$$(\mathbf{B} \cdot \nabla)\alpha = 0. \tag{3.16}$$

This implies that the scalar function α remains constant along any given magnetic field line. If α is independent of space, then we obtain the *linear* or *constant-α* force-free fields. In this case, taking the curl of equation (3.15) gives us the vector Helmholtz equation,

$$(\nabla^2 + \alpha^2)\mathbf{B} = 0. \tag{3.17}$$

Equation (3.17) is easier to solve compared to the more general *nonlinear* force-free field problem where α varies as a function of space.

3.2.1 Properties of force-free fields

3.2.1.1 Virial theorem for magnetic energy

In order to estimate the energy in force-free fields using the Virial theorem, we start with the following volume integral (Chandrasekhar, 1961)

$$\int_V \mathbf{r}\cdot(\mathbf{J}\times\mathbf{B})\mathrm{d}V = \int_V \nabla\times\mathbf{B}\cdot(\mathbf{B}\times\mathbf{r})\mathrm{d}\mathbf{B}. \tag{3.18}$$

Using the identity

$$\int_V \Phi\cdot\nabla\times\Psi\mathrm{d}V = \int_V \Psi\cdot\nabla\times\Phi\mathrm{d}V - \int_S(\Phi\times\Psi)\cdot\mathrm{d}\mathbf{S} \tag{3.19}$$

and substituting $\Psi=\mathbf{B}$ and $\Phi=\mathbf{B}\times\mathbf{r}$, we get upon rearranging

$$\int_V \mathbf{r}\cdot(\nabla\times\mathbf{B}\times\mathbf{B})\mathrm{d}V = \int_V \mathbf{B}\cdot[\nabla\times(\mathbf{B}\times\mathbf{r})]\mathrm{d}V - \int_S(\mathbf{B}\times\mathbf{r})\times\mathbf{B}\cdot\mathrm{d}\mathbf{S} \tag{3.20}$$

The last term in the RHS of equation (3.20) can be written as

$$\int_S(\mathbf{B}\times\mathbf{r})\times\mathbf{B}\cdot\mathrm{d}\mathbf{S} = \int_S|\mathbf{B}|^2\mathbf{r}\cdot\mathrm{d}\mathbf{S} + \int_S(\mathbf{B}\cdot\mathbf{r})(\mathbf{B}\cdot\mathrm{d}\mathbf{S}) \tag{3.21}$$

while the first terms in the RHS of equation (3.20) can be calculated through the following steps

$$\begin{aligned}
&\int_V \mathbf{B}\cdot[\nabla\times(\mathbf{B}\times\mathbf{r})]\mathrm{d}V\\
=\;&\int_V \mathbf{B}\cdot[\mathbf{B}(\nabla\cdot\mathbf{r}) - \mathbf{r}(\nabla\cdot\mathbf{B}) + (\mathbf{r}\cdot\nabla)\mathbf{B} - (\mathbf{B}\cdot\nabla)\mathbf{r}]\mathrm{d}V\\
=\;&\int_V 3|\mathbf{B}|^2\mathrm{d}V + \mathbf{B}\cdot[(\mathbf{r}\nabla)\mathbf{B} - (\mathbf{B}\cdot)\mathbf{r}]\mathrm{d}V\\
=\;&2\int_V|\mathbf{B}|^2\mathrm{d}V + \frac{1}{2}\int_V\mathbf{r}\cdot\nabla|\mathbf{B}|^2\mathrm{d}V\\
=\;&\frac{1}{2}\int_V|\mathbf{B}|^2\mathrm{d}V + \frac{1}{2}\int_S|\mathbf{B}|^2\mathbf{r}\cdot\mathrm{d}\mathbf{S}.
\end{aligned} \tag{3.22}$$

Substituting equations (3.21) & (3.22) into equation (3.20), we get

$$\int_V \mathbf{r}\cdot(\nabla\times\mathbf{B}\times\mathbf{B})\mathrm{d}V = \frac{1}{2}\int_V|\mathbf{B}|^2\mathrm{d}V - \frac{1}{2}\int_S|\mathbf{B}|^2\mathbf{r}\cdot\mathrm{d}\mathbf{S} + \int_S(\mathbf{B}\cdot\mathbf{r})(\mathbf{B}\cdot\mathrm{d}\mathbf{S}). \tag{3.23}$$

For force-free fields $\nabla \times \mathbf{B} \times \mathbf{B} = 0$, thus equation (3.23) reduces to

$$\frac{1}{2}\int_V |\mathbf{B}|^2 \mathrm{d}V = \frac{1}{2}\int_S |\mathbf{B}|^2 \mathbf{r} \cdot \mathrm{d}\mathbf{S} - 2\int_S (\mathbf{B}\cdot\mathbf{r})(\mathbf{B}\cdot\mathrm{d}\mathbf{S}). \tag{3.24}$$

Rewriting equation (3.24) in terms of the magnetic energy, we get

$$W = \int_V B^2/(2\mu_0)\mathrm{d}V = \int_S [(\mathbf{r}\cdot\mathbf{B})\mathbf{B} - \frac{1}{2}B^2\mathbf{r}]\cdot\mathrm{d}\mathbf{S}/\mu_0. \tag{3.25}$$

The magnetic virial theorem thus allows us to calculate the magnetic energy contained in a coronal force-free magnetic field by a surface integral at the photospheric boundary involving the three components of the vector magnetic field (Klimchuk, Canfield, and Rhoads, 1992).

3.2.1.2 Woltjer's theorem

Consider the following problem (Sturrock, 1994): What is the magnetic-field configuration when the plasma relaxes to a state that minimizes the magnetic energy, subject to the constraint that the magnetic helicity is constant? We have to minimize the magnetic energy $\left(\frac{1}{8\pi}\int_V |\nabla\times\mathbf{A}|^2\,\mathrm{d}V\right)$ subject to the condition that magnetic helicity $\left(\int_V \mathbf{A}\cdot\nabla\times\mathbf{A}\mathrm{d}V\right)$ is conserved (Woltjer, 1958). Then

$$\delta\int_V \left(|\nabla\times\mathbf{A}|^2 - \alpha\mathbf{A}\cdot\nabla\times\mathbf{A}\right)\mathrm{d}V = 0 \tag{3.26}$$

Expanding the above equation, we can write

$$\int_V [2(\nabla\times\mathbf{A})\cdot(\nabla\times\delta\mathbf{A}) - \alpha(\delta\mathbf{A}\cdot\nabla\times\mathbf{A} + \mathbf{A}\cdot\nabla\times\delta\mathbf{A})]\mathrm{d}V = 0. \tag{3.27}$$

$$\begin{aligned}\text{Now}\int_V (\mathbf{A}\cdot\nabla\times\delta\mathbf{A})\mathrm{d}V &= \int_V (\nabla\times\mathbf{A})\cdot\delta\mathbf{A}\mathrm{d}V - \int_V \nabla\cdot(\mathbf{A}\times\delta\mathbf{A})\mathrm{d}V \\ &= \int_V (\nabla\times\mathbf{A})\cdot\delta\mathbf{A}\mathrm{d}V - \oint_S (\mathbf{A}\times\delta\mathbf{A})\cdot\mathrm{d}\mathbf{S}\end{aligned}$$

The surface integral vanishes as $\delta\mathbf{A}$ is taken to be zero on the boundary, and thus

$$\int_V (\mathbf{A}\cdot\nabla\times\delta\mathbf{A})\mathrm{d}V = \int_V (\nabla\times\mathbf{A})\cdot\delta\mathbf{A}\mathrm{d}V$$

$$\begin{aligned}\text{Also}\qquad & \int_V (\nabla\times\mathbf{A})\cdot(\nabla\times\delta\mathbf{A})\mathrm{d}V \\ = & \int_V \delta\mathbf{A}\cdot\nabla\times(\nabla\times\mathbf{A})\mathrm{d}V - \int_V \nabla\cdot(\nabla\times\mathbf{A}\times\delta\mathbf{A})\mathrm{d}V \\ = & \int_V \delta\mathbf{A}\cdot\nabla\times(\nabla\times\mathbf{A})\mathrm{d}V - \oint_S (\nabla\times\mathbf{A}\times\delta\mathbf{A})\cdot\mathrm{d}\mathbf{S}\end{aligned}$$

Dropping the surface integral as $\delta\mathbf{A}=0$ on the boundary, we get

$$\begin{aligned}& \int_V (\nabla\times\mathbf{A})\cdot(\nabla\times\delta\mathbf{A})\mathrm{d}V = \int_V \nabla\times(\nabla\times\mathbf{A})\cdot\delta\mathbf{A}\mathrm{d}V \\ \Rightarrow\qquad & \int_V (\nabla\times(\nabla\times\mathbf{A}) - \alpha\nabla\times\mathbf{A})\cdot\delta\mathbf{A}\mathrm{d}V = 0. \qquad (3.28)\end{aligned}$$

Since $\delta\mathbf{A}$ is arbitrary, the integrand must vanish identically and we must have

$$\begin{aligned}& \nabla\times\nabla\times\mathbf{A} - \alpha\nabla\times\mathbf{A} = 0. \\ \Rightarrow\qquad & \nabla\times\mathbf{B} = \alpha\mathbf{B}. \qquad (3.29)\end{aligned}$$

Thus the force-free fields with a constant α represents the lowest state of magnetic energy which a closed system can attain. This has two important consequences:

1. It proves in a general way the stability of force-free field with constant α.

2. It shows that in a system which the magnetic forces are dominant and in which there is a mechanism to dissipate the fluid motions, the force-free fields with a constant α are the natural end configurations.

3.2.1.3 Taylor's hypothesis

Taylor (1974, 1976) pointed out that in a perfectly conducting plasma the magnetic helicity $H = \int_V \mathbf{A} \cdot \mathbf{B} \mathrm{d}V$ is an invariant for every infinitesimal tube. The minimum-energy field subject to this constraint is given by the nonlinear force-free fields $\nabla \times \mathbf{B} = \alpha(\mathbf{r})\mathbf{B}$, where $\alpha(\mathbf{r})$ is constant for a given field line. Taylor suggested that even for non-ideal systems having a large magnetic Reynolds number, the magnetic field topology changes are accompanied with small changes in the total magnetic helicity in such a way that the helicity density $(\mathbf{A} \cdot \mathbf{B})$ is redistributed among the field lines but its integral over all field lines, the magnetic helicity H remains unchanged. A more general class of force-free fields is obtained when the energy of the system is minimized with constraints of total mass, angular momentum, cross helicity, and relative helicity (Mangalam and Krishan, 2000).

3.3 Solutions to linear force-free fields

Here we discuss axisymmetric solutions to linear force-free fields which where first presented in Chandrasekhar (1956). Any axisymmetric magnetic field can be expressed as the sum of a toroidal field T and a poloidal field ψ given by

$$\mathbf{B} = \hat{z} \times \mathbf{r}T + \nabla \times (\hat{z} \times \mathbf{r}\psi), \tag{3.30}$$

where $\hat{z}$ is the unit vector along the axis of symmetry (assumed here to be the z axis) and ψ and T are scalar functions which are independent of ϕ. Now onwards we will use the notation of (r, θ, ϕ) for spherical polar coordinates and (ϖ, ϕ, z) for cylindrical polar coordinates.

In cylindrical coordinates, equation (3.30) takes the following form

$$\mathbf{B} = -\varpi\frac{\partial\psi}{\partial z}\hat{\varpi} + \varpi T\hat{\phi} + \frac{1}{\varpi}\frac{\partial(\varpi^2\psi)}{\partial\varpi}\hat{z}, \tag{3.31}$$

where $\hat{\varpi}$, $\hat{\phi}$ represent the unit vectors along ϖ and ϕ. Taking a curl of equation (3.31), we obtain (Chandrasekhar, 1956)

$$\nabla\times\mathbf{B} = -\varpi\frac{\partial T}{\partial z}\hat{\varpi} - \varpi\Delta_5\psi\hat{\phi} + \frac{1}{\varpi}\frac{\partial(\varpi^2 T)}{\partial\varpi}\hat{z}, \tag{3.32}$$

where Δ_5 is an operator defined as

$$\Delta_5 = \frac{\partial^2}{\partial\varpi^2} + \frac{3}{\varpi}\frac{\partial}{\partial\varpi} + \frac{\partial^2}{\partial z^2} \tag{3.33}$$

Combining the force-free condition given in equation (3.15) and equations (3.31) & (3.32), we obtain

$$\alpha\nabla(\varpi^2\psi) = \nabla(\varpi^2 T) \tag{3.34}$$

$$\Delta_5\psi = -\alpha T. \tag{3.35}$$

If α is a constant then equation (3.34) implies (without loss of any generality)

$$\alpha\psi = T \tag{3.36}$$

and equation (3.35) now becomes

$$\Delta_5\psi = -\alpha^2\psi. \tag{3.37}$$

In spherical coordinates equation (3.58) can be written as (Chandrasekhar, 1956)

$$\left(\frac{\partial^2}{\partial r^2} + \frac{4}{r}\frac{\partial}{\partial r} + \frac{1-\mu^2}{r^2}\frac{\partial^2}{\partial\mu^2} - \frac{4\mu}{r^2}\frac{\partial}{\partial\mu} + \alpha^2\right)\psi = 0, \tag{3.38}$$

where $\mu = \cos\theta$. The general separable solutions to equation (3.38) were first presented in Chandrasekhar (1956), which are given by

$$\psi_n = \frac{\mathcal{C}_{n+3/2}(\alpha r)}{r^{3/2}}C_n^{3/2}(\mu), \tag{3.39}$$

where $C_n^{3/2}(\mu)$ denotes the Gegenbauer polynomials and $\mathcal{C}_{n+3/2}$ are linear combinations of cylindrical Bessel functions $J_{n+3/2}(\alpha r)$ and $J_{-(n+3/2)}(\alpha r)$. The expression for magnetic field now given by (cf. equation 3.31)

$$\mathbf{B} = \alpha(\hat{z} \times \mathbf{r})\psi_n - \frac{1}{\varpi^2}(\hat{z} \times \mathbf{r}) \times \nabla(\psi_n \varpi^2). \tag{3.40}$$

Writing out the various components of $\mathbf{B}$ given by equation (3.40) explicitly in spherical polar coordinates, we get

$$\mathbf{B} = \left(\frac{-1}{r^2} \frac{\partial}{\partial \mu}[\psi_n r^2(1-\mu^2)], \frac{-1}{r(1-\mu^2)^{1/2}} \frac{\partial}{\partial r}[\psi_n r^2(1-\mu^2)], \alpha r(1-\mu^2)^{1/2}\psi_n \right). \tag{3.41}$$

Non-axisymmetric solutions to the linear force-free field equation were presented in Chandrasekhar and Kendall (1957).

3.3.1 Solutions to force-free equations in cylindrical geometry

The magnetic fields in the corona of galactic or accretion discs are expected to be in a Taylor-like relaxed state following a force-free field geometry (Mangalam and Subramanian, 1994). Here we present the solutions of the force-free equation in cylindrical geometry that can be applied the cases of accretion or galactic discs. The magnetic field follows the force-free equation given by

$$\nabla \times \mathbf{B} = \mu \mathbf{B}, \quad \nabla \cdot \mathbf{B} = 0 \tag{3.42}$$

where μ is a constant. Here $\mu = 0$ corresponds to taking the region outside to be current-free, which is likely initial state. We can expect μ to increase to higher non-zero values and relax to a stable configuration as the corona builds up outside the disc. By taking the curl of equation (3.42), we get

$$\nabla^2 \mathbf{B} = -\mu^2 \mathbf{B}. \tag{3.43}$$

We first split the magnetic field $\mathbf{B}$ into poloidal ($\mathbf{B}_P$) and toroidal ($\mathbf{B}_T$) parts, which under axisymmetry can be written as

$$\mathbf{B}_P = B_r\hat{r} + B_z\hat{z} = \frac{1}{r}\nabla\psi\times\hat{\phi} = \left(\frac{-1}{r}\frac{\partial}{\partial z}\hat{r} + \frac{1}{r}\frac{\partial}{\partial r}\hat{z}\right)\psi \equiv \hat{P}\psi \quad (3.44)$$

$$\mathbf{B}_\phi = \frac{T}{r}\hat{\phi}. \quad (3.45)$$

We can now split equation (3.43) into poloidal and toroidal parts. We write out following equations for the poloidal field

$$\nabla^2\hat{P}\psi = -\mu^2\hat{P}\psi \Rightarrow \quad \hat{P}\Lambda\psi = \hat{P}(-\mu^2\psi) \Rightarrow \quad \Lambda\psi = -\mu^2\psi \quad (3.46)$$

where

$$\Lambda = r^2\nabla\cdot\left(\frac{\nabla}{r^2}\right) = r\frac{\partial}{\partial r}\left(\frac{1}{r}\frac{\partial}{\partial r}\right) + \frac{\partial^2}{\partial z^2} \quad (3.47)$$

which follows the property $\nabla^2\hat{P} = \hat{P}\Lambda$ (see §3.A & Appendix A in Mangalam and Subramanian (1994) for a derivation). Similarly for the toroidal field, we write

$$\nabla^2(T/r) = -\mu^2(T/r) \Rightarrow \quad \frac{1}{r}\Lambda T = -\mu^2\frac{T}{r} \Rightarrow \Lambda T = -\mu^2 T. \quad (3.48)$$

Since both equations (3.46) & (3.48) have the same functional form, we now proceed to solve equation (3.46) by writing out Λ explicitly as

$$r\frac{\partial}{\partial r}\left(\frac{1}{r}\frac{\partial\psi}{\partial r}\right) + \frac{\partial^2\psi}{\partial z^2} = -\mu^2\psi. \quad (3.49)$$

Using separation of variables, we write $\psi(r,z) = R(r)Z(z)$. Equation (3.48) can be written as

$$\begin{aligned} Zr\frac{\mathrm{d}}{\mathrm{d}r}\left(\frac{1}{r}\frac{\mathrm{d}R}{\mathrm{d}r}\right) + R\frac{\mathrm{d}^2z}{\mathrm{d}z^2} &= -\mu^2RZ \\ \frac{1}{R}r\frac{\mathrm{d}}{\mathrm{d}r}\left(\frac{1}{r}\frac{\mathrm{d}R}{\mathrm{d}r}\right) + \frac{1}{Z}\frac{\mathrm{d}^2z}{\mathrm{d}z^2} &= -\mu^2 = k_z^2 - k_r^2 \\ \left[\frac{1}{R}r\frac{\mathrm{d}}{\mathrm{d}r}\left(\frac{1}{r}\frac{\mathrm{d}R}{\mathrm{d}r}\right) + k_r^2\right] + \left[\frac{1}{Z}\frac{\mathrm{d}^2z}{\mathrm{d}z^2} - k_z^2\right] &= 0. \end{aligned} \quad (3.50)$$

Since the first term in the LHS of equation (3.50) is a function of r only and the second term is a function of z only, the equality holds only if both the terms are independently zero. The z part of equation (3.50) can be written as

$$\frac{\mathrm{d}^2 Z}{\mathrm{d}z^2} - k_z^2 Z = 0 \tag{3.51}$$

whose solutions are given by

$$Z = c_1 \exp(k_z z) + c_2 \exp(-k_z z) \tag{3.52}$$

where c_1 and c_2 are arbitrary Since the solution should be finite for large values of z, we choose solutions that are decaying at infinity. Thus, we get

$$Z = c \exp(-k_z z). \tag{3.53}$$

The radial part of equation (3.50) is given by

$$r \frac{\mathrm{d}}{\mathrm{d}r}\left(\frac{1}{r}\frac{\mathrm{d}R}{\mathrm{d}r}\right) + k_r^2 R = 0. \tag{3.54}$$

Substituting $R = rf$ in equation (3.54), we get the following equation after rearranging terms

$$r^2 \frac{\mathrm{d}^2 f}{\mathrm{d}r^2} + r \frac{\mathrm{d}f}{\mathrm{d}r} + (k_r^2 r^2 - 1) f = 0 \tag{3.55}$$

which is the Bessel's differential equation, with the solutions given as

$$f = J_1(k_r r) + Y_1(k_r r). \tag{3.56}$$

If we demand $f = 0$ at $r = 0$, we obtain

$$R = r J_1(k_r r). \tag{3.57}$$

If we call $k_r = p$, then $k_z = \sqrt{p^2 - \mu^2}$. Since p can take continuous values, the solution given in equation (3.57) will have continuous coefficients, $a(p)$. Integrating all these solutions, we get

$$\psi(r, z) = \int a(p) \exp\left(-\sqrt{p^2 - \mu^2}|z|\right) r J_1(pr) \mathrm{d}p. \tag{3.58}$$

Similarly, we can write the toroidal solution as

$$T(r,z) = \int b(p) \exp\left(-\sqrt{q^2-\mu^2}|z|\right) rJ_1(qr)\mathrm{d}q. \tag{3.59}$$

From the force-free condition, the following steps follow

$$\begin{aligned} \nabla \times \mathbf{B}_\phi &= \mu \mathbf{B}_\phi \\ \Rightarrow \hat{P}(rB_\phi) &= \mu \hat{P}\psi \\ \Rightarrow \hat{P}T &= \hat{P}(\mu\psi). \end{aligned} \tag{3.60}$$

Thus the amplitudes in equations (3.58) & (3.59) are related by

$$b(k) = \mu a(k). \tag{3.61}$$

3.4 Solutions to the nonlinear force-free field equation

When we allow α to be function of space, solving equation (3.15) becomes very difficult, even when the field is independent of one of the spatial coordinates. In Cartesian coordinates a 2.5 dimensional field $\mathbf{B}(x,z)$ can be written in terms of a flux function ψ in the following manner (Priest, 2014)

$$B_x = \frac{\partial \psi}{\partial z}, \quad B_y(x,z), \quad B_z = -\frac{\partial \psi}{\partial x} \tag{3.62}$$

which satisfies $\nabla \cdot \mathbf{B} = 0$ automatically. The components of $\mathbf{J} \times \mathbf{B} = 0$ can then be written as

$$\nabla^2\psi \frac{\partial \psi}{\partial x} + B_y \frac{\partial B_y}{\partial x} = 0, \tag{3.63}$$

$$\frac{\partial B_y}{\partial z}\frac{\partial \psi}{\partial x} - \frac{\partial B_y}{\partial x}\frac{\partial \psi}{\partial z} = 0, \tag{3.64}$$

$$\nabla^2\psi \frac{\partial \psi}{\partial z} + B_y \frac{\partial B_y}{\partial z} = 0. \tag{3.65}$$

From equation (3.64) we find that B_y is a function of ψ alone and remains constant on surfaces $\psi = constant$. Equation (3.63) or (3.63) then gives (Priest, 2014)

$$\nabla^2\psi = \frac{\mathrm{d}}{\mathrm{d}\psi}\left(\frac{1}{2}B_y^2\right), \tag{3.66}$$

which is known as the *Grad-Shafranov equation*. Equation (3.66) determines ψ and thus B_x andB_z, once $B_y(\psi)$ and the boundary conditions are prescribed.

In cylindrical polar (ϖ, ϕ, z), the axisymmetric field has the form

$$\mathbf{B} = \left(-\frac{1}{\varpi}\frac{\partial\psi}{\partial z}, \frac{b_\phi}{\varpi}, \frac{1}{\varpi}\frac{\partial\psi}{\partial\varpi}\right), \tag{3.67}$$

where b_ϕ is a function of ψ alone and $\alpha = \mathrm{d}b_\phi/\mathrm{d}\psi$. Using $\nabla \times \mathbf{B} = \alpha\mathbf{B}$, we get

$$\frac{\partial^2\psi}{\partial\varpi^2} - \frac{1}{\varpi}\frac{\partial\psi}{\partial\varpi} + \frac{\partial^2\psi}{\partial z^2} = -\frac{\mathrm{d}}{\mathrm{d}\psi}\left(\frac{1}{2}b_\phi^2\right). \tag{3.68}$$

In spherical polar coordinates (r, θ, ϕ), axisymmetric fields exist in the form (Priest, 2014)

$$\mathbf{B} = \frac{1}{r\sin\theta}\left(\frac{1}{r}\frac{\partial}{\partial\psi}\theta, -\frac{\partial\psi}{\partial r}, b_\phi(\psi)\right), \tag{3.69}$$

where b_ϕ depends only on ψ. The force-free condition then gives

$$\frac{\partial^2\psi}{\partial r^2} + \frac{\sin\theta}{r^2}\frac{\partial}{\partial\theta}\left(\frac{1}{\sin\theta}\frac{\partial\psi}{\partial\theta}\right) + \frac{\mathrm{d}}{\mathrm{d}\psi}\left(\frac{1}{2}b_\phi^2\right) = 0. \tag{3.70}$$

Analytical solutions to equation (3.70) that are confined between two cones with $rJ_\phi = c\psi^{1+2/l}$ and decreasing with distance as r^{-l} have been applied to astrophysical jets and coronal arcades (Lynden-Bell and Boily, 1994; Gourgouliatos, 2008).

Low and Lou (1990) applied nonlinear force-free fields to model active regions in the solar corona. Here the poloidal and toroidal components of the magnetic field is written as

$$\mathbf{B}_P = \frac{1}{r}\nabla\psi \times \hat{\phi}, \quad T = \frac{Q(\psi)}{r\sin\theta}, \tag{3.71}$$

then the magnetic field is given by

$$\mathbf{B} = \frac{1}{r\sin\theta}\left(\frac{1}{r}\frac{\partial\psi}{\partial\theta}, -\frac{\partial\psi}{\partial r}, Q(\psi)\right), \tag{3.72}$$

where Q depends only on ψ. $\nabla \times \mathbf{B} = \alpha\mathbf{B}$ then gives

$$\frac{\partial^2\psi}{\partial r^2} + \frac{1-\mu^2}{r^2}\frac{\partial^2\psi}{\partial\mu^2} + Q\frac{\mathrm{d}Q}{\mathrm{d}\psi} = 0, \quad \alpha = \frac{\mathrm{d}Q}{\mathrm{d}\psi} \tag{3.73}$$

where $\mu = \cos\theta$. Equation (3.73) allows for separable solutions of the form

$$\psi = \frac{P(\mu)}{r^n}, \quad Q(\psi) = a\psi^{1+1/n} \tag{3.74}$$

where a and n are constants and the scalar function P satisfies the following differential equation (Low and Lou, 1990)

$$(1-\mu^2)\frac{\mathrm{d}^2P}{\mathrm{d}\mu^2} + n(n+1)P + a^2\frac{(1+n)}{n}\psi^{1+2/n} = 0. \tag{3.75}$$

Equation (3.75) needs to be solved numerically for the condition $P(\pm1) = 0$, which determines the eigenvalues (a_{nm}) of a. For the particular case of $a = 0$, which corresponds to potential fields with $\alpha = 0$, equation (3.75) simplifies to

$$(1-\mu^2)\frac{\mathrm{d}^2P}{\mathrm{d}\mu^2} + n(n+1)P = 0, \tag{3.76}$$

whose solutions are given by

$$P = (1-\mu^2)^{1/2}P_n^1(\mu) \tag{3.77}$$

where $P_n^1(\mu)$ are the associated Legendre functions of the first kind for the integer n.

3.4.1 Numerical methods for nonlinear force-free fields

There have been several numerical methods proposed to extrapolate the non-linear force-free field in the active regions of the corona using the magnetic

field measured at the photosphere as boundary conditions. The aim is to solve the equations $\nabla \times \mathbf{B} = \alpha \mathbf{B}$ and $(\mathbf{B}.\nabla)\alpha = 0$ with the divergence-free condition $\nabla \cdot \mathbf{B} = 0$. As the system of equation has a mixed elliptic-hyperbolic nature, it is difficult to formulate it as a well-defined boundary value problem (Priest, 2014). For a given α, the equation for $\mathbf{B}$ is elliptic and thus we can impose the normal component of the field (B_n) as the boundary condition, whereas for a given $\mathbf{B}$, the equation for α is hyperbolic which can be solved by prescribing α at one end of a field line. Imposing all three components of the magnetic field (as obtained from the vector magnetograms) gives extra conditions which makes the problem ill-posed. Even if the problem is posed properly, the existence and uniqueness of solutions is not guaranteed and has been demonstrated only for small values of α (Boulmezaoud and Amari, 2000). Below we give a short description of the various numerical extrapolation techniques (Wiegelmann, 2008; Priest, 2014)

1. *The upward integration method*: In this method (Nakagawa, 1974; Demoulin and Priest, 1992), equations (3.15) & (3.16) are written as four equations for $\partial B_x/\partial z$, $\partial B_y/\partial z$, $\partial B_z/\partial z$, $\partial \alpha/\partial z$ are integrated integrated upwards as a Cauchy problem from the lower boundary ($z = 0$), with $\mathbf{B}(x, y, 0)$ and $\alpha(x, y, 0)$ taken as the initial values.

2. *The Grad-Rubin method*: This method was proposed for fusion plasmas by (Grad and Rubin, 1958) and first applied to coronal magnetic fields by Sakurai (1981). In the form used by Amari *et al.* (1997); Amari, Boulmezaoud, and Mikic (1999); Amari, Boulmezaoud, and Aly (2006), Régnier, Amari, and Kersalé (2002), Inhester and Wiegelmann (2006), the iterative scheme is written as

$$\mathbf{B}^n.\nabla\alpha^n = 0, \quad \nabla \times \mathbf{B}^{n+1} = \alpha^n \mathbf{B}^n, \quad \nabla \cdot \mathbf{B}^{n+1} = 0. \tag{3.78}$$

3. *The MHD relaxation method*: In this method time dependent MHD codes are used to relax an initial field towards a final configuration which satisfies the stated boundary conditions. This method was applied to force-free coronal magnetic fields by Mikic and McClymont (1994) where an initial potential field configuration was driven at the boundaries using viscosity to dissipate the flow energy while the topology changes due to resistivity. In Roumeliotis (1996), a *stress-and-relax* method is used in which field configuration is driven from the boundary and relaxed in alternating steps.

4. *Optimization methods*: This approach was proposed by Wheatland, Sturrock, and Roumeliotis (2000) based on an earlier variational principle of Sakurai (1979) and later developed by Wiegelmann (2004) and Wiegelmann, Inhester, and Sakurai (2006). Here a functional

$$L = \int [B^{-2}|(\nabla \times \mathbf{B}) \times \mathbf{B}|^2 + |\nabla \cdot \mathbf{B}|^2] \mathrm{d}V \tag{3.79}$$

   is setup and minimized in an evolutionary manner. A force-free configuration is achieved when L reduces to zero.

5. *The boundary element (or Greens function like) method*: In this method developed by Yan (1995, 2003) and Yan and Sakurai (2000) a tensor Green's function is used to rewrite the nonlinear integral equations over the volume, together with a surface integral which is discretized using the boundary-element method.

All the numerical techniques face the challenge of obtaining realistic field configurations that can be compared to the observations (Schrijver *et al.*, 2006; Metcalf *et al.*, 2008). A major challenge is to make a fast and accurate code that can account for the noise in the measurements (Wiegelmann and

Inhester, 2010). Furthermore, the magnetic fields are measured at the photosphere which is not force free region (chromospheric magnetograms are still not accurate). One needs to develop magneto-hydrostatic codes which can accurately model the forces in the photosphere. In many models a technique called preprocessing is used to derive boundary conditions that are force free and consistent with the photospheric measurements (Wiegelmann, Inhester, and Sakurai, 2006; Wiegelmann, 2008). Finally, the the boundary conditions taken at the lateral and upper boundaries greatly affect greatly the solutions.

We propose a new and relatively fast technique to compute NLFF fields that has several advantages in Chapter 6.

Appendix

3.A Properties of operators $\hat{P}$ and Λ

Here we give a derivation of the relation $\nabla^2\hat{P} = \hat{P}\Lambda$ used in §3.3.1. We write

$$\hat{P} = -\frac{\hat{r}}{r}\partial_z + \frac{\hat{z}}{r}\partial_r \quad \text{and} \quad \Lambda = r\partial_r\frac{1}{r}\partial_r + \partial_z^2,$$

where the partial derivatives have been abbreviated. We point out that the r and z eigenfunctions of Λ are

$$\Lambda_r = r\ J_1(k_r r) \text{ and } \Lambda_z = \exp(k_z z). \tag{3.80}$$

Now,

$$[\nabla^2\hat{P}]_z = \left(\frac{1}{r}\partial_r r\partial_r + \partial_z^2\right)\left(\frac{1}{r}\partial_r\right) = \left(\frac{1}{r}\partial_r\right)\left(r\partial_r\frac{1}{r}\partial_r + \partial_z^2\right) = \hat{P}_z\Lambda, \tag{3.81}$$

for the z component and for the r component, we find that

$$[\nabla^2\hat{P}]_r = \left(\partial_r\frac{1}{r}\partial_r r + \partial_z^2\right)\left(-\frac{1}{r}\partial_z\right) = -\partial_z\partial_r\frac{1}{r}\partial_r - \frac{1}{r}\partial_z\partial_z^2 = \hat{P}_r\Lambda. \tag{3.82}$$

Similarly one can show

$$\nabla\times\hat{P} = -\hat{\phi}\ \frac{\Lambda}{r} \quad \text{and} \quad \hat{P}(r\Omega) = \nabla\times(\Omega\hat{\phi}) \tag{3.83}$$

where Ω is an arbitrary axisymmetric function.

Chapter 4

Coronal heating mechanisms and braided magnetic fields

4.1 Overview of coronal heating mechanisms

In this chapter we give a brief overview of the different coronal heating mechanisms. In particular we describe braiding in coronal magnetic fields and calculate the energy released in the corona due to small-scale reconnection events occurring in these braided structures.

The corona is composed of very tenuous gas with an average density $\sim 10^8$ cm^{-3}. The energy requirement to compensate the radiative and conductive losses and maintain a million degree corona can be estimated to be (Withbroe and Noyes, 1977; Klimchuk, 2015)

- Active regions: 10^7 ergs $\mathrm{cm}^2\mathrm{s}^{-1}$ and
- Quiet regions: 3×10^5 ergs $\mathrm{cm}^2\mathrm{s}^{-1}$.

It is a basic requirement of the coronal heating theory to identify the energy source that can maintain these losses. The mechanical motions in

and below the photosphere are thought to be the source of this energy. It is customary to classify coronal heating models into two groups:

1. Alternating Current (AC) heating: If the photospheric motion changes on a time scale faster than what the coronal loop can adjust to (e.g., by damping and dissipation of Alfvén waves), the dissipation of waves is referred to as AC heating.

2. Direct Current (DC) heating: If the random motions displace the footpoints of the coronal magnetic field lines on time scales much longer than the Alfvén transit time along a coronal loop, so that the loop can adjust to the changing boundary condition in a quasi-static way, the dissipation of magnetic stresses is referred to as DC heating.

Brief discussions on both AC and DC heating mechanisms are presented in the following subsections.

4.1.1 AC heating

In AC heating models, energy is provided by dissipation of waves in the corona. In general, turbulent convective motions on the solar surface generate three different types of waves involving the magnetic field waves propagating upwards in the solar atmosphere. These waves are

1. Alfvén waves

2. Fast magneto-acoustic wave and

3. Slow magneto-acoustic wave.

The Alfvén waves travel along the magnetic field, while fast and slow magneto-acoustic waves can also travel across the magnetic field. The speed of the

magneto-acoustic waves depend on the direction of propagation and on the plasma properties, so these waves reflect against the transition region where there is a large gradient in pressure and density. Thus these waves cannot transport energy from the photosphere to the corona. The natural candidate for heating then are the Alfvén waves (Alfvén, 1947). Alfvén waves are much more resilient and do not dissipate in the corona except at small scales. It is thus very difficult to convert the wave energy into heat. The following are the two broadly proposed mechanisms for AC heating of the corona:

1. Resonant absorption (Ionson, 1978; Hollweg, 1984; Davila, 1987): If the frequency of a standing wave excited in a magnetic loop matches that of the Alfvén wave, then resonance in the loop creates large velocity gradients, which in turn leads to a dissipation of energy. The resonant Alfvén waves have also been found to generate slow magneto-acoustic waves (Beliën, Martens, and Keppens, 1999; Ballai and Erdelyi, 1998; Erdélyi, Ballai, and Goossens, 2001), which are compressional waves. These waves give rise to density variations which further fragment the resonant layers.

2. Phase mixing (Heyvaerts and Priest, 1983): The excitation of the magnetic field by the Alfvén waves leads to a gradient in the wave speed. The waves in the nearby field lines then propagate at different speeds (phase mixing), which results in instabilities and dissipation of energy. Phase mixing is an essential ingredient of resonant absorption (Poedts, 2002) but it does not need resonances to be effective. Phase mixing can cause a cascade of energy to small length scales, where dissipation becomes more efficient (Poedts *et al.*, 1997).

4.1.2 DC heating

The footpoints of the coronal magnetic fields are constantly shuffled by the photospheric granular and super granular flows, which have random walk characteristics. Due to the high electrical conductivity of the corona, the magnetic field lines are frozen-in with the plasma. The magnetic field lines then get twisted and wrapped around each other (Fig. 4.1), which leads to formation of current sheets in highly stressed regions. When the current in these sheets reaches a threshold value, reconnection sets in, which releases the magnetic energy and heats up the corona.

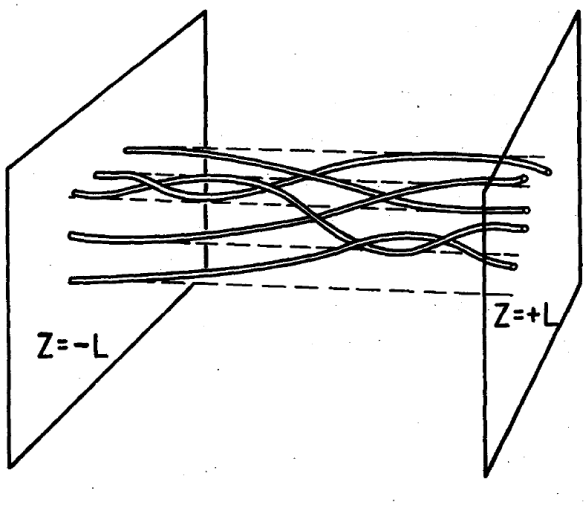

Figure 4.1: Magnetic flux tubes twisted and braided by stochastic footpoint motions. Figure courtesy: (Parker, 1972)

Suppose we start with a magnetic field configuration of flux $\Phi = \pi r^2 B_0$ with a uniform magnetic field B_0 and radius r extending between two planes at height $z = 0$ (photosphere), up to a plane $z = L$ in which its footpoints are fixed (as shown in Fig. 4.2). If the footpoint of a given elemental flux tube moves in the photosphere with random velocity v, the rate of non potential energy build-up per unit area ($\mathrm{d}W/\mathrm{d}t$) integrated over the volume $V = \pi r^2 L$

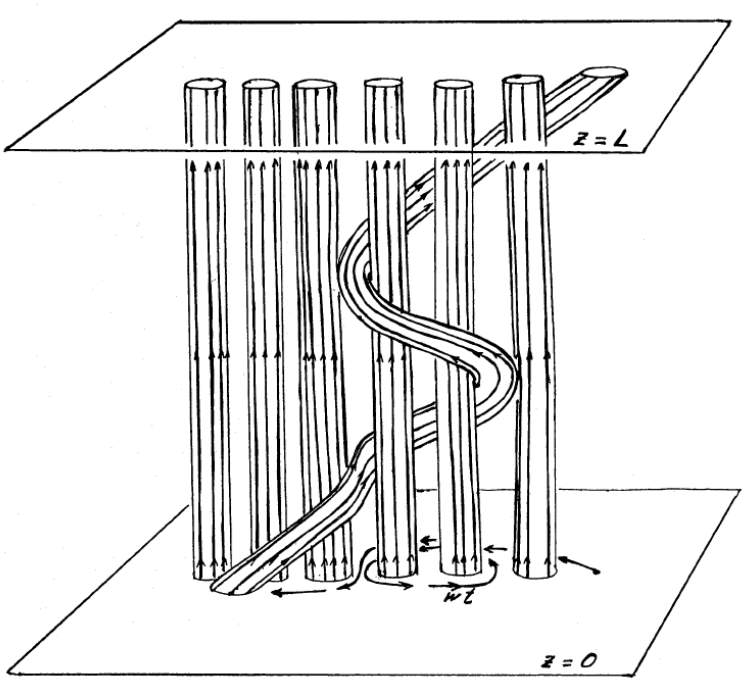

Figure 4.2: Magnetic flux tubes extending between the photosphere ($z = 0$) and a plane at $z = l$ get wound among its neighbors due to the random footpoint motions. Figure courtesy: (Parker, 1983)

would be (Sturrock and Uchida, 1981; Aschwanden, 2004),

$$\int \frac{\mathrm{d}W}{\mathrm{d}t}\mathrm{d}V = \frac{\Phi B_0 v^2 \tau_c}{4\pi}, \tag{4.1}$$

where τ_c is the correlation time scale of random motion. Sturrock and Uchida (1981) estimated that for the observed field strengths of ∼1500 G in the flux tubes with radius of the order of 150 km and mean velocities of 1 kms^{-1} over a coherence time of 2×10^3s, the magnetic energy input to the flux tube is equal to the radiative and conductive losses ($\sim 10^7$ ergs cm^{-2}s^{-1}).

The Sturrock-Uchida model has been further investigated by Berger (1991) and Karpen *et al.* (1993) where they calculate the root mean square twist induced in the field lines due to photospheric motions. If **v** represents the

two-dimensional random velocity, then the twist rate is written as (Berger, 1994)

$$\nabla \mathbf{v} = \begin{pmatrix} \partial_x v_x & \partial_x v_y \\ \partial_y v_x & \partial_y v_y \end{pmatrix} = \frac{1}{2}\left[\omega_z \begin{pmatrix} 0 & 1 \\ -1 & 0 \end{pmatrix} + (\nabla \cdot \mathbf{v}) \begin{pmatrix} 1 & 0 \\ 0 & 1 \end{pmatrix} + \mathbf{S}\right] \tag{4.2}$$

where $w_z = \partial_x v_y - \partial_y v_x$ is the vorticity and $\mathbf{S}$ is the symmetric shear tensor. The term $\nabla \cdot \mathbf{v}$ term does not contribute to the rotation, while the symmetric shear part contributes up to 50% as much as the vorticity term for a turbulent velocity field. Assuming that both senses of rotation are equally likely, the average twist is zero. We define T to be the number of turns a field line takes about the axis of the coronal tube and τ_c and λ to be the correlation time and correlation length of the flow. Then using the relation $\boldsymbol{\omega} = \nabla \times \mathbf{v} = 2\boldsymbol{\Omega}$, where $\mathbf{v} = \boldsymbol{\Omega} \times \mathbf{r}$, we can write $\omega_z = \dfrac{2v}{\lambda}$. Thus, the expression for mean square vorticity is given by $\overline{\omega_z^2} = \dfrac{4v^2}{\lambda^2}$, where v^2 represents the mean square velocity. If the twist angle is written as $\delta\theta = \Omega\tau_c$, then we can write after time t

$$T = \frac{\delta\theta\sqrt{N}}{2\pi} = \frac{\Omega\tau_c N}{2\pi}. \tag{4.3}$$

where $N = t/\tau_c$. The root mean square twist T (for twisting at both ends) can be written as (cf. Berger, 1994)

$$\overline{T^2} = 2 \times \frac{3\overline{\Omega^2}\tau_c t}{4\pi^2} = 2 \times \frac{3\overline{\omega^2}\tau_c t}{16\pi^2} = \frac{3\tau_c v^2}{2\pi^2\lambda^2} t. \tag{4.4}$$

For granular motions with $\lambda = 800$ km, $\tau_c = 800$ s and $v = 1$ km/s, the above equation gives $\overline{T^2} = t/(1.5 \text{ hours})$. To obtain the energy flux, we consider a single photospheric flux element $\Phi_* = \pi R_c^2 B_z$, where R_c is coronal radius and B_z the vertical field strength. For a magnetic field with axisymmetric and uniform twist over length L, we write

$$\mathbf{B} = B_z(\hat{z} + 2\pi r T L^{-1}\hat{\theta}). \tag{4.5}$$

Rotations at both ends provide a mean energy density of

$$W = \frac{1}{\pi R_c^2 L 8\pi} \int (2\pi r T B_z/L)^2 \mathrm{d}V = \frac{B_z \Phi_* T^2}{4L^2}. \tag{4.6}$$

The mean energy input per unit area is (Berger, 1994)

$$P = \frac{L}{2}\frac{\mathrm{d}W}{\mathrm{d}t} = \frac{3B_z^2 \Phi_* v^2 \tau_c}{16\pi^2 L \lambda^2}. \tag{4.7}$$

At the photosphere, the flux Φ_* is compressed into small intense flux element of radius R_* and field strength B_*. For the values $B_* = 1500$ G, $R_* = 250$ km, and $B_z = 100$ G, we get the power $P = 7 \times 10^5$ ergs cm^{-2} s^{-1}, which is an order of magnitude less than the requirement for coronal heating.

We now present the energy estimate given by Parker (1983, 1988): If $B_t \simeq \dfrac{B_0 vt}{L}$ represents the transverse component of the magnetic field built due to the random motions after a time t, then the magnetic stress in the flux tube is given by $\dfrac{B_t B_0}{4\pi}$. The rate of energy build-up of can be estimated to be Parker (1972, 1983, 1988); Aschwanden (2004)

$$\frac{\mathrm{d}W}{\mathrm{d}t} = \frac{B_0 B_t v}{4\pi} = \frac{B_0^2 v^2 t}{4\pi L}. \tag{4.8}$$

With the values $B_0 = 100$ G, $v = 0.5$ km s^{-1}, $L = 10^{10}$ cm, it follows that an energy build-up rate of $dW/dt = 10^7$ erg cm^{-2} s^{-1}, can be achieved in a timescale of about $t = 5 \times 10^4$ s. At this point, $B_t \sim B_0/4$ and the deviation of the field line from vertical, $\theta = \arctan\left(\dfrac{vt}{L}\right)$ is around 14°. At this critical angle, the tangential discontinuity produced in the coronal field ΔB (see Fig. 4.2) is of the same order as the transverse field $B_t = 25$ G. With a velocity $v = 0.5$ km s^{-1}, the footpoint traverses a distance ~ 25 Mm during a period of $t = 5 \times 10^4$ s. If we associate each random step of the footpoint with a lifetime of the adjacent granules, $\tau = 500$ s, and length $l = v\tau = 250$ kms^{-1}, the total path length is then covered in $n = t/\tau = 100$ random steps. The wrapping of the individual flux bundle can be assumed to follow the winding

of the footpoint. We then expect each flux bundle to undergo $n = 100$ windings along the vertical height L. Thus the vertical extent of the braid along the tube is given by

$$\Delta L \approx L/n = l \cot\theta = \frac{lL}{vt} = 10^3 \text{km}. \tag{4.9}$$

The energy $\mathcal{E}$ in the magnetic field associated with the braiding is of the order $\frac{B_t^2}{8\pi}$ multiplied by the volume $V \approx l^2 \Delta L$ associated with each winding. With the values $l = 250$ km, $\Delta L = 10^3$ km, $B_t = 25$ G, we get

$$\mathcal{E} = \frac{l^2 \Delta L B_t^2}{8\pi} \approx 6 \times 10^{24} \text{ergs}. \tag{4.10}$$

The amount of released energy per dissipation event is about nine orders of magnitude smaller than in the largest flares, which defines the term *nanoflare*. In the following section we discuss the observations and statistical properties related to these flares.

4.2 Statistical properties of flares

The Parker model involves heating of the solar corona through nanoflares due to reconnection of braided magnetic flux elements. Most of this braiding happens between the unresolved strands in the coronal loops. The X-ray corona can simply be thought as the superposition of a very large number of these nanoflares. From observations, we find a wide range in the spatial scale and energies for these events. The distribution of the peak flare energy has been found to be following a power-law with the logarithmic slope near 1.8 (Charbonneau *et al.*, 2001). It was suggested by Lu and Hamilton (1991) that the phenomenon of SOC can be the underlying mechanism that gives rise to this power-law distribution. In the Lu and Hamilton (1991) model, the random stressing of the magnetic field footpoint by the photospheric motions

provides the input energy while the large number of small-scale flare events provide the output. Initially a local increase in magnetic energy excites a nanoflare, which triggers an avalanche of nanoflares in its neighborhood thus resulting in a large flare. The energetics of the power-law distribution can be understood as follows.

If $F(E)\mathrm{d}E$ is the energy between E and $E + \mathrm{d}E$ released in a flare per unit time, then the frequency distribution $F(E)$ reconstructed from UV, EUV, and X-ray observations can be represented as (Charbonneau *et al.*, 2001)

$$F(E) = F_0 E^{-\alpha}, \quad \alpha > 0. \tag{4.11}$$

Then the total energy released by these flares per unit time from equation (4.11) is given by,

$$E_{tot} = \int_{E_{min}}^{E_{max}} F(E) E \mathrm{d}E = F_0 \left[\frac{E^{2-\alpha}}{2-\alpha}\right]_{E_{min}}^{E_{max}}, \quad \alpha \neq 2, \tag{4.12}$$

(with $E_{tot} = F_0 \log\left(E_{max}/E_{min}\right)$ for $\alpha = 2$). If $\alpha \leq 2$, the energy released is dominated by the large flares, whereas if $\alpha \geq 2$ the smallest flare are energetically dominant. From equation (4.12), we see that Parker's conjecture evidently requires $\alpha > 2$ (Parnell and De Moortel, 2012). The distribution of flares, microflares and nanoflares were determined by Crosby, Aschwanden, and Dennis (1993); Parnell and Jupp (2000); Aschwanden *et al.* (2000); Aschwanden and Parnell (2002) using instruments like Solar Maximum Mission/Hard X-ray Burst Spectrometer, Yohkoh/Soft X-ray Telescope, SOHO/EIT and TRACE. The power-law index for the distribution of event energies was reported to be in the range $1.5 < \alpha < 2.7$. It is currently not possible to accurately determine the power-law index of distribution flare energies using the direct detection techniques, but the nanoflare heating can still be treated as one of the most promising candidates for the coronal heat-

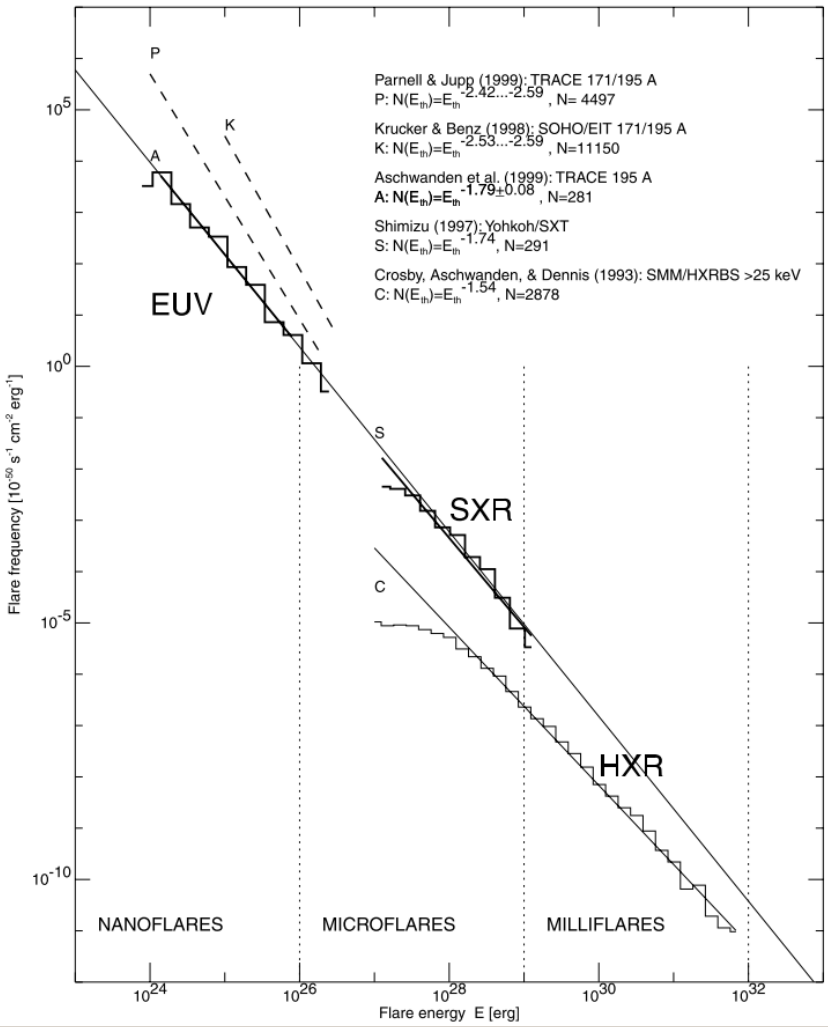

Figure 4.3: Frequency of observed flare events in the EUV, SXR and HXR plotted with the estimated energy release. A power-law with index -1.8 extending over the energy range $10^{24} - 10^{32}$ ergs is shown for comparison. Figure courtesy: (Aschwanden *et al.*, 2000)

ing mechanism. The following section presents analytic techniques that can be used to quantify the self-organized braiding in the magnetic field structures and estimate the power-law index for the frequency distribution of the peak flare energies.

4.3 Braided magnetic fields

The coronal loops observed by TRACE and Hinode show a highly regular structure (Fig. 1.6). The loops are almost parallel and of similar diameters. The coherence in the structure of the loops (given the fragmented nature of magnetic field generation) and the existence of a power law in the distribution of flare energies suggests the presence of a mechanism through which the field reorganizes itself by releasing the excess energy. The large number of small scale reconnection events between the magnetic flux elements (micro and nanoflares) could be responsible for this, which also leads to heating of the corona (Parker, 1988; Berger and Asgari-Targhi, 2009). The magnetic field lines get twisted due to the random rotations of the footpoints, while braided structures are created due to the random walk of the footpoints. Such braided magnetic strands were recently reported in the high resolution (0.2 arc seconds) observations of the solar corona (Cirtain *et al.*, 2013) and also found in simulations using Nonlinear Force-Free Field (NLFFF) as shown in Fig. 4.4 (Thalmann, Tiwari, and Wiegelmann, 2014).

4.3.1 Analytical modeling of braided magnetic fields

A braid defines a collection of curves stretching between two parallel planes. Fig.4.5 shows two configurations of curves extending between $z = 0$ and $z = L$. It is possible to deform one configuration to the other, hence they are said to be topologically equivalent.

If we consider N coronal flux tubes, whose footpoints are constantly moving around each other in the photosphere. These tubes quickly get braided against each other. The increase in the topological complexity leads to increase in the magnetic energy of the system. For continuous fields without

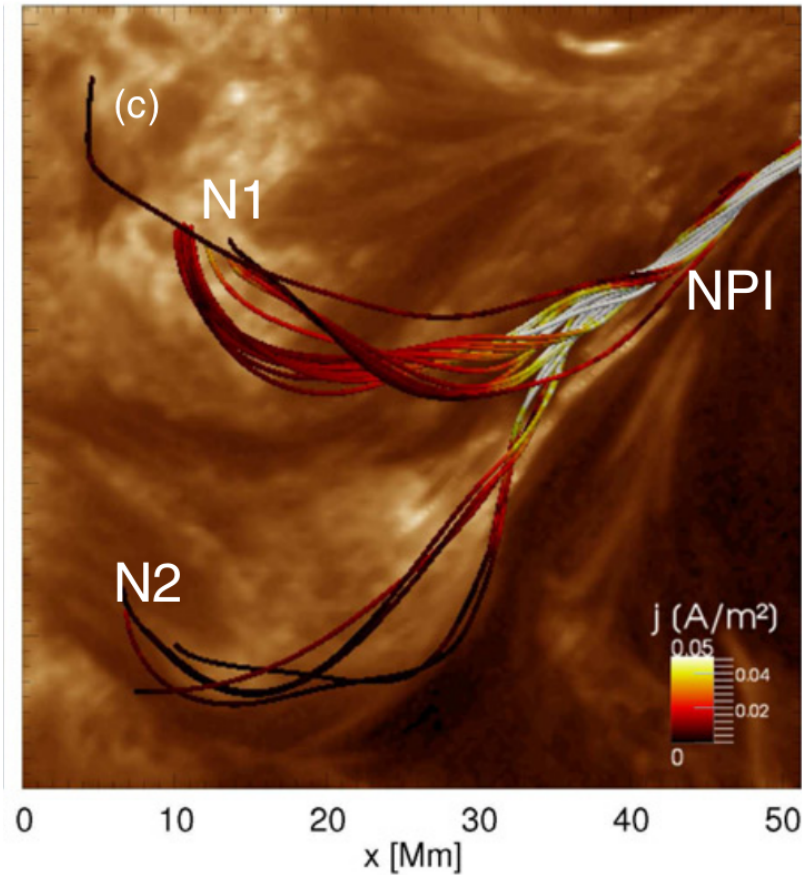

Figure 4.4: Braided field lines simulated from NLFF magnetic field model for a AIA 19.3 nm image observed on July 11, 2012 at 19:00 UT. Figure courtesy: (Thalmann, Tiwari, and Wiegelmann, 2014)

distinct flux tube structures, some number N of individual field lines can be chosen within the loop, and the braiding between these lines can be quantified. Wilmot-Smith, Hornig, and Pontin (2009) present such a semi-analytic force-free model of a pigtail braid where three magnetic field lines cross each other six times. In the following analysis, we only deal with field lines that are divided into discrete flux elements, as we know from observations that the magnetic flux in the photosphere is highly localized. In order to deter-

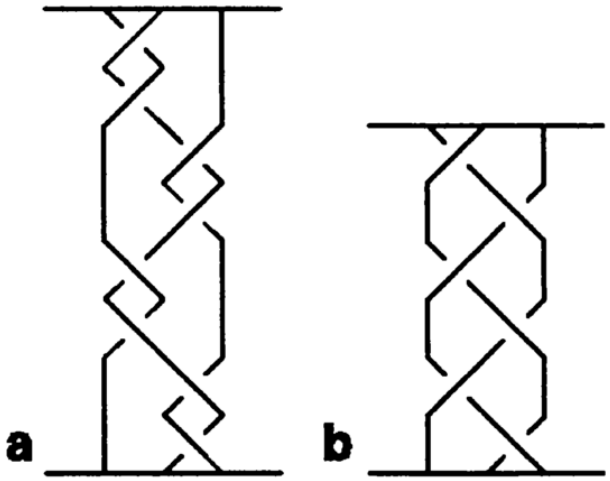

Figure 4.5: Topologically equivalent configurations of a 3-braid. Figure courtesy: (Berger, 1994)

mine the amount of free energy stored in these configurations, we need to estimate the extent of braiding in the coronal loop. It is extremely difficult to determine the equilibrium configuration of highly tangled fields through direct calculations. Berger (1993) defines a quantity called the "asymptotic crossing number" which provides a measure of the braiding in the system. Consider two field lines stretching between two planes $z = 0$ and $z = L$. Let ϕ be the polar angle in the x-y plane. When the curves are observed from a viewing angle ϕ the two curves will exhibit a certain number of crossovers, $c(\phi)$. Note that $c(\phi)$ is dependent on the viewing angle (see Fig. 4.6), but the integrated quantity $\overline{c} = \dfrac{1}{\pi}\displaystyle\int_0^{\pi} c(\phi)\mathrm{d}\phi$ gives an independent measure.

To compute the crossing number directly, we represent the two curves as $\mathbf{x_1}(z)$ and $\mathbf{x_1}(z)$, where $\mathbf{x_1}(z) = (x_1, y_1)$. Also the displacement vector $\mathbf{r_{12}}(z) = \mathbf{x_2}(z) - \mathbf{x_1}(z)$ is assumed to be making an angle $\theta_{12}(z)$ with the z axis. An observer with a viewing angle ϕ will see crossovers wherever

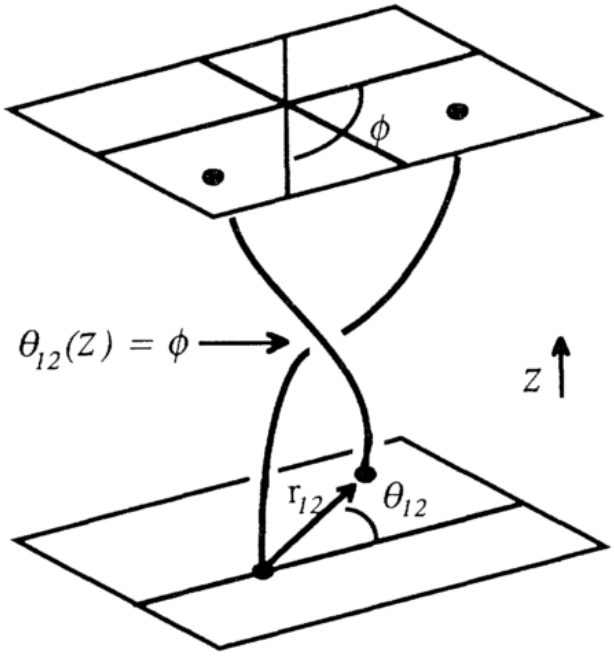

Figure 4.6: Crossover of two curves as seen from a viewing angle ϕ. Figure courtesy: (Berger, 1993)

$\Delta\theta_{12}(z) = \phi$ or $\phi + \pi$. If the net angle swept by $\mathbf{r_{12}}(z)$ is given by $\Delta\theta_{12} = \int \left|\frac{\mathrm{d}\theta_{12}}{\mathrm{d}z}\right| \mathrm{d}z$, then a crossover will be seen by a fraction $\Delta\theta_{12}/\pi$ of randomly distributed observers. Then the asymptotic crossing number for these curves can be written as

$$\overline{c} = \frac{1}{\pi} \int_0^L \left|\frac{\mathrm{d}\theta_{12}}{\mathrm{d}z}\right| \mathrm{d}z. \tag{4.13}$$

This quantity is not a topological invariant, but like the magnetic energy it has a positive minimum value for a given magnetic topology. The minimum asymptotic crossing number, times a constant coefficient, provides a lower bound for the equilibrium energy. We now consider that all the magnetic field is confined within a cylinder of radius R and sum the crossing number $\overline{c}$ for all pairs of lines to obtain the crossing number for the magnetic field

(Berger, 1993):

$$C \equiv \frac{1}{\pi}\int_0^L \int\int B_{z1}B_{z2}\left|\frac{\mathrm{d}\theta_{12}}{\mathrm{d}z}\right| \mathrm{d}^2x_1\mathrm{d}^2x_2\mathrm{d}z. \tag{4.14}$$

We assume that the axial field is much stronger than the horizontal field, so the equilibrium magnetic field can be written as (van Ballegooijen, 1985; Berger, 1994)

$$\mathbf{B} = B_z(\mathbf{b} + \hat{z}), \quad \mathbf{b} = (b_x, b_y) \tag{4.15}$$

where B_z is a constant. The free energy of the field is then defined to be

$$E_f = \frac{B_z^2}{8\pi}\int b^2\mathrm{d}^3x. \tag{4.16}$$

Then a lower bound for the free energy for any field $\mathbf{b}$ is given by (Berger, 1993)

$$E_f \geq 9.18\times10^{-3}\left(LR^4B_z^2\right)^{-1}C^2. \tag{4.17}$$

When derived for a field consisting of N discrete flux tubes, E_f is to be multiplied by the factor $N/(N-1)$. Berger (1994) estimates the power input to an X-ray loop consisting of three braids, each with flux Φ and radius $R/\sqrt{3}$ to be

$$E_{fmin} \geq (3/2)\times9.18\times10^{-3}(LR^4B_z^2)^{-1}\Phi^4K^2 = 1.5\times10^{-2}\Phi^2L^{-1}K^2, \tag{4.18}$$

where $K = \min(\bar{c})$. If $K(t)$ evolves with time due to footpoint motion, which are assumed to be in random walk within a circular area of radius d. Then the minimum power input is given by

$$P = \frac{3\times10^{-2}\Phi^2}{\pi R^2L}K\frac{\mathrm{d}K}{\mathrm{d}t}. \tag{4.19}$$

In numerical simulations of three random braids with step size λ and V/λ steps per second it was observed that (Berger, 1994):

$$\frac{\mathrm{d}K}{\mathrm{d}t} = q_0V\lambda t/d^2 \tag{4.20}$$

where $q_0 \approx 0.5$. We assume that the energy loss through reconnection balances the input when the transverse field reaches a critical value $b = B_1/B_z = \mu$. Then we get $K \approx 1.6\mu L/R_c$ and the power as (Berger, 1994):

$$P = 0.05\mu\epsilon_0 V B_z^2 \lambda R_c/d^2. \tag{4.21}$$

Using the values $d \approx \lambda$, $V = 1$ km s^{-1}, B_z=100 G, $\mu = 0.25$ and $R_c/d = 2$, we get $P \approx 10^7$ erg cm^{-2}s^{-1} which is the amount of energy required for heating the active region corona (Withbroe, 1988).

In Chapter 7, we discuss the of self-organization process in these braided magnetic fields through analytical modeling and estimate the free energy content in the braiding for active regions.

Chapter 5

Turbulent Dynamos

5.1 Introduction

The magnetic fields in a conducting medium is thought to be amplified by the inductive effects associated with the motions present in the medium. This process through which the kinetic energy associated with the fluid motions is converted to magnetic energy is generally referred to as a 'dynamo'. In particular, the large-scale magnetic field in disc galaxies is generated through to a combination of turbulent motions in the ISM and the differential rotation in the disc which transforms the kinetic energy into magnetic energy. The mean toroidal field is generated from mean poloidal field by the radial shear, in a process known as the Ω effect. The mean poloidal field of the same sign is regenerated from mean toroidal field by a process known as the α effect (Parker, 1955).

Other ideas like the 'primordial fields' theory have also been proposed to explain galactic large-scale magnetic fields. This theory posits that large-scale field currently observed in the galaxy is a result of amplified by compression and differential rotation of frozen-in fields that were present at the

time of galaxy formation. This theory suffers from various shortcomings. It doesn't explain the origin of the primordial field itself. Also, this theory predicts pitch angle of the regular magnetic field that is much smaller than those that are observed (Shukurov, 2005). Moreover, the turbulent diffusion (which is much stronger than the Ohmic diffusion), is expected to severely limit the growth of such fields or cause them to decay. Mean-field successfully explains the general properties of the observed galactic magnetic fields, such as growth rates, symmetry and the large scale-structure (Ruzmaikin, Sokolov, and Shukurov, 1988; Shukurov, 2005). Both direct numerical simulations and analytic approaches are required to understand how these dynamos operate and saturate. In the following section, we give a brief outline of the mean-field turbulent dynamos.

5.2 Large-scale turbulent dynamos

The large-scale magnetic field generation in the Sun and spiral galaxies is generally attributed to a turbulent dynamo. The generation mechanism of this turbulent dynamo can be understood from the Mean Field Dynamo (MFD) theory (Moffatt, 1978; Krause and Rädler, 1980).

In the MFD theory, it is customary to split any field $\mathbf{F}$ into a mean-field $\overline{\mathbf{F}}$ and a fluctuating part $\mathbf{f}$. The total field, $\mathbf{F} = \overline{\mathbf{F}} + \mathbf{f}$ and $\overline{\mathbf{f}} = 0$. The overbars denote ensemble averaging which could be practically thought of as spatial average over length scales which are intermediate between the size of the system and the scale of turbulence. The magnetic field $\mathbf{B}$ and the velocity field $\mathbf{U}$ are thus expressed as,

$$\mathbf{B} = \overline{\mathbf{B}} + \mathbf{b}, \quad \mathbf{U} = \overline{\mathbf{U}} + \mathbf{u} \tag{5.1}$$

where $\mathbf{U}$ and $\mathbf{B}$ are the mean velocity and magnetic fields with $\mathbf{u}$ and $\mathbf{b}$ being

their fluctuating parts. The Ohm's law (equation 2.3) can now be written as

$$\mathbf{J} = \overline{\mathbf{J}} + \mathbf{j} = \sigma \left[\overline{\mathbf{E}} + \mathbf{E}' + (\overline{\mathbf{U}} + \mathbf{u}) \times (\overline{\mathbf{B}} + \mathbf{b})\right] \tag{5.2}$$

where $\overline{\mathbf{E}}$ and $\mathbf{E}'$ are the large and small-scale components of the electric field $\mathbf{E}$ respectively. Taking the ensemble average of the last term in the RHS of equation (5.2) gives

$$\begin{aligned} \overline{(\overline{\mathbf{U}} + \mathbf{u}) \times (\overline{\mathbf{B}} + \mathbf{b})} &= \overline{\overline{\mathbf{U}} \times \overline{\mathbf{B}}} + \overline{\mathbf{u} \times \overline{\mathbf{B}}} + \overline{\overline{\mathbf{U}} \times \mathbf{b}} + \overline{\mathbf{u} \times \mathbf{b}} \\ &= \overline{\mathbf{U}} \times \overline{\mathbf{B}} + \overline{\mathbf{u}} \times \overline{\mathbf{B}} + \overline{\mathbf{U}} \times \overline{\mathbf{b}} + \overline{\mathbf{u} \times \mathbf{b}} \\ &= \overline{\mathbf{U}} \times \overline{\mathbf{B}} + \overline{\mathbf{u} \times \mathbf{b}} \end{aligned} \tag{5.3}$$

Taking the ensemble average of equation (5.2) and substituting equation (5.3) gives

$$\overline{\mathbf{J}} = \sigma(\overline{\mathbf{E}} + \overline{\mathbf{U}} \times \overline{\mathbf{B}} + \mathcal{E}), \tag{5.4}$$

where $\mathcal{E} = \overline{\mathbf{u} \times \mathbf{b}}$ is known as the mean electromotive force (emf). The induction equation (2.12) can be expanded as

$$\frac{\partial \overline{\mathbf{B}}}{\partial t} + \frac{\partial \mathbf{b}}{\partial t} = \nabla \times (\overline{\mathbf{U}} \times \overline{\mathbf{B}} + \mathbf{u} \times \overline{\mathbf{B}} + \overline{\mathbf{U}} \times \mathbf{b} + \mathbf{u} \times \mathbf{b}) + \eta \nabla^2 (\overline{\mathbf{B}} + \mathbf{b}). \tag{5.5}$$

Averaging equation (5.5) gives us the equation for evolution of the mean magnetic field

$$\frac{\partial \overline{\mathbf{B}}}{\partial t} = \nabla \times (\overline{\mathbf{U}} \times \overline{\mathbf{B}}) + \nabla \times \mathcal{E} + \eta \nabla^2 \overline{\mathbf{B}} \tag{5.6}$$

whereas, averaging equation (2.5) (for incompressible flows), we get the evolution equations for the mean velocity $\mathbf{U}$ as

$$\left[\frac{\partial \overline{\mathbf{U}}}{\partial t} + \overline{\mathbf{U}} \cdot \nabla \overline{\mathbf{U}}\right] = -\frac{\nabla \overline{p}}{\rho} + \frac{\overline{\mathbf{J}} \times \overline{\mathbf{B}}}{\rho} + \nu \nabla^2 \overline{\mathbf{U}} + \overline{\mathbf{F}} + \mathcal{F} \tag{5.7}$$

where $\mathcal{F}$ is given by

$$\mathcal{F} = -\overline{\mathbf{u} \cdot \nabla \mathbf{u}} + \frac{1}{\rho} \overline{\mathbf{j} \times \mathbf{b}}. \tag{5.8}$$

The mean emf $\mathcal{E} = \overline{\mathbf{u} \times \mathbf{b}}$ in equation (5.6) depends on the statistical properties of the turbulent fields $\mathbf{u}$ and $\mathbf{b}$. If velocity fluctuations $\mathbf{u}$ and field fluctuation $\mathbf{b}$ were completely uncorrelated we would have $\overline{\mathbf{u} \times \mathbf{b}}=\overline{\mathbf{u}} \times \overline{\mathbf{b}} = 0$. $\mathcal{E}$ could be non zero only if there is a correlation between $\mathbf{u}$ and $\mathbf{b}$. The next critical step central is to find an expression for the $\mathcal{E}$ in terms of $\overline{\mathbf{B}}$, $\overline{\mathbf{U}}$ and $\mathbf{u}$ and its derivatives. There are various approaches that are used to express the mean emf, $\mathcal{E}$ in terms of the mean-field $\mathbf{B}$. Evaluating the term $\mathcal{E}$, requires one to solve the evolution equations for the fluctuating magnetic field $\mathbf{b}$ and the fluctuating velocity field $\mathbf{u}$ simultaneously. The first step is to evaluate $\mathbf{b}$ in terms of the mean fields. Fluctuating part of equation (5.5) is given by

$$\frac{\partial \mathbf{b}}{\partial t} = \nabla \times (\mathbf{u} \times \overline{\mathbf{B}} + \overline{\mathbf{U}} \times \mathbf{b}) + \eta \nabla^2 \mathbf{b} + \mathbf{G}. \tag{5.9}$$

Here $\mathbf{G} = \mathbf{u} \times \mathbf{b} - \mathcal{E}$ is the nonlinear term. We can also derive the equation for $\mathbf{u}$ by subtracting the averaged momentum equation (5.7) from the full momentum equation (2.5). With the assumption of incompressible flows ($\nabla \cdot \mathbf{u} = 0$) and constant kinematic viscosity (ν), we get,

$$\begin{aligned} \frac{\partial \mathbf{u}}{\partial t} &= -\mathbf{u} \cdot \nabla \overline{\mathbf{U}} - \overline{\mathbf{U}} \cdot \nabla \mathbf{u} - \frac{1}{\rho} \nabla \left(p' + \frac{1}{\mu} \overline{\mathbf{B}} \cdot \mathbf{b} \right) + \nu \nabla^2 \mathbf{u} \\ &+ \frac{1}{\mu \rho} \left[(\overline{\mathbf{B}} \cdot \nabla) \mathbf{b} + (\mathbf{b} \cdot \nabla) \overline{\mathbf{B}} \right] + \mathbf{f} + \mathbf{T} \end{aligned} \tag{5.10}$$

Here p' and $\mathbf{f}$ are the fluctuating components of pressure and force respectively, and

$$\mathbf{T} = -(\mathbf{u} \cdot \mathbf{u})' - \frac{1}{\mu \rho} \left[(\mathbf{b} \cdot \nabla \mathbf{b})' - \frac{1}{2} \nabla (\mathbf{b}^2)' \right] \tag{5.11}$$

contains terms that are nonlinear in $\mathbf{u}$ and $\mathbf{b}$. Now, in order to find an expression for $\mathcal{E}$, one can take recourse to various closure schemes such as First-Order Smoothing Approximation (FOSA) or Minimal-τ Approximation (MTA). Outline of these two schemes are presented next.

5.2.1 First-order smoothing approximation (FOSA)

The first-order smoothing approximation (FOSA) or the Second Order Correlation Approximation (SOCA) is one of the simplest way of expressing the turbulent emf, $\mathcal{E}$ in terms of the mean magnetic field $\overline{\mathbf{B}}$ and its derivatives. In this approximation the equations for the fluctuating quantities are linearized by neglecting the terms that are nonlinear in fluctuations and $\mathcal{E} = \overline{\mathbf{u} \times \mathbf{b}}$ is then evaluated for a prescribed velocity field, $\mathbf{u}$. In doing so, one must keep in mind that neglecting the nonlinear term $\mathbf{G} = \mathbf{u} \times \mathbf{b} - \overline{\mathbf{u} \times \mathbf{b}}$, is justified only when the fluctuations are small as compared to the mean values. This is true when the magnetic Reynolds number R_m is small i.e $R_m \ll 1$. In the absence of the term $\mathbf{G}$ (assuming $\mathbf{U} = 0$ for simplicity), $\mathbf{b}$ is generated at a rate $\simeq u\overline{B}/l$ while it is dissipated at a rate $\simeq ub/l^2$. For the equilibrium condition for the rate of generation and dissipation of $\mathbf{b}$, one finds $b \simeq R_m B$. Therefore, $\mathbf{b}$ is very small when $R_m \ll 1$ and can be treated as a perturbation to the mean field $\mathbf{B}$. However, in most astrophysical scenarios, $R_m \gg 1$. FOSA is still thought to be applicable here, provided the correlation time of turbulence τ is small, such that $\tau u_{rms} k_f \ll 1$, where u_{rms} and k_f are the root mean square (rms) velocity and the correlation wavenumber associated with the fluctuating velocity field $\mathbf{u}$ (Moffatt, 1978; Brandenburg and Subramanian, 2005a). Under such conditions, it can be shown that $\mathbf{G} \ll (\partial \mathbf{b}/\partial t)$. Thus neglecting the nonlinear term $\mathbf{G}$ and the resistive term (since $R_m \gg 1$) in equation (5.9) we get,

$$\frac{\partial \mathbf{b}}{\partial t} = \nabla \times (\mathbf{u} \times \overline{\mathbf{B}}) \tag{5.12}$$

Hence the departure $\mathbf{b}$ from $\overline{\mathbf{B}}$ resulting from $\mathbf{u}$ operating for the correlation time τ is

$$\begin{aligned}\mathbf{b} &\approx \tau\nabla\times(\mathbf{u}\times\overline{\mathbf{B}})\\ \mathbf{b} &= \tau(\overline{\mathbf{B}}\cdot\nabla)\mathbf{u}-\tau(\mathbf{u}\cdot\nabla)\overline{\mathbf{B}}. \qquad (5.13)\end{aligned}$$

where we have assumed $\nabla\cdot\mathbf{u}=0$ because of incompressibility and$\nabla\cdot\overline{\mathbf{B}}=0$). Using equation (5.13) to evaluate $\mathcal{E}$, we get

$$\begin{aligned}(\mathbf{u}\times\mathbf{b})_i &= \epsilon_{ijk}u'_jB'_k\\ &= \epsilon_{ijk}u'_j\overline{B}_l\frac{\partial u'_k}{\partial x_l}\tau-\epsilon_{ijk}u'_ju'_l\frac{\partial\overline{B}_k}{\partial x_l}\tau. \qquad (5.14)\end{aligned}$$

Taking the ensemble average and interchanging l and j we get

$$\begin{aligned}\mathcal{E}_i &= \epsilon_{ilk}\overline{u'_l\frac{\partial u'_k}{\partial x_j}}\tau\overline{B}_j-\epsilon_{ilk}\overline{u'_lu'_j}\tau\frac{\partial\overline{B}_k}{\partial x_j}\\ \mathcal{E}_i &= \alpha_{ij}\overline{B}_j+\beta_{ijk}\frac{\partial\overline{B}_k}{\partial x_j} \qquad (5.15)\\ \text{where } \alpha_{ij} &= \epsilon_{ilk}\overline{u'_l\frac{\partial u'_k}{\partial x_j}}\tau, \quad \beta_{ijk}=-\epsilon_{ilk}\overline{u'_lu'_j}\tau. \qquad (5.16)\end{aligned}$$

If the turbulence is assumed to be isotropic then we can write

$$\alpha_{ij}=\alpha\delta_{ij},\beta_{ijk}=-\eta_t\epsilon_{ijk} \qquad (5.17)$$

which leads to the following equations

$$\begin{aligned}\alpha &= \frac{1}{3}\alpha_{ii}=\frac{1}{3}\epsilon_{ilk}\overline{u'_l\frac{\partial u'_k}{\partial x_i}}\tau=-\frac{1}{3}\overline{u'_l\epsilon_{lik}\frac{\partial u'_k}{\partial x_i}}\tau\\ \beta_{ijk} &= -\frac{1}{3}\epsilon_{ijk}\overline{u'_lu'_j}\tau\delta_{jl}.=-\frac{1}{3}\overline{u'_ju'_j}\tau\epsilon_{ijk}=-\eta_t\epsilon_{ijk}. \qquad (5.18)\end{aligned}$$

We thus get the following equations for α and η_t

$$\begin{aligned}\alpha &= -\frac{1}{3}\overline{\mathbf{u}\cdot(\nabla\times\mathbf{u})}\tau \qquad (5.19)\\ \eta_t &= \frac{1}{3}\overline{\mathbf{u}\cdot\mathbf{u}}\tau \qquad (5.20)\end{aligned}$$

Thus the mean emf for isotropic turbulence is given by

$$\mathcal{E} = \alpha\overline{\mathbf{B}} - \eta_t \nabla \times \overline{\mathbf{B}}. \tag{5.21}$$

substituting equation (5.21) in equation (5.6) gives

$$\frac{\partial \overline{\mathbf{B}}}{\partial t} = \nabla \times (\overline{\mathbf{U}} \times \overline{\mathbf{B}}) + \nabla \times (\alpha\overline{\mathbf{B}}) + (\eta + \eta_t)\nabla^2\overline{\mathbf{B}} \tag{5.22}$$

where we have neglected the spatial variation of η_t. η_t is the coefficient of turbulent diffusion, α which is directly proportional to $\overline{\mathbf{u} \cdot (\nabla \times \mathbf{u})}$ is a measure of helical motion in the turbulent fluid. Usually $\eta << \eta_t$ and dropping the bar denoting averages equation (5.22) becomes

$$\frac{\partial \mathbf{B}}{\partial t} = \nabla \times (\mathbf{U} \times \mathbf{B}) + \nabla \times (\alpha\mathbf{B}) + \eta_t\nabla^2\mathbf{B} \tag{5.23}$$

which is the basic mean-field dynamo equation.

5.2.2 Minimal-τ approximation (MTA)

The 'minimal'-tau approximation (MTA) is a simplified version of the τ-approximation first introduced by Orszag (1970) and subsequently used by Pouquet, Frisch, and Leorat (1976) in the context of the Eddy Damped Quasi-Normal Markovian (EDQNM) approximation. The MTA as introduced by Blackman and Field (2002) uses the triple correlations arising from the quadratic nonlinearities in the equations for $\dot{\mathbf{u}}$ and $\dot{\mathbf{b}}$ assuming their sum is to be proportional to a negative multiple of the mean emf $\mathcal{E}$ with the relaxation time being the proportionality coefficient. This is motivated from the more general EDQNM closure, where a damping term is introduced in order to express third order moments in terms of lower order moments. In both FOSA and MTA, the linear terms in the evolution equations for the fluctuations are solved exactly. In the MTA, we begin by writing an equation for

the time derivative of the $\mathcal{E}$ (Blackman and Field, 2002),

$$\frac{\partial \mathcal{E}}{\partial t} = \overline{\mathbf{u} \times \dot{\mathbf{b}}} + \overline{\dot{\mathbf{u}} \times \mathbf{b}}, \tag{5.24}$$

where dots denote time derivatives. For $\dot{\mathbf{b}}$, we substitute equation (5.9) and for $\dot{\mathbf{u}}$, the Euler equation for the fluctuating velocity field

$$\frac{\partial \mathbf{u}}{\partial t} = -\nabla p' + \mathbf{f} + \nu \nabla^2 \mathbf{u} + \mathbf{H} \tag{5.25}$$

where $\mathbf{H} = -\mathbf{u} \cdot \nabla \mathbf{u} + \overline{\mathbf{u} \cdot \nabla \mathbf{u}}$ is the nonlinear term, $\mathbf{f}$ is a stochastic forcing with zero divergence and $\nu \nabla^2 \mathbf{u}$ is the viscous term (assuming $\nabla \cdot \mathbf{u} = 0$). Equation (5.25) assumes the absence of a mean flow ($\mathbf{U} = 0$) in the kinematic regime, where the Lorentz forces are small. The contribution to $\overline{\dot{\mathbf{u}} \times \mathbf{b}}$ comes only from the triple correlation involving $\mathbf{b}$ and $\mathbf{H}$. Combining all these terms and rearranging them in equation (5.24) we obtain,

$$\frac{\partial \mathcal{E}}{\partial t} = \tilde{\alpha} \overline{\mathbf{B}} - \tilde{\eta}_t \overline{\mathbf{J}} - \frac{\mathcal{E}}{\tau} \tag{5.26}$$

where all triple correlations are now contained in the damping term, $\mathcal{E}/\tau$. Blackman and Field (2002) motivate this term by arguing that in the absence of any mean-field $\overline{\mathbf{B}}$, the turbulent emf $\mathcal{E}$ should always decay to zero. Here,

$$\tilde{\alpha} = -\frac{1}{3} \overline{\mathbf{u} \cdot \boldsymbol{\omega}}, \quad \tilde{\eta}_t = \frac{1}{3} \overline{\mathbf{u}^2} \tag{5.27}$$

where $\boldsymbol{\omega} = \nabla \times \mathbf{u}$ are the turbulent transport co-efficients which are closely related to α and η_t previously obtained in equations (5.19) and (5.20) through the relations $\alpha = \tau \tilde{\alpha}$ and $\eta_t = \tau \tilde{\eta}_t$. We now find that the inclusion of the Lorentz force in equation (5.25) results in new small scale magnetic correction in the expression for $\tilde{\alpha}$ given by,

$$\tilde{\alpha} = -\frac{1}{3} (\overline{\mathbf{u} \cdot \boldsymbol{\omega}} - \overline{\mathbf{j} \cdot \mathbf{b}}), \quad \tilde{\eta}_t = \frac{1}{3} \overline{\mathbf{u}^2}. \tag{5.28}$$

In the steady state, the solution of equation (5.26) yields,

$$\mathcal{E} \simeq \tau\tilde{\alpha}\overline{\mathbf{B}} - \tau\tilde{\eta}_t\overline{\mathbf{J}} \simeq \alpha\overline{\mathbf{B}} - \eta_t\overline{\mathbf{J}} \tag{5.29}$$

where,

$$\alpha = -\frac{1}{3}\tau\overline{\mathbf{u}\cdot\boldsymbol{\omega}} = \alpha_k + \alpha_m, \eta_t = \frac{1}{3}\tau\overline{\mathbf{u}^2} \tag{5.30}$$

with $\alpha_k = -\frac{1}{3}\tau\overline{\mathbf{u}\cdot\boldsymbol{\omega}}$ and $\alpha_m = \frac{1}{3}\overline{\mathbf{j}\cdot\mathbf{b}}$. The presence of additional term which is proportional to the current helicity $\overline{\mathbf{j}\cdot\mathbf{b}}$ provides a negative feedback which quenches the total α-effect (Pouquet, Frisch, and Leorat, 1976). This has interesting consequences for the saturation of large-scale magnetic fields which will be presented in greater detail in the subsequent chapters.

5.3 Magnetic field generation in disc galaxies

Spiral galaxies are flat, rotating discs containing stars, gas and dust. There is a central concentration of stars known as the bulge, which is surrounded by a much fainter spherically symmetric distribution of stars called the halo. The average number density of the interstellar medium is about $n \sim 1$ cm^{-3}, which corresponds to a mass density of $\rho \approx 2 \times 10^{-24}$ g cm^{-3}. The radius of the galactic disc is $R \sim 15$ kpc, while its half-thickness is $h \sim 0.5$ kpc. The magnetic diffusivity in the ISM (assuming the plasma to be fully ionized) is given by $\eta = 10^7(T/10^4\ \mathrm{K})^{-3/2}$ cm^2 s^{-1}. The temperature of the warm diffuse gas is estimated to be 10^4 K which gives a $\eta \simeq 10^7$ cm^2 s^{-1}. The diffusion timescale for the magnetic field based on the molecular diffusivity is $h^2/\eta \sim 10^{27}$ yr. Since this timescale is much larger than the age of the galaxy ($\sim 10^{10}$ yr), it would suggest suggest that magnetic fields once generated during the formation of galaxy would survive and thus additional generation through the dynamo action is not required. This is not true because

the ISM in spiral galaxies is turbulent (due to the energy supplied by random Supernovae (SNe) explosions occurring at different places in the disc). The diffusion timescale thus must be based on turbulent magnetic diffusivity η_t. The turbulent diffusivity for SN driven turbulence can be estimated as $\eta_t \sim \frac{1}{3}u^2\tau \sim \frac{1}{3}l_0u_0$; where l_0 ($\sim$ 100 pc) is the correlation scale of interstellar turbulence and u_0 ($\sim$ 10 km/s) is the turbulent velocity (Shukurov, 2007). The corresponding turbulent diffusivity $\eta_t \simeq (0.5-3)\times 10^{26}$ cm^2 s^{-1} gives a turbulent diffusion time scale, $t_d = h^2/\eta_t \simeq \times 10^9$ yr (for $h = .5$ kpc) which is much shorter than the galactic lifetime. We therefore need dynamo operation in the galaxy to maintain a steady magnetic field of the observable magnitude.

Galaxies exhibit differential rotation with the inner region rotating faster than the outer region. As the plasma in ISM in highly conducting, the magnetic flux is frozen with the motion of the plasma. Due to the differential rotation of the disc, the poloidal component of the magnetic field gets wounded up and amplified to produce a toroidal component (as shown in Fig. 5.1). For the dynamo to operate, one needs to regenerate the poloidal component of the magnetic field from the toroidal one. This is accomplished through the α-effect arising out of the cyclonic turbulence present in the galactic disc. Due to combined effect of the galactic rotation and density stratification the SN driven turbulence becomes helical. Under these conditions, a blob of plasma moving upwards expands due to the decrease in density. The Coriolis force acting on this expanding bubble imparts a angular momentum about the vertical axis generating a negative (positive) kinetic helicity in the northern (southern) hemisphere. We can easily see, that the kinetic helicity $\langle \mathbf{u}\cdot\boldsymbol{\omega}\rangle$ has the same sign for both the ascending and descending vortices in a given hemisphere. The helical motions of the gas perpendicular to the disc can pull

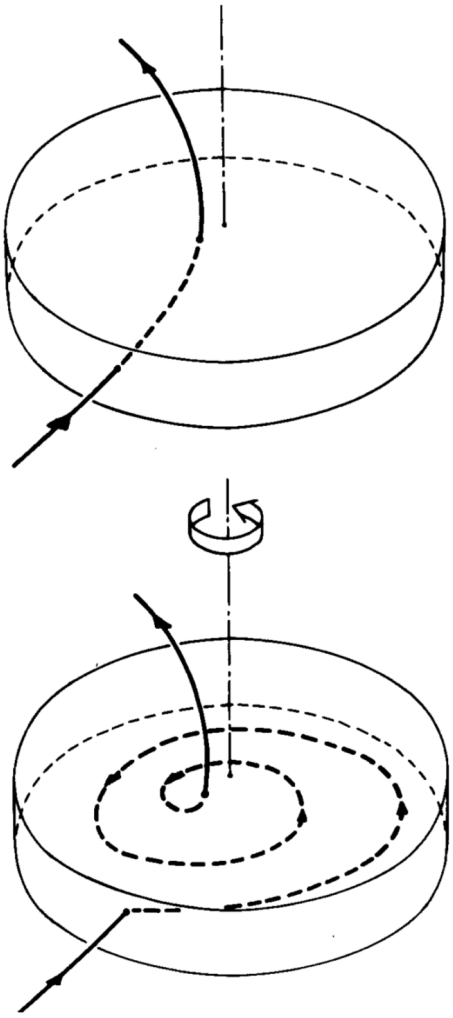

Figure 5.1: The poloidal magnetic field (upper panel) is twisted and wounded up by the differentially rotating galactic disc to produce a toroidal field (lower panel). Figure courtesy: Ruzmaikin, Sokolov, and Shukurov (1988)

out the toroidal field into a Ω shaped loop. For motions having a non-zero net helicity, the component of the current parallel to the toroidal field add up coherently resulting in generation of poloidal fields. Theses fields then reconnect due to the finite microscopic diffusivity and eventually produce the large-scale poloidal magnetic field (see Fig. 5.2). This toroidal-poloidal

regeneration cycle leads to an exponential growth of the mean field.

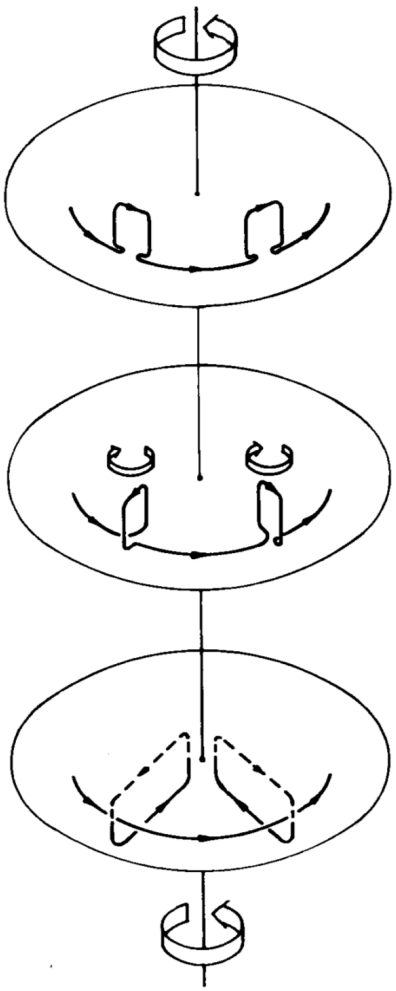

Figure 5.2: The poloidal magnetic field is re-generated from the toroidal field due to helical turbulent motions resulting in twisted magnetic loops. The upper part of the field (shown in dashed in the lowest panel) leaves the disc. Figure courtesy: Ruzmaikin, Sokolov, and Shukurov (1988)

5.3.1 The galactic dynamo formalism

The following treatment is based on (Ruzmaikin, Sokolov, and Shukurov, 1988). We consider the galactic disc as a thin turbulized slab of thickness $2h$ which rotates with angular velocity $\Omega(r)$. The equation for the mean axisymmetric magnetic field has the following components in polar cylindrical coordinates (r, ϕ, z) with the z-axis coincident with the rotation axis (Baryshnikova *et al.*, 1987)

$$\begin{aligned} \frac{\partial B_r}{\partial t} &= -\frac{\partial}{\partial z}(\alpha B_\phi) + \eta(\Delta \mathbf{B})_r \\ \frac{\partial B_\phi}{\partial t} &= G B_r + \eta(\Delta \mathbf{B})_\phi \\ \frac{\partial B_z}{\partial t} &= -\frac{1}{r}\frac{\partial}{\partial r}(r\alpha B_\phi) + \eta(\Delta \mathbf{B})_z \end{aligned} \tag{5.31}$$

where B_r, B_ϕ and B_z are the components of the mean magnetic field, and $G = r\dfrac{\mathrm{d}\Omega}{\mathrm{d}r}$ is the measure of differential rotation. Because of axial symmetry $\dfrac{\partial}{\partial \phi} = 0$, and we can express B_r and B_z in terms of azimuthal component of the vector potential A_ϕ.

$$B_r = -\frac{\partial A_\phi}{\partial z}, \quad B_z = \frac{1}{r}\frac{\partial}{\partial r}(rA_\phi) \tag{5.32}$$

which guarantees $\nabla \cdot \mathbf{B} = 0$.

We try to get solution at fixed radius. In this case

$$(\Delta \mathbf{B})_r = \frac{\partial^2 B_r}{\partial z^2}, \quad (\Delta \mathbf{B})_\phi = \frac{\partial^2 B_\phi}{\partial z^2}, \quad (\Delta \mathbf{B})_z = \frac{\partial^2 B_z}{\partial z^2}$$

The first two equations from equation (5.31) become

$$\frac{\partial A}{\partial t} = \alpha B + \eta\frac{\partial^2 A}{\partial z^2}, \quad \frac{\partial B}{\partial t} = -G\frac{\partial A}{\partial z} + \eta\frac{\partial^2 B}{\partial z^2} \tag{5.33}$$

where we have dropped the subscript ϕ from A and B. The axial symmetry implies $B = 0$ for $|z| > h$, while potential A obeys the following equation:

$$\frac{\partial^2 A}{\partial z^2} + \frac{\partial}{\partial r}\left(\frac{1}{r}\frac{\partial}{\partial r}(rA)\right) = 0, \tag{5.34}$$

whose solution is a linear combination of function of the form $\exp(kz)J_1(kr)$, with the boundary conditions $\nabla \times \mathbf{B} = 0$ at $r = R$ and $\dfrac{\partial A}{\partial z} = kA \approx 0$ ($k \sim R^{-1} << h$, with R the radius of the galactic disc). The boundary conditions at $|z| = h$ are

$$B(\pm h) = 0, \quad B_r = -\frac{\partial A}{\partial z}(h) \approx 0. \tag{5.35}$$

These boundary conditions are referred to as vacuum boundary conditions. Adopting these conditions we seek the solutions to the equation (5.32) of the form

$$B(t,z) = B(z)e^{\gamma t}, \quad B_r(t,z) = B_r(z)e^{\gamma t}, \quad A(t,z) = A(z)e^{\gamma t}. \tag{5.36}$$

We introduce dimensionless variables $z \to z/h, t \to h^2/\eta, \gamma \to \gamma/(\eta/h^2)$ and $\alpha \to \alpha_0\alpha(z)$ and dimensionless amplitudes of the field and potential whose ratio is $A_0/B_0 = \alpha_0 h^2/\eta$. We denote the dimensionless quantities with the same symbols as the dimensional ones. In dimensionless form, the generation equations are

$$\begin{aligned} \left(\gamma - \frac{\partial^2}{\partial z^2}\right) B_r &= -\frac{\partial}{\partial z}(\alpha B) \\ \left(\gamma - \frac{\partial^2}{\partial z^2}\right) B &= DB_r \\ B(\pm 1) &= B_r(\pm 1) = -\frac{\partial A}{\partial z}(\pm 1) = 0 \end{aligned} \tag{5.37}$$

and $D = G\alpha_0 h^3/\eta^2$ is a dimensionless quantity called the dynamo number. The first equation in equation (5.37) can be replaced by

$$\left(\gamma - \frac{\partial^2}{\partial z^2}\right) A = \alpha B. \tag{5.38}$$

Properties of solutions:

1. Symmetry. The equations possess an important symmetry since $\alpha(z) =$

$-\alpha(z)$. The system of equations (5.37,5.38) is invariant with respect to transformation $z \to -z$, provided

$A(-z) = A(z), \quad B_r(-z) = -B_r(z), \quad B(-z) = -B(z)$ or otherwise

$A(-z) = -A(z), \quad B_r(-z) = B_r(z), \quad B(-z) = B(z)$

Therefore, solutions to the generation equations can be divided into two classes conveniently distinguished accordingly to the symmetry of $B(z)$: the odd solutions (dipolar in B_r, B_z) and the even ones (quadrupolar in B_r, B_z).

2. Decay modes. The generation equation can be easily solved in absence of the sources, $\alpha = G = 0$. Growth rates of the odd modes are

$\gamma_k^D = -k^2\pi^2$

while for the even modes

$\gamma_k^Q = -(k + 1/2)^2\pi^2$

where $k = 0, 1, 2...$

The lowest quadrupole mode decays four times as weakly as the lowest dipole one and is thus generated preferentially at a larger growth rate then the dipole ones.

3. Small dynamo numbers. In this limiting case the right hand side of equation (5.37) can be considered as small perturbations. We re-normalize $B_r \to |D|^{1/2} B_r$ and recast the generation equation as

$$\left(\frac{\mathrm{d}^2}{\mathrm{d}z^2} - \gamma - V\right)\begin{pmatrix} B_r \\ B \end{pmatrix} = 0 \tag{5.39}$$

where $V = |D|^{1/2}\begin{pmatrix} 0 & \frac{\partial\alpha}{\partial z} \\ 1 & 0 \end{pmatrix}$.

The standard perturbation theory for a doubly degenerate energy level gives the following first approximation correction to the eigenvalue of the decaying of the decaying mode:

$$\Delta = \pm(V_{12}V_{21})^{1/2}$$

where V_{12} and V_{21} are the corresponding matrix elements calculated from undisturbed, free decaying eigenfunctions. We put $\alpha = z$ for the sake of simplicity. This gives

$$\begin{aligned} \gamma^D &= -\pi^2 \pm |D|^{1/2} \\ \gamma^Q &= -\frac{\pi^2}{4} \pm |D|^{1/2} \end{aligned} \tag{5.40}$$

for the dipole and the quadrupole modes, respectively. Thus the lowest order quadrupolar solutions can be written as:

$$B(z,t) = \cos\left[\left(\pi^2/4 - \sqrt{D}\right)^{1/2} z\right] \exp\left(-\pi^2/4 + \sqrt{D}\right) t \tag{5.41}$$

$$A(z,t) = \sin\left[\left(\pi^2/4 - \sqrt{D}\right)^{1/2} z\right] \exp\left(-\pi^2/4 + \sqrt{D}\right) t \tag{5.42}$$

5.3.2 Radial field distribution

When the radial dependence of both the generators and the field is included, the generation equation for the axisymmetric field take the form

$$\begin{aligned} \frac{\partial B}{\partial t} &= -G\frac{\partial A}{\partial z} + \eta\frac{\partial^2 B}{\partial z^2} + \eta\frac{\partial}{\partial r}\left[\frac{1}{r}\frac{\partial}{\partial r}(rB)\right] \\ \frac{\partial A}{\partial t} &= \alpha B + \eta\frac{\partial^2 A}{\partial z^2} + \eta\frac{\partial}{\partial r}\left[\frac{1}{r}\frac{\partial}{\partial r}(rA)\right] \end{aligned} \tag{5.43}$$

We consider exponentially growing solutions $(A, B) \propto \exp(\Gamma t)$ with the growth rate denoted by Γ and introduce the dimensionless variables (R, Z, T) such that $Z = z/h_0, \quad R = r/r_0, \quad T = t\eta/h_0^2$.

We also introduce dimensionless angular velocity, its shear, and helicity: $\omega = \Omega/\Omega_0, \quad g = G/\Omega_0, \quad \alpha_* = \alpha/\alpha_0$.

The units convenient for applications to spiral galaxies are $h_0 = 400$ pc, $r_0 = 10$ kpc, $h_0^2/\eta = 5 \times 10^8$ years, $\Omega_0 = 10^{-15} s^{-1}$, $\alpha_0 = 1$ kms^{-1}. Further, we normalize the magnetic field by some arbitrary amplitude for instance the initial one B_0

$A_* = A/(B_0 h_0) \quad B_* = B\alpha_0 h_0/(B_0 \eta)$,

and measure the growth rate Γ in units of the inverse diffusion time, $\eta/h_0^2 (\approx (5 \times 10^8 \text{ year})^{-1})$. The asterisks at the dimensionless field, potential and helicity will be dropped below.

In terms of dimensionless variables equations (5.43) are

$$\begin{aligned} \Gamma B &= -Dg\frac{\partial A}{\partial Z} + \eta\frac{\partial^2 B}{\partial Z^2} + \lambda^2\frac{\partial}{\partial R}\left[\frac{1}{R}\frac{\partial}{\partial R}(RB)\right] \\ \Gamma A &= \alpha B + \eta\frac{\partial^2 A}{\partial Z^2} + \lambda^2\frac{\partial}{\partial R}\left[\frac{1}{R}\frac{\partial}{\partial R}(RA)\right] \end{aligned} \tag{5.44}$$

where the dynamo number is defined as

$$D = \frac{\alpha_0 \Omega_0 h_0^3}{\eta^2}$$

while $\lambda = h_0/r_0$. For the chosen units, $\lambda = 0.04$. The small value of λ which characterizes the galactic disc allows us to obtain a simple asymptotic solution of the dynamo equations (5.44). Let us represent the solutions as

$B(R,Z) = Q(R)\hat{B}(R,Z)$

$A(R,Z) = Q(R)\hat{A}(R,Z)$

where $\hat{A}(R,Z)$ and $\hat{B}(R,Z)$ satisfy, by definition, the following one-dimensional equations:

$$\begin{aligned} \gamma(R)\hat{B} &= -Dg\frac{\partial \hat{A}}{\partial Z} + \eta\frac{\partial^2 \hat{B}}{\partial Z^2} \\ \gamma(R)\hat{A} &= \alpha\hat{B} + \eta\frac{\partial^2 \hat{A}}{\partial Z^2} \end{aligned} \tag{5.45}$$

whose forms coincide with the dynamo equations (5.37) for an infinitesimally thin slab. The quantity $\gamma(R)$ may be considered as the local growth rate of the field. We introduce the dimensionless half-thickness, $H(R) = h(R)/h_0$. Presuming that there are no electric currents flowing outside the disc, the boundary conditions are

$$\frac{\partial \hat{A}}{\partial Z}(\pm H, R) = \hat{B}(\pm H, R) = 0. \tag{5.46}$$

We decompose the coefficient $\alpha(R,Z)$ as

$$\alpha = \alpha_1(R)\cdot\alpha_2(Z)$$

and introduce new variables

$$\tilde{Z} = Z/H(R), \quad \tilde{B} = \hat{B}\alpha_1(R)H^2(R), \quad \tilde{A} = \hat{A}.$$

Eqns. (5.45,5.46) are recast as

$$\begin{aligned} \tilde{\gamma}(R)\tilde{B} &= -D_{eff}(R)\frac{\partial\tilde{A}}{\partial\tilde{Z}} + \frac{\partial^2\tilde{B}}{\partial\tilde{Z}^2} \\ \tilde{\gamma}(R)\tilde{A} &= \alpha_2(\tilde{Z})\tilde{B} + \frac{\partial^2\tilde{A}}{\partial\tilde{Z}^2} \\ \frac{\partial\tilde{A}}{\partial\tilde{Z}}(\pm1) &= \tilde{B}(\pm1) = 0, \end{aligned} \tag{5.47}$$

where

$$\tilde{\gamma}(R) = \gamma(R)H^2(R) \tag{5.48}$$

and the effective dynamo number

$$D_{eff} = D\alpha_1(R)g(R)H^3(R) \tag{5.49}$$

is defined like the local dynamo number but includes the radial variations of both the generators, α and G, and the disc thickness.

Simultaneously with the equations (5.45), the following Schrödinger equation is derived for $Q(R)$:

$$\lambda^2\frac{\mathrm{d}}{\mathrm{d}R}\left[\frac{1}{R}\frac{\mathrm{d}}{\mathrm{d}R}(RQ)\right] + [\gamma(R) - \Gamma]Q = 0, \tag{5.50}$$

in which $-\gamma(R)$ plays the role of potential and the growth rate taken with opposite sign takes the place of total energy.

We take the simplest model in which generation sources are uniformly distributed across the ring $R_1 \le R \le R_2$ with impervious radial boundaries:

$$\gamma(R) = \begin{cases} \gamma_m & \text{for} \quad R_1 \le R \le R_2 \\ -\infty & \text{for} \quad R > R_2 \text{ and } R > R_1 \end{cases}$$

equation (5.50) is reduced to the Bessel Equation whose solution is given by

$$Q(R) = C_1 J_1\left(\frac{(\gamma_m - \Gamma)^{1/2}}{\lambda} R\right) + C_2 Y_1\left(\frac{(\gamma_m - \Gamma)^{1/2}}{\lambda} R\right),$$

where J_1 and Y_1 are the Bessel Functions of the first and second kind, respectively. The boundary conditions are $Q(R_1) = Q(R_2) = 0$. The eigenvalues can be estimated with the help of the asymptotic form of the Bessel functions

$$\begin{aligned} J_1(x) &\simeq \left(\frac{2}{\pi x}\right)^{1/2} \cos\left(x - \frac{3\pi}{4}\right), \\ Y_1(x) &\simeq \left(\frac{2}{\pi x}\right)^{1/2} \sin\left(x - \frac{3\pi}{4}\right), \end{aligned}$$

which are applicable for sufficiently high energy levels $\gamma_m - \Gamma >> \lambda^2 R^{-2}$. This gives

$$\Gamma_n \simeq \gamma_m - \frac{\pi n \lambda^2}{R_2 - R_1},$$

where n is an integer.

5.3.3 External fields

We introduce the magnetic stream function ψ (equivalently, the poloidal flux), which determines the poloidal field strength (Mangalam and Subramanian, 1994),

$$\mathbf{B_p} = B_r \hat{\mathbf{r}} + B_z \hat{\mathbf{z}} = \hat{\boldsymbol{\phi}} \times \left(\frac{1}{r} \nabla \psi\right) \equiv \hat{\mathbf{P}} \psi. \tag{5.51}$$

$$\psi = -r A_\phi \tag{5.52}$$

We also define the poloidal current function T by

$$T = r B_\phi = -\frac{c}{2} i_p, \tag{5.53}$$

where i_p is the poloidal current and B_ϕ is the toroidal field.

We take the external field to be a force-fee vacuum field satisfying the equation

$$\nabla^2 \mathbf{B} = 0. \tag{5.54}$$

The general solution of the above equation can be split into poloidal and toroidal parts, and under axisymmetry we can write

$$\psi_e(r,z) = \sum_{n=1}^{N} A_n r J_1(k_n r) \exp(-k_n z) \tag{5.55}$$

$$T_e = 0 \tag{5.56}$$

5.3.4 Lowest order solutions

Using the boundary conditions (5.38) and the continuity of fields inside and outside the disc, we get the solutions for the lowest quadrupole mode as:

$$T(r,z) = \begin{cases} \cos\left[\left(\frac{3\pi}{2}\right) z\right] r J_1(k_1 r) & r < 1, z < 1 \\ 0 & r > 1, z > 1 \end{cases} \tag{5.57}$$

$$\psi(r,z) = \begin{cases} \sin\left[\left(\frac{3\pi}{2}\right) z\right] r J_1(k_1 r) & r < 1, z < 1 \\ \exp[k_1(1-z)] r J_1(k_1 r) & r > 1, z > 1 \end{cases} \tag{5.58}$$

which gives the saturation value for the dynamo number as $D = \pi^2 + 1 = 10.86$.

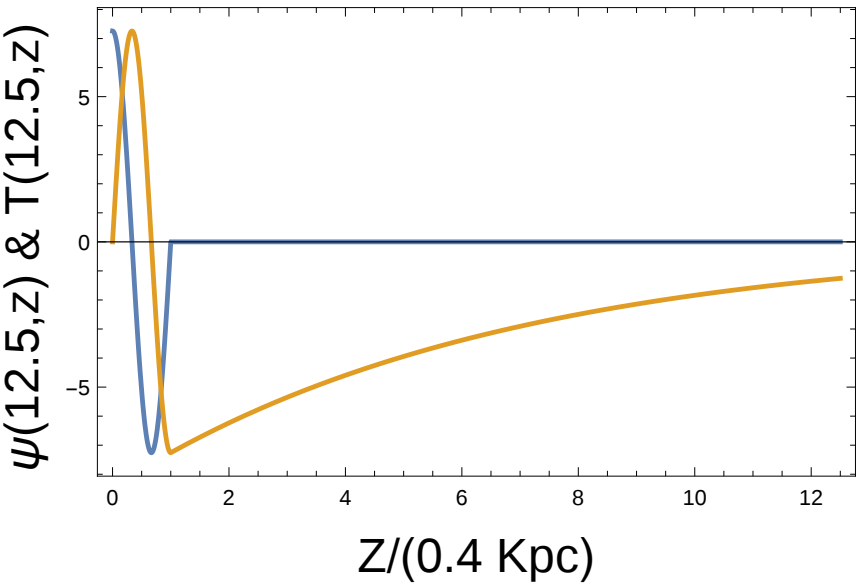

Figure 5.3: Variation of T(blue curve) and ψ (yellow curve) functions with z at $r = 5$ Kpc.

5.4 Current issues in dynamo theory

One of the central issues in the mean-field dynamo (MFD) theory, is expressing the mean turbulent electromotive force $\mathcal{E}$ in terms of the mean magnetic field and its derivatives using closure approximations. These closure approximations closure approximations like the First-order smoothing approximation (FOSA) and the Minimal-τ approximation (MTA) give the dynamo coefficients - the α-effect and the turbulent magnetic diffusivity η_t, both of which are related to the statistical properties of the turbulent flow. The α-effect is crucial in driving the mean-field dynamos, while η_t enhances mean magnetic field diffusion. In spite of extensive studies for the past few decades, several potential problems associated with the dynamo paradigm remain unexplained. The first issue is, whether one can relate the turbulent transport coefficients namely, α and η_t to the statistical properties flow in the kinematic

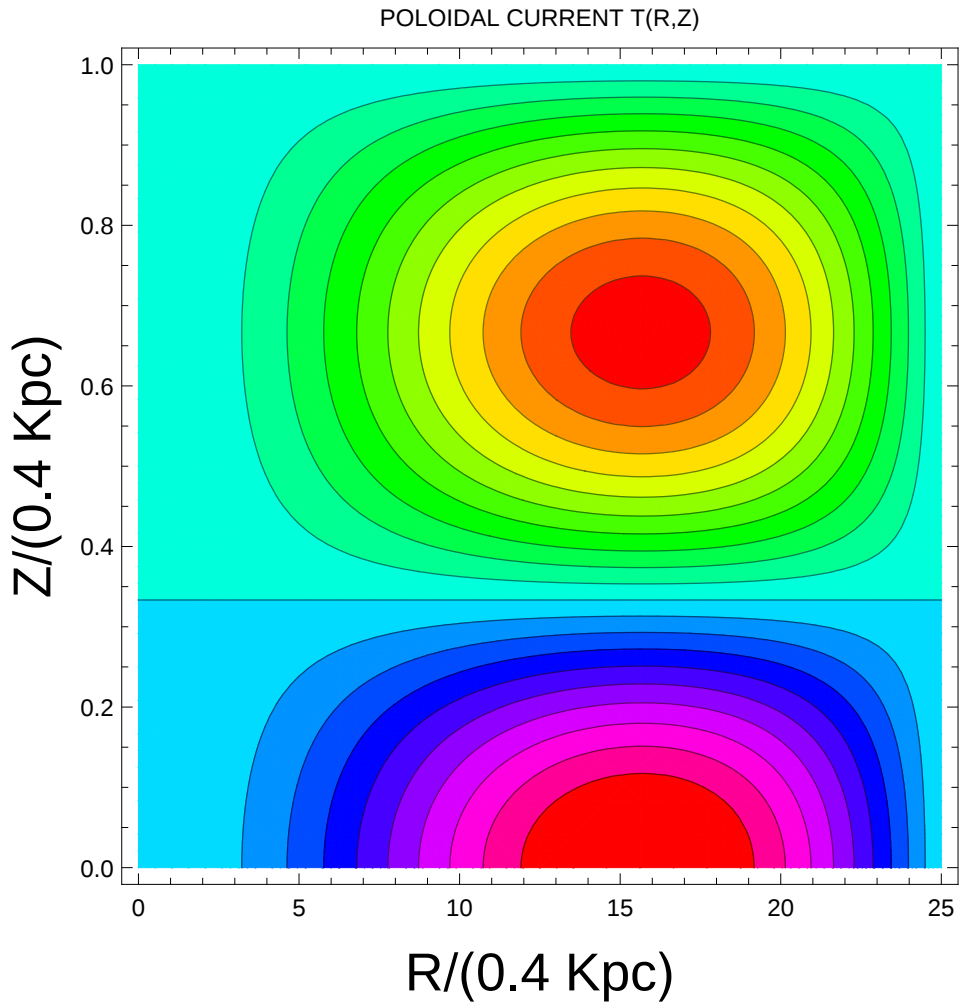

Figure 5.4: Meridional cross-section contour plot of poloidal current function T for disc radius = 10 kpc and half width = 400 pc. The poloidal current increases radially and achieves a maximum at 6 Kpc. The current density reverses sign and goes to zero as we move towards the disc edge.

regime. Another question is the applicability of approximations like FOSA and MTA for large magnetic Reynolds number (R_m) systems, as it is seen in such systems, that the small-scale dynamo produces random magnetic fields at a rate much faster than the mean-field. Since, the correlation time of the turbulence measured in units of the eddy turnover time is not small for

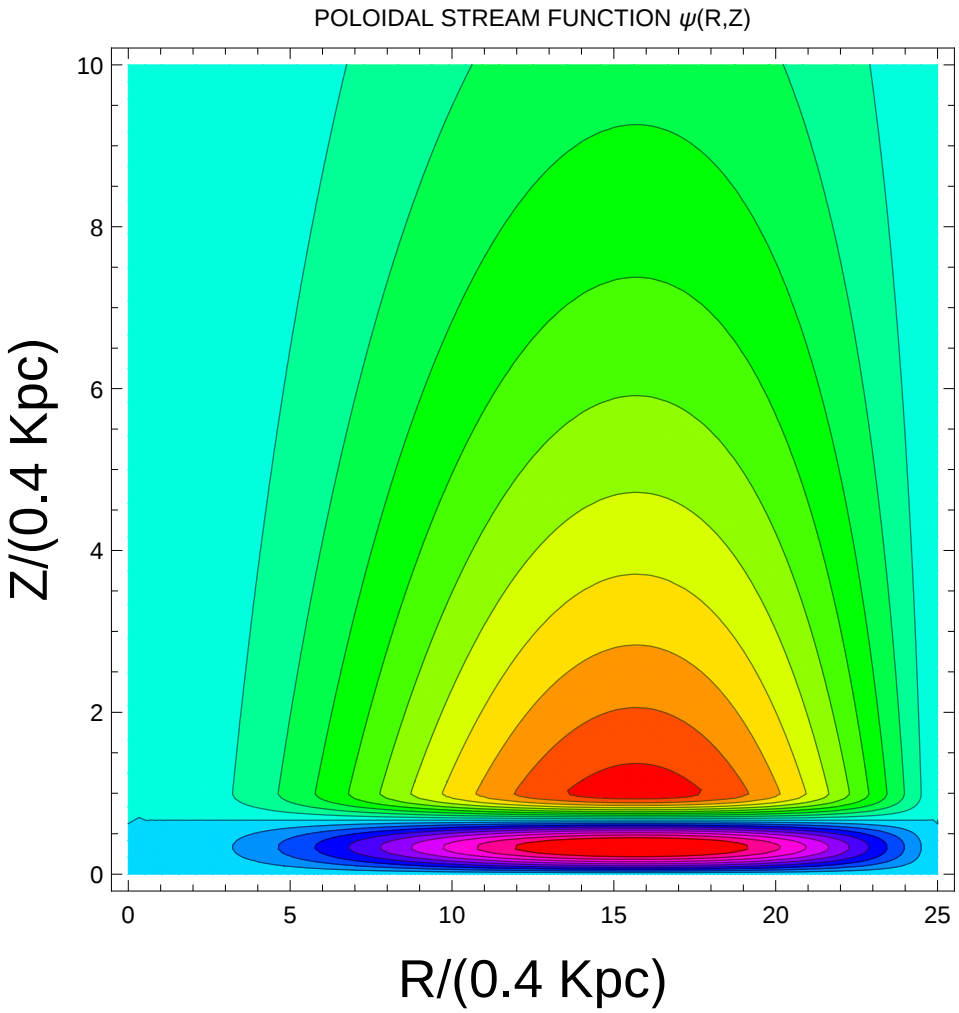

Figure 5.5: Meridional cross-section contour plot of poloidal stream function ψ for disc radius = 10 kpc and half width = 400 pc. The contours indicate the poloidal component of the field lines.

turbulent flows, it becomes difficult to relate the transport coefficients with the statistical properties of the flow. Using Direct Numerical Simulations (DNS) of helically forced turbulence, Sur, Subramanian, and Brandenburg (2007) show that in the kinematic regime, up to moderate $R_m \sim 220$, homogeneous, isotropic, helical turbulence leads to an α-effect and η_t, whose

values are independent of R_m, for R_m ¿ 1 and consistent with expectations from the closure approximations.

Another long standing problems in the MFD theory is the effect of non-linear back reaction on the transport coefficients, which occurs when the Lorentz force becomes strong enough to affect the fluid motions. It is argued by several authors (Pouquet, Frisch, and Leorat, 1976; Gruzinov and Diamond, 1994; Blackman and Field, 2002) that this back reaction leads to the modification of the α-effect by a term which is proportional to the current helicity of the small-scale field. A greater understanding of the back reaction from the small-scale fields is crucial in explaining the saturation of turbulent dynamos. As the magnetic helicity is conserved in high R_m systems, the addition of a magnetic alpha to the kinetic alpha profoundly impacts the large-scale dynamo action. The conservation law implies that, equal and opposite amounts of helicity are produced in the large- and small-scale fields. The current helicity associated with the growing small-scale field contributes to the magnetic alpha (α_m) which suppresses the total α-effect and eventually leads to quenching of the dynamo. Thus, to explain the existence of coherent magnetic fields, one has to search for mechanisms that are capable of shedding the small-scale magnetic helicity. In this context, Sur, Shukurov, and Subramanian (2007) study the influence of various kinds of magnetic helicity fluxes on galactic dynamos. They discuss the implications of two types of magnetic helicity flux, one produced by advection (e.g., due to the galactic fountain or wind) and the other - the Vishniac-Cho flux, arising from anisotropy of turbulence and shear. They find that the steady-state strength of the large-scale magnetic field supported by the helicity advection is still weaker than that corresponding to equipartition with the turbulent energy. However, inclusion of the Vishniac-Cho helicity flux allows the magnetic field to achieve energy

equipartition with turbulence. Chamandy *et al.* (2014) present a comparison of different models and approximations for non-linear mean-field dynamos in disc galaxies and assess their applicability and accuracy. They consider two dynamo saturation mechanisms, namely, the magnetic helicity balance involving helicity fluxes (the dynamical α-quenching) and the algebraic α-quenching. The non-linear solutions are then compared with the marginal kinematic and asymptotic solutions. They find that the different models lead to similar solutions for the mean magnetic field and that the algebraic α-quenching non-linearity can be obtained from a more physical dynamical α-quenching model in the limit of nearly azimuthal magnetic fields. They also incorporate galactic outflows into a simple analytical dynamo model to show that the outflow can produce leading magnetic spirals near the disc surface.

In Chapter 8, we present a global three-dimensional model of the non-linear turbulent dynamo which is applied to a disc galaxy with a force-free corona. We show that a global helicity conservation requires a build up of a force-free corona due to the small-scale magnetic helicity fluxes. We also discuss the global structure of the field and the nonlinear saturation of the dynamo.

Chapter 6

Force free reconstruction from photosphere to the corona

6.1 Introduction

The active regions in solar photosphere are locations of high magnetic field where magnetic pressure starts to dominate over gas pressure. In such conditions the plasma is likely to follow a force-free equation of state, where the Lorentz force vanishes at all points. It was shown by Taylor (1974) that in systems where magnetic forces are dominant in the presence of kinematic viscosity, linear force-free fields are natural end configurations. A more general class of force-free fields is obtained when the energy of the system is minimized with constraints of total mass, angular momentum, cross-helicity

The work presented in this chapter was published in:

i. Prasad, A., and Mangalam, A. (2013), eds. Gopalswamy, N., Hasan, S. S., Rao, P. B., & Subramanian, P 2013, ASI Conf. Ser. 10, 53

ii. Prasad, A., Mangalam, A. and Ravindra, B., 2014, ApJ, 786, 81

and relative helicity (e.g. Finn and Antonsen (1983), Mangalam and Krishan (2000)). Within the context of force -free configurations, there are numerous possibilities that can be obtained due to underlying geometry and symmetry of the problem in addition to the invariants involved. There have been several attempts to construct such full three dimensional models from two dimensional data obtained at one level vector magnetograms. A summary of the various numerical techniques are discussed in Schrijver *et al.* (2006) and Metcalf *et al.* (2008). They compare six algorithms for the computation of nonlinear force-free (NLFF) magnetic fields which include optimization (Wheatland, Sturrock, and Roumeliotis, 2000; Wiegelmann, 2004; Wiegelmann, Inhester, and Sakurai, 2006), magneto frictional (Yang, Sturrock, and Antiochos, 1986; McClymont and Mikic, 1994; Roumeliotis, 1996; McClymont, Jiao, and Mikic, 1997), Grad–Rubin based (Amari *et al.*, 1997; Amari, Boulmezaoud, and Aly, 2006; Wheatland, 2007; Wheatland and Régnier, 2009), and Green's function-based methods (Yan and Sakurai, 1997, 2000) by evaluating their performance in tests on analytical force-free-field models for which boundary conditions are specified either for the entire surface area of a cubic volume or for an extended lower boundary. Figures of merit were used to compare the input vector field to the resulting model fields. Based on these, they argue that all algorithms yield NLFF fields that agree best with the input field in the lower central region of the volume, where the field and electrical currents are strongest and the effects of boundary conditions the weakest. The NLFF codes when applied to solar data, do not necessarily converge to a single solution. To address this Wheatland and Leka (2011) include uncertainties on the electric current densities at the boundaries iteratively until the two non-linear solutions agree, leading to a more reliable construction.

Since the NLFF techniques require good input fields for fast convergence and are subject to uncertainties at the boundary conditions which propagate during extrapolation, we are exploring fits of the data directly to analytic solutions. The best fit to a well known (non-) linear (semi-) analytic solution, would give us more insight into the kind of structure that could be present in the volume given an optimal correlation with the fields observed on the magnetogram. The solution thus found can then be exploited to yield quantities of interest such as relative helicity and free energy that can be computed for the 3D configuration. Further, one can explore the stability and dynamics of these structures at a later stage.

While there are several possible topologies for various geometries and boundary conditions e.g. Marsh (2006), it is our goal here to take the simplest geometric approach of a sphere. We show that separability condition leads to two classes of solutions: linear and non-linear force-free fields. We call these linear fields as Chandrasekhar solution (Chandrasekhar, 1956), hereafter referred to as C modes and the non-linear fields as Low-Lou solutions (Low and Lou, 1990), hereafter referred to as LL modes. These computationally cheap three dimensional analytic models are comparable with other numerics or with observations and this allows us to make more precise predictions of the physically relevant configurations. Since the validity of physical assumptions can vary from active region to active region, we restrict our selves to explore the most simplest of solutions involving the least number of parameters, namely the choice of the modes and the two of the three Euler angles that will represent any arbitrary rotation of the configuration space into the coordinates of the observed magnetogram.

The chapter is presented as follows: In §6.2 we describe the formulation of the free energy and relative helicity in a shell geometry. In §6.3, we show

that the force-free field equation under assumption of axisymmetry leads to linear (C modes) and non-linear (LL modes) force-free fields which are discussed in §6.4 and §6.5 respectively. In §6.6, we present the construction of magnetogram templates and the search strategy for obtaining the best fit using suitable fitting parameters. In §6.7 and §6.8 we present the data used for this study and compare them with the simulated models. The summary and conclusions are presented in §6.9. Details of mathematical derivations for some of the relations are referred to the Appendices. Table 6.6 provides a formulary for the C and LL modes.

6.2 Formulation of the free energy and relative helicity in shell geometry

In this chapter, we study the solutions of axisymmetric linear and non-linear force-free fields in a spherical shell geometry and calculate the relevant quantities like free energy and relative helicity for these configurations. The free energy of the system is the difference between the energies of a force-free field and a potential field in the entire volume. The expression for free energy E_{free} is given by

$$E_{free} = E_{ff} - E_P, \tag{6.1}$$

where E_{ff} and E_P are the energies of the force-free field and the potential field respectively. Since the potential field is the minimum energy configuration for a given boundary condition, E_{free} is always positive.

Relative helicity is a gauge invariant measure of linkages between the field lines with respect to a potential field matching to the perpendicular field at the surface (Berger and Field, 1984). Relative helicity can be computed using

the Finn-Antonsen formula (Finn and Antonsen, 1983)

$$H_{rel} = \int_V (\mathbf{A} + \mathbf{A}_P) \cdot (\mathbf{B} - \mathbf{B}_P) \mathrm{d}V. \tag{6.2}$$

where $\mathbf{A}_P$ and $\mathbf{B}_P$ are the vector potential and magnetic field for the potential field with the constraint that $(\mathbf{B}_P)_r = \mathbf{B}_r$, where r represents the radius at the boundary. Another expression that can be used for calculating relative helicity in spherical geometry which is independent of the potential field by following the treatment given in Berger (1985), where

$$H_{rel} = 2 \int_V \mathbf{L}P \cdot \mathbf{L}T \mathrm{d}V, \tag{6.3}$$

$\mathbf{L} = -\mathbf{r} \times \nabla$ is the angular momentum operator, and P, T are the poloidal and toroidal components of the magnetic field respectively. The expression in equation (6.3) can be further simplified for axisymmetric magnetic fields in spherical geometry. The toroidal component $\mathbf{L}T = B_\phi \hat{\phi}$, whereas $\mathbf{L}P = A_\phi \hat{\phi} + \nabla\psi$ which includes the gauge term $\nabla\psi$; A_ϕ and B_ϕ are the ϕ components of the vector potential and the magnetic field. We now use the gauge invariance of equation (6.3) to get the final expression for relative helicity to be

$$\int_V \mathbf{L}P \cdot \mathbf{L}T \mathrm{d}V = \int_V A_\phi B_\phi \mathrm{d}V + \int_V \nabla\psi \cdot (B_\phi \hat{\phi}) \mathrm{d}V. \tag{6.4}$$

The last term in the RHS of equation (6.4) vanishes as

$$\int_V \nabla\psi \cdot (B_\phi \hat{\phi}) \mathrm{d}V = \int_V \nabla \cdot (\psi B_\phi \hat{\phi}) \mathrm{d}V = \int_S (\psi B_\phi) \hat{\phi}.\hat{r} \mathrm{d}S = 0. \tag{6.5}$$

Thus equation (6.4) simplifies to

$$H_{rel} = 2 \int_V A_\phi B_\phi \mathrm{d}V. \tag{6.6}$$

In the above derivation, it is seen that $\mathbf{L}P$ and $\mathbf{L}T$ are parallel to each other and perpendicular to the surface normal which leads to H_{rel} being

independent of the choice of ψ. This is peculiar only to certain geometries like spherical and planar. Also see Low (2006) where an absolute helicity is derived independent of the potential field in the special geometries which employs Euler potentials. In the case of linear models used here (C modes; §6.4) the energy and helicity are finite and in the case of the non-linear model used here (LL modes; §6.5), $\mathbf{B} \propto r^{-n-2}$ $(n > 1)$ and energy and helicity show singular behavior at the origin.

6.3 Axisymmetric linear & non-linear force-free fields

The force-free magnetic field $\mathbf{B}$ is described by the equation

$$\nabla \times \mathbf{B} = \alpha \mathbf{B} \tag{6.7}$$

from which it follows that $\mathbf{B} \cdot \nabla \alpha = 0$. This requires α to be a constant along the magnetic field lines. Following the treatment in Low and Lou (1990), we assume an axisymmetric magnetic field configuration and express it in terms of two scalar functions ψ and $Q(\psi)$ in spherical polar coordinates

$$\mathbf{B} = \frac{1}{r \sin\theta} \left(\frac{1}{r} \frac{\partial \psi}{\partial \theta} \hat{\mathbf{r}} - \frac{\partial \psi}{\partial r} \hat{\boldsymbol{\theta}} + Q \hat{\boldsymbol{\phi}} \right), \tag{6.8}$$

which is divergence free by construction. For an orthonormal coordinate system with a metric defined as $\mathrm{d}s^2 = g_{ii} \mathrm{d}x^i \mathrm{d}x^i$, the line element along the magnetic field line $\mathrm{d}l$ is given by $\hat{\mathbf{l}} = \sqrt{g_{ii}} \frac{\mathrm{d}x^i}{\mathrm{d}s} \hat{i} = \frac{B_i}{|\mathbf{B}|} \hat{i}$; hence $\frac{\sqrt{g_{ii}} \mathrm{d}x^i}{B_i}$ represents the equation for lines of force and applying this in axisymmetry gives $\psi = \text{const.}$ whose contours represent the poloidal field lines. Combining the equations (6.7, 6.8), we obtain

$$\alpha = \frac{\mathrm{d}Q}{\mathrm{d}\psi} \tag{6.9}$$

and

$$\frac{\partial^2\psi}{\partial r^2} + \frac{(1-\mu^2)}{r^2}\frac{\partial^2\psi}{\partial\mu^2} + Q\frac{\mathrm{d}Q}{\mathrm{d}\psi} = 0, \tag{6.10}$$

where $\mu = \cos\theta$. To solve the above equation we choose a separable form of the type

$$\psi = f(r)P(\mu), \quad Q = a\psi^{\beta}, \tag{6.11}$$

where f and P are scalar functions of r and μ respectively; a and β are constants. Combining equations (6.10) and (6.11), it follows that

$$r^2\frac{f''}{f} + (1-\mu^2)\frac{P''}{P} + a^2\beta r^2 f^{2\beta-2}P^{2\beta-2} = 0. \tag{6.12}$$

The first term in the LHS of the above equation is a function of r alone and the second term is that of μ alone. The resulting two possibilities for obtaining separable solutions are that the third term be a function of either,

(a) r alone, which is satisfied if $\beta = 1$; these solutions were presented in Chandrasekhar (1956) and which we refer to as C modes or

(b) μ alone, which is satisfied if $r^2 f^{2\beta-2} = 1$; these solutions were partially explored by Low & Lou (1990) and are termed here as LL modes.

6.4 The $\beta = 1$ case: C modes

The C modes pertain to the linear force-free fields since the condition $\beta = 1$ along with equation (8.70) implies $\alpha = a$ and it follows from equation (6.12) that

$$r^2\frac{f''}{f} + a^2r^2 + (1-\mu^2)\frac{P''}{P} = 0. \tag{6.13}$$

The radial part of the above equation is given by

$$r^2\frac{f''}{f} + a^2r^2 = n'(n'+1) \tag{6.14}$$

where n' is a constant whose solutions are

$$f_{n'}(r) = c_1\sqrt{r}J_{(1+2n')/2,}(ar) + c_2\sqrt{r}Y_{(1+2n')/2}(ar) \tag{6.15}$$

where J and Y are cylindrical Bessel functions; c_1 and c_2 are constants to be determined from the boundary conditions. The angular part of equation (6.13) is given by

$$(1-\mu^2)\frac{P''}{P} = -n'(n'+1), \tag{6.16}$$

whose solution is given by

$$P(\mu) = (1-\mu^2)^{1/2}P^1_{n'}(\mu), \tag{6.17}$$

where $P^1_{n'}$ is the associated Legendre function of the first kind for integer n'. This solution is equivalent to that obtained in Chandrasekhar (1956) and the following equations give the correspondence between the solutions

$$\begin{aligned} a &\leftrightarrow \alpha \\ f_{n'}(r) &\leftrightarrow \sqrt{r}g_{m+3/2}(\alpha r) \\ P^1_{n'}(\mu) &\leftrightarrow -(1-\mu^2)^{1/2}C^{3/2}_m(\mu) \\ n' &\leftrightarrow m+1 \end{aligned} \tag{6.18}$$

where $C^{3/2}_m(\mu)$ denotes the Gegenbauer polynomial and $g_{m+3/2}(\alpha r)$ represents any arbitrary linear combination of the cylindrical Bessel functions $J_{m+3/2}(\alpha r)$ and $Y_{m+3/2}(\alpha r)$. Henceforth for the calculations of C modes we will be using the expressions from Chandrasekhar (1956). ψ can now be rewritten as

$$\psi = f(r)P(\mu) = f_{n'}(r)(1-\mu^2)^{1/2}P^1_{n'}(\mu) = r^2S_m(r)(1-\mu^2), \tag{6.19}$$

where

$$S_m = \frac{g_{m+3/2}(\alpha r)}{r^{3/2}}C^{3/2}_m(\mu). \tag{6.20}$$

The application of these solutions to the case of finite spheres, under suitable boundary conditions are discussed in §6.A.

The above expression can be further simplified by substituting for S_m using equations (6.20) and (6.64) to

$$\begin{aligned}\mathbf{B} &= \left(\frac{-J_{m+3/2}(\alpha r)}{r^{3/2}}\frac{\mathrm{d}}{\mathrm{d}\mu}[(1-\mu^2)C_m^{3/2}(\mu)], \frac{-1}{r}\frac{\mathrm{d}}{\mathrm{d}r}[r^{1/2}J_{m+3/2}(\alpha r)]\right. \\ &\quad \left.(1-\mu^2)^{1/2}C_m^{3/2}(\mu), \frac{\alpha J_{m+3/2}(\alpha r)}{r^{1/2}}(1-\mu^2)^{1/2}C_m^{3/2}(\mu)\right). \qquad (6.21)\end{aligned}$$

The derivation for the potential field corresponding to equation (6.66) is given in §6.C. The final expressions for the potential field is found to be

$$\begin{aligned}\mathbf{B}_P &= \left(\left[(m+1)a_{m+1}r^m - \frac{(m+2)b_{m+1}}{r^{m+3}}\right]P_{m+1}(\mu),\right. \\ &- \left.(1-\mu^2)^{1/2}\left[a_{m+1}r^m + \frac{b_{m+1}}{r^{m+3}}\right]\frac{\mathrm{d}P_{m+1}}{\mathrm{d}\mu}, 0\right). \qquad (6.22)\end{aligned}$$

$P_{(m+1)}(\mu)$ are the Legendre polynomials, where the coefficients are calculated to be

$$\chi_l = \chi_{m+1}(r_1) = \frac{(m+1)(m+2)}{r_1^{3/2}}J(m+3/2, \alpha r_1) \qquad (6.23)$$

$$\begin{aligned}a_l = a_{m+1} &= \frac{\chi_{m+1}(r_1)}{(m+1)}\frac{r_1^{m+3}}{r_1^{2m+3}-r_2^{2m+3}} \\ b_l = b_{m+1} &= \frac{(m+1)}{(m+2)}a_{m+1}r_2^{(2m+3)} \qquad (6.24)\end{aligned}$$

For the general case of open field lines, where the field has a non-zero normal component at the boundaries, the energy of the force-free field is given by

$$E_{ff}(\alpha, n, m, r_1, r_2) = \frac{1}{4}\int_{r_1}^{r_2}\int_{-1}^{1}(B_r^2 + B_\theta^2 + B_\phi^2)r^2\mathrm{d}r\mathrm{d}\mu. \qquad (6.25)$$

Upon evaluation, the above equation takes the following form

$$E_{ff}(\alpha,n,m,r_1,r_2) = \frac{(m+1)(m+2)}{2(2m+3)}\Bigg[2\int_{r_1}^{r_2}\alpha^2 r J^2_{m+3/2}(\alpha r)\mathrm{d}r - r_1^{1/2}J_{m+3/2}(\alpha r_1)\frac{\mathrm{d}}{\mathrm{d}r}\{r^{1/2}J_{m+3/2}(\alpha r)\}|_{r=r_1}\Bigg] \quad (6.26)$$

An alternative and equivalent expression for the energy can also be obtained from equation (6.72), from which $E_{ff} = E_v(r_2) - E_v(r_1)$, where

$$E_v(r) = \frac{(m+1)(m+2)}{2(2m+3)}\Bigg[r\left[\frac{\mathrm{d}}{\mathrm{d}r}\left\{r^{1/2}J_{m+3/2}(\alpha r)\right\}\right]^2 + \left\{\alpha^2r^2-(m+1)(m+2)\right\}J^2_{m+3/2}(\alpha r)\Bigg]. \quad (6.27)$$

We have verified that equations (6.27 & 6.26) are analytically equivalent through the use of equation (6.14) and algebraic manipulation of Bessel identities. In order to calculate the free-energy of the configuration using equation (6.1), we compute the energy of the potential field constructed from this force-free field (see §6.C.1) which is given by

$$E_{pot}(m,r_1,r_2) = \frac{1}{2(2m+3)}\int_{r_1}^{r_2}\Bigg[\left((m+1)a_{m+1}r^{m+1}-\frac{(m+2)b_{m+1}}{r^{m+2}}\right)^2 + (m+1)(m+2)\left(a_{m+1}r^{m+1}+\frac{b_{m+1}}{r^{m+2}}\right)^2\Bigg]\mathrm{d}r. \quad (6.28)$$

We now calculate the relative helicity of the configuration using equation (6.2). The relevant quantities to be calculated for this purpose are the vector potentials for the force-free field $\mathbf{A}$ and that of the potential field $\mathbf{A_P}$. We use gauge freedom for the vector potential to write $\mathbf{A} = \mathbf{B}/\alpha$. The vector potential for the potential field is calculated in §6.D, and is given by

$$\mathbf{A}_P = \left(0, 0, (1-\mu^2)^{1/2}P'_{m+1}(\mu)\left[\frac{a_{m+1}r^{m+1}}{m+2}-\frac{b_{m+1}}{(m+1)r^{m+2}}\right]\right). \quad (6.29)$$

The relative helicity for region II can be written as

$$H_{rel}(\alpha, n, m, r_1, r_2) = \int \left(\frac{B^2}{\alpha} + \mathbf{A}_P \cdot \mathbf{B} - \frac{\mathbf{B}}{\alpha} \cdot \mathbf{B}_P \right) \mathrm{d}V$$
$$= \frac{8\pi E_{ff}}{\alpha} + \frac{4\pi(m+1)(m+2)}{\alpha(2m+3)} \Big[\alpha^2 \int_{r_1}^{r_2} \Big(\frac{a_{m+1} r^{m+1}}{m+2} - \frac{b_{m+1}}{(m+1) r^{m+2}} \Big)$$
$$r^{3/2} J_{m+3/2}(\alpha r) \mathrm{d}r + r_1^{1/2} \left(a_{m+1} r_1^{m+1} + \frac{b_{m+1}}{r_1^{m+2}} \right) J_{m+3/2}(\alpha r_1) \Big]. \qquad (6.30)$$

An equivalent formula for the relative helicity obtained using equation (6.6) works out to be

$$H_{rel}(\alpha, n, m, r_1, r_2) = \frac{2}{\alpha} \int_V B_\phi^2 \mathrm{d}V = \frac{8\pi\alpha(m+1)(m+2)}{2m+3} \int_{r_1}^{r_2} r J_{m+3/2}^2(\alpha r) \mathrm{d}r. \qquad (6.31)$$

The analytical equivalence of equations (6.30 & 6.31) is presented in §6.F.1.

6.5 The $r^2 f^{2\beta-2} = 1$ case: LL modes

We now study the second set of solutions obtained in §6.3 namely the LL modes. The condition $r^2 f^{2\beta-2} = 1$ along with equation (6.12) implies

$$f^{\beta-1} = r^{-1}. \qquad (6.32)$$

Assuming the functional form

$$f(r) = r^{-n}, \qquad (6.33)$$

where n is a constant, gives the condition $\beta = (n+1)/n$ and equation (6.12) then yields the following equation as obtained by Low and Lou (1990)

$$r^2 \frac{f''}{f} = n(n+1) \qquad (6.34)$$

$$(1-\mu^2) P'' + a^2 \frac{n+1}{n} P^{1+2/n} + n(n+1) P = 0. \qquad (6.35)$$

There is an arbitrary amplitude of P in equation (6.35) which can be scaled away. Then this ODE together with the homogeneous boundary conditions pose an eigenvalue problem to determine the scaled parameter a as an eigenvalue. Recalling equation (6.8), we have the following expression for the non-linear force-free modes

$$\mathbf{B} = \frac{-1}{r\sqrt{1-\mu^2}}\left(\frac{\sqrt{1-\mu^2}}{r}\frac{\partial\psi}{\partial\mu}\hat{r} + \frac{\partial\psi}{\partial r}\hat{\theta} - Q\hat{\phi}\right) \tag{6.36}$$

where $\psi = P(\mu)/r^n$ and $Q = a\psi^{(n+1)/n}$. Now P is the solution of equation (6.35) and equation (6.36) which takes the form

$$\mathbf{B} = \left(\frac{-1}{r^{n+2}}\frac{\mathrm{d}P}{\partial\mu}, \frac{n}{r^{n+2}}\frac{P}{(1-\mu^2)^{1/2}}, \frac{a}{r^{n+2}}\frac{P^{(n+1)/n}}{(1-\mu^2)^{1/2}}\right). \tag{6.37}$$

Eqn (6.35) is not straightforward to integrate numerically except for the case $n = 1$, which was presented in Low and Lou (1990), as there is an inherent singularity at $\mu = 0$. We extend these solutions to higher values of odd n, by using the following transformation

$$P(\mu) = (1-\mu^2)^{1/2}F(\mu), \tag{6.38}$$

through which equation (6.37) stands as

$$\mathbf{B} = \left(\frac{-1}{r^{n+2}}\left[(1-\mu^2)^{1/2}F'(\mu) - \frac{\mu F(\mu)}{(1-\mu^2)^{1/2}}\right], \frac{n}{r^{n+2}}F, \frac{a}{r^{n+2}}(1-\mu^2)^{\frac{1}{2n}}F^{\frac{n+1}{n}}\right) \tag{6.39}$$

and equation (6.35) becomes

$$(1-\mu^2)F'' - 2\mu F' + \left[n(n+1) - \frac{1}{(1-\mu^2)}\right]F + \frac{a^2(n+1)}{n}F^{\frac{(n+2)}{n}}(1-\mu^2)^{\frac{1}{n}} = 0. \tag{6.40}$$

Eqn (6.40) can be solved for all values of positive n, which represent the physically interesting cases. The initial requirement of $\psi = P/r^n$ requires only $n > 0$ where n can take any positive rational or integral value. A

stringent condition on n is enforced if we demand $Q = a\psi^{1+1/n}$ is real which is required for physically acceptable solutions. This means that for rational values of $n = p/q$, $Q = a\psi\psi^{q/p}$ and ψ^q should be positive for all even values of p. Also this implies possibilities like (odd p, odd q) and (even q, odd p) are permissible. In summary, solutions exist for all odd values of p while for even p, it exists only if $F(\mu) > 0$ in the domain $-1 \leq \mu \leq 1$. As examples, the solutions for $n = 2/3, 2/5, 4/7$ etc are allowed. Therefore the acceptable values of n form a sufficiently dense set in the range $0 < n < \infty$, so that one can find instances of p/q arbitrarily close to a given n. Recently, semi-analytic solutions to equation (6.35) for $n = 5, 7...$ 201 under the assumption of self-similarity were presented in Zhang, Flyer, and Chye Low (2012).

6.5.1 Conditions for physically acceptable solutions

The following conditions are required to be satisfied for obtaining physically acceptable solutions:

1. The field should be finite as $r \to \infty$. This is ensured if n is positive.

2. The field should be well behaved and finite along the axis of symmetry. Since we have
$$B_\theta, B_\phi \propto \frac{1}{(1-\mu^2)^{1/2}} P(\mu);$$
this requires that $P(\mu)$ should vanish at $\mu = 1, -1$. This gives the condition
$$P(\mu) \to (1-\mu^2)^s \quad \text{at} \quad \mu = \pm 1$$
where $s \geq 1/2$.

The function $F(\mu)$ satisfies the boundary condition (see §6.H)

$$F(\mu) = 0 \quad \text{at} \quad \mu = \pm 1. \tag{6.41}$$

Further, it follows that equation (6.40) reduces to the equation for the associated Legendre polynomials (where the last term is ignorable compared to the third term) in the limit $\mu^2 \to 1$. So we can construct LL solutions by direct integration of equation (6.40) subject to equation (6.41) for any positive n. We have cross-verified with the only case, $n = 1$, that was given in Low and Lou (1990) and calculated other allowed values of n as well. The cases for the modes $n = 1$ to $n = 3$ are shown in Fig. 6.1 for the first three eigenvalues m of the variable a. These solutions are singular at the origin, so the energy and helicity calculation are done excluding a spherical region around the origin. As specific examples of the non-integer type, we depict realizations of radial modes $n = 7/5, 3/2, 9/5$, in the left column of Fig. 6.5.

6.5.2 Energy and relative helicity for the LL modes

The energy in the magnetic field is given by equation (6.71)

$$E_{ff}(n, m, r_1) = \frac{1}{4(2n+1)r_1^{2n+1}} \int_{-1}^{1} \mathrm{d}\mu \left[P'(\mu)^2 + \frac{n^2 P(\mu)^2}{1-\mu^2} + \frac{a^2 P(\mu)^{(2n+2)/n}}{1-\mu^2} \right] \tag{6.42}$$

where the expression for the field from equation (6.37) is used. The energy of the force-free field calculated using the virial theorem of equation (6.72) gives the equivalent expression,

$$E_{ff} = \frac{1}{4r_1^{2n+1}} \int_{-1}^{1} \left\{ \left(\frac{\mathrm{d}P}{\mathrm{d}\mu} \right)^2 - \frac{(n^2 + a^2 P^{2/n}) P^2}{(1-\mu^2)} \right\} \mathrm{d}\mu. \tag{6.43}$$

The equation (6.42) reduces to equation (6.43) by the use of equation (6.35). It may noted the function $P(\mu)$ is implicitly dependent on the parameters n and m. The contour plot in Fig. 6.2 shows the dependence of energy on the variables n and m and we find that the magnetic energy of the field

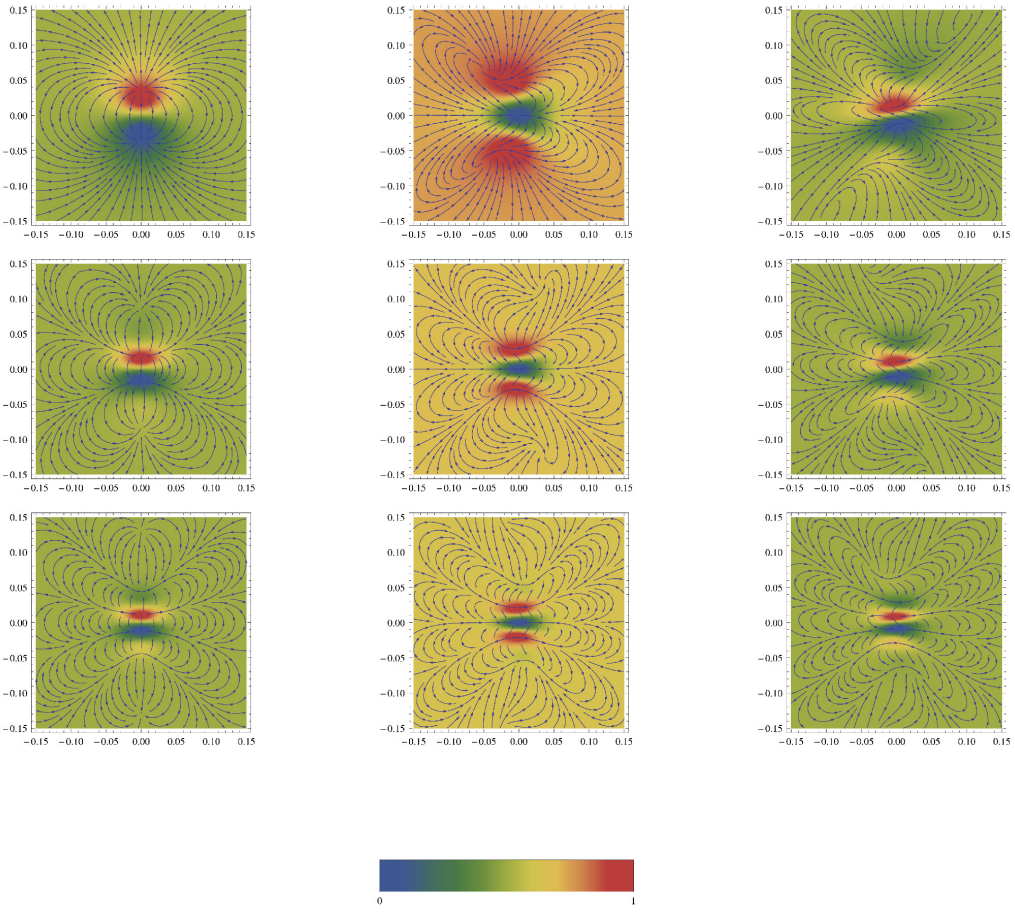

Figure 6.1: The sections (avoiding the origin where the fields are singular) shown above are taken perpendicular to the radius at $r = 0.05$ for different solutions of LL, with angular modes m $= 1$ to $m = 3$ (columns) and radial modes $n = 1$ to $n = 3$ (rows). The contours represent the magnetic field lines projected on the plane and the density plot represents the strength of the field perpendicular to the plane of the figure. The values 0 and 1 in the color bar correspond to the minimum and maximum values of the perpendicular magnetic field respectively.

increases with both the variables. The change in energy is very sharp with n as compared to m, so the value of contours are given in logarithmic scale. The potential field corresponding to the LL mode is calculated in §6.C.2 and its final expression is given by

$$\mathbf{B}_P = \left(\sum_{l=0}^{\infty} -(l+1)\frac{b_l}{r^{l+2}} P_l(\mu), \sum_{l=0}^{\infty} \frac{-b_l}{r^{l+2}} (1-\mu^2)^{1/2} \frac{\mathrm{d}P_l}{\mathrm{d}\mu}, 0 \right). \tag{6.44}$$

where

$$a_l = 0, \quad b_l = \frac{2l+1}{2(l+1)} r_1^{l-n} \int_{-1}^{1} \frac{\mathrm{d}P}{\mathrm{d}\mu} P_l(\mu) \mathrm{d}\mu. \tag{6.45}$$

The energy for the potential field constructed from the LL modes (see §6.C.2) is given by

$$E_{pot}(l, r_1) = \sum_{l=0}^{\infty} \frac{b_l^2 (l+1)}{2(2l+1) r_1^{2l+1}}. \tag{6.46}$$

In order to calculate the relative helicity, we find the vector potential for the LL modes in §6.E, given by

$$\mathbf{A} = \left(0, \frac{-a}{n r^{n+1}} \frac{P(\mu)^{(n+1)/n}}{(1-\mu^2)^{1/2}}, \frac{1}{r^{n+1}} \frac{P(\mu)}{(1-\mu^2)^{1/2}} \right). \tag{6.47}$$

The vector potential for the potential field is given by equation (6.107) with a_l and b_l as defined in equation (6.45). Then the relative helicity is calculated from equation (6.2) to be

$$H_{rel}(n, m, r_1) = \int_V (\mathbf{A}_P \cdot \mathbf{B} - \mathbf{A} \cdot \mathbf{B}_P) \mathrm{d}V \tag{6.48}$$

since $\mathbf{A} \cdot \mathbf{B} = \mathbf{A}_P \cdot \mathbf{B}_P = 0$. Thus, even if the absolute helicity $\mathbf{A} \cdot \mathbf{B}$ is zero in our chosen gauge, the cross terms in the Finn Antonesen formula give rise to the non-zero values of the relative helicity. The expression in equation (6.48) can be further simplified to

$$H_{rel}(n, m, r_1) = -2\pi a \sum_{l=0}^{\infty} \int_{-1}^{1} \frac{b_l}{n l r_1^{n+l}} P^{1+1/n} \frac{\mathrm{d}P_l}{\mathrm{d}\mu} \mathrm{d}\mu. \tag{6.49}$$

Using equation (6.6), we get an equivalent form for the relative helicity which works out to be

$$H_{rel}(n,m,r_1) = \frac{2\pi a}{n r_1^{2n}} \int_{-1}^{1} \frac{P^{2+1/n}}{(1-\mu^2)} \mathrm{d}\mu. \tag{6.50}$$

The two formulae in equations (6.49 & 6.50) are equivalent as shown in §6.F.2.

6.6 Simulation of magnetograms

In this chapter, our aim is to get reasonably good and quick estimates of free energy and relative helicity for the active region observed in the magnetograms. It is well known that NLFF fields best represent the solar active regions and the most useful and widely used analytic solution is the Low-Lou solution in the spherical geometry. Hence this geometry was naturally chosen. In our scheme, we first compute a large set of linear and non-linear three dimensional force-free modes in a spherical shell volume where the magnetogram is a tangent plane to the lower boundary, see Fig. 6.3.

For the linear case, the field is defined between radii r_0 and r_2. A plane representing the magnetogram is placed tangential to a shell of radius r_1. A potential field is constructed in the spherical shell between radii r_1 and r_2 (region II) using the normal components of the force-free field at the lower boundary, r_1. For the non-linear case, the field is defined outside a shell of radius r_1 (region II) where the plane representing the magnetogram is placed tangentially. Again the potential field is constructed using the normal components of the force-free field at r_1. The fit to the magnetogram data selects a particular mode of force-free field in spherical geometry (details given below). Apart from this, the magnetogram also sets a length-scale for the problem and fixes an amplitude of the magnetic field. Both the force-free field and

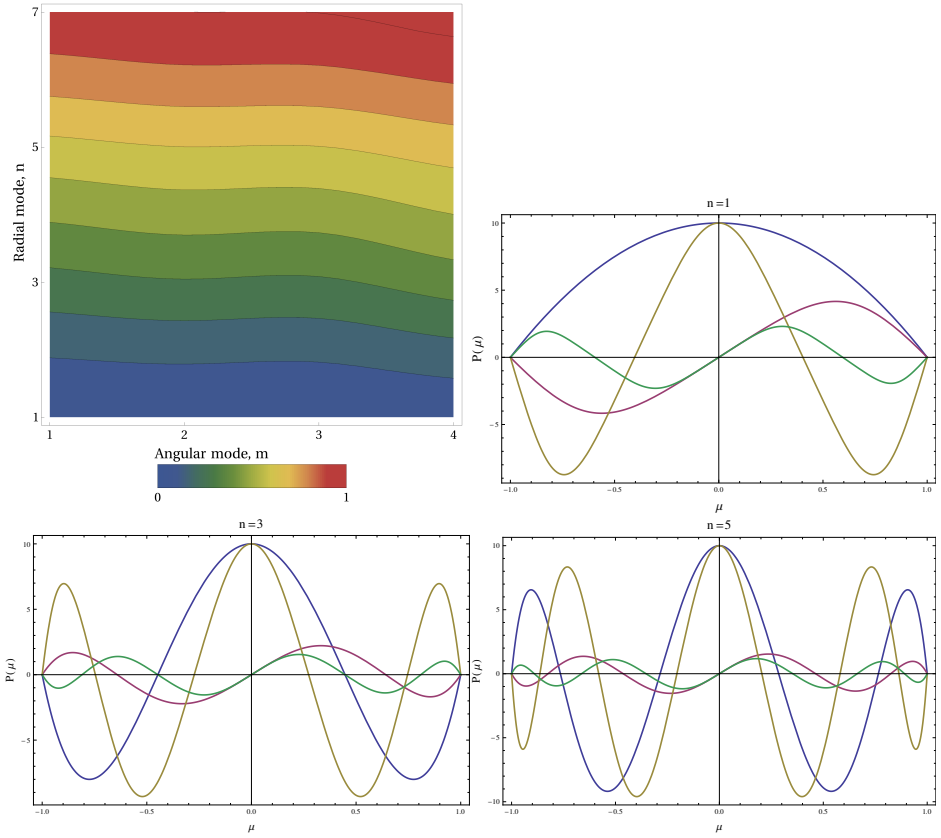

Figure 6.2: The top left panel shows contours of energy for different angular and radial modes for the LL modes. The energies (normalized with respect to the maximum) are shown for different modes at the same lower boundary $r_1 = 0.5$. The value of contours are given in logarithmic scale as the parametric dependence is very sharp. The values 0 and 1 in the color bar correspond to the minimum and maximum values of energy respectively. The next three panels show the realizations of $P(\mu)$ for the cases of $m = 1$ to 4 for $n = 1, 3$ and 5. Note that the number of polarities for a given (n, m) set is given by $n + m - 1$.

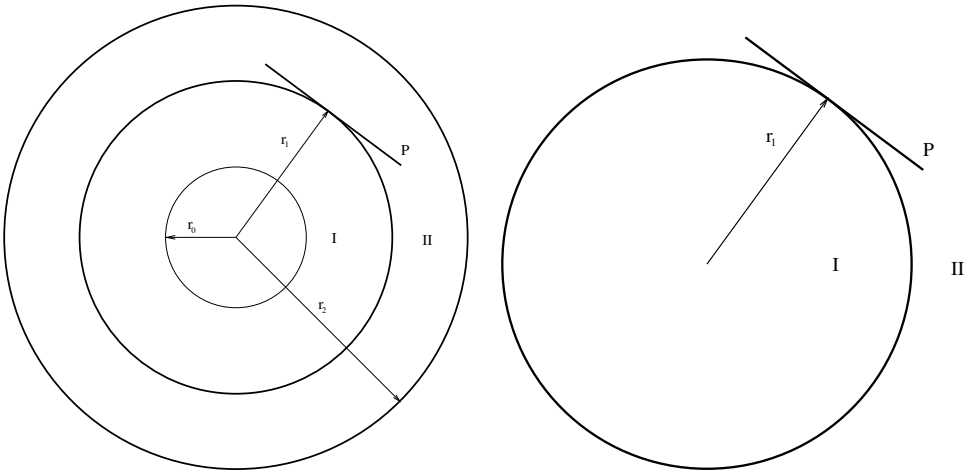

Figure 6.3: This figure shows the geometry used in the problem for the linear (left panel) and non-linear (right panel) fields. For the linear case, the field is first computed between radii r_0 and r_2. A plane representing the magnetogram is placed tangential to a shell of radius r_1. A potential field is constructed in the spherical shell between radii r_1 and r_2 (region II) using the normal components of the force-free field at the lower boundary, r_1. For the non-linear case, the field is computed outside a shell of radius r_1 where the plane representing the magnetogram is placed tangentially. Again the potential field is constructed using the normal components of the force-free field at r_1.

potential field are known completely in region II, so we calculate the free energy and relative helicity (using Finn-Antonesen and Berger formula) in region II. In order to compare with the other estimates available in literature, where the potential fields are usually extended from the planar surface of the magnetogram to a cuboidal volume over the magnetogram, we rescale our physical quantities obtained for a hemisphere by the factor of the solid angle subtended by the magnetogram at the center. We would like to emphasize that our problem is to reconstruct the entire field from the knowledge of the field in a two dimensional plane which does not a priori force any choice of

geometry. So calculation of free energy and relative helicity in the shell geometry does not compromise our original goal, which is to get quick reasonable estimates of these quantities over the solid angle subtended by the magnetogram. The validity of this approximation can be seen from the general agreement with other estimates (including observations, presented later in Table 6.5). An advantage in this method is its ease and utility to calculate these physical quantities, in particular the relative helicity is thus far not calculated by other approaches. Further, we don't have to assume any other boundary condition for the side walls, as required in the other extrapolation techniques using the cuboidal volume.

We now use the library of LL and C modes by taking two dimensional sections of the force-free spheres appropriately and compare these sections with the observed magnetograms. We describe the best fit mode and figure of merit of fit in §6.6.2. The following steps are taken in simulating the sections:

1. We compute the 3D force-free magnetic field in spherical geometry corresponding to a given C and LL mode from equation (6.66) and equation (6.37) respectively.

2. The coordinates on the magnetogram are labeled as the x and y axes, where the $x, y \in [-0.5, 0.5]$, so that the magnetogram is of unit length.

3. A cross-section of the sphere is taken at a radius r_1 and all three components of magnetic field are computed over this two dimensional surface, see Fig. 6.4. The orientation of the magnetogram is given by the three Euler angles (ϕ', θ', ψ') of which the angle ϕ' is redundant as the fields are axisymmetric. The transformation matrix for the Euler rotation is

given by

$$\Lambda(\theta', \psi') = \begin{bmatrix} \cos\psi' & \cos\theta' \sin\psi' & \sin\psi' \sin\theta' \\ -\sin\psi' & \cos\theta' \cos\psi' & \cos\psi' \sin\theta' \\ 0 & -\sin\theta' & \cos\theta' \end{bmatrix}. \tag{6.51}$$

In effect the position and orientation of the section is fixed by three parameters (r_1, θ', ψ'). We then transform a point on the magnetogram with coordinates (x, y, z) by the inverse of Λ.

4. The coordinates in spherical $\mathbf{x}_S \equiv (r, \theta, \phi)$ are obtained from Cartesian coordinates $\mathbf{x}_C \equiv (x, y, z)$ through the operator S given by

$$\begin{aligned} \mathbf{x}_S &= S(\mathbf{x}_C) \\ r &= (x^2 + y^2 + z^2)^{1/2} \\ \phi &= \begin{cases} \arctan(y/x) & x > 0 \\ \arctan(y/x) + \pi & x \leq 0 \end{cases} \\ \theta &= \arccos\left(z/(x^2 + y^2 + z^2)^{1/2}\right) \end{aligned}$$

to get $\mathbf{x}_S$ as a function of (x, y, z), so that we have the coordinates of all the points on the magnetogram in spherical coordinates

$$\mathbf{x}_S = S\left(\Lambda^{-1}(\theta', \psi')\mathbf{x}_C\right). \tag{6.52}$$

5. We now evaluate the magnetic field in spherical coordinates $\mathbf{B}_S(\mathbf{x}_S)$ and then convert the components of magnetic field from spherical polar to Cartesian coordinate system so that

$$\mathbf{B}_C[\mathbf{x}_C, \theta', \psi', x, y] = \Lambda(\theta', \psi') T\left(\mathbf{B}_S\left[S(\Lambda^{-1}(\theta', \psi')\mathbf{x}_C)\right]\right). \tag{6.53}$$

where

$$T = \begin{bmatrix} \sin\theta\cos\phi & \cos\theta\cos\phi & -\sin\phi \\ \sin\theta\sin\phi & \cos\theta\sin\phi & \cos\phi \\ \cos\theta & -\sin\theta & 0 \end{bmatrix}, \tag{6.54}$$

is the transformation from spherical to Cartesian. Here the coordinate θ and ϕ are locations on the magnetogram computed from equation (6.52). Since Λ and T are orthogonal, their inverses are the corresponding transposes.

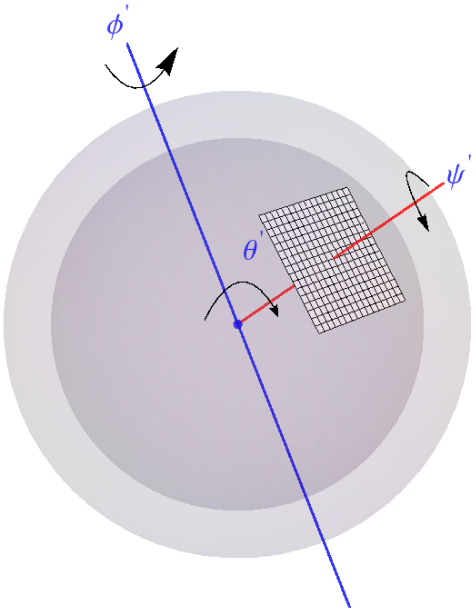

Figure 6.4: A magnetogram is simulated by taking a cross-section of the axisymmetric 3D force-free field at a radius r_1.The magnetogram is then rotated through the Euler angles θ' and ψ' to match the components of the observed magnetogram. The rotation ϕ' is redundant as the field is axisymmetric.

We illustrate simulated sections thus generated for the LL modes $(n, m) = \{(7/5, 2),\ (3/2, 3),\ (9/5, 1)\}$ in Fig. 6.5. The parameter values (r_1, θ, ϕ)

chosen are indicated in the caption and the resulting sections are typical of the single and double polarity active regions seen in observations.

6.6.1 Search strategy

We have the following free parameters in the problem:

1. The radial and angular mode numbers, n and m: the values for n and m fix the force-free modes (for both C and LL solutions). While n takes only integral values for C modes, LL modes can take integral as well as fractional values (with the exceptions mentioned in §6.5). The value of m takes only integers for both C and LL modes.

2. The first derivative $d = F'(\mu = -1)$: the value of the derivative of $F(\mu)$ at the boundary which is used as a boundary condition for solving equation (6.40) is a free parameter; this only scales the solution by an arbitrary constant. In this chapter we have used $d = 10$ as a constant input for all calculations.

3. Euler angles, θ' and ψ': The C modes repeat in θ' at an interval of $\pi/(m+1)$ for a given m and θ' was taken to be the larger of this value and the angle subtended by the magnetogram at the center to avoid redundancy; $\theta' = \max\{\pi/(m+1), \arctan(L/r_1)\}$. For LL modes we search in the domain $\theta' \in [0, \pi]$. For both cases, we search for ψ in the range, $\psi' \in [0, 2\pi]$. If the magnetogram has n_p polarities in a range $\Delta\mu = 1 - \cos\gamma$ for a mode which has m_p total polarities over the domain $[-1, 1]$, then we estimate

$$\frac{n_p}{m_p} \simeq \frac{\Delta\mu}{2} = \frac{1-\cos\gamma}{2} = 1/(1+(r_1/L)^2 4) \tag{6.55}$$

where γ is the angle subtended by the magnetogram at the center.

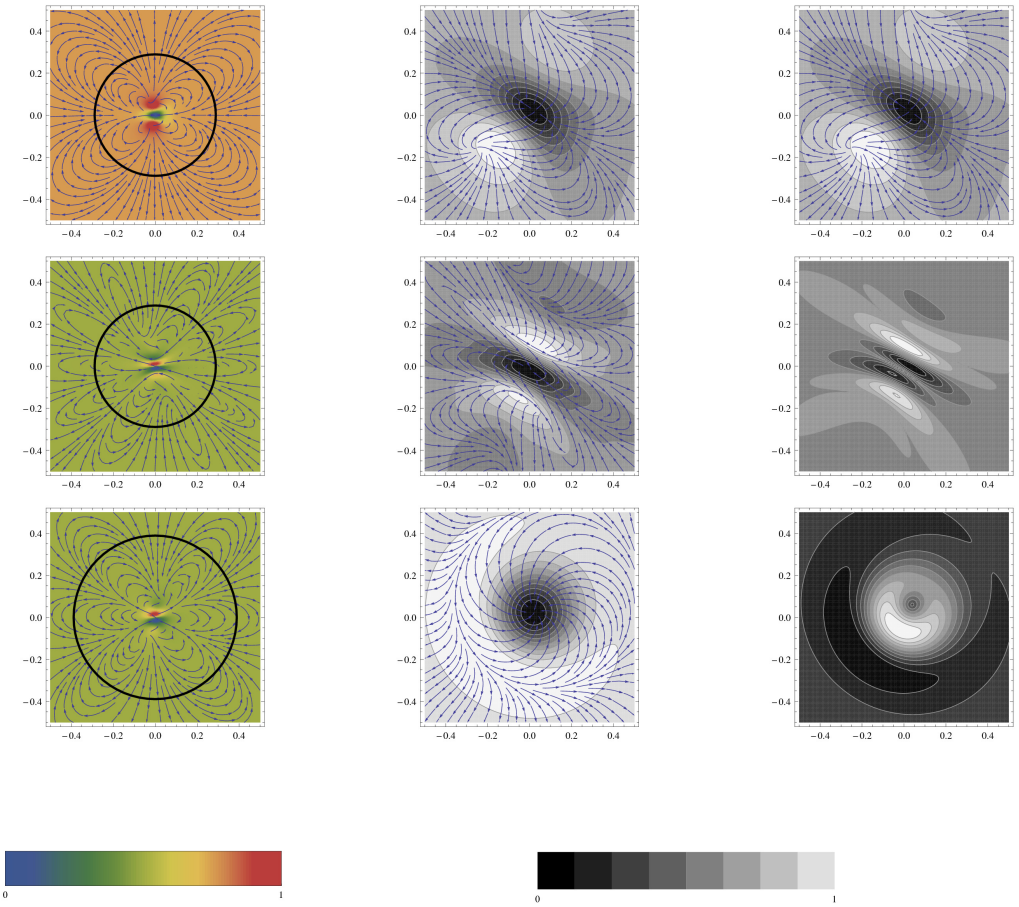

Figure 6.5: The sections for different LL solutions, taken perpendicular to the radius at $r = 0.05$ with parameters $(n, m, r_1, \theta, \phi)$={(7/5, 2, 0.29,1.75,4.14), (3/2, 3, 0.29,1.75,4.14), (9/5, 1, 0.39, 0.18, 4.14)} are shown in the top, middle and bottom rows respectively. In the left column, the contours represent the magnetic field projected on to the plane of the figure and the density plot represents the strength of the field perpendicular to it. The circles are drawn at radius r_1. The middle column is a section of the field and the right column is a section of the resulting current density; for an illustration of the section geometry and the parameters, see Fig. 6.4. The legends representing the strength of component normal to the page are shown below corresponding to the left and middle/right columns. The 0 and 1 in the legend scale correspond to the minimum and maximum values of the normal magnetic field respectively.

4. The radius r_1 at which the cross-section is to be taken is in the range 0 to r_2. Here r_2 is the outer radius up to which the energies and helicity are calculated. In case of C modes r_2 is finite and necessarily at the root of $J(m+3/2, \alpha r)$. We have restricted the calculations to only one radial oscillation (corresponding to only one visible closed loop along the line of sight), whereas for LL modes r_2 is infinite as the fields tend to zero only at infinity. The finite radial boundary r_2 is needed for the C modes and not the LL modes. For a linear force-free field in the Taylor theory of relaxation in the unbounded atmosphere, the minimum energy state is a C mode provided the domain is finite (Low, 1996). In case of C modes, the constraint that the magnetogram is contained within the sphere of radius r_2 leads to the condition

$$r_1 \leq \sqrt{r_2^2 - L^2/4}. \tag{6.56}$$

   In case of LL modes, there is no obvious constraint on r_1.

5. The force-free parameter α: for C modes, α is a constant and has to be given as an input. We restrict α^{-1} to be of order unity in line with typical observed magnetograms where the field reverses over this length.

To summarize, the parameter space to search for C modes is $(n, m, r_1, r_2, \alpha, \theta', \phi')$. We start sweeping from lowest combinations of (n, m), in increasing energy and searching for r_1 with the constraint on the range of θ' and r_1 given above and allowing only for one radial oscillation.

For LL modes, we have to search for the parameters $(n, m, r_1, \theta', \phi')$. Here, we start by sweeping from lowest combinations of (n, m) and looking for r_1 near unity to find the best fit lowest energy modes within the allowed range of θ' and ψ'. Due to computational constraints involved we were only able to

survey a subset of the parameter space. The run time for a combination of (n, m, α) for C modes and (n, m) for LL modes is about 8 hrs upon parallel computation on three computers with second generation Intel i7 processors. The search for the best fit parameter is done in the following manner. For a particular mode of the solution by (specified by the values of n, m and α, in case of C modes), we choose 6 equispaced grid points in the θ' and ψ' domain and 8 equispaced points for r. For the C modes the values for r are chosen between two Bessel zeros, whereas for the LL modes we start with an initial guess of $r = 1$. Then for each combination of (r, θ', ψ') the field is computed over a 380×380 grid (for a typical magnetogram). Thus, each mode of the solution involves evaluating the field for about 42 million combinations. All the template grids thus generated are compared with the observed data; following this initial search, the best fit set is selected and a finer grid of (r, θ', ψ') defined about this set with four grid points each is searched to obtain the final parameter set. We plan to expand upon the search in the future when we are able to make our code, which is already parallelized, to run on a faster cluster.

6.6.2 Fitting parameters

In the previous section we described how we explore the parameter space and generate a large ensemble of magnetograms. In order to select the best fit with the observations, we define a figure of merit, c for the magnetic field $\mathbf{B}$ as

$$c = \frac{\langle (\mathbf{B}_T \cdot \mathbf{B}_O)|\mathbf{B}_O| \rangle}{\langle |\mathbf{B}_T|^3 \rangle^{1/3} \langle |\mathbf{B}_O|^3 \rangle^{2/3}},$$

which is the normalized dot product between the observed, $\mathbf{B}_O$, and the theoretically simulated field, $\mathbf{B}_T$, weighted by the strength of the observed magnetic field so that $|c|$ would be unity for a perfect correlation. Here $\langle\rangle$

represents the mean computed over the entire grid. We also calculate the following correlation parameters to estimate the goodness of the fit for the selected configuration

$$d = \frac{\langle(\mathbf{B}_O \cdot \mathbf{B}_T/|\mathbf{B}_T|)\rangle}{\langle|\mathbf{B}_O|\rangle}, \qquad \text{and} \tag{6.57}$$

$$\epsilon = \frac{\langle|\mathbf{B}_T|^2\rangle}{\langle|\mathbf{B}_O|^2\rangle}, \tag{6.58}$$

where d is the average of the cosine of the angle between the two fields computed over the entire grid which is normalized by the strength of the observed field, while ϵ is the ratio of the magnetic energies of the theoretical and observed fields. The amplitude of the theoretical field is set by multiplying a scaling constant, g where

$$g^2 = \frac{\langle|\mathbf{B}_O|^3\rangle/\langle|\mathbf{B}_O|\rangle}{\langle|\mathbf{B}_T|^3\rangle/\langle|\mathbf{B}_T|\rangle}, \tag{6.59}$$

which is deduced from the weighted ratio of energies. Since the energy and helicity are computed for the entire sphere, we need to scale down these quantities by the fraction solid angle subtended by the magnetogram. The fraction of solid angle subtended by square loop of size L placed at a distance r_1 from the center is given by

$$\begin{aligned}
\Omega_f &= \frac{1}{\pi}\int_0^{L/2}\int_0^{L/2} \frac{r_1\,\mathrm{d}x\,\mathrm{d}y}{(r_1^2+x^2+y^2)^{3/2}} = \frac{1}{\pi}\int_0^{L/2} \frac{\mathrm{d}x}{r_1^2+x^2}\int_0^{\frac{L}{(2\sqrt{x^2+r_1^2})}} \frac{r_1\,\mathrm{d}z}{(1+z^2)^{3/2}} \\
&= \frac{Lr_1}{2\pi}\int_0^{L/2} \frac{\mathrm{d}x}{(r_1^2+x^2)\sqrt{L^2/4+r_1^2+x^2}} = \frac{1}{\pi}\int_0^{\arctan\left[\frac{L}{2r_1}\right]} \frac{\cos\theta \mathrm{d}\theta}{\sqrt{\cos\theta^2+4r_1^2/L^2}} \\
&= \frac{1}{\pi}\arcsin\left(\frac{L^2}{L^2+4r_1^2}\right).
\end{aligned} \tag{6.60}$$

The final expressions for energy and helicity as given by

$$\overline{E} = E\Omega_f g^2 L^3 \quad \text{and} \quad \overline{H}_{rel} = H_{rel}\Omega_f g^2 L^4, \tag{6.61}$$

where $\overline{E}$ and $\overline{H}_{rel}$ represent the energy and relative helicity respectively calculated over the volume containing the magnetogram.

6.6.3 Effectiveness of the search strategy

In order to estimate the effectiveness of our search strategy, we try to recover the field configurations and energies of known input fields. The input fields used as test cases are

(a) a pure dipole field

(b) an axisymmetric linear force-free field (C modes)

(c) a non-axisymmetric linear force-free field, Chandrasekhar and Kendall (1957) (CK modes).

In each of these case, we gave a two dimensional cross-section of the magnetic field as an input to our code and obtained a best fit with axisymmetric non-linear force-free fields (LL modes). The parameter search grid used for this analysis is the same as that used for the observed field. The details of the fit and the comparison of energy and helicity are presented in Table 6.1.

No.	Test Field	Mode n, m	Correlation, c	Energy (input field)	Energy (best fit field)	Relative Helicity (input field)	Relative Helicity (best fit field)
a.	Dipole field	1, 1	0.9925	7.77	6.76	0	0
b.	C mode	3, 1	0.662	1.24	1.34	-4.97	0
c.	CK mode	3, 1	0.636	0.237	0.134	-0.327	0

Table 6.1: The table presents the correlation parameter for fits of the input test field with the LL modes along with a comparison of energy and relative helicity. In all the cases above the length-scale of the two dimensional cross-section is taken to be unity.

The summary of our investigations can be presented as follows.

(a) Pure dipole field: We find that the dipolar field gives an almost exact fit to the LL mode. This is because it is an exact solution to the $n = 1$,

$m = 1$ LL mode. The accuracy of the fit can be improved by taking more grid points in our parameter space. In this case, axis of symmetry does not match exactly due to smaller grid resolution that is chosen because of numerical constraints. Of course when the exact values of the parameters are chosen, we recover perfect fits. We also see that the energy of the best fit field closely matches with that of the original field.

(b) C mode: We obtain a moderately good fit with 66% correlation with the original field. The $n = 3$, $m = 1$ mode is picked up which represents a potential field. This may be suggestive of the fact that the only constant α solution allowed within the LL modes is the potential $\alpha = 0$ mode. We find that the energies of the best fit field matches with that of the original field within a factor of 2.

(c) CK mode: We get a fit of 64% correlation with the original field. Again in this case the $n = 3$, $m = 1$ mode is picked up as in the previous case. The non-axisymmetry of this field makes it further difficult to fit with a axisymmetric non-linear force-free field which accounts for the low correlation.

Thus, we find that we are able to get the correct configuration for the input field (as in the dipole case). The accuracy of the fits can be improved by taking more grid points in our parameter search space. This is computationally extensive and will be taken up in near future. We do not get good matches to linear/non-axisymmetric linear force-free fields using non-linear axisymmetric fields where the relative helicity in these cases could not be obtained accurately, the energy however has been obtained in all cases within a factor of two. The morphological match in all the three cases are shown in

Fig. 6.6. We see that the overall features of fields are well captured in the fits. In this context, we remark that our fits for observed data are higher.

6.7 Preparation of observational data

In order to compare the analytic solutions computed in this chapter with the real magnetic field measurements and its associated quantities, we use the active region magnetic field data from spectro-polarimeter onboard Hinode. Spectro-polarimeter (SP) is one of the instrument of the solar optical telescope (SOT). The SOT/SP obtains Stokes profiles with a spatial resolution of $0.3''$ (Ichimoto *et al.*, 2008) in magnetically sensitive Fe I lines at 630.15 and 630.25 nm. The SOT/SP can make the map of an active regions in four modes, these are normal map, fast map, dynamics and deep magnetogram modes. In this study, we use the data from fast mode, spatial resolution along the slit direction is $0.295''$ and in the scanning direction it is $0.317''$/pixel. The obtained Stokes profiles were calibrated using the solar software suites for the SP. The Stokes vectors have been inverted using the Milne-Eddington inversion (Skumanich and Lites, 1987; Lites and Skumanich, 1990; Lites *et al.*, 1993) and the three components of magnetic field were obtained. The 180°ambiguity in the transverse field has been resolved using the minimum energy algorithm developed by Metcalf (1994) and implemented by Leka, Barnes, and Crouch (2009) in Fortran. This algorithm minimizes the electric current density and divergence simultaneously, selecting the field orientation with minimum free energy. The algorithm is best among the several codes for automatically resolving the 180°ambiguity (Metcalf *et al.*, 2006). The resulting vector components have been transformed to the disk center (Venkatakrishnan, Hagyard, and Hathaway, 1988). The

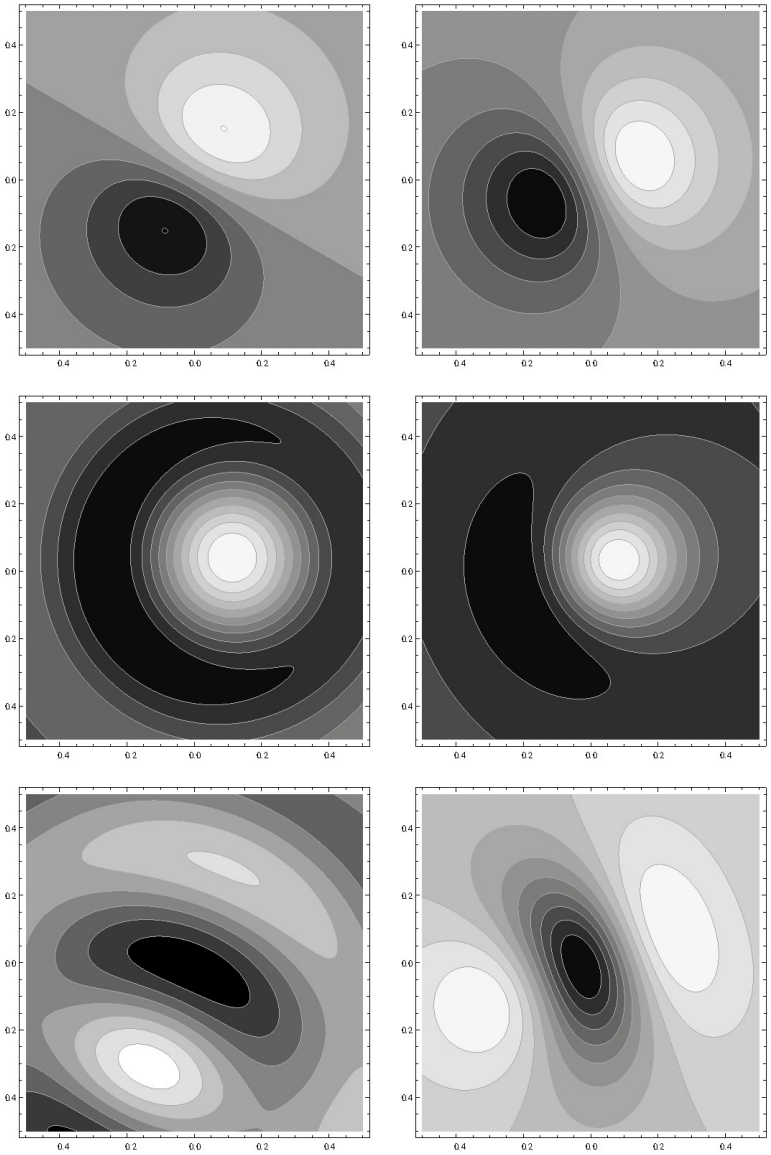

Figure 6.6: The left panels in the figure represent the input fields whereas the right panels represent the corresponding best fits by LL modes. The input in the top, middle and bottom rows are: dipole, C mode and CK mode respectively. More details are given in Table 6.1.

resulting vertical, B_z, and transverse, B_t, field strengths have 1-σ error bars of 8 and 30 G respectively.

We have chosen magnetograms of 3 active regions (Table 6.2) spanning the years 2006 to 2007 for our analysis. Most of the AR appeared in the southern hemisphere at a latitude close to the equator.

No.	Active Region	Date & Time of Obs.	Latitude	Pixel resolution	Length, L (10^9) cm
1.	NOAA 10930	2006-Dec-12, 2000 UT	S05	0.306″	8.0
2.		2006-Dec-13, 0400 UT		0.306″	8.0
3.		2006-Dec-14, 1700 UT		0.306″	8.44
4.		2006-Dec-14, 2200 UT		0.306″	8.44
5.		2006-Dec-15, 0545 UT		0.306″	8.44
6.	NOAA 10923	2006-Nov-11, 1430 UT	S04	0.306″	8.44
7.	NOAA 10933	2007-Jan-07, 0000 UT	S05	0.306″	8.44

Table 6.2: Serial numbers are assigned to the active regions in the first column for reference. The date, time and latitude for the observations are given in the next two columns. The last two columns represent the mean pixel resolution and the physical length-scale of the magnetogram.

6.8 Comparison of models to observations

6.8.1 Results

We list our findings below:

1. All the field configurations analyzed were found to be negatively twisted as seen from the α for the C modes and the sign of the helicity for the LL modes. The fits with non-linear LL modes are substantially better than the linear C modes confirming the non-linear nature of the force-free fields.

C mode parameters								LL mode parameters					
AR #.	Modes n, m	α^{-1}/L	$r_1/L,\ r_2/L$ $\theta'/\ \pi,\ \psi'/\pi$	$\overline{E}_{ff}$ 10^{33} erg	$\overline{E}_{pot}$ 10^{33} erg	$\overline{E}_{free}$ 10^{33} erg	$\overline{H}_{rel}$ 10^{43} Mx^2	Modes n, m	r_1/L $\theta'/\ \pi,\ \psi'/\pi$	$\overline{E}_{ff}$ 10^{33} erg	$\overline{E}_{pot}$ 10^{33} erg	$\overline{E}_{free}$ 10^{33} erg	$\overline{H}_{rel}$ 10^{43} Mx^2
1.	1, 10	-0.09	1.32, 1.45 0.034, 1.142	1.50	0.905	0.595	$-$ 1.91	3, 2	0.53 0.117, 1.37	3.46	2.77	0.69	-0.322
2.	2, 10	-0.091	1.34, 1.85 -0.04, 0.095	6.27	0.760	5.51	$-$ 10.69	3, 2	0.57 0.67, 0.45	11.69	9.34	2.35	-1.17
3.	1, 5	-0.094	0.81, 0.99 -0.02, 0.38	2.71	1.18	1.53	-4.96	3, 2	0.57 0.167, 1.37	5.21	4.16	1.05	-0.552
4.	1, 8	-0.089	1.10, 1.24 0.015, 1.25	1.633	0.928	0.705	-2.30	3,2	0.67 0.117, 1.29	4.41	3.52	0.89	-5.49
5.	1, 8	-0.089	1.10, 1.24 0.015, 1.25	1.54	0.877	0.663	-2.18	3, 2	0.67 0.117, 1.29	4.16	3.32	0.84	-0.518
6.	1, 0	-0.461	1.65, 2.07 -0.97, 0.75	119.4	90.5	28.9	-535.3	1, 1	0.43 0.83, 1.33	10.70	10.70	0.0	0.0
7.	1, 0	-0.75	2.95, 3.37 -1.0, -0.15	178.1	161.1	17	-530.2	3, 1	0.57 3.18×10^{-7}, 1.67	2.063	2.063	0.0	0.0

Table 6.3: Parameters of simulation for the best fit of C and LL modes with the corresponding estimations of the free energy and relative helicity. Details of the active regions are given in Table 6.2. The numbers (n, m) refer to the radial and angular modes, α is the force-free parameter. L is the length-scale of the magnetogram. The inner radius is represented by r_1 where the magnetogram is placed and r_2 is the outer radius of the computation region. The Euler angles through which the magnetogram is rotated are represented by θ' and ψ'. $\overline{E}_{ff}$, $\overline{E}_{pot}$, $\overline{E}_{free}$ and $\overline{H}_{rel}$ are the normalized force-free energy, potential energy, free energy and the relative helicity of the magnetic field configuration respectively.

2. Table 6.4 lists all the parameters compiled for the AR listed in Table 6.2.

3. The AR 10930 has been fit by LL modes with a figure of merit $c = 0.7$–0.8 and $d = 0.65$–0.7. The energy ratio, ϵ is away from unity due to the fact that the data is noisy and that we had not done any pre-processing. There was a X3.4 class flare on December 13, 2006 and we confirm in both models a substantial decrease in free energy and relative helicity after the flare. The relative helicity and free energy in the C mode increased and in the LL mode decreased marginally after the X1.5 class flare on December 14, 2006.

4. The two ARs 10923, 10933 with single polarity fitted with potential fields with a high figure of merit $> 90\%$. They also show good correlation numbers for d and ϵ (near unity).

5. The formula (6.55) for the predicted $m_p(n_p, r_1/L)$ bears out for the force-free configurations found for AR 10930 (see first five rows of Table 6.3 for the modes (n, m) for C and LL modes. For example, in the case of C modes, $m_p = 2m - 2 = \{18, 18, 8, 14, 14\}$ for the five cases and we find the estimated m_p from equation (6.55) to be $\{16, 16, 7.25, 11.7, 11.7\}$. For the five cases of LL, $m_p = n + m - 1 = 4$ in all the five cases while the estimated $m_p = \{4.25, 4.6, 4.6, 3.8, 3.8\}$ from equation (6.55). It is clear that since the m_p estimates are closer for the LL modes as compared to the C modes, the corresponding figures of merit are higher for the C modes. The suggested m_p estimates are for lowest energy configurations.

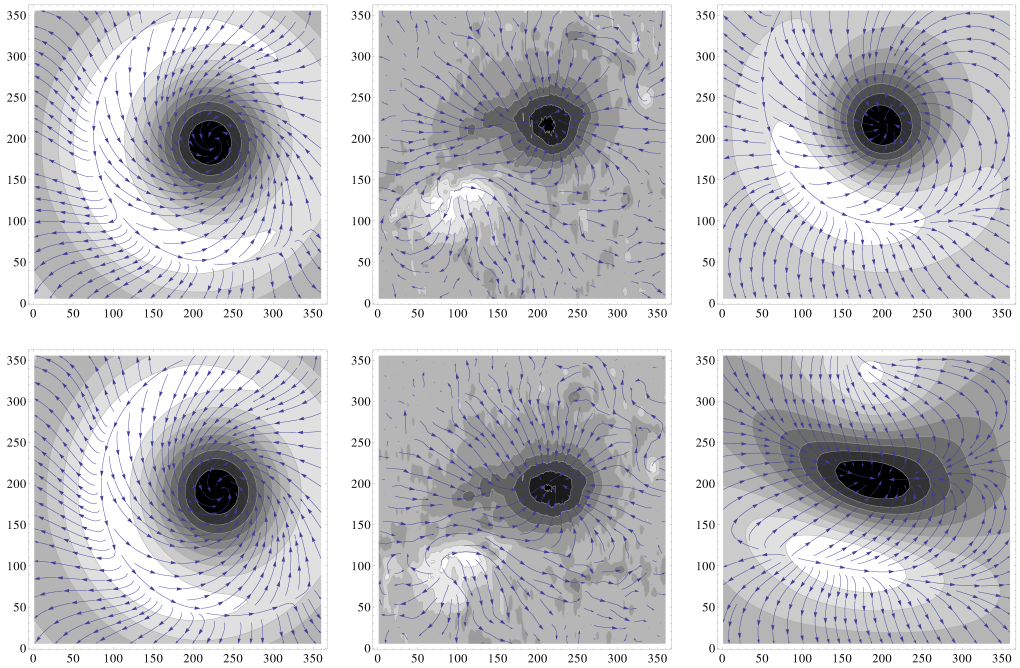

Figure 6.7: The magnetograms for active region NOAA 10930 are shown in the top and bottom panels of the figure for the dates 12th and 13th Dec 2006 respectively. The left and right panels represent the magnetograms simulated by the C and LL modes respectively. The middle panel represents the magnetogram observation by HINODE. There was an occurrence of a X 3.4 class flare between the dates; the figure depicts the field configuration before and after the flare.

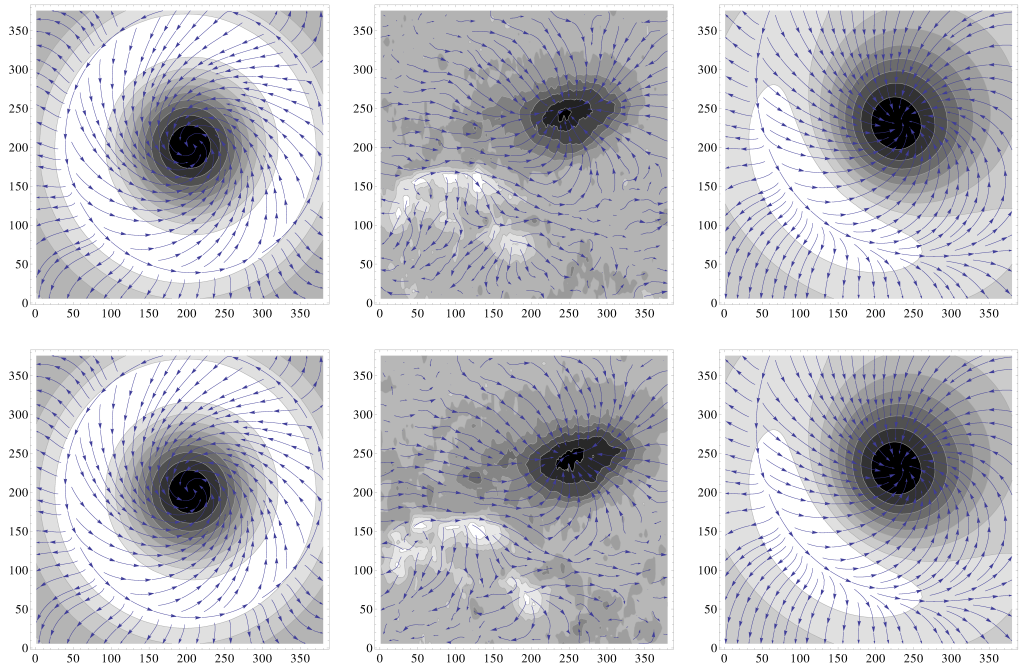

Figure 6.8: The magnetograms for active region NOAA 10930 are shown in the top and bottom panels of the figure for the dates 14th and 15th Dec 2006 respectively. The left and right panels represent the magnetograms simulated by the C and LL modes respectively. The middle panel represents the magnetogram observation by HINODE. There was an occurrence of a X 1.5 class flare between the dates; the figure depicts the field configuration before and after the flare.

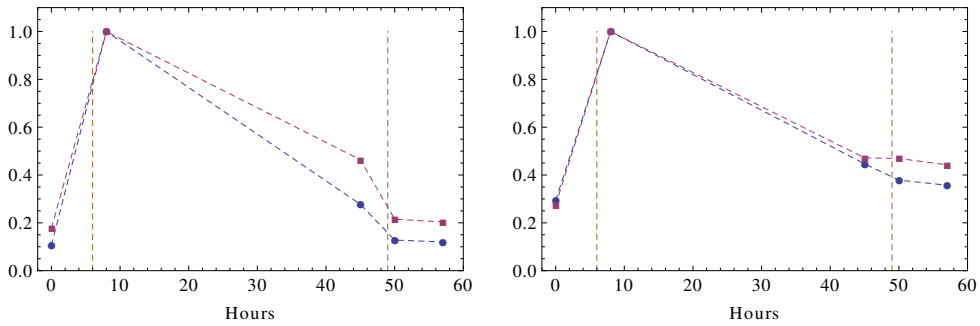

Figure 6.9: Free energy (circle) and relative magnetic helicity (square) simulated for AR 10930 (see rows 1 to 5 in Table 6.3) for the C (left) and LL (right) mode are plotted as a function of time. The time of the first observation (Dec 12, 2006; UT 2000) is set as zero hrs. The vertical lines represent the times of X3.4 and X1.3 class flares respectively. The values in y axis have been normalized with respect to their maximum.

6.8.2 Discussion of the results

AR 10923 and AR10933 show good fits ($c > 90\%$) with single polarity potential configurations and are negatively twisted with the energies of 10.7×10^{33} and 2.063×10^{33} ergs respectively. The corresponding goodness of fit parameters (d, ϵ) are near unity and indicate good fits, (see Table 6.4).

Active region NOAA 10930 is a center of focus for several studies and the HINODE/SOT has followed the active region for several days in many wavelength regions. The spectro-polarimeter (SP) produced vector magnetograms of this region till it disappeared on the West limb of the Sun. Using the vector magnetic field measurements at the photospheric levels and by applying a technique called pre-processing several authors employ NLFF extrapolation methods to compute the coronal magnetic fields (e.g., Schrijver et al. 2008). An X3.4 class flare has occurred in this active region on December

		C mode			LL mode		
N0.	AR #	c	d	ϵ	c	d	ϵ
1.		0.58	0.521	1.834	0.81	0.695	1.273
2.		0.581	0.511	1.876	0.70	0.645	1.88
3.	NOAA 10930	0.33	0.324	1.791	0.75	0.673	1.687
4.		0.42	0.395	1.724	0.76	0.698	1.765
5.		0.40	0.374	1.644	0.74	0.697	1.682
6.	NOAA 10923	0.76	0.888	1.517	0.92	0.928	0.943
7.	NOAA 10933	0.56	0.788	2.40	0.95	0.871	1.113

Table 6.4: The correlation parameters obtained for estimating the goodness of fit for different active regions. The definitions of the correlation parameters are given in §6.6.2.

13, 2006. Using the three-dimensional magnetic fields information, Schrijver et al. (2008) found that 3×10^{32} ergs of drop in free energy after the flare compared to the pre-flare free energy. On the other hand, Guo et al. (2008) find that only 2.4×10^{31} ergs of energy was released during the flare. At the same time, using a similar technique, Jing et al. (2010) did not find any release in free energy during the flare, instead they found a slight increase in free energy after the flare. These results are summarized in Table 6.5 along with our results.

Model^{ref}	Pre-flare					Post-flare					$\Delta\overline{E}_{free}$	$\Delta\overline{H}_{rel}$
	$\overline{E}_{ff}$ 10^{33} erg	$\overline{E}_{pot}$ 10^{33} erg	$\overline{E}_{ff}/\overline{E}_{pot}$	$\overline{E}_{free}$ 10^{33} erg	$\overline{H}_{rel}$ 10^{43} Mx^2	$\overline{E}_{ff}$ 10^{33} erg	$\overline{E}_{pot}$ 10^{33} erg	$\overline{E}_{ff}/\overline{E}_{pot}$	$\overline{E}_{free}$ 10^{33} erg	$\overline{H}_{rel}$ 10^{43} Mx^2	10^{33} erg	10^{43} Mx^2
C modes[a]	1.5	0.905	1.66	0.595	− 1.91	6.27	0.76	8.25	5.51	−10.69	4.915	−8.78
LL modes[a]	3.46	2.77	1.249	0.69	−0.322	11.69	9.34	1.252	2.35	−1.17	1.66	−0.848
Current-field iteration [b]			1.32					1.14			− .32	
Optimization[c]	1.33	1.2	1.13	1.11		1.27	1.16	.11	1.09		− .02	
Weighted optimization[d]				∼.75					∼.85		.1	

Table 6.5: The values for the energy of the force-free field and the corresponding potential field for the active region NOAA 10930 mentioned in literature are compiled in the table along with our results for reference. The quantities such as the free energy of the configuration, ratio between energies of the force-free and potential field and the change in free energy before and after the flare are also mentioned. a: current chapter, b: Schrijver et. al. (2008) , c: Guo et. al. (2008), d: Jing et. al. (2010)

We find that free energies derived from the LL model are consistent with a drop after both the flare events (note that the time coverage before and after the flare is not complete), indicating a strong probability of a peak in the free energy (and relative helicity) just before the first flare event, see Fig.

6.9. This picture is conducive to the idea that the loss of the free energy in the photosphere is strongly related to the energy dissipated in the flare events.

The coronal mass ejection (CME) associated with this event carried kinetic energy (deprojected velocity) of 4.5×10^{32} ergs with it (Ravindra and Howard, 2010). This is in rough agreement with our estimate of a loss of 1.66×10^{33} ergs (LL modes) as about half of this would be released in the kinetic energy channel. The magnetic cloud associated with the CME had a helicity of about -7×10^{41} Mx^2 as estimated here by Ravindra, Yoshimura, and Dasso (2011) which is much less than the drop in helicity estimated for the LL modes to be -0.322 $\times10^{43}$ Mx^2. However our estimate of the relative helicity injected into the active region corona is found to be -0.848×10^{43} Mx^2 before the initiation of X3.4 class flare which is comparable to the -4.3×10^{43} Mx^2 found by Park et al. (2010). All the NLFF extrapolation techniques employed (other than this work) in computing the free energy using the vector magnetic field data made use of pre-processing technique to make the field more close to force-free. However, in doing so the field gets smoothed and there by reducing the field strength and hence the free energy.

For the same datasets other authors using different NLFF extrapolation techniques for the analysis obtain slightly different results. In some cases, there is an increase in the free energy after the flare whereas in other cases they find that it decreases. In our analysis, both the free-energy and relative helicity increase after the first flare, as can be seen from the last two columns in Table 6.5. The ratio of the energies of the force-free field and the potential field that remains almost constant before and after the flare for the LL mode while for the C mode it increases. This can be used to infer that during the flare process there is a dynamic evolution of both the force-free field and the

potential field from a lower to higher energy state, implying that there was a peak in free-energy and relative helicity between the two observations which are separated by a large time gap of 8 hrs.

6.9 Summary & conclusions

Here we first summarize the key results of this chapter.

1. *Analytic results*

   We have shown that there are two solutions possible (albeit known already and denoted here as C and LL) from the separability assumption. We calculate the energies and relative helicity of the allowed force-free fields in a shell geometry.The final expression for the field of C modes is given in equation (6.66). We then calculated the corresponding potential field for calculating relative helicity in this region. The expressions for the potential field and its vector potential are given in equations (6.67) and (6.29). The relative helicity thus calculated is given by equation (6.30). The expression for energies of the force-free field and the potential field are given by equations (6.26) and (6.28) respectively whereby we can calculate the free energy of the system using equation (6.1). The alternative expressions for the energy of the force-free field and relative helicity are given in equations (6.27) and (6.31) respectively which are analytically in agreement with the previous expressions.

   For the LL mode we were able to extend the solution set obtained in Low and Lou (1990) from $n = 1$ to all rational values of $n = \frac{p}{q}$ by solving the equation (6.40) for all cases of odd p and for cases of $q > p$ for even p, in effect extending solution to practically all n. The final expression for the magnetic field is given by equation (6.39) and its vector

C MODES

$\mathbf{B}(r_1<r<r_2)=\left(\frac{-J_{m+3/2}(\alpha r)}{r^{3/2}}\frac{\mathrm{d}}{\mathrm{d}\mu}[(1-\mu^2)C_m^{3/2}(\mu)],\frac{-1}{r}\frac{\mathrm{d}}{\mathrm{d}r}[r^{1/2}J_{m+3/2}(\alpha r)](1-\mu^2)^{1/2}C_m^{3/2}(\mu),\frac{\alpha J_{m+3/2}(\alpha r)}{r^{1/2}}(1-\mu^2)^{1/2}C_m^{3/2}(\mu)\right)$

$\mathbf{A}(r_1<r<r_2)=\mathbf{B}/\alpha;\quad a_{m+1}=\frac{(m+2)r_1^{m+3/2}J_{m+3/2}(\alpha r_1)}{r_1^{2m+3}-r_2^{2m+3}};\quad b_{m+1}=\frac{(m+1)r_2^{2m+3}r_1^{m+3/2}J_{m+3/2}(\alpha r_1)}{r_1^{2m+3}-r_2^{2m+3}}$

$\mathbf{B}_P(r_1<r<r_2)=\left(\left[(m+1)a_{m+1}r^m-\frac{(m+2)b_{m+1}}{r^{m+3}}\right]P_{m+1}(\mu),\ -(1-\mu^2)^{1/2}\left[a_{m+1}r^m+\frac{b_{m+1}}{r^{m+3}}\right]\frac{\mathrm{d}P_{m+1}}{\mathrm{d}\mu},0\right)$

$\mathbf{A}_P(r_1<r<r_2)=\left(0,0,(1-\mu^2)^{1/2}P_l'(\mu)\left[\frac{a_l r^l}{l+1}-\frac{b_l}{lr^{l+1}}\right]\right)$

$E_v(r)=\frac{(m+1)(m+2)}{2(2m+3)}\left[r\left[\frac{\mathrm{d}}{\mathrm{d}r}\left\{r^{1/2}J_{m+3/2}(\alpha r)\right\}\right]^2+\left\{\alpha^2r^2-(m+1)(m+2)\right\}J^2_{m+3/2}(\alpha r)\right];$

$E_{ff}(\alpha,n,m,r_1,r_2)=E_v(r_2)-E_v(r_1)=\frac{(m+1)(m+2)}{2(2m+3)}\left[2\int_{r_1}^{r_2}\alpha^2rJ^2_{m+3/2}(\alpha r)\mathrm{d}r-r_1^{1/2}J_{m+3/2}(\alpha r_1)\frac{\mathrm{d}}{\mathrm{d}r}\{r^{1/2}J_{m+3/2}(\alpha r)\}|_{r=r_1}\right]$

$E_{pot}(m,r_1,r_2)=\frac{1}{2(2m+3)}\int_{r_1}^{r_2}\left[\left((m+1)a_{m+1}r^{m+1}-\frac{(m+2)b_{m+1}}{r^{m+2}}\right)^2+(m+1)(m+2)\left(a_{m+1}r^{m+1}+\frac{b_{m+1}}{r^{m+2}}\right)^2\right]\mathrm{d}r$

$H^{FA}_{rel}(\alpha,n,m,r_1,r_2)=\frac{8\pi E_{ff}}{\alpha}+\frac{4\pi(m+1)(m+2)}{\alpha(2m+3)}\Big[\alpha^2\int_{r_1}^{r_2}\left(\frac{a_{m+1}r^{m+1}}{m+2}-\frac{b_{m+1}}{(m+1)r^{m+2}}\right)r^{3/2}J_{m+3/2}(\alpha r)\mathrm{d}r$
$+r_1^{1/2}\left(a_{m+1}r_1^{m+1}+\frac{b_{m+1}}{r_1^{m+2}}\right)J_{m+3/2}(\alpha r_1)\Big]$

$H^B_{rel}(\alpha,n,m,r_1,r_2)=\frac{8\pi\alpha(m+1)(m+2)}{2m+3}\int_{r_1}^{r_2}rJ^2_{m+3/2}(\alpha r)\mathrm{d}r.$

LL MODES

$\mathbf{B}(r<r_2)=\left(\frac{-1}{r^{n+2}}\frac{\mathrm{d}P}{\partial\mu},\frac{n}{r^{n+2}}\frac{P}{(1-\mu^2)^{1/2}},\frac{a}{r^{n+2}}\frac{P^{(n+1)/n}}{(1-\mu^2)^{1/2}}\right);\quad \mathbf{A}(r<r_2)=\left(0,\frac{-a}{nr^{n+1}}\frac{P(\mu)^{(n+1)/n}}{(1-\mu^2)^{1/2}},\frac{1}{r^{n+1}}\frac{P(\mu)}{(1-\mu^2)^{1/2}}\right)$

$a_l=0,\quad b_l=\frac{2l+1}{2(l+1)}r_1^{l-n}\int_{-1}^{1}\frac{\mathrm{d}P}{\mathrm{d}\mu}P_l(\mu)\mathrm{d}\mu;\quad \mathbf{B}_P(r_1<r<r_2)=\left(\sum_{l=0}^{\infty}-(l+1)\frac{b_l}{r^{l+2}}P_l(\mu),\sum_{l=0}^{\infty}\frac{-b_l}{r^{l+2}}(1-\mu^2)^{1/2}\frac{\mathrm{d}P_l}{\mathrm{d}\mu},0\right).$

$\mathbf{A}_P(r_1<r<r_2)=\left(0,0,(1-\mu^2)^{1/2}P_l'(\mu)\left[\frac{a_lr^l}{l+1}-\frac{b_l}{lr^{l+1}}\right]\right);\quad E_{pot}(l,r_1)=\sum_{l=0}^{\infty}\frac{b_l^2(l+1)}{2(2l+1)r_1^{2l+1}}$

$E_{ff}(n,m,r_1)=\frac{1}{4(2n+1)r_1^{2n+1}}\int_{-1}^{1}\mathrm{d}\mu\left[P'(\mu)^2+\frac{n^2P(\mu)^2}{1-\mu^2}+\frac{a^2P(\mu)^{(2n+2)/n}}{1-\mu^2}\right]=\frac{1}{4r_1^{2n+1}}\int_{-1}^{1}\left\{\left(\frac{\mathrm{d}P}{\mathrm{d}\mu}\right)^2-\frac{(n^2+a^2P^{2/n})P^2}{(1-\mu^2)}\right\}\mathrm{d}\mu$

$H^{FA}_{rel}(n,m,r_1)=-2\pi a\sum_{l=0}^{\infty}\int_{-1}^{1}\frac{b_l}{nlr_1^{n+l}}P^{1+1/n}\frac{\mathrm{d}P_l}{\mathrm{d}\mu}\mathrm{d}\mu=H^B_{rel}(n,m,r_1)=\frac{2\pi a}{nr_1^{2n}}\int_{-1}^{1}\frac{P^{2+1/n}}{(1-\mu^2)}\mathrm{d}\mu.$

Table 6.6: Formulary for the various quantities calculated for the C and LL modes. **B** and **A** denote the force-free magnetic field and its corresponding vector potential. The same quantities for the potential field are denoted by $\mathbf{B}_P$ and $\mathbf{A}_P$ respectively. E_{ff}, E_{pot}, E_{free} and H_{rel} are the force-free energy, potential energy, free energy and the relative helicity of the magnetic field configuration respectively calculated using the Finn Antonesen & Berger formulae that are analytically equivalent.

potential by equation (6.47) respectively. The expression for the potential field consistent with this force-free field is given by equation (6.44) and the corresponding vector potential is given by equation (6.29) with the constants evaluated from equation (6.45). The relative helicity in the region using the Finn-Antonsen formula is given by equation (6.49). The energies for the force-free and potential fields are given by equations (6.42) and (6.46) respectively. Again, the alternative expressions for the energy of the force-free field and relative helicity are given in equations (6.43) and (6.50) respectively which are analytically in agreement with the previous expressions. For convenience these results are included in the formularies for C and LL modes in Table 6.6.

2. *Numerical Results*

We formulated a search strategy with parameters including two Euler rotations of the force-free sphere and a variable set that corresponds to the various C and LL modes, see §6.6. A study of effectiveness of our search strategy is presented in §6.6.3. Here we find that we are able to get the correct configuration for the input field (as in the dipole case) and are able to fit the energies within a factor of 2. We then studied the field configurations for 3 active regions, c.f. Table 6.2 and calculated the free-energy and relative helicity for these cases. We were able to get reasonable fits for the above cases, c.f. Table 6.4. All the field configurations analyzed were found to be negatively twisted as seen from the α for the C modes and the helicity of the LL modes, c.f. Table 6.3. The fits with non-linear LL modes seem to be better than the linear C modes. In the case of AR 10930, there was a X3.4 class flare on December 13, 2006 and we confirm in both modes a substantial decrease in free energy and relative helicity after

the flare. A comparison of results obtained in this chapter with those in literature for the same flare event is presented in Table 6.5. The relative helicity and free energy in the C mode increased and in the LL mode decreased marginally after the X1.5 class flare on December 14, 2006. The two ARs 10923, 10933 with single polarity show very high correlation ($> 90\%$) with potential fields. We were not able to explore the full parameter space because of computational constraints mentioned in §6.6. Since our best fit with the observational data for the LL modes is substantially better (75%) than those obtained in the test cases, this lends much credibility to the results presented in the chapter.

We find that the approach taken here is fairly good in estimating the quantities of interest namely relative helicity and free energy, see Table 6.5 and §6.8. In order to compare with the other estimates available in literature, where the potential fields are usually extended from the planar surface of the magnetogram to a cuboidal volume over the magnetogram, we rescale our physical quantities obtained for a hemisphere by the factor of the solid angle subtended by the magnetogram at the center. This enables us to approximate their trend before and after a flare event. The validity of this approximation can be seen from the general agreement with other estimates (including observations). An advantage in this method is its ease and utility to calculate these physical quantities, in particular the relative helicity is thus far not calculated by other approaches. Further, we don't have to assume any other boundary conditions for the side walls, as required in the other extrapolation techniques using the cuboidal volume. This method can also provide useful reconstruction of the non-linear force-free fields as well as reasonable input field for other numerical techniques. It is clear that non-

linear LL modes are dominantly better fits than the linear C modes. The search is now limited by computational constraints; in future, we hope to improve the fits by applying the method to a larger space of geometrical parameters and in more cases of mode numbers n and m.

The LL solution of ($n = 1$ in Low and Lou (1990) and $n = 5, 7, 9$ (odd cases) in Flyer *et al.* (2004)) have been extended here to the cases of nearly all n. The topological properties of these extended solutions can be further studied by considering other boundary conditions.The analytic solutions for LL suffer from the problem of a singularity at the origin which render them unphysical; this implies that more realistic boundary conditions are necessary.

To learn more about the evolution and genesis of these structures, it would be useful to carry out dynamical simulations allowing for footpoint motions with the analytic input fields constructed above to study how the non-linearity develops; a stability analysis of the non-linear modes would also be a useful tool (Berger (1985) has analyzed the linear constant α case). Clearly, these are difficult mathematical problems to be addressed in the future.

Appendix

6.A Boundary conditions and formulae for C mode fields

The conditions to be satisfied at a interface (where α has a discontinuity) are

1. The divergence condition implies the continuity of normal component of the magnetic field, whereas the absence of surface currents on the boundaries leads to continuity of the parallel components of the field. Therefore magnetic field **B** should be continuous.

2. The normal component of the current density **J** should be continuous as there is no accumulation of charges at the boundary.

The second condition requires the continuity of the normal component of $\alpha\mathbf{B}$; on the other hand, the first condition requires normal component of **B** to be continuous. If α changes discontinuously at a spherical shell (say at a radius $\mathcal{R}$), then the two conditions can be met only if the normal component of **B** vanishes. In spherical coordinates, the conditions at the shell are therefore, $B_r = 0$, B_θ and B_ϕ are continuous. This condition on B_r at $r = \mathcal{R}$ can be met only if

$$g_{m+3/2}(\alpha r)|_{r=\mathcal{R}} = 0. \tag{6.62}$$

and $\alpha\mathcal{R}$ is the zero the function. Let

$$g_{m+3/2}(\alpha r) = c_1 J_{m+3/2}(\alpha r) + c_2 Y_{m+3/2}(\alpha r) \tag{6.63}$$

where c_1 and c_2 are constants to be determined from the boundary conditions. Finiteness of g at $r = 0$ demands $c_2 = 0$; physically this implies that the poloidal flux, is finite. Then

$$g_{m+3/2}(\alpha r) = c_1 J_{m+3/2}(\alpha r). \tag{6.64}$$

Finally, the expression for magnetic field is given by

$$\mathbf{B} = \left(\frac{-1}{r^2}\frac{\partial}{\partial\mu}[S_m r^2(1-\mu^2)], \frac{-1}{r\sqrt{(1-\mu^2)}}\frac{\partial}{\partial r}[S_m r^2(1-\mu^2)], \alpha r\sqrt{(1-\mu^2)}S_m \right). \tag{6.65}$$

The above expression can be further simplified by substituting for S_m using equations (6.20) and (6.64) to

$$\begin{aligned} \mathbf{B} &= \left(\frac{-J_{m+3/2}(\alpha r)}{r^{3/2}}\frac{\mathrm{d}}{\mathrm{d}\mu}[(1-\mu^2)C_m^{3/2}(\mu)], \frac{-1}{r}\frac{\mathrm{d}}{\mathrm{d}r}[r^{1/2}J_{m+3/2}(\alpha r)] \right. \\ &\quad \left. (1-\mu^2)^{1/2}C_m^{3/2}(\mu), \frac{\alpha J_{m+3/2}(\alpha r)}{r^{1/2}}(1-\mu^2)^{1/2}C_m^{3/2}(\mu) \right). \end{aligned} \tag{6.66}$$

The various modes of C modes are shown in Fig.6.10 for different values of the variable m. Note that m represents the number of angular oscillations of the mode. The total number of poles in the sphere being $2m$. The self similarity of the solutions is evident from Figure 6.10.

The derivation for the potential field corresponding to equation (6.66)is given in §6.C. The final expressions for the potential field is found to be

$$\begin{aligned} \mathbf{B}_P &= \left(\left[(m+1)a_{m+1}r^m - \frac{(m+2)b_{m+1}}{r^{m+3}} \right] P_{m+1}(\mu), -(1-\mu^2)^{1/2} \right. \\ &\quad \left. \left[a_{m+1}r^m + \frac{b_{m+1}}{r^{m+3}} \right] \frac{\mathrm{d}P_{m+1}}{\mathrm{d}\mu}, 0 \right). \end{aligned} \tag{6.67}$$

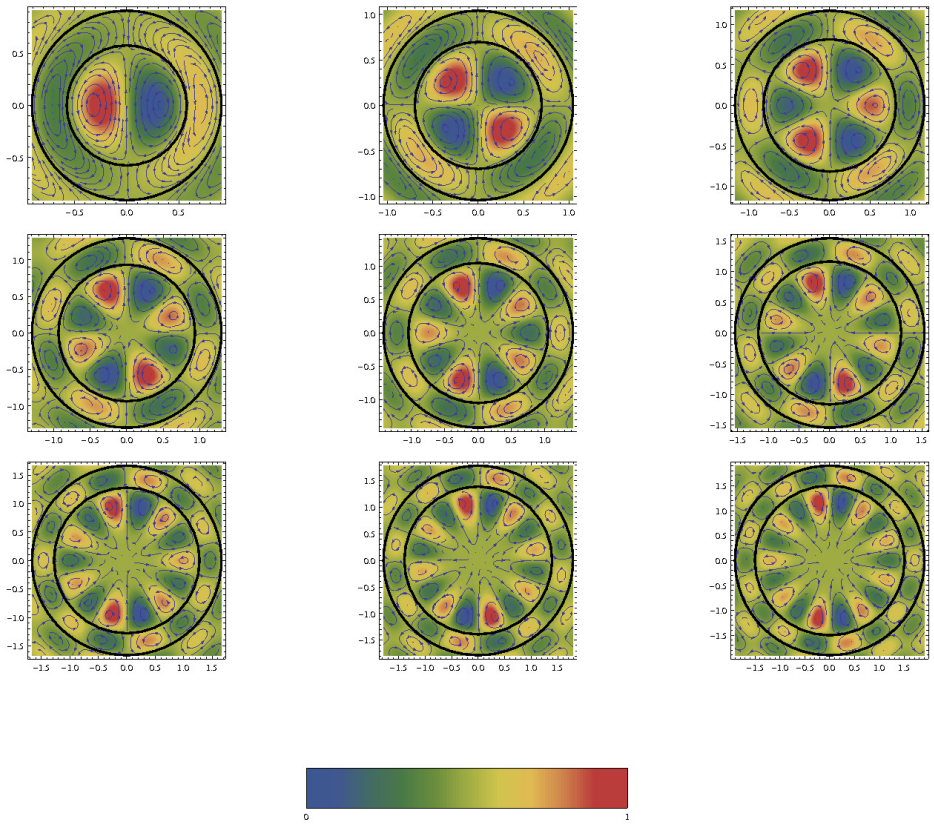

Figure 6.10: The different angular modes from $m = 1$ (top left) to $m = 9$ (bottom right) are shown in the figure. The contours represent the poloidal stream function ψ and the density plot represents the strength of the azimuthal field B_ϕ. The two circles are drawn at first and second radial roots. The 0 and 1 in the legend corresponds to the minimum and maximum value of B_ϕ respectively.

$P_{(m+1)}(\mu)$ are the Legendre polynomials, and where the coefficients are given as

$$\chi_l = \chi_{m+1}(r_1) = \frac{(m+1)(m+2)}{r_1^{3/2}} J(m+3/2, \alpha r_1) \tag{6.68}$$

$$a_l = a_{m+1} = \frac{\chi_{m+1}(r_1)}{(m+1)} \frac{r_1^{m+3}}{r_1^{2m+3} - r_2^{2m+3}}$$

$$b_l = b_{m+1} = \frac{(m+1)}{(m+2)} a_{m+1} r_2^{(2m+3)} \tag{6.69}$$

The above expressions can be further simplified by substituting for χ_l, which gives

$$a_{m+1} = \frac{(m+2) r_1^{m+3/2} J_{m+3/2}(\alpha r_1)}{r_1^{2m+3} - r_2^{2m+3}}$$

$$b_{m+1} = \frac{(m+1) r_2^{2m+3} r_1^{m+3/2} J_{m+3/2}(\alpha r_1)}{r_1^{2m+3} - r_2^{2m+3}} \tag{6.70}$$

6.B Energy for closed field lines of C mode

The energy of force-free magnetic field in a spherical shell geometry is given by

$$E(\mathbf{B}) = \frac{1}{8\pi} \int_{r_1}^{r_2} \int_{-1}^{1} \int_{0}^{2\pi} |\mathbf{B}|^2 r^2 \mathrm{d}r \mathrm{d}\mu \mathrm{d}\phi = \frac{1}{4} \int_{r_1}^{r_2} \int_{-1}^{1} |\mathbf{B}|^2 r^2 \mathrm{d}r \mathrm{d}\mu \tag{6.71}$$

where axisymmetry is applied in the last step. The expression for energy for the force-free field given in equation (6.71) uses a volume integral, whereas we can calculate it via a surface integral using the virial theorem for force-free fields (Chandrasekhar 1961) in spherical geometry as

$$E_{ff} = \frac{1}{8\pi} \int_V |\mathbf{B}|^2 \mathrm{d}V = \frac{1}{8\pi} \int_S |\mathbf{B}|^2 \mathbf{r} \cdot \mathrm{d}\mathbf{S} - \frac{1}{4\pi} \int_S (\mathbf{B} \cdot \mathbf{r})(\mathbf{B} \cdot \mathrm{d}\mathbf{S}) \tag{6.72}$$

where S is the surface enclosing the volume of interest V. In axisymmetry, the equation (6.72) reduces to

$$E_{ff} = \frac{1}{8\pi} \int_V |\mathbf{B}|^2 \mathrm{d}V = \frac{\mathcal{R}^3}{4} \int_{-1}^{1} (B_\theta^2 + B_\phi^2 - B_r^2) \mathrm{d}\mu. \tag{6.73}$$

where $\mathcal{R}$ is the radius of the shell. For the energy of a potential field, we use $E_P = E(\mathbf{B}_P)$, which is calculated from equation (6.71). In order to study the dependence of energy on the various radial and angular modes, we first calculate the contribution from the toroidal component given by

$$E_T = \frac{\alpha^2}{4} \int_{r_1}^{r_2} \mathrm{d}r \; r J^2_{m+3/2}(\alpha r) \int_{-1}^{1} \mathrm{d}\mu (1-\mu^2) \left[C_m^{3/2}(\mu) \right]^2 \tag{6.74}$$

using equation (6.71) and $E(\mathbf{B}) = E(\mathbf{B}_T) + E(\mathbf{B}_P)$, the total energy (for volumes containing closed field lines) is given by $E_{ff} = 2E_T$ (Chandrasekhar, 1961). The energy for C mode can be calculated analytically if the field lines close at the inner and outer boundaries. The radial part of the integration in equation (6.74) can be written as

$$R = \alpha^2 \int_{r_1}^{r_2} \mathrm{d}r \; r J^2_{m+3/2}(\alpha r). \tag{6.75}$$

If $r_1 = 0$ and $r_2 = r_{nm}$, where $Z_{nm} = \alpha r_{nm}$ is the nth root of $J_{m+3/2}(\alpha r)$, then equation (6.75) can be written as

$$R = \frac{1}{2} (Z_{nm})^2 \left[J_{m+5/2}(Z_{nm}) \right]^2 . \tag{6.76}$$

The angular part of equation (6.74) can be written as

$$\Theta = \int_{-1}^{1} \mathrm{d}\mu (1-\mu^2) C_m^{3/2}(\mu)^2. \tag{6.77}$$

Using the orthogonality properties of Gegenbauer polynomials, the above integral can be evaluated as

$$\Theta = \frac{\pi \Gamma(m+3)}{4!(m+3/2)[\Gamma(3/2)]^2} = \frac{2(m+1)(m+2)}{2m+3}. \tag{6.78}$$

Combining equations (6.76 & 6.78), we obtain the following expression for equation (6.74)

$$E_T = \frac{Z_{nm}^2}{4} \frac{(m+1)(m+2)}{2m+3} \left[J_{m+5/2}(Z_{nm}) \right]^2 . \tag{6.79}$$

and plot contours of the result in Fig. 6.11 (left panel). We find that for a sphere of fixed radius, the energy increases with higher angular m and radial n modes. The radial modes of the solution are given by the Bessel functions, which represents the number of radial oscillations and the energy of the field increases with the number of oscillations. The angular modes are given by $(1-\mu)^{1/2}C_m^{3/2}(\mu)$ which are presented in the right panel of Fig. 6.11 and the field reverses $(m+1)$ times for a given value of m.

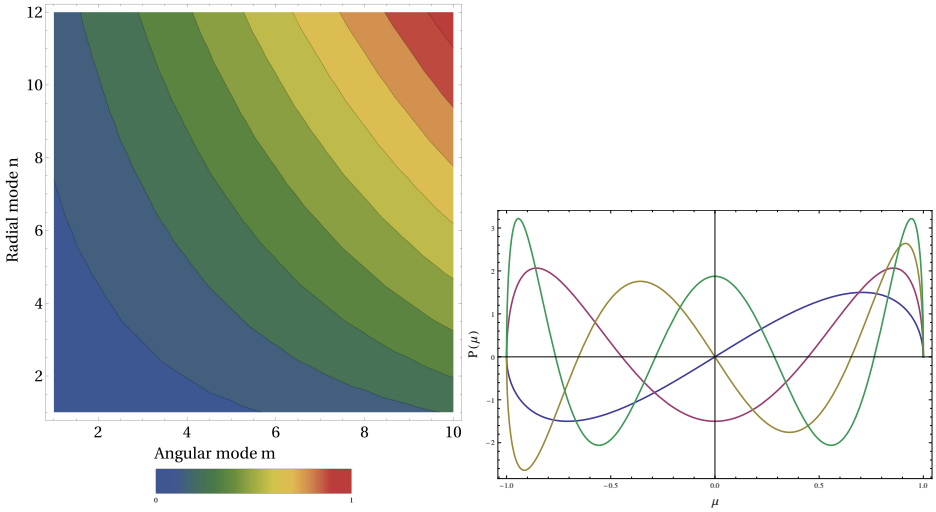

Figure 6.11: The left panel shows contours of energy for different angular and radial modes for C modes computed for the same volume and normalized with respect to the maximum. The 0 and 1 in the legend refer to the maximum and minimum values of the energies respectively. The right panel shows the behavior of $P(\mu)$ which changes sign $(m+1)$ times in the domain for a given value of m.

6.C Calculating potential fields corresponding to the force-free fields

A potential field is defined by the equation

$$\nabla \times \mathbf{B}_P = 0. \tag{6.80}$$

Thus the field can be expressed as $\mathbf{B}_P = \nabla\Phi_P$ for a scalar potential Φ_P which satisfies the Laplace equation $\nabla^2\Phi_P = 0$. The general solution for this equation in spherical coordinates is given by

$$\Phi_P(r,\mu) = \sum_{l=0}^{\infty}(a_l r^l + \frac{b_l}{r^{l+1}})P_l(\mu) \tag{6.81}$$

where $P_l(\mu)$ is the Legendre polynomial of order l; a_l and b_l are constant coefficients to be determined by matching the normal components of potential field with that of the force-free field at the boundaries. We have to solve the Laplace equation for a spherical shell with r_1 and r_2 as inner and outer boundaries.

The radial component of the potential field $[B_r(r,\mu)]_P$is given by

$$[B_r(r,\mu)]_P = (\nabla\Phi)_r = \frac{\partial\Phi}{\partial r} = \sum_{l=0}^{\infty} P_l(\mu)\chi_l(r) \tag{6.82}$$

where χ_l is given by

$$\chi_l(r) = \left[l a_l r^{l-1} - (l+1)\frac{b_l}{r^{l+2}}\right]. \tag{6.83}$$

We assume that the radial component of the force-free magnetic field can be separated as functions of r and μ denoted by $R(r)$ and $\Theta(\mu)$ respectively:

$$[B_r(r,\mu)]_{ff} = R(r)\Theta(\mu). \tag{6.84}$$

To match the radial components of potential and force-free fields, we use equations (6.82) and (6.84) and equate the two fields at the lower boundary,

$r = r_1$

$$R(r_1)\Theta(\mu) = \sum_{l=0}^{\infty} P_l(\mu)\chi_l(r_1). \tag{6.85}$$

Using the orthogonality property of Legendre functions we get

$$R(r_1)\int_{-1}^{1}\Theta(\mu)P_l(\mu)\mathrm{d}\mu = \frac{2}{(2l+1)}\chi_l(r_1). \tag{6.86}$$

So, the expansion coefficients for the potential field can be obtained from equation (6.86) as

$$\chi_l(r_1) = \frac{(2l+1)}{2}R(r_1)\int_{-1}^{1}\Theta(\mu)P_l(\mu)\mathrm{d}\mu \tag{6.87}$$

6.C.1 Matching potential field to C modes at the inner shell

Using equations (6.87) and (6.64) we can write at the inner boundary $r = r_1$

$$\begin{aligned}\chi_l(r_1) &= \frac{(2l+1)J_{m+3/2}(\alpha r_1)}{2r_1^{3/2}} \\ &\quad \int_1^{-1}\frac{\partial}{\partial\mu}\left[C_m^{3/2}(\mu)(1-\mu^2)\right]P_l(\mu)\mathrm{d}\mu \qquad (6.88)\\ &= \frac{(m+1)(m+2)}{r_1^{3/2}}J_{m+3/2}(\alpha r_1), \qquad (6.89)\end{aligned}$$

where $l = m+1$, the calculation of the μ integral in equation (6.88) is given in Appendix 6.G. At the outer boundary at $r = r_2$, we have $\chi_l(r_2) = 0$, which results in the following condition for the coefficients a_l and b_l

$$b_l = b_{(m+1)} = \frac{(m+1)}{(m+2)}a_{(m+1)}r_2^{(2m+3)}. \tag{6.90}$$

Using equation (6.83) and the above equation, we find the following expression for the coefficient $a_{(m+1)}$

$$a_l = a_{(m+1)} = \frac{\chi_{(m+1)}(r_1)}{(m+1)}\frac{r_1^{(m+3)}}{r_1^{(2m+3)} - r_2^{(2m+3)}}. \tag{6.91}$$

Upon simplification the coefficients can be written as

$$\begin{aligned} a_{m+1} &= \frac{(m+2)r_1^{m+3/2}J_{m+3/2}(\alpha r_1)}{r_1^{2m+3}-r_2^{2m+3}} \\ b_{m+1} &= \frac{(m+1)r_2^{2m+3}r_1^{m+3/2}J_{m+3/2}(\alpha r_1)}{r_1^{2m+3}-r_2^{2m+3}} \end{aligned} \tag{6.92}$$

Thus the expression for the potential field is given by

$$\begin{aligned} \mathbf{B}_P &= \Big(\left[(m+1)a_{(m+1)}r^m - \frac{(m+2)b_{(m+1)}}{r^{(m+3)}}\right]P_{(m+1)}(\mu), \\ &- (1-\mu^2)^{1/2}\left[a_{(m+1)}r^m + \frac{b_{(m+1)}}{r^{(m+3)}}\right]\frac{\mathrm{d}P_{(m+1)}}{\mathrm{d}\mu}, 0\Big). \end{aligned} \tag{6.93}$$

6.C.2 Matching potential field to LL modes at the inner shell

We recall the definitions for the general potential field from equation (6.81). Now the boundary condition at the outer boundary $r_2(=\infty)$ is given by $\chi_l(r_2) = 0$, and since the potential should be finite for all values of r, it implies that

$$a_l = 0 \tag{6.94}$$

and the scalar potential takes the form

$$\Phi_P(r,\mu) = \sum_{l=0}^{\infty}\frac{b_l}{r^{l+1}}P_l(\mu) \tag{6.95}$$

while the radial component of the potential field is given by

$$B_r(r,\mu) = \sum_{l=0}^{\infty} -(l+1)\frac{b_l}{r^{l+2}}P_l(\mu). \tag{6.96}$$

From equation (6.36) we recall that the radial component of the non-linear field has the following form

$$B_r(r,\mu) = -\frac{1}{r^{n+2}}\frac{\mathrm{d}P}{\mathrm{d}\mu}. \tag{6.97}$$

Equating the two radial fields at the lower boundary, $r = r_1$ we get

$$\sum_{l=0}^{\infty} -(l+1)\frac{b_l}{r_1^{l+2}}P_l(\mu) = -\frac{1}{r_1^{n+2}}\frac{\mathrm{d}P}{\mathrm{d}\mu}. \tag{6.98}$$

Using the orthogonality property of the Legendre polynomials we get the following expression for the expansion coefficient b_l

$$b_l = \frac{2l+1}{2(l+1)}r_1^{l-n}\int_{-1}^{1}\frac{\mathrm{d}P}{\mathrm{d}\mu}P_l(\mu)\mathrm{d}\mu. \tag{6.99}$$

So the final expression for the potential field matched to LL modes is given by

$$\mathbf{B}_P = \left(\sum_{l=0}^{\infty} -(l+1)\frac{b_l}{r^{l+2}}P_l(\mu), \sum_{l=0}^{\infty}\frac{-b_l}{r^{l+2}}(1-\mu^2)^{1/2}\frac{\mathrm{d}P_l}{\mathrm{d}\mu}, 0\right). \tag{6.100}$$

6.D Vector potential of potential fields

The vector potential for the potential field is given by the relation

$$\nabla \times \mathbf{A}_P = \nabla\Phi_P \tag{6.101}$$

where Φ_P is the scalar potential obtained from equation (6.81). Since a potential field is entirely poloidal and curl of a toroidal field is always poloidal, we expect $\mathbf{A}_P$ to have only toroidal component. Then for an axisymmetric field $\mathbf{A}_P$ will be of the following form,

$$\mathbf{A}_P = A_\phi(r,\mu)\hat{\phi} \tag{6.102}$$

Expanding the above equation in spherical polar coordinates, we obtain the following pair of equations

$$\frac{-1}{r}\frac{\partial}{\partial\mu}\left[(1-\mu^2)^{1/2}A_\phi\right] = \frac{\partial\Phi_P}{\partial r} \tag{6.103}$$

$$\frac{1}{r}\frac{\partial}{\partial r}(rA_\phi) = \frac{(1-\mu^2)^{1/2}}{r}\frac{\partial\Phi_P}{\partial\mu} \tag{6.104}$$

Solving the above two equations simultaneously, we find the unique solution

$$A_\phi(r,\mu) = \sum_{l=0}^{\infty}(1-\mu^2)^{1/2}P_l'(\mu)\left[\frac{a_l r^l}{l+1} - \frac{b_l}{l r^{l+1}}\right]. \tag{6.105}$$

$$A_\phi(r,\mu) = \sum_{l=0}^{\infty}(1-\mu^2)^{1/2}P_l'(\mu)\left[\frac{a_l r^l}{l+1} - \frac{b_l}{l r^{l+1}}\right]. \tag{6.106}$$

So, the final expression is given by

$$\mathbf{A}_P = \sum_{l=0}^{\infty}\left(0,0,(1-\mu^2)^{1/2}P_l'(\mu)\left[\frac{a_l r^l}{l+1} - \frac{b_l}{l r^{l+1}}\right]\right). \tag{6.107}$$

6.E Vector potential for LL modes

Since $\mathbf{A}$ is uncertain within a choice of gauge, we choose a convenient gauge such that the radial component of the vector potential, A_r is zero. Then the vector potential in spherical polar coordinates can be written as

$$\mathbf{A} = (0, A_\theta, A_\phi). \tag{6.108}$$

Using the definition $\mathbf{B} = \nabla \times \mathbf{A}$, we get the following three equations for the components of $\mathbf{A}$

$$\begin{aligned}
\frac{-1}{r^2}\frac{\partial\psi}{\partial\mu} &= \frac{-1}{r}\frac{\partial}{\partial\mu}\left[(1-\mu^2)^{1/2}A_\phi\right] \\
\frac{-1}{r(1-\mu^2)^{1/2}}\frac{\partial\psi}{\partial r} &= \frac{-1}{r}\frac{\partial}{\partial r}(rA_\phi) \\
\frac{a\psi^{(n+1)/n}}{(1-\mu^2)^{1/2}} &= \frac{\partial(rA_\theta)}{\partial r}.
\end{aligned} \tag{6.109}$$

By solving the above set of equations, we find

$$\mathbf{A} = \left(0, \frac{-a}{nr^{n+1}}\frac{P(\mu)^{(n+1)/n}}{(1-\mu^2)^{1/2}}, \frac{1}{r^{n+1}}\frac{P(\mu)}{(1-\mu^2)^{1/2}}\right) \tag{6.110}$$

As a consequence of equations (6.36, 6.110), $\mathbf{A}\cdot\mathbf{B} = 0$ everywhere. For closed field lines in a volume, the magnetic helicity

$$H = \int \mathbf{A}\cdot\mathbf{B}\; dV = 0. \tag{6.111}$$

6.F Equivalence of Finn Antonsen and Berger formulae for force-free spheres

6.F.1 C modes

To show the equivalence of expressions of relative helicity obtained from equations (6.30 & 6.31), we first express equation (6.30) as

$$H_r = \frac{8\pi E_{ff}}{\alpha} + \frac{4\pi(m+1)(m+2)}{\alpha(2m+3)}(I_1 + I_2) \tag{6.112}$$

where E_{ff} is given by equation (6.26), I_1 is the integral given by

$$I_1 = \int_{r_1}^{r_2} \alpha^2 \left(\frac{a_{m+1} r^{m+1}}{m+2} - \frac{b_{m+1}}{(m+1) r^{m+2}} \right) r^{3/2} J_{m+3/2}(\alpha r) \tag{6.113}$$

and I_2 is the boundary term given by

$$I_2 = r_1^{1/2} \left(a_{m+1} r_1^{m+1} + \frac{b_{m+1}}{r_1^{m+2}} \right) J_{m+3/2}(\alpha r_1). \tag{6.114}$$

Upon simplification, we get

$$I_1 + I_2 = \left(\frac{a_{m+1} r_1^{m+2}}{m+2} - \frac{b_{m+1}}{(m+1) r_1^{m+1}} \right) \frac{\mathrm{d}}{\mathrm{d}r} \left[r^{1/2} J_{m+3/2}(\alpha r) \right] |_{r=r_1}. \tag{6.115}$$

Now from the continuity of the radial component of the force-free field to the potential field at $r = r_1$, $(\mathbf{B}_P)_r = (\mathbf{B})_r$, where $\mathbf{B}$ and $\mathbf{B}_P$ are given by equations (6.66) and (6.67) respectively, we find

$$\left(\frac{a_{m+1} r_1^{m+2}}{m+2} - \frac{b_{m+1}}{(m+1) r_1^{m+1}} \right) = r_1^{1/2} J_{m+3/2}(\alpha r_1) \tag{6.116}$$

which leads to

$$I_1 + I_2 = r_1^{1/2} J_{m+3/2}(\alpha r_1) \frac{\mathrm{d}}{\mathrm{d}r} \left[r^{1/2} J_{m+3/2}(\alpha r) \right] |_{r=r_1}. \tag{6.117}$$

Substituting equations (6.26 & 6.117) in equation (6.112) we arrive at equation (6.31).

6.F.2 LL modes

To prove the equivalence of the expressions of relative helicity given in equations (6.49 & 6.50), we start with equation (6.98) which can be rewritten as

$$\sum_{l=0}^{\infty}(l+1)\frac{b_l}{r_1^l}P_l(\mu) = \frac{1}{r_1^n}\frac{\mathrm{d}P}{\mathrm{d}\mu}. \tag{6.118}$$

Integrating the above equation with respect to μ and rearranging the terms, we get

$$\sum_{l=0}^{\infty}(l+1)\frac{b_l}{r_1^{l-n}}\int P_l(\mu)\mathrm{d}\mu = P. \tag{6.119}$$

Now from the Legendre differential equation, we have the identity

$$\left[(1-\mu^2)\frac{\mathrm{d}P_l}{\mathrm{d}\mu}\right] = -l(l+1)\int P_l\mathrm{d}\mu. \tag{6.120}$$

Substituting equation (6.120) in equation (6.119), we get

$$-\sum_{l=0}^{\infty}\frac{b_l}{lr_1^{l-n}}\left[(1-\mu^2)\frac{\mathrm{d}P_l}{\mathrm{d}\mu}\right] = P. \tag{6.121}$$

Multiplying both sides of equation (6.121) by $\dfrac{2\pi a P^{1+1/n}}{nr_1^{2n}(1-\mu^2)}$ we get the equality between the integrands of equations (6.49 & 6.50).

6.G Calculation of angular integral in the expression (6.88)

Here we give the derivation of the angular integral in equation (6.88).

$$\int_{-1}^{1}\frac{\partial}{\partial\mu}\left[C_m^{3/2}(\mu)(1-\mu^2)\right]P_l(\mu)\mathrm{d}\mu. \tag{6.122}$$

We now expand Gegenbauer polynomials in terms of Legendre polynomials by using the following relation

$$(1-\mu^2)C_m^{3/2}(\mu) = (1+m)\left[P_m(\mu) - \mu P_{m+1}(\mu)\right] = (1-\mu^2)P'_{m+1}(\mu). \quad (6.123)$$

Equation (6.122) can now be written as

$$\begin{aligned}
&\int_{-1}^{1} \frac{\partial}{\partial\mu}\left[(1-\mu^2)P'_{m+1}(\mu)\right] P_l(\mu)\mathrm{d}\mu \\
= \;& \left[P_l(\mu)(1-\mu^2)P'_{m+1}(\mu)\right]_{-1}^{1} - \int_{-1}^{1} P'_l(\mu)P'_{m+1}(\mu)(1-\mu^2)\mathrm{d}\mu \\
= \;& \int_{-1}^{1} P'_l(\mu)\mathrm{d}\mu \int (m+1)(m+2)P_{m+1}(\mu)\mathrm{d}\mu \\
= \;& \left[\int (m+1)(m+2)P_{m+1}(\mu)P_l(\mu)\mathrm{d}\mu\right]_{-1}^{1} \\
- \;& \int (m+1)(m+2)P_{m+1}(\mu)P_l(\mu)\mathrm{d}\mu \\
= \;& -(m+1)(m+2)\delta_{0,m+1}P_l(\mu) - \frac{2(m+1)(m+2)}{2l+1}\delta_{l,m+1} \\
= \;& -\frac{2(m+1)(m+2)}{2m+3}
\end{aligned} \quad (6.124)$$

where we have used Legendre differential equation to substitute for the derivative of $P'_{m+1}(\mu)$ in the third step and the orthogonality property of Legendre polynomials in the final step.

6.H Boundary conditions for F in equation (6.40)

We motivate the transformation of the variable from P to F by $P = (1-\mu^2)^{1/2}F$. This enables us to write an ODE equation (6.40) to solve directly for LL fields for all the allowed cases of n that is numerically difficult to implement with the ODE for P, given by equation (6.35). The angular part

of the LL mode is given by equation (6.35)

$$(1-\mu^2)P'' + a^2\frac{n+1}{n}P^{1+2/n} + n(n+1)P = 0. \tag{6.125}$$

We assume

$$P(\mu) = (1-\mu^2)^\Gamma g(\mu), \tag{6.126}$$

as $P(\mu = \pm 1) = 0$ for the highest possible $\Gamma > 0$ such that $g(\mu = \pm 1) \neq 0$. Substituting for P in equation (6.35) we obtain

$$\begin{aligned}&(1-\mu^2)^2 g'' + \left[-2\Gamma(1-\mu^2) + 4\mu^2\Gamma(\Gamma-1) + n(n+1)(1-\mu^2)\right] g \\ &-4\mu\Gamma(1-\mu^2)g' + a^2\frac{(n+1)}{n}g^{\frac{n+2}{n}}(1-\mu^2)^{\frac{2\Gamma}{n}+1} = 0.\end{aligned} \tag{6.127}$$

We now expand P using equation (6.126) in a power series of $(1-\mu^2)$ near $\mu = \pm 1$,

$$P(\mu) = (1-\mu^2)^\Gamma \sum_{\gamma=0}^{\infty} C_\gamma (1-\mu^2)^\gamma, \tag{6.128}$$

where C_0 is the leading term which is non-zero by definition. Comparing equation (6.126) and (6.128), we can expand $g(\mu)$ near $\mu^2 = 1$ in a power series with coefficients C_γ as

$$\lim_{\mu^2 \to 1} g(\mu) = C_0 + C_1(1-\mu^2) + C_2(1-\mu^2)^2 + ... \tag{6.129}$$

t is clear from above that in the limit $\mu^2 \to 1$, $g \to C_0$ which is a constant. Also we know that g' and g'' are finite as $\mu^2 \to 1$ since $P(\mu)$ is finite in this limit. As a result, upon the substitution $\mu^2 \to 1$, equation (6.127) gives

$$4\mu^2\Gamma(\Gamma-1)g = 0, \tag{6.130}$$

leading to $\Gamma = 0, 1$. The $\Gamma = 0$ solution is not allowed whereas $\Gamma = 1$ implies

$$P(\mu) = (1-\mu^2)g = (1-\mu^2)^{1/2}F. \tag{6.131}$$

Thus F satisfies the boundary conditions

$$F(\mu) = 0 \quad \text{at} \quad \mu = -1, 1. \tag{6.132}$$

Chapter 7

Analytical modeling of braided magnetic fields

7.1 Introduction

In this chapter, we estimate the free-energy available in braided structures using topological quantities and compare them with the numerical estimates made in Chapter 6. This free energy provides a reservoir for coronal heating by micro- and nanoflares. We first describe the analytical modeling of braiding and propose a self-regulatory mechanism of twist and reconnection for obtaining a steady heating rate. We then apply this model to one of the active regions studied in Chapter 6 and calculate the distribution of flare energies. These results provide useful information on the coronal loop structure and also imply that the coronal heating can be supplied by the braiding in the case of the active sun.

The work presented in part in Section 7.2 is in preparation for submission.

7.2 Analytic modeling of the self-organized braided magnetic fields

A simple analytic model of braided magnetic fields which gives a power-law distribution of energy releases is presented in Berger and Asgari-Targhi (2009). Following is a brief overview of this model. Consider a braid on three strings as shown in Fig. 7.1. The sections of the braid where the two strings on the left twist about each other are called *coherent sequences* and single crossings which swap the middle string on the right are called *interchanges*.

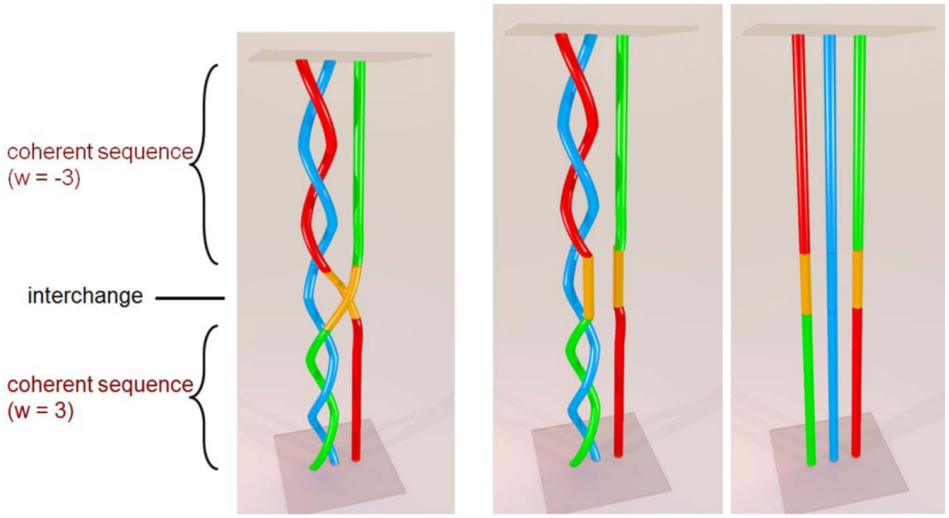

Figure 7.1: (a) A three-braid configuration with two coherent sequences separated by an interchange. (b) The interchange is removed by reconnection. (c) The final relax configuration with the crossings canceled out. Figure courtesy: Berger and Asgari-Targhi (2009)

The braid structure is assumed to be generated at the boundaries by a succession of the following two motions which alternate with each other:

1. The first motion rotates the leftmost and middle endpoints through

some net twist angle θ, where θ is a multiple of π. This generates a winding w in the strings between the boundaries which correspond to $\bar{c} = |w|$ crossings ($w = \theta/\pi$ or $-\theta/\pi$ for upper and lower boundary motions respectively). The crossing can be right- handed or left-handed based on the sign of w.

2. The second motion gives a single half-twist between the middle- and right-hand end point which generates an interchange.

For example, the braid of Figure 7.1 can be generated from three straight curves by the following steps:

1. The leftmost end points rotate at the top boundary through three anti-clockwise half-turns ($w = +3$) which gives the strings below three positive (right-handed) half-twists.

2. The second motion exchanges the third string with the middle string.

3. A twist of three clockwise turns gives the two strings on the left three negative half-twists ($w = -3$). The twists cannot cancel because of the interchange (which can be removed only by reconnection). The result of reconnection on the curves involved in the interchange is shown in the middle configuration in Figure 7.1. Now the positive and negative twists connect to each other and cancel out.

In order to model the distribution of coherent braid sequences, we consider the evolution of the braid by random processes which can either add a new structure or remove/simplify an old structure. We begin with some arbitrary initial braid having m sequences separated by $m - 1$ interchanges. At each step, one new coherent sequence is added with one new interchange. Simultaneously, a reconnection event randomly removes one of the existing

interchanges due to which, the sequences on either side either merge or cancel out. After iterating this for many steps, the braid reaches a statistical steady state which is independent of the initial structure. The braid structure can then be thought of as self-organized. If number of sequences with crossing number w is given by $n(w)$, then

$$m = \sum_{w=-\infty}^{\infty} n(w), \tag{7.1}$$

and the total number of crossings is given by

$$\overline{c}_{tot} = \sum_{w=-\infty}^{\infty} |w| n(w). \tag{7.2}$$

We can then define $f(w) = n(w)/m$ as the probability distribution function for the sequence lengths w. For simplification, w is assumed to be continuous rather than a discrete variable. The number of crossings between w and $w + \delta w$ can then be written as $n(w)\delta w$. At each time step, one new sequence and one new interchange is added, while one of the interior interchanges is removed by reconnection. We take the probability distribution of new sequence lengths to be $p(w)$. At each time step, the probability distribution function $f(w)$ changes by $\delta f(w)$, which is contributed by the following factors:

1. A probability of $p(w)$ that the new sequence will add to $f(w)$.

2. A sequence will disappear, if the sequence to the left of the reconnecting interchange has a winding w. So, there is a probability $f(w)$ that the number $n(w) = mf(w)$ of sequences with crossing number w will decrease by one.

3. The sequence to the right of the obstruction has probability of $f(w)$ of removing a w sequence.

4. If the left sequence has w_1 windings and the right sequence has $w_2 = w - w_1$ windings, a new w-sequence will be created.

Combining all the above factors, we write

$$\begin{aligned}\delta n(w) &= [p(w) - 2f(w)] + \int_{-\infty}^{\infty} f(w_1)dw_1 \times \int_{-\infty}^{\infty} f(w_2)dw_2\delta[w - (w_2 + w_1)] \\ &= [p(w) - 2f(w)] + \int_{-\infty}^{\infty} f(w_1)f(w - w_1)dw_1\end{aligned}$$

In a steady state, the left-hand side of the above equation vanishes. So

$$p(w) - 2f(w) + (f * f)(w) = 0, \tag{7.3}$$

where $f * f$ represents the Fourier convolution. To solve this, we take the Fourier transform of the previous equation,

$$\tilde{p}(k) - 2\tilde{f}(k) + \tilde{f}^2(k) = 0, \tag{7.4}$$

whose solution is given by

$$\tilde{f}(k) = 1 - \sqrt{1 - \tilde{p}(k)}. \tag{7.5}$$

If the input a new sequence follows a Poisson process for some λ, then

$$p(w) = \frac{\lambda}{2}\exp^{-\lambda|w|}, \quad \text{and} \quad \tilde{p}(k) = \frac{\lambda^2}{\lambda^2 + k^2}, \tag{7.6}$$

Substituting $\tilde{p}(k)$ in equation (7.5), we obtain

$$\tilde{f}(k) = \left(1 - \frac{|k|}{\sqrt{\lambda^2 + k^2}}\right). \tag{7.7}$$

Using standard integrals to solve the inverse transform of $\tilde{f}(k)$, we get

$$f(w) = \frac{\lambda}{2}\left(L_{-1}(\lambda w) - I_1(\lambda w)\right) \tag{7.8}$$

where I is a Bessel function and L is a Struve L function. The function $f(w)$ asymptotically behaves as w^{-2}.

In order to calculate the distribution of flare energies $F(E)$ corresponding to distribution of coherent braid sequences $f(w)$, we rewrite the free energy of a set of braided magnetic flux tubes using equation (4.17) as $E_{free} = a\overline{c}^2$, where the constant a depends on the length and diameter of the tubes. If the reconnection event reduces the number of crossings from $\overline{c}_{initial}$ to $\overline{c}_{final}$ then the flare energy can be defined as (ignoring the constant a)

$$E = \Delta E_{free}/a = \overline{c}^2_{initial} - \overline{c}^2_{final}. \tag{7.9}$$

We assume that reconnection occurs when the total crossing number reaches some critical value $\overline{c}_{crit}$. We start with two coherent sequences of length w_1 and w_2 ($|w_2|$ ¿ $|w_1|$) which are of opposite sign, they merge to form a single sequence of length $|w_2|$-$|w_1|$. The total length of the two sequences was initially $|w_2| + |w_1|$, thus the loss of crossings is $2|w_1|$ and the change in crossing number squared is

$$E = \overline{c}^2_{crit} - (\overline{c}_{crit} - 2|w_1|)^2 = 4\overline{c}_{crit}|w_1| - 4w_1^2. \tag{7.10}$$

We assume $w_1 \ll w_{crit}$ so the term $4w_1^2$ can be neglected. If the second sequence has a larger crossing number, i.e., $|w_2| > |w_1|$, then the probability of obtaining E is

$$F(E) = 2\int_0^\infty \int_{-\infty}^{-w_1} f(w_1)f(w_2)\delta(E - 4w_1\overline{c}_{crit})\mathrm{d}w_2\mathrm{d}w_1. \tag{7.11}$$

Assuming distribution of coherence lengths follows the power-law, $f(w_1) = b|w_1|^{-\beta}$ with $\beta > 1$, we get

$$\begin{aligned} F(E) &= 2b^2 \int_0^\infty w_1^{-\beta} \frac{w_1^{1-\beta}}{1-\beta} \delta(E - 4w_1\overline{c}_{crit})\mathrm{d}w_1 \\ &= \left(\frac{2b^2}{\beta - 1}\left(\frac{1}{4\overline{c}_{crit}}\right)^{2-2\beta}\right) E^{1-2\beta}. \end{aligned} \tag{7.12}$$

Using α for the energy slope. we find

$$F(E) \propto E^{-\alpha} \rightarrow \alpha = 2\beta - 1. \tag{7.13}$$

If $\beta = 2$ (as in our analytic model), then the distribution of flares with energy E decreases as the third power of E, i.e., $F(E) \propto E^{-3}$. The model thus demonstrates that braid patterns can organize themselves so that coherence lengths and flare energies obey power-law energy distributions.

7.3 Results

In this section we present the result of our analysis of free energy content and distribution of flare energies based on the nonlinear force-free field (NLFFF) solutions previously presented in Prasad, Mangalam, and Ravindra (2014). We start by taking the NLFFF configuration obtained for the Active Region (AR) 10930 as observed on UT 2000, December 12, 2006 and choose a sample of 50 points along the Polarity Inversion Line (PIL) (as shown in Fig. 7.2).

The sample points were chosen along the PIL because this region was found to be most stressed in the analysis which initiated an X 3.4 class flare (He *et al.*, 2014). The amount of braiding was calculated for all possible pairs using the crossing number formula given in equation (4.14). We then calculated the free energy content of the system using equation (4.17).

$$E_f \geq \left(8k^2 L\overline{\Phi}^2\right)^{-1} C^2 \tag{7.14}$$

where k^2=13.6 and $C = \overline{\Phi}^2 c$. Here Φ represents the flux contribution from a single sample point. We then calculate the mean flux over an area ΔA covered by the sample points and then scale the result by a factor $A/\Delta A$ to obtain a free-energy estimate for the entire region. Here A represents the area on the photospheric surface covered by the entire magnetogram. Thus

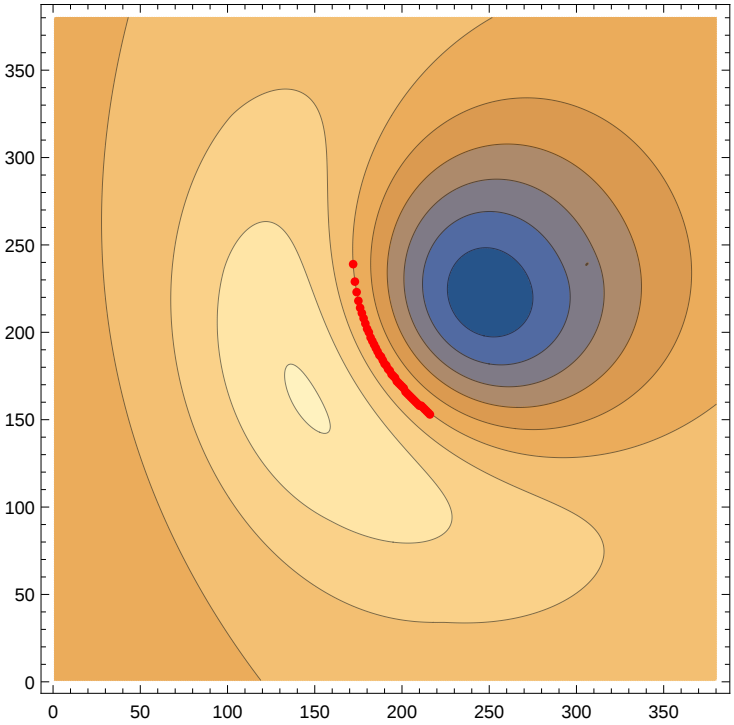

Figure 7.2: The points are sampled along the neutral line of the simulated active region (shown in red dots).

the free energy for the entire region, arising from the braided topology of the magnetic field is given by

$$E_f = \frac{c^2 B_z^2 A \Delta A}{8k^2 L} = 1.9 \times 10^{32} \text{ergs} \tag{7.15}$$

which roughly agrees with the value of the free energy content of 6.9×10^{32} ergs, previously reported in Prasad, Mangalam, and Ravindra (2014) from the exact calculations using nonlinear force-free fields. We then used the model of self-organized braiding presented in Berger and Asgari-Targhi (2009) to study the number distribution of braid sequence lengths and the flare energy distribution. A discussion regarding evolution of self-organized critical states in braided magnetic fields maintained by a balance of topological structure input (following a Poisson distribution) and loss through re-

connection process is presented in §s:berg. It is seen that an initially random braid can become highly ordered, with coherence lengths obeying power-law distributions. We carry out this analysis to obtain the distribution for coherent length sequences $f(w)$ for the NLFFF solution obtained from vector magnetograms of AR 10930 on 12th and 14th December, 2006. We find that the distribution of coherent length sequences is having an asymptotic slope, $-\beta = -2$ for $f(w)$ (see Fig. 7.3), which in reasonable agreement with the analytical distribution (equation 7.8) given in Berger and Asgari-Targhi (2009). The energy released during reconnection is known to follow a power law with an index between $2.7 < \alpha < 1.5$ (see Fig. 4.3). The energy distribution is then given by $F(E) \propto E^{-\alpha}$ with $\alpha = 2\beta - 1$ (Berger and Asgari-Targhi, 2009). For $\beta = 2$, as obtained from our analysis, we obtain the slope of energy distribution of flares as $-\alpha = -3$. We also repeated this analysis numerically with the Gaussian, $p_G(w)$ and Lorentzian distribution, $p_L(w)$ as choices for input functions, $p(w)$ in equation (7.6). The functional form of these distributions are given below:

$$p_G(w) = \frac{\exp(-(x-\mu)^2/2\sigma^2)}{\sqrt{2\pi}\lambda} \tag{7.16}$$

$$p_L(w) = \frac{\lambda}{\pi\left(\lambda^2 + w^2\right)} \tag{7.17}$$

A comparison of distribution of coherent length sequences obtained for SOC models with different input functions and the NLFFF solutions is shown in Fig. 7.4. We find that the model with Poisson distribution as the input function fits best with the NLFFF solutions.

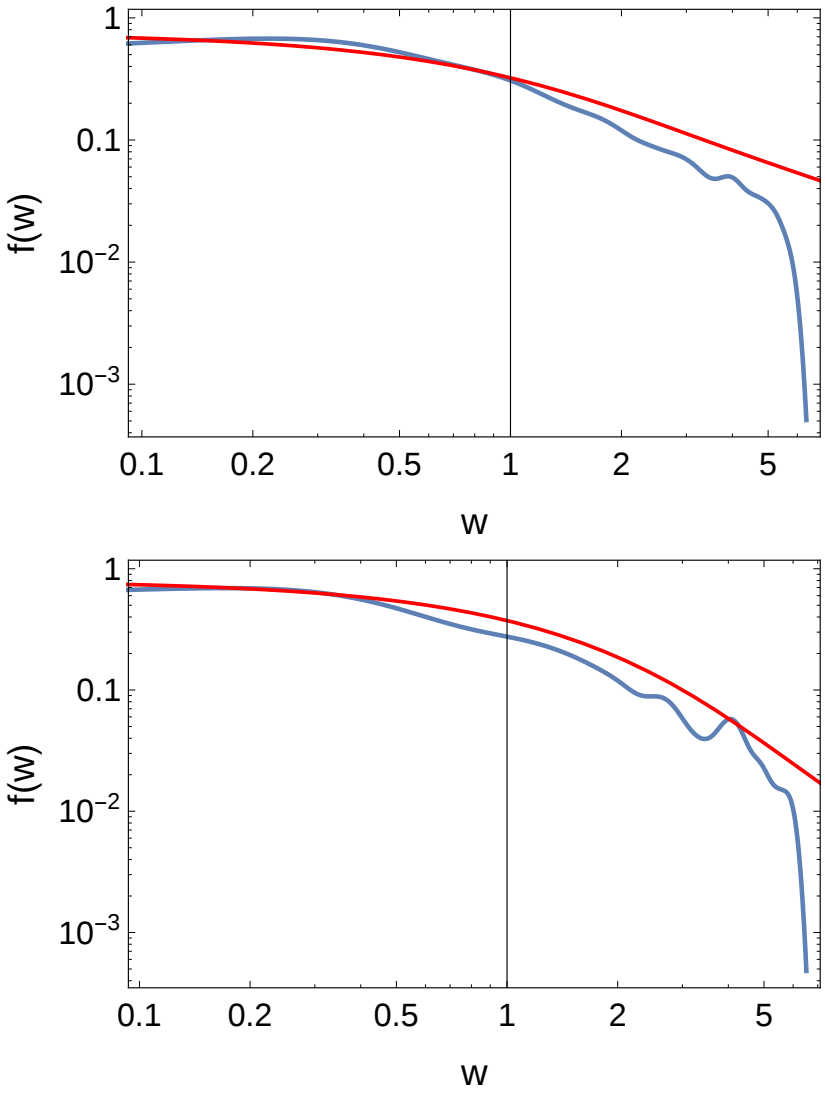

Figure 7.3: Distribution $f(w)$ where w is the braid sequence length for magnetograms simulated for December 12 (top) and 14 (bottom), 2006.

7.4 Summary and future directions

The 3D geometry of active regions from vector magnetogram observations was obtained in Prasad, Mangalam, and Ravindra (2014) by solving nonlinear force-free field equation semi-analytically. We use these solutions here, to

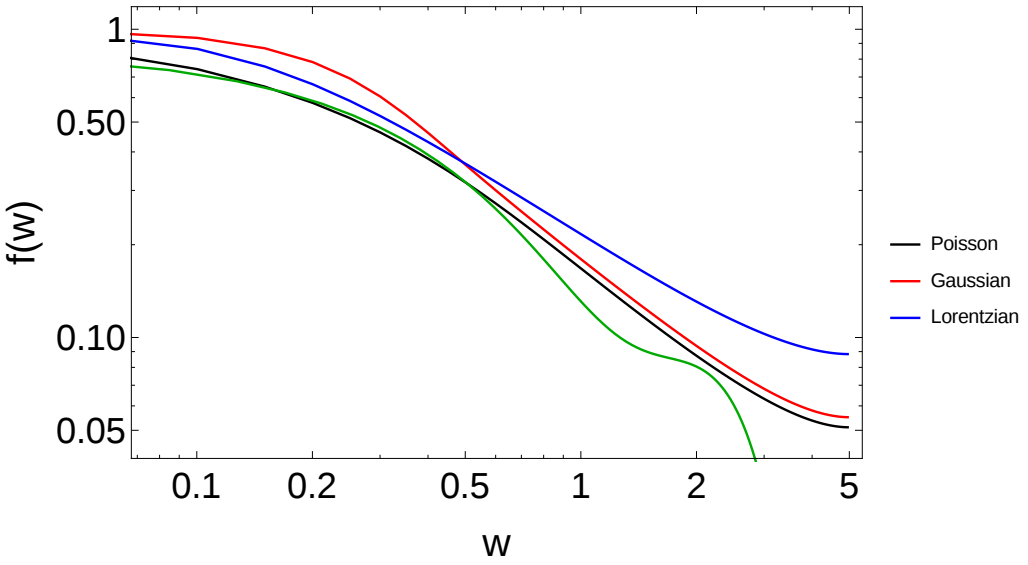

Figure 7.4: Comparison of the distribution of coherent length sequences $f(w)$ for the choice of Poisson (black), Gaussian (red) and Lorentzian (blue) distribution as input function with the distribution from NLFF fields (green curve).

evaluate the topology of the field lines using the crossing numbers (Berger, 1993) as measures. We use the crossing number of the braided field to estimate the free energy of AR 10930 (observed between 12-15 December 2006), which is found to be in agreement to those previously obtained in (Prasad, Mangalam, and Ravindra, 2014) using exact integration of these NLFF fields. We also calculate the power-law distribution for the length of the coherent braid sequence and the peak-flare energy distribution using the NLFF fields. We find that our estimates for these distributions are in good agreement with the SOC model presented in (Berger and Asgari-Targhi, 2009). We also extend the SOC model of Berger and Asgari-Targhi (2009) by including the cases of Gaussian and Lorentzian as input distributions.

In future, we plan to get an semi-analytical expression of free energy for the force-free solutions obtained in Prasad, Mangalam, and Ravindra (2014),

in terms of the crossing number and estimate the total energy released in the corona from these braided structures. We then plan to explore the energy content braided magnetic structures and its significance with regards to the energy budget for the active Sun. We would also like to find out how the energy released through small scale reconnection events can be correlated to the energy content in these force-free fields. We also plan to incorporate the semi analytic force-free model for the 3 braided magnetic field presented in Wilmot-Smith, Hornig, and Pontin (2009).

Chapter 8

Galactic dynamo with helicity and coronal fields

8.1 Introduction

Large-scale magnetic fields with strength of the order of 1-10 μG have been observed in disc galaxies (e.g. Beck *et al.*, 1996; Fletcher, 2010; Beck, 2012; Beck and Wielebinski, 2013; Van Eck *et al.*, 2014). The origin of these fields can be explained through mean-field dynamo theory (Ruzmaikin, Sokolov, and Shukurov, 1988; Beck *et al.*, 1996; Brandenburg and Subramanian, 2005a; Kulsrud and Zweibel, 2008). The conservation of magnetic helicity is one of the key constraints in these models, which also leads to suppression of the α-effect. The operation of the mean field dynamo automatically leads to the growth of helicity of opposite signs between the large scale and small scale fields (Pouquet, Frisch, and Leorat, 1976; Gruzinov and Diamond, 1994; Blackman and Field, 2002). To avoid the catastrophic suppression of the dy-

The work presented in this chapter has been submitted to the Astrophysical Journal and is currently under review.

namo action, the magnetic helicity due to the small-scale field should be removed from the system (Blackman and Field, 2000, 2001; Kleeorin *et al.*, 2000). Mechanisms suggested to produce these small-scale helicity fluxes are: advection of magnetic fields by an outflow from the disc through the galactic fountain or wind (Shukurov *et al.*, 2006; Sur, Shukurov, and Subramanian, 2007; Chamandy *et al.*, 2014), helicity flux from anisotropy of the turbulence produced by differential rotation (Vishniac and Cho, 2001; Subramanian and Brandenburg, 2004, 2006; Sur, Shukurov, and Subramanian, 2007; Vishniac and Shapovalov, 2014) and through diffusive flux (Kleeorin *et al.*, 2000, 2002; Brandenburg, Candelaresi, and Chatterjee, 2009; Mitra *et al.*, 2010; Chamandy *et al.*, 2014). The outflow of magnetic helicity from the disc through dynamo operation leads to formation of a corona (Blackman and Field, 2000). According to Taylor's hypothesis, an infinitely conducting corona would resistively relax to force-free field configurations under the constraint of global helicity conservation (Woltjer, 1960; Taylor, 1974; Finn and Antonsen, 1983; Berger and Field, 1984; Mangalam and Krishan, 2000). In this chapter, we include advective and diffusive fluxes in a simple analytic model of galactic dynamo which transfers helicity outside the disc and consequently builds up a corona in course of time. The magnetic helicity of the mean field in the disc and corona is calculated using the gauge invariant prescription given in Low (2006, 2011). We develop a formalism for the 3D axisymmetric time-dependent dynamo problem by first solving for the steady-state solutions and then using them as a basis for a expansion of the time-dependent solutions. We then investigate the dependence of the saturated mean field strength and it's geometry on the helicity fluxes within the disc and corresponding evolution of the force-free field in the corona.

The organization of the chapter is as follows. In §2 & 3, we present the

theoretical formulation of the nonlinear mean-field dynamo and magnetic helicity transport. The steady state and time dependent dynamo solutions are discussed in §4. In §5, we set up the equations for time dependence of α and evolution of the coronal field. The results of the chapter are presented in §6, where we discuss the strength and geometry of the saturated mean field and its dependence on the helicity fluxes. The conclusions of the chapter are discussed in §7. In addition, the detailed equations for magnetic helicity dynamics, derivations of various equations referred in the main text and a discussion on the gauge invariant of of absolute magnetic helicity for cylindrical geometry are presented in Appendices 8.A - 8.F.

8.2 Non-linear mean-field dynamo and helicity dynamics

The magnetic and velocity fields under the mean-field magnetohydrodynamics (Krause and Rädler, 1980) can be written as the sum of their mean and fluctuating parts

$$\mathbf{B} = \overline{\mathbf{B}} + \mathbf{b}; \quad \mathbf{U} = \overline{\mathbf{U}} + \mathbf{u} \tag{8.1}$$

with $\overline{\mathbf{u}} = 0$ and $\overline{\mathbf{b}} = 0$. The overbar formally denotes ensemble averaging, but for all practical purposes can be thought of as spatial averaging over scales greater than the turbulent scale and less than the scale of the system (Germano, 1992; Gent *et al.*, 2013). The mean magnetic field generated from small-scale turbulent motion is then described by the mean-field induction equation (Moffatt, 1978; Krause and Rädler, 1980):

$$\frac{\partial \overline{\mathbf{B}}}{\partial t} = \nabla \times \left(\overline{\mathbf{U}} \times \overline{\mathbf{B}} - \eta \nabla \times \overline{\mathbf{B}} + \boldsymbol{\mathcal{E}} \right). \tag{8.2}$$

Here $\boldsymbol{\mathcal{E}} \equiv \overline{\mathbf{u}\times\mathbf{b}} = \alpha\overline{\mathbf{B}} - \eta_t\overline{\mathbf{J}}$, is the mean turbulent emf with turbulent transport coefficients α and η_t. The Ohmic magnetic diffusivity is given by η, while $\overline{\mathbf{J}} = \dfrac{\nabla\times\overline{\mathbf{B}}}{\mu_0}$ is the current density with μ_0 being the permeability of free space (hereafter we assume $\mu_0 = 1$). Following the closure models, such as EDQNM (Pouquet, Frisch, and Leorat, 1976) and τ-approximation (Blackman and Field, 2002; Rädler, Kleeorin, and Rogachevskii, 2003; Brandenburg and Subramanian, 2005b), we represent the effect of the small-scale magnetic field on the α-effect as, $\alpha = \alpha_k + \alpha_m$ (e.g. Gruzinov and Diamond, 1994; Brandenburg and Subramanian, 2005a), where $\alpha_k = -\dfrac{1}{3}\tau\overline{\mathbf{u}\cdot\nabla\times\mathbf{u}}$ represents the kinetic α-effect related to the mean helicity of the random flow $\overline{\mathbf{u}\cdot\nabla\times\mathbf{u}}$, and $\alpha_m = \dfrac{1}{3\rho}\tau\overline{\mathbf{j}\cdot\mathbf{b}}$ is the magnetic contribution to the α-effect. The fluid density is given by ρ and τ is the correlation time of the turbulent flow $\mathbf{u}$.

The magnetic helicity dynamics using the above construction can be represented by equations for the evolution of the large scale helicity $\overline{H} = \int \overline{\mathbf{A}}\cdot\overline{\mathbf{B}}\mathrm{d}V$ and the mean small scale helicity $H' = \int \overline{\mathbf{a}\cdot\mathbf{b}}\mathrm{d}V$. These equations including all the interaction terms can be written as (cf. Mangalam, 2008, also see Appendix 8.A for a derivation)

$$\frac{\mathrm{d}\overline{H}}{\mathrm{d}t} = 2\int \boldsymbol{\mathcal{E}}\cdot\overline{\mathbf{B}}\mathrm{d}V - 2\int \eta\overline{\mathbf{J}}\cdot\overline{\mathbf{B}}\mathrm{d}V - \oint \mathbf{F}\cdot\hat{n}\mathrm{d}S \tag{8.3}$$

$$\frac{\mathrm{d}H'}{\mathrm{d}t} = -2\int \boldsymbol{\mathcal{E}}\cdot\overline{\mathbf{B}}\mathrm{d}V - 2\int \eta\overline{\mathbf{j}\cdot\mathbf{b}}\mathrm{d}V - \oint \mathbf{f}\cdot\hat{n}\mathrm{d}S, \tag{8.4}$$

where $\hat{n}$ represents the normal to the surface S enclosing volume V. The surface fluxes for $\overline{H}$ and H' are given by $\mathbf{F}$ and $\mathbf{f}$ respectively which can be written as

$$\mathbf{F} = (\eta\overline{\mathbf{J}} - \overline{\mathbf{U}}\times\overline{\mathbf{B}} - \boldsymbol{\mathcal{E}} - \nabla\varphi_1)\times\overline{\mathbf{A}} - 2\varphi_1\overline{\mathbf{B}} \tag{8.5}$$

$$\begin{aligned}\mathbf{f} = {} & \overline{(\mathbf{a}\cdot\overline{\mathbf{B}})\mathbf{u}} - \overline{(\mathbf{a}\cdot\mathbf{u})\overline{\mathbf{B}}} - \overline{(\mathbf{a}\cdot\overline{\mathbf{U}})\mathbf{b}} + \overline{(\mathbf{a}\cdot\mathbf{b})\overline{\mathbf{U}}} - \overline{(\mathbf{a}\cdot\mathbf{u})\mathbf{b}} + \overline{(\mathbf{a}\cdot\mathbf{b})\mathbf{u}} \\ & + \overline{\boldsymbol{\mathcal{E}}\times\mathbf{a}} + \eta\overline{\mathbf{j}\times\mathbf{a}} - \overline{\nabla\varphi_2\times\mathbf{a}} - 2\overline{\varphi_2\mathbf{b}}\end{aligned} \tag{8.6}$$

where φ_1 and φ_2 are scalar functions representing the gauge freedom for the large and small scale vector potentials respectively. Below, we discuss some terms in the surface fluxes that have been identified and found to be significant in simulations and we leave the investigation of the remaining terms in (8.5) and (8.6) for the future studies aided by simulations. The relative contribution from each term to the small-scale helicity transport equation has been explored through numerical simulations (Vishniac and Shapovalov, 2014; Ebrahimi and Bhattacharjee, 2014). Vishniac and Shapovalov (2014) find that the advective flux, $\overline{(\mathbf{a}\cdot\mathbf{b})\overline{\mathbf{U}}}$ is the most dominant term in equation (8.4), contributing to about 80% of the helicity flux. The next dominant term be related to $\overline{(\mathbf{a}\cdot\mathbf{u})\overline{\mathbf{B}}}$ is from the Vishniac-Cho flux (Vishniac and Cho, 2001), which is driven through the anisotropy of the turbulence. Apart from this, a term relating to a Fickian diffusion, $\sim \kappa\nabla\alpha_m$ (Kleeorin *et al.*, 2002; Brandenburg, Candelaresi, and Chatterjee, 2009) has been argued to exist on physical and phenomenological grounds. It has been found in direct numerical simulations that $\kappa \approx 0.3\eta_t$ (Mitra *et al.*, 2010; Hubbard, Rheinhardt, and Brandenburg, 2011; Candelaresi *et al.*, 2011). In this chapter, we consider only the advective and diffusive flux terms. The effect of inclusion of the other terms from equation (8.4) will be taken up in later studies.

Usually, α_m is amplified in the dynamo action with opposite sign to α_k which balances the kinetic α-effect leading to saturation of the mean magnetic field. To constraint α_m, we write the transport equation for small-scale helicity density χ using the helicity conservation equation given by (Subramanian and Brandenburg, 2006; Shukurov *et al.*, 2006; Sur, Shukurov, and Subramanian, 2007; Chamandy *et al.*, 2014):

$$\frac{\partial\chi}{\partial t} = -2\boldsymbol{\mathcal{E}}\cdot\overline{\mathbf{B}} - 2\eta\overline{\mathbf{j}\cdot\mathbf{b}} - \nabla\cdot\mathbf{f}, \tag{8.7}$$

where χ is approximately equal to $\overline{\mathbf{a}\cdot\mathbf{b}}$; $\mathbf{a}$ being the vector potential for

$\mathbf{b}$ in the Coulomb gauge. The small-scale flux density is given by $\mathbf{f}$ and $\mathbf{j} = \nabla \times \mathbf{b}$. The small-scale helicity density χ can be related to α_m by arguing that α_m is mainly contributed from the integral scale of turbulence, $l_0 = \dfrac{2\pi}{k_0}$ (Shukurov *et al.*, 2006; Sur, Shukurov, and Subramanian, 2007), which gives $\overline{\mathbf{j} \cdot \mathbf{b}} \simeq l_0^{-2}\overline{\mathbf{a} \cdot \mathbf{b}}$ and $\alpha_m \simeq \dfrac{1}{3}\tau\dfrac{\chi}{\rho l_0^2}$. Introducing a reference (equipartition) magnetic field $B_{eq}^2 \equiv \rho\overline{\mathbf{u}}^2$ and the magnetic Reynolds number as $R_m = \dfrac{\eta_t}{\eta}$, gives $\alpha_m \simeq \dfrac{\eta_t}{l_0^2 B_{eq}^2}\chi$, where $\eta_t \simeq \dfrac{1}{3}\tau\overline{\mathbf{u^2}}$. We can rewrite equation (8.7) in terms of α_m (Sur, Shukurov, and Subramanian, 2007) as

$$\frac{\partial \alpha_m}{\partial t} = -\frac{2\eta_t}{l_0^2}\left(\frac{\boldsymbol{\mathcal{E}} \cdot \overline{\mathbf{B}}}{B_{eq}^2} + \frac{\alpha_m}{R_m}\right) - \nabla \cdot \mathcal{F}. \tag{8.8}$$

Here $\mathcal{F}$ is flux density of α_m taken as (Chamandy *et al.*, 2014):

$$\mathcal{F} = \mathcal{F}_a + \mathcal{F}_d, \tag{8.9}$$

where $\mathcal{F}_a$ is the advective flux density given by (Shukurov *et al.*, 2006; Sur, Shukurov, and Subramanian, 2007; Heald, 2012)

$$\mathcal{F}_a = \overline{\mathbf{U}}\alpha_m, \tag{8.10}$$

and $\mathcal{F}_d$ is the diffusive flux density given by (Kleeorin *et al.*, 2002; Brandenburg, Candelaresi, and Chatterjee, 2009)

$$\mathcal{F}_d = -\kappa\nabla\alpha_m, \quad \kappa \approx 0.3\eta_t. \tag{8.11}$$

As the dynamo operates within the disc, we allow for the large-scale flux to be redistributed by advection in the disc but not escape; the small-scale magnetic helicity flux on the other hand escapes through the vertical efflux. As the adjustment timescale in the corona is much small due to high conductivity, the corona is expected to be in a relaxed force-free state according to Taylor's hypothesis (Taylor, 1974; Mangalam and Subramanian, 1994).

This is also motivated by the corona of the Sun where the magnetic field structure is dominated by nonlinear force-free fields. The strength of field in the corona is much smaller compared to the disc and the precise prescription of the coronal field does not affect the overall results for the disc. We thus adopt an *ansatz*, that the coronal magnetic field can be described by a linear force-free field with a dynamic force-free parameter $\mu(t)$. A global conservation of magnetic helicity then implies that the mean magnetic helicity in the corona, $\overline{H_c}$, grows at the same rate as the loss of magnetic helicity in the disc through helicity fluxes. So, we write the equation for the rate of change of the mean magnetic helicity in the corona as

$$\frac{\mathrm{d}\overline{H_c}}{\mathrm{d}t} = \int (\nabla \cdot \mathbf{f})\, \mathrm{d}V = \int \left(\frac{l_0^2 B_{eq}^2}{\eta_t} \nabla \cdot \mathcal{F} \right) \mathrm{d}V \tag{8.12}$$

where V represents the volume of the corona.

8.3 The dynamo equations

We represent the axisymmetric magnetic field $\overline{\mathbf{B}}$ in terms of their poloidal $\overline{\mathbf{B}}_P$ and toroidal $\overline{\mathbf{B}}_T$ components using the stream functions $\overline{\psi}$ and $\overline{T}$ in the cylindrical coordinates as :

$$\overline{\mathbf{B}}_P = \overline{B_r}\hat{r} + \overline{B_z}\hat{z} = \frac{1}{r}\nabla\overline{\psi} \times \hat{\phi} = \left(\frac{-1}{r}\frac{\partial}{\partial z}\hat{r} + \frac{1}{r}\frac{\partial}{\partial r}\hat{z} \right) \overline{\psi} \equiv \hat{P}\overline{\psi} \tag{8.13}$$

and

$$\overline{\mathbf{B}}_\phi = \frac{\overline{T}}{r}\hat{\phi}. \tag{8.14}$$

Upon substituting equation equations (8.13) and (8.14) in equation (8.2), we get (Mangalam and Subramanian, 1994)

$$\left(\frac{\partial}{\partial t} + \overline{\mathbf{U}}_P \cdot \nabla - \eta_t \Lambda\right) \overline{\psi} = \alpha \overline{T} \tag{8.15}$$

$$\left(\frac{\partial}{\partial t} + \overline{\mathbf{U}}_P \cdot \nabla - \eta_t \Lambda\right) \overline{T} = -\alpha \Lambda \overline{\psi} - \nabla\alpha \cdot \nabla\overline{\psi} + r\nabla\left(\frac{1}{r}\overline{U}_\phi\right) \times \nabla\overline{\psi} - r^2 \overline{T} \nabla \cdot \left(\frac{\overline{U}_P}{r^2}\right) + \nabla\eta_t \cdot \nabla\overline{T} \tag{8.16}$$

where the operator Λ is defined as

$$\Lambda = r^2 \nabla \cdot \left(\frac{\nabla}{r^2}\right) = r\frac{\partial}{\partial r}\left(\frac{1}{r}\frac{\partial}{\partial r}\right) + \frac{\partial^2}{\partial z^2} \tag{8.17}$$

and $\overline{U}_P, \overline{U}_\phi$ are the poloidal and toroidal components of velocity. The right hand side of equation (8.15) represents the generation of poloidal fields from toroidal fields and the right hand side of equation (8.16) contains terms representing generation of toroidal fields from poloidal fields through α-effect, shear, compression, transport and advection of $\overline{T}$ due to varying η_t. The term representing field transport is on the left hand side of both the equations. We consider a mean-flow consisting of differential rotation and vertical advection given as $\overline{\mathbf{U}} = (0, \overline{\mathbf{U}}_\phi, \overline{\mathbf{U}}_z)$, where

$$\overline{\mathbf{U}}_\phi = r\Omega(r); \quad \Omega(r) = \frac{r_0 \Omega_0}{r}. \tag{8.18}$$

This gives $\overline{\mathbf{U}}_\phi = 250$ km s^{-1} = constant, for the values $r_0 = 4$ kpc and Ω_0=62.5 km s^{-1} kpc^{-1}. Since, there is no radial component of velocity, we get $\nabla \cdot \left(\frac{\overline{U}_P}{r^2}\right) = \frac{\partial}{\partial z}\left(\frac{U_z}{r^2}\right)$. We neglect the first and second term in the right hand side (RHS) of equation (8.16) as they are much smaller compared to the shear term, i.e., we take the dynamo to be of the $\alpha - \omega$ type. For mathematical simplification, we also neglect the last term in RHS of equation (8.16) as it is of the order $(z/r)^2$ smaller than the z diffusion terms. Thus

keeping only the dominant terms in the RHS of equations (8.15) and (8.16), we get a simplified set of equations as

$$\left(\frac{\partial}{\partial t}+\overline{U}_z\frac{\partial}{\partial z}-\eta_t\Lambda\right)\overline{\psi} = \alpha\overline{T} \tag{8.19}$$

$$\left(\frac{\partial}{\partial t}+\overline{U}_z\frac{\partial}{\partial z}-\eta_t\Lambda\right)\overline{T} = -r\frac{\mathrm{d}\Omega}{\mathrm{dr}}\frac{\partial\overline{\psi}}{\partial z}-\overline{T}\frac{\partial U_z}{\partial z}. \tag{8.20}$$

In order to estimate the turbulence parameters α and η_t, we investigate two possible scenarios for turbulence in the disc: Magneto-rotational Instability (MRI) driven turbulence and supernovae (SNe) driven turbulence. The details for these cases are given below.

1. *MRI driven turbulence:* Weak magnetic fields can generate turbulence in a differentially rotating disc (Velikhov, 1959; Chandrasekhar, 1960; Balbus and Hawley, 1991). Such a MRI driven turbulence can be responsible for the amplification of magnetic field in the outer parts of the galaxy (Sellwood and Balbus, 1999). The turbulence parameters in this case can then be defined as (Arlt and Rüdiger, 1999)

$$\eta_t=\frac{\mathcal{M}^2h^2}{\tau_{MRI}},\quad \alpha_0=\frac{\mathcal{M}^2h}{\tau_{MRI}}, \tag{8.21}$$

where $\tau_{MRI}=2\pi/\Omega(r)=\dfrac{2\pi r}{r_0\Omega_0}$ is the rotational time period at radius r. Here, the Mach number, $\mathcal{M}$ is calculated as $\mathcal{M}=\dfrac{u}{c}\sim\dfrac{u}{h\Omega(r=h)}$ (Pudritz, 1981; Mangalam and Subramanian, 1994), with u and c being the velocity of turbulence and sound respectively. The half-width of the galactic disc is given by h. Thus, both the turbulence parameters η_t and α_0 vary as $1/r$ over the disc. A similar treatment of turbulence parameters for the case of accretion discs was presented in Pudritz (1981).

2. *SNe driven turbulence:* In this case we adopt the form for η_t and α as

$$\eta_t = \frac{\mathcal{M}^2 h^2}{\tau_{SN}}, \quad \alpha_0 = \frac{l^2}{h\tau_{SN}}, \tag{8.22}$$

where the correlation time τ_{SN} is taken as the time interval between supernova shocks (McKee and Ostriker, 1977; Cox, 1990; Shukurov, 2004). In order to estimate the spatial dependence of τ_{SN}, we proceed as follows. The locations of the SN stars tend to cluster in the regions of intense star formation (known as OB associations). The SNe occurrence is thus related to the star formation rate (SFR), (Shukurov, 2004; Rodrigues *et al.*, 2015). The SFR depends on the density and the dynamics of the interstellar gas, which is represented by a Schmidt power-law relation $R = a\Sigma_g^p$ with the index $p = 1.3 \pm 0.3$ (Schmidt, 1959; Kennicutt, 1989). The mean gas surface density, Σ_g is related to the threshold surface density for gravitational stability, Σ_c, as $\Sigma_g/\Sigma_c \sim 0.7$ (Kennicutt, 1989). For a flat rotation curve, the stability condition gives $\Sigma_c \propto \dfrac{r_0\Omega_0}{r}$ (Toomre, 1964; Cowie, 1981). This implies both Σ_g and SFR can be expected to vary as $1/r^p$, with $p \sim 1$ over the galactic disc. We represent this dependence as

$$1/\tau_{SN} = \nu_{SN}(r) = \frac{r_0\nu_{SN0}}{r} \tag{8.23}$$

where ν_{SN0}=150 km s^{-1}kpc^{-1} is the corresponding frequency at r_0=4 kpc. Substituting equation (8.23) in equation (8.22), we again find (similar to the case for MRI driven turbulence) that both the turbulence parameters η_t and α_0 vary as $1/r$ across the disc.

The energy input from the SNe produces a hot super bubble that can break away from the galactic disc (Tenorio-Tagle, Bodenheimer, and Franco, 1988). This gives rise to the vertical outflow of gas, known as the galactic fountain

(Shapiro and Field, 1976; Shukurov, 2004). The radial variation of this advective flow is dependent on the SNe distribution and thus $\propto$ SFR (Rodrigues *et al.*, 2015). As discussed above, the SFR has a radial dependence of r^p with $p = 1.3 \pm 0.3$. Here for mathematical simplification, we take this variation as $1/r$, which is true for most of the galaxies that fall under 1σ range of this distribution. The vertical advection is taken have the same radial dependence given as

$$U_z = \frac{U_0 r_0}{r}, \tag{8.24}$$

where U_0= 0-2 km s^{-1}. Note that the last term in the RHS of equation (8.20) goes to zero for this choice of U_z. We now write

$$\alpha(z,t) = [\alpha_k(t) + \alpha_m(t)][\theta(z) + \theta(-z)] \tag{8.25}$$

in the most general case, where $\theta(z)$ is the step function. In the steady state, the time dependent part is a constant and we can write $\alpha = \alpha_{sat}$. The kinetic α term can be split into r and z dependent parts as $\alpha_k = \alpha_0(r)\tilde{\alpha}(z)$. It is then convenient to define the following dimensionless parameters

$$R_\alpha = \frac{\alpha_0 h}{\eta_t}, \quad R_\omega = \frac{h^2\Omega}{\eta_t}, \quad R_U = \frac{\overline{U}_z h}{\eta_t}. \tag{8.26}$$

Since the quantities α_0, η_t, Ω and U_z have the similar $1/r$ radial dependence; *all the parameters defined in equation* (8.26) *are nearly independent of r.* This greatly simplifies our formulation. We now rewrite equations (8.19) and (8.20) in dimensionless form through the following substitutions

$$\begin{aligned} \tilde{r} &= \frac{r}{h}, \quad \tilde{z} = \frac{z}{h}, \quad \tau = t\frac{r_0}{h t_d}, \quad \tilde{\alpha} = \frac{\alpha}{\alpha_0} \\ \tilde{T} &= \frac{hT}{\psi_0}, \quad \tilde{\Lambda} = h^2\Lambda, \quad \tilde{\psi} = \frac{\psi}{\psi_0}, \end{aligned} \tag{8.27}$$

where $\psi_0 = B_{eq}h^2$ and $t_d = \dfrac{h^2}{\eta_t(r_0)}$ is the diffusion timescale calculated at radius $r = r_0$. Here $h = 400$ pc is the half-width of the disc; $r_0 = 4$ kpc is

the radius at which parameters are calculated and $R_0 = 16$ kpc is the radius of the galactic disc. The equipartition field strength is taken as $B_{eq} = 5$ μG and the amplitude of α effect is set by α_0 given in Table 8.1. Dropping the tilde for the sake of clarity, we get the dynamo equations in dimensionless form as (see Appendix 8.B for a detailed derivation)

$$\left(r\frac{\partial}{\partial\tau} + R_U\frac{\partial}{\partial z} - \Lambda\right)\psi = R_\alpha\alpha(z)T \tag{8.28a}$$

$$\left(r\frac{\partial}{\partial\tau} + R_U\frac{\partial}{\partial z} - \Lambda\right)T = R_\omega\frac{\partial\psi}{\partial z}. \tag{8.28b}$$

A comparison of timescales of operation and the dynamo parameters for both MRI and SNe driven turbulence scenarios is presented in Table 8.1. As the turbulent parameters in both the cases have similar r dependence, both the processes can be contributing towards the dynamo operation simultaneously. The combined treatment however is beyond the scope of this chapter. We note that the MRI driven dynamo operates at a much slower rate as compared to SNe driven dynamo, and thus the SNe driven dynamo is likely to be the dominant source of magnetic field generation within the galactic disc.

8.4 Solutions to the dynamo equations

8.4.1 Steady-state solutions

In this section, we first analytically solve the global dynamo equations for the steady-state. The full time-dependent solutions are presented in the next subsection.

Source of turbulence	τ_{MRI} or τ_{SN} (Myr)	u (km/s)	c (km/s)	$\mathcal{M}$	l_0 (pc)	η_t (10^{26}cm^2/s)	α_0 (km/s)	R_α	R_ω	R_U	t_d (Myr)
MRI	98	10	40	0.25	100	0.3	0.25	1	16	0-8	155
SN	6.5	10	60	0.167	100	2.05	3.75	2.25	36	0-1.2	23.5

Table 8.1: A comparison of parameters for MRI and SNe driven turbulence with the corresponding timescales. The characteristic time scale for MRI and SNe are given by τ_{MRI} and τ_{SN} respectively. The turbulent velocity and sound speed are denoted by u and c respectively while $\mathcal{M}$ gives the Mach number. The length scale of turbulence and turbulent diffusivity are given by l_0 and η_t respectively while the strength of α effect is set by α_0. The dimensionless dynamo parameters defined in equation (8.26) are given by R_α, R_ω and R_U. The diffusion time scale is given by t_d.

The steady-state solutions are written assuming a separable form such that

$$\psi^s(r,z) = Q(r)a^s(z), \quad T^s(r,z) = Q(r)b^s(z) \tag{8.29}$$

where we have used the superscript s to denote steady-state solutions. Substituting equation (8.29) in equations (8.28a) & (8.28b) with the time derivative term dropped (as we are looking for steady-state solutions), we get the following equations

$$\left[r\frac{\mathrm{d}}{\mathrm{d}r}\left(\frac{1}{r}\frac{\mathrm{d}Q}{\mathrm{d}r}\right)\right]a^s(z) + \left[\frac{\mathrm{d}^2a^s(z)}{\mathrm{d}z^2} - R_U\frac{\mathrm{d}a^s(z)}{\mathrm{d}z} + R_\alpha\left[1+\alpha_m(z)\right]b^s(z)\right]Q = 0 \tag{8.30}$$

$$\left[r\frac{\mathrm{d}}{\mathrm{d}r}\left(\frac{1}{r}\frac{\mathrm{d}Q(r)}{\mathrm{d}r}\right)\right]b^s(z) + \left[\frac{\mathrm{d}^2b^s(z)}{\mathrm{d}z^2} - R_U\frac{\mathrm{d}b^s(z)}{\mathrm{d}z} + R_\omega\frac{\mathrm{d}a^s(z)}{\mathrm{d}z}\right]Q(r) = 0 \tag{8.31}$$

We divide equation (8.30) by $Q(r)a^s(z)$ and equation (8.31) by $Q(r)b^s(z)$,

and combine the resulting equations to get

$$\frac{r}{Q(r)}\frac{\mathrm{d}}{\mathrm{d}r}\left(\frac{1}{r}\frac{\mathrm{d}Q(r)}{\mathrm{d}r}\right) = \frac{-1}{a^s(z)}\left[\frac{\mathrm{d}^2a^s(z)}{\mathrm{d}z^2} - R_U\frac{\mathrm{d}a^s(z)}{\mathrm{d}z} + R_\alpha\left[1+\alpha_m(z)\right]b^s(z)\right]$$
$$= -\frac{1}{b^s(z)}\left[\frac{\mathrm{d}^2b^s(z)}{\mathrm{d}z^2} - R_U\frac{\mathrm{d}b^s(z)}{\mathrm{d}z} + R_\omega\frac{\mathrm{d}a^s(z)}{\mathrm{d}z}\right] = -\gamma^s. \tag{8.32}$$

Since the left-hand side (LHS) of equation (8.32) is a function of only variable r while its right-hand side (RHS) is function of only variable z, the equality can hold only when both the sides are actually equal to a constant (taken to be $-\gamma^s$). Rearranging the terms in equation (8.32), we get the following set of equations (cf. Mangalam and Subramanian, 1994)

$$\frac{\mathrm{d}^2Q_n(r)}{\mathrm{d}r^2} - \frac{1}{r}\frac{\mathrm{d}Q_n(r)}{\mathrm{d}r} = -\gamma_n^sQ_n(r) \tag{8.33}$$

$$\frac{\mathrm{d}^2a_n^s(z)}{\mathrm{d}z^2} - R_U\frac{\mathrm{d}a_n^s(z)}{\mathrm{d}z} + R_\alpha[1+\alpha_m(z)]b_n^s(z) = \gamma_n^sa_n^s(z) \tag{8.34}$$

$$\frac{\mathrm{d}^2b_n^s(z)}{\mathrm{d}z^2} - R_U\frac{\mathrm{d}b_n^s(z)}{\mathrm{d}z} + R_\omega\frac{\mathrm{d}a_n^s(z)}{\mathrm{d}z} = \gamma_n^sb_n^s(z) \tag{8.35}$$

where we have introduced the subscript n to represent a set of solutions $\{Q_n(r),\, a_n(z),\, b_n(z)\}$ for a given value of local growth rate γ_n^s which satisfy the radial and vertical boundary conditions. Upon substituting $Q_n(r) = rf_n(r)$, equation (8.33) becomes

$$\frac{\mathrm{d}^2f_n}{\mathrm{d}r^2} + \frac{1}{r}\frac{\mathrm{d}f_n}{\mathrm{d}r} + \left(\gamma_n^s - \frac{1}{r^2}\right)f_n = 0, \tag{8.36}$$

which is the well known Bessel's equation and the general solution for $\gamma_n^s > 0$ is given by

$$Q_n(r) = rJ_1\left(\sqrt{\gamma_n^s}r\right) \equiv rJ_n^s(r). \tag{8.37}$$

From equation (8.35), we obtain

$$b_n^s(z) = -\left(\frac{\mathrm{d}^2}{\mathrm{d}z^2} - R_U\frac{\mathrm{d}}{\mathrm{d}z} - \gamma_n^s\right)^{-1}R_\omega\frac{\mathrm{d}a_n^s}{\mathrm{d}z}, \tag{8.38}$$

which is substituted into equation (8.34) to get the following differential equation for $a_n^s(z)$ (cf. Mangalam and Subramanian, 1994)

$$\frac{\mathrm{d}^4 a_n^s}{\mathrm{d}z^4} - 2R_U \frac{\mathrm{d}^3 a_n^s}{\mathrm{d}z^3} + (R_U^2 - 2\gamma_n^s)\frac{\mathrm{d}^2 a_n^s}{\mathrm{d}z^2} + [2R_U\gamma_n^s - (1+\alpha_m)R_\alpha R_\omega]\,\frac{\mathrm{d}a_n^s}{\mathrm{d}z} + (\gamma_n^s)^2 a_n^s = 0. \tag{8.39}$$

The above fourth-order differential equation can be solved by expanding a_n^s in terms of four eigenfunctions with eigenvalues λ_{nj}, given as

$$a_n^s(z) = \sum_{j=1}^{4} c_{nj} \exp(\lambda_{nj} z). \tag{8.40}$$

Substituting equation (8.40) in equation (8.39), we get a fourth-order equation for λ_{nj} given by

$$\lambda_{nj}^4 - 2R_U\lambda_{nj}^3 + (R_U^2 - 2\gamma_n^s)\lambda_{nj}^2 + [2R_U\gamma_n^s - (1+\alpha_m)R_\alpha R_\omega]\,\lambda_{nj} + (\gamma_n^s)^2 = 0. \tag{8.41}$$

The solutions to dynamo equations within the galactic disc critically depend on the boundary conditions and the eigenfunctions present in the corona. Here, we are consider a scenario in which a corona continuously forms around the galactic disc during the course of dynamo action due to the contributions from the small-scale magnetic helicity fluxes as given in equations (8.10) and (8.11). We assume that the magnetic field topology in the infinitely conducting corona quickly relaxes into a force-free field, which minimizes the energy while conserving the global magnetic helicity (Woltjer, 1960; Taylor, 1974; Finn and Antonsen, 1983; Berger and Field, 1984; Mangalam and Krishan, 2000). Following the treatment in (Mangalam and Subramanian, 1994), we consider that the coronal magnetic field follows the linear force-free field configuration with a parameter μ (which has no spatial dependence). Thus, we write the following equations for the coronal magnetic field

$$\nabla \times \mathbf{B} = \mu \mathbf{B}, \quad \nabla \cdot \mathbf{B} = 0. \tag{8.42}$$

Here $\mu = 0$ corresponds to the vacuum field outside the disc, which is a likely initial condition. In the course of dynamo action, as the corona builds up , we expect $|\mu|$ to take higher non-zero values. Taking the curl of equation (8.42), we get

$$\nabla^2 \mathbf{B} = -\mu^2 \mathbf{B}. \tag{8.43}$$

Splitting the above equation into poloidal (ψ_c) and toroidal (T_c) components using the definitions given in equations (8.13) & (8.14), we can write

$$\Lambda\psi_c = -\mu^2\psi_c \tag{8.44}$$

$$\Lambda T_c = -\mu^2 T_c, \tag{8.45}$$

where Λ is defined in equation (8.17). We have added a subscript c to distinguish the coronal fields from the fields generated in the disc. The derivations for equations (8.44) & (8.45) are given in Appendix A of Mangalam and Subramanian (1994). The general solutions to these equations are given in §3.3.1 (Mangalam and Subramanian, 1994)

$$\psi_c(r,z) = \int a(p)\exp(-\sqrt{p^2-\mu^2}|z|)rJ_1(pr)\mathrm{d}p, \tag{8.46}$$

$$T_c(r,z) = \int b(q)\exp(-\sqrt{q^2-\mu^2}|z|)rJ_1(qr)\mathrm{d}q, \tag{8.47}$$

where the amplitudes are related by $b(k) = \mu a(k)$, which follows from the force-free condition given in equation (8.42). For a finite disc of radius R_0, and under the condition that the solution goes to zero at $r = R_0$, the functions ψ_c and T_c can be written in discrete form given by (Mangalam and Subramanian, 1994)

$$\psi_c(r,z) = \sum_{n=1}^{N} e_n r J_1(k_n r)\exp\left(-\sqrt{k_n^2-\mu^2}|z|\right), \quad T_c(r,z) = \mu\psi_c(r,z), \tag{8.48}$$

where e_n are the coefficients to be evaluated from the boundary conditions and $k_n r_0$ are the zeros of Bessel J_1. Due to the symmetry of the solutions

about the mid-plane of the disc, we solve the equation only for the upper half of the disc and use the symmetry for the lower half solution. A description of the boundary conditions written for the upper disc surface is given below. The continuity of the radial component of the magnetic field, $B_r = -\frac{1}{r}\frac{\partial \psi}{\partial z}$, at the top boundary would mean that both ψ and $\frac{\partial \psi}{\partial z}$ are continuous at $z = 1$. This is written as

$$[\psi](1) = 0 \tag{8.49a}$$

$$\left[\frac{\partial \psi}{\partial z}\right](1) = 0 \tag{8.49b}$$

where the square bracket indicates continuity of the function across the boundary. Since the field generated in the disc connect to the linear force-free at the surface, the amplitudes of a_n and b_n satisfy the same conditions (given in equations 8.46 & 8.47) at the boundary. Thus

$$b_n(1) = \mu a_n(1). \tag{8.50}$$

The equatorial boundary conditions specify the symmetry of the solution. For the quadrupolar mode, we write

$$\psi(0) = 0 \tag{8.51a}$$

$$\frac{\partial T}{\partial z}(0) = 0. \tag{8.51b}$$

and for the dipolar mode we write

$$\frac{\partial \psi}{\partial z}(0) = 0 \tag{8.52a}$$

$$T(0) = 0 \tag{8.52b}$$

From equations (8.37) & (8.48), we find that the radial part of ψ has the same functional form for both the disc and the corona. The requirement of continuity of ψ at the boundary (equation 8.49a), which is valid even

as $r \to 0$, implies that only one term survives in the summation given in equation (8.48), which satisfies the condition $k_n = \sqrt{\gamma_n^s}$. Thus, equation (8.48) can now takes the form

$$\psi_c(r,z) = \sum_{n=1}^{N} e_n r J_1\left(\sqrt{\gamma_n^s} r\right) \exp\left(-\sqrt{\gamma_n^s - \mu^2}|z|\right), \quad T_c(r,z) = \mu\psi_c(r,z), \tag{8.53}$$

Upon substituting the expressions for ψ and T in the disc (equations 8.29, 8.37, 8.40) and the corona (equation 8.53) in the boundary conditions for quadrupolar symmetry (equations 8.49-8.51), we find that the radial part cancels out and the following equations are obtained for the four eigenfunctions of a_n^s (see Appendix 8.C for details)

$$\sum_{j=1}^{4} \left(\lambda_{nj} + \sqrt{\gamma_n^s - \mu^2}\right) c_{nj} \exp(\lambda_{nj}) = 0 \tag{8.54a}$$

$$\sum_{j=1}^{4} \mu \left[R_\alpha(1+\alpha_m) + \lambda_{nj}^2 - R_U\lambda_{nj} - \gamma_n^s\right] c_{nj} \exp(\lambda_{nj}) = 0 \tag{8.54b}$$

$$\sum_{j=1}^{4} c_{nj} = 0 \tag{8.54c}$$

$$\sum_{j=1}^{4} \left(\gamma_n^s \lambda_{nj} + R_U\lambda_{nj}^2 - \lambda_{nj}^3\right) c_{nj} = 0. \tag{8.54d}$$

The above set of equations can be written in a compact form as $\tilde{O}\tilde{C} = 0$, where $\tilde{O}$ is a 4×4 matrix comprising of the coefficients c_{nj} in equation (8.54) and $\tilde{C}$ is a 4×1 column vector comprising of c_{nj}. The condition for non-trivial solutions demand that the determinant of $\tilde{O}$ vanishes, Det $\tilde{O} = 0$ (cf. Appendix B in Mangalam and Subramanian, 1994). This condition is used to evaluate γ_n^s as a function of inputs α_m and μ. Since the scale of coefficients is arbitrary, we can set $c_{n4} = 1$, without loss of generality and solve for the other coefficients using the first three equations in (8.54).

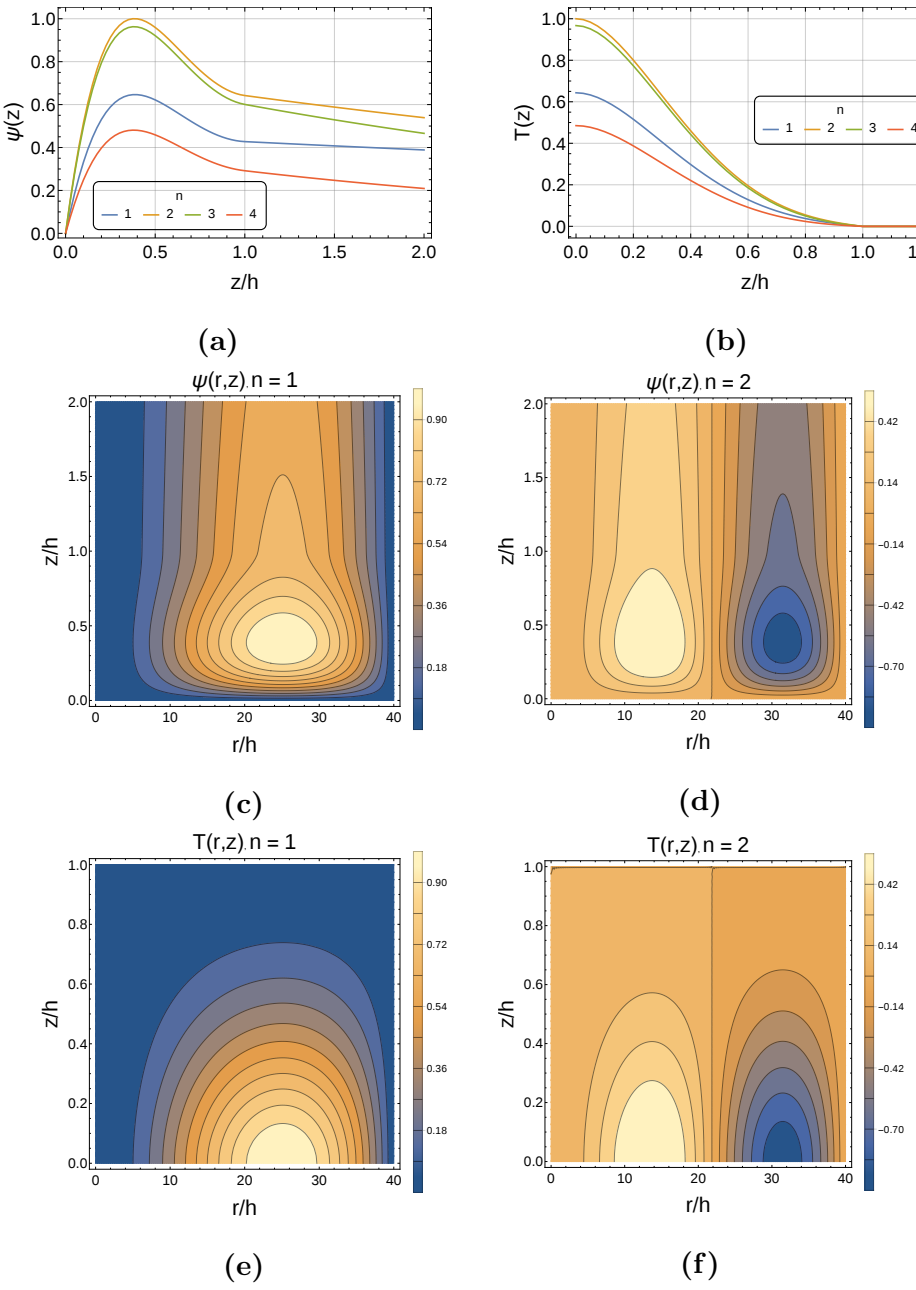

Figure 8.1: Normalized vertical cross sections of the stream functions ψ and T for different values of n and advective flux $R_U = 0.3$ at a radius of 4 kpc are shown in panel (a) and (b). Panels (c) and (d) represent the meridional contour plots of ψ for n= 1 & 2 respectively whereas panels (e) and (f) represent the same for T. The contour plots are normalized with respect to the corresponding value of n=1 so as to compare their relative strengths of the quantities.

The steady state solutions for advective flux $R_U = 0.3$ and $\mu(\sim \sqrt{\gamma_1^s}) = -0.01$ are presented in Figure 8.1 for illustration. A detailed study of the parametric dependence of time-dependent dynamo solutions constructed using these steady-state solution is presented in a later section. The vertical distribution of ψ and T for different values of parameter n at a radius, $r = 4$ kpc are shown in Fig. 8.1a & 8.1b. The plots are scaled with respect to the maximum value of ψ and T at $n = 2$ so as to compare the relative strengths of the different modes. The field lines are evidently continuous across the vertical boundary ($z = 1$). For all the cases in Fig. 8.1a, the stream function ψ peaks around $z = 0.4h$ and then falls off with increase in height. The strengths of the different radial modes are comparable with $n = 2$ being the most dominant mode at $r = 4$ kpc. The poloidal current T, shown in Fig. 8.1b starts with its maximum strength at the mid plane which then falls off sharply with increase in height. The value of T is negligible outside the disc as the force-free parameter μ is very small. Thus the force-free fields in the halo are very close to potential fields. The variation of ψ and T with both r and z, for n =1 & 2 are shown in Figs. 8.1c - 8.1f. The contour plots have been normalized with respect to its corresponding maximum value for $n = 1$ so as to compare the strength of the two modes. The mode n corresponds to the number of oscillations in the radial direction. In both the cases the strength of the $n = 1$ mode is higher than $n = 2$. The quadrupolar nature of the fields are quite evident from the contour plots.

8.4.2 Time-dependent formulation

It is easy to see that, under the closure principle offered by the Sturm-Liouville theory and the no-z approximation, the radial behavior will be a linear combination of the various radial modes obtained for the steady case.

Retaining the time-dependence in the z part of the solutions, We express the time-dependent ψ and T as

$$\psi(r,z,\tau;\alpha,\mu) = \sum_{n=1}^{N} w_n(\tau)Q_n(r)a_n(z;\alpha,\mu) \tag{8.55a}$$

$$T(r,z,\tau;\alpha,\mu) = \sum_{n=1}^{N} w_n(\tau)Q_n(r)b_n(z;\alpha,\mu) \tag{8.55b}$$

where $Q_n(r)$ represents the radial part of the steady-state solutions; $a_n(z;\alpha,\mu)$ and $b_n(z;\alpha,\mu)$ explicitly depend on z and implicitly on time through α and μ. Upon substituting equation (8.55) in equation (8.28a), we get

$$\sum_{n=1}^{N}\Big[r\dot{w}_nQ_na_n + rw_nQ_n\left\{\left(\frac{\partial a_n}{\partial\alpha}\right)\dot{\alpha} + \left(\frac{\partial a_n}{\partial\mu}\right)\dot{\mu}\right\} + R_Uw_nQ_na_n' \\ -w_n(\Lambda_rQ_n)a_n - w_nQ_n(\Lambda_za_n) - R_\alpha(1+\alpha_m)w_nQ_nb_n\Big] = 0. \tag{8.56}$$

where $\dot{w}_n = \dfrac{\mathrm{d}w_n}{\mathrm{d}\tau}$, $\dot{\alpha} = \dfrac{\mathrm{d}\alpha}{\mathrm{d}\tau}$, $\dot{\mu} = \dfrac{\mathrm{d}\mu}{\mathrm{d}\tau}$, $a_n'(z) = \dfrac{\mathrm{d}a_n}{\mathrm{d}z}$; Λ_r and Λ_z are the r and z dependent parts of operator Λ defined in equation (8.17). We neglect the terms containing partial derivatives of a_n with respect to α and μ as they are small compared to the derivatives with respect to z. We have checked this by evaluating these terms numerically and thus these assumptions have been justified a posteriori. Dividing equation (8.56) throughout with $w_nQ_na_n$, we get upon rearranging

$$\left[\sum_{n=1}^{N}\frac{[\Lambda_za_n(z,\tau)]}{a_n(z,\tau)} - \frac{R_Ua_n'(z,\tau)}{a_n(z,\tau)} + R_\alpha(1+\alpha_m)\frac{b_n(z,\tau)}{a_n(z,\tau)}\right] \\ = \left[\sum_{n=1}^{N}\frac{r\dot{w}_n(\tau)}{w_n(\tau)} - \frac{[\Lambda_rQ_n(r)]}{Q_n(r)}\right] = \sum_{n=1}^{N}\gamma_n(\tau). \tag{8.57}$$

Since the left-hand side is function of (r,τ) and the right-hand side is function of (z,τ), the equality is satisfied only if both are equal to $\gamma_n(\tau)$, which depends only on τ. Following similar steps with equations (8.28b) & (8.55),

we obtain

$$\left[\sum_{n=1}^{N}\frac{[\Lambda_z b_n(z,\tau)]}{b_n(z,\tau)}-\frac{R_U b_n'(z,\tau)}{b_n(z,\tau)}+R_\omega\frac{a_n'(z,\tau)}{b_n(z,\tau)}\right]$$
$$=\left[\sum_{n=1}^{N}\frac{r\dot{w}_n(\tau)}{w_n(\tau)}-\frac{[\Lambda_r Q_n(r)]}{Q_n(r)}\right]=\sum_{n=1}^{N}\gamma_n(\tau). \tag{8.58}$$

Combining equations (8.57) & (8.58), we obtain the following set of equations

$$\sum_{n=1}^{N}\frac{r\dot{w}_n(\tau)}{w_n(\tau)}-\frac{[\Lambda_r Q_n(r)]}{Q_n(r)}-\gamma_n(\tau)=0 \tag{8.59a}$$
$$\sum_{n=1}^{N}\frac{[\Lambda_z a_n(z,\tau)]}{a_n(z,\tau)}-R_U\frac{a_n'(z,\tau)}{a_n(z,\tau)}+R_\alpha(1+\alpha_m)\frac{b_n(z,\tau)}{a_n(z,\tau)}-\gamma_n(\tau)=0 \tag{8.59b}$$
$$\sum_{n=1}^{N}\frac{[\Lambda_z b_n(z,\tau)]}{b_n(z,\tau)}-R_U\frac{b_n'(z,\tau)}{b_n(z,\tau)}+R_\omega\frac{a_n'(z,\tau)}{b_n(z,\tau)}-\gamma_n(\tau)=0 \tag{8.59c}$$

The last two equations in equation (8.59) are same as that in equations (8.34) and (8.35), except that γ_n now changes with time. Hence $a_n(z,\tau)$ and $b_n(z,\tau)$ can be calculated using the same steps as followed in §8.4.1 for the instantaneous value of γ_n. Multiplying equation (8.59a) by $w_n Q_n$, we get

$$\sum_{n=1}^{N}[r\dot{w}_n Q_n-w_n(\Lambda_r Q_n)-\gamma_n(\tau)w_n Q_n]=0. \tag{8.60}$$

Substituting $\Lambda_r Q_n=-\gamma_n^s Q_n$ from equation (8.33) in equation (8.60), we get

$$\sum_{n=1}^{N}\left[r\dot{w}_n+[\gamma_n^s-\gamma_n(\tau)]w_n\right]Q_n=0. \tag{8.61}$$

Now substituting for $Q_n(r)$ in the previous equation using equation (8.37) we get

$$\sum_{n=1}^{N}[rJ_n^s\dot{w}_n+[\gamma_n^s-\gamma_n(\tau)]J_n^s w_n]=0. \tag{8.62}$$

Multiplying both sides with J_m^s and using the orthogonality property of Bessel functions, we get the following equation after integrating over r

$$\sum_{n=1}^{N} \langle J_m^s | r J_n^s \rangle \dot{w}_n + \langle J_m^s | J_n^s \rangle [\gamma_n^s - \gamma_n(\tau)] w_n = 0, \tag{8.63}$$

where the orthogonality of Bessel functions give

$$\langle J_m^s | r J_n^s \rangle = \int_0^{R_0} r J_m^s J_n^s \mathrm{d}r = \delta_{n,m} \frac{R_0^2}{2} J_2^2(\sqrt{\gamma_n^s} R_0) \tag{8.64}$$

and $\langle J_m^s | J_n^s \rangle = \int_0^{R_0} J_m^s J_n^s \mathrm{d}r$. Here R_0 represents the radius of the disc in units of h.

8.5 Time dependence of α and coronal helicity

To obtain an equation for the evolution of α_m with time, we first calculate the divergence of the small-scale helicity fluxes given in equations (8.10) & (8.11). The divergence of the advective flux density obtained using equations (8.10), (8.18) & (8.24) is given by

$$\nabla \cdot \mathcal{F}_a = \nabla \cdot (\overline{\mathbf{U}} \alpha_m) = \frac{\partial}{r \partial \phi}(r \omega \alpha_m) + \frac{\partial}{\partial z}(U_0 \alpha_m). \tag{8.65}$$

The first term in the RHS of the equation (8.65) goes to zero due to axisymmetry and since U_0 is assumed to be independent of z, we get

$$\nabla \cdot \mathcal{F}_a = U_0 \frac{\partial \alpha_m}{\partial z}. \tag{8.66}$$

From equation (8.11), we can write

$$\nabla \cdot \mathcal{F}_\kappa = -\nabla \cdot (\kappa \nabla \alpha_m) = -0.3 \nabla \cdot (\eta_t \nabla \alpha_m). \tag{8.67}$$

Evaluating $\nabla \cdot (\eta_t \nabla \alpha_m)$ separately, we write

$$\nabla \cdot (\eta_t \nabla \alpha_m) = \eta_t \nabla^2 \alpha_m + \nabla \alpha_m \cdot \nabla \eta_t. \tag{8.68}$$

Since the z derivatives dominate over the r derivatives, we can write $\eta_t \nabla^2 \alpha_m \approx \eta_t \dfrac{\partial^2 \alpha_m}{\partial z^2}$. Also, the second term in the right-hand side of equation (8.68), $\nabla \alpha_m \cdot \nabla \eta_t \left(\sim \dfrac{\alpha_m \eta_t}{h R_0} \right)$ is small compared to the first term, $\eta_t \nabla^2 \alpha_m \left(\sim \dfrac{\alpha_m \eta_t}{h^2} \right)$ and can be neglected. Thus equation (8.67) can now be written as

$$\nabla \cdot \mathcal{F}_\kappa = -0.3 \eta_t \frac{\partial^2 \alpha_m}{\partial z^2} = -\kappa \frac{\partial^2 \alpha_m}{\partial z^2}. \tag{8.69}$$

The helicity transport equation along with the flux terms can now be written by combining equations (8.8), (8.66) & (8.69) as

$$\frac{\partial \alpha_m}{\partial t} = \frac{-2\eta_t}{l_0^2} \left(\frac{\alpha \overline{B^2} - \eta_t \overline{\mathbf{J} \cdot \mathbf{B}}}{B_{eq}^2} + \frac{\alpha_m}{R_m} \right) - U_0 \frac{\partial \alpha_m}{\partial z} + \kappa \frac{\partial^2 \alpha_m}{\partial z^2}. \tag{8.70}$$

Rescaling equation (8.70) using the relations given in equation (8.27), we write

$$\frac{r_0 \eta_t(r_0) \alpha_0}{h^3} \frac{\partial \tilde{\alpha}_m}{\partial \tau} = -\frac{2\eta_t}{l_0^2} \left(\alpha_0 \tilde{\alpha} \overline{\tilde{B}^2} - \frac{\eta_t(r)}{h} \overline{\tilde{\mathbf{J}} \cdot \tilde{\mathbf{B}}} + \frac{\alpha_0 \tilde{\alpha}_m}{R_m} \right) - \frac{U_0 \alpha_0 \tilde{\alpha}_m}{h} - \frac{\kappa \alpha_0 \tilde{\alpha}_m}{h^2} \tag{8.71}$$

where $\tilde{\mathbf{B}} = \dfrac{\mathbf{B}}{B_{eq}}$ and $\tilde{\mathbf{J}} = \dfrac{h\mathbf{J}}{B_{eq}}$. We have also used the 'no-z' approximation (Subramanian and Mestel, 1993; Moss, 1995; Chamandy *et al.*, 2014) for the z derivatives of α, setting $\dfrac{\partial}{\partial z} \to \dfrac{1}{h}$ and $\dfrac{\partial^2}{\partial z^2} \to \dfrac{-1}{h^2}$. Multiplying equation (8.71) by the factor $\dfrac{h^2}{\alpha_0 \eta_t(r)}$, we obtain

$$\frac{r_0}{h} \left[\frac{\eta_t(r_0)}{\eta_t(r)} \right] \frac{\partial \tilde{\alpha_m}}{\partial \tau} = -2 \left(\frac{h}{l_0} \right)^2 \left[\tilde{\alpha} \overline{\tilde{B}^2} - \left(\frac{\eta_t}{\alpha_0 h} \right) \overline{\tilde{\mathbf{J}} \cdot \tilde{\mathbf{B}}} + \frac{\tilde{\alpha}_m}{R_m} \right] - \left(\frac{U_0 h}{\eta_t} - \frac{\kappa}{\eta_t} \right) \tilde{\alpha}_m. \tag{8.72}$$

Using $\tilde{\alpha} = 1 + \tilde{\alpha_m}$, equation (8.108) and the definitions given in equation (8.26), we write equation (8.72) as

$$r \frac{\mathrm{d}\alpha_m}{\mathrm{d}\tau} = -C \left[(1 + \alpha_m) \overline{B^2} - R_\alpha^{-1} \overline{\mathbf{J} \cdot \mathbf{B}} \right] - (R_U + R_\kappa) \alpha_m, \tag{8.73}$$

where

$$C = 2\left(\frac{h}{l_0}\right)^2, \quad R_\kappa = \frac{\kappa}{\eta_t}. \tag{8.74}$$

We have dropped the tildes for clarity and also neglected the $\dfrac{\alpha_m}{R_m}$ term in the above equation as it is very small, $\sim 10^{-5}$ times compared to the other terms (Sur, Shukurov, and Subramanian, 2007). In order to get an equation for dynamical evolution of α_m, we take a spatial average equation (8.73) over the entire volume of the disc, which removes the r dependence from the equation. The resulting equation can now be written as

$$\langle r\rangle \frac{\mathrm{d}\alpha_m}{\mathrm{d}\tau} = -C\left[(1+\alpha_m)\langle\overline{B^2}\rangle - R_\alpha^{-1}\langle\overline{\mathbf{J}\cdot\mathbf{B}}\rangle\right] - (R_U + R_\kappa)\alpha_m, \tag{8.75}$$

where the angular brackets represent volume averaging. Now

$$\langle r\rangle = \frac{2}{R_0^2}\int_0^{R_0} r^2 \mathrm{d}r = \frac{2R_0}{3}, \tag{8.76}$$

and the expressions for $\langle\overline{B^2}\rangle$ and $\langle\overline{\mathbf{J}\cdot\mathbf{B}}\rangle$ are given by (see Appendix 8.D for details)

$$\langle\overline{B^2}\rangle = \left[J_2^2(\sqrt{\gamma_n^s}R_0)\langle a_n'^2 + b_n^2\rangle + \gamma_n^s J_0^2(\sqrt{\gamma_n^s}R_0)\langle a_n^2\rangle\right] w_n^2 \tag{8.77}$$

$$\langle\overline{\mathbf{J}\cdot\mathbf{B}}\rangle = \left[J_2^2(\sqrt{\gamma_n^s}R_0)\langle a_n' b_n' + a_n'' b_n - \gamma_n^s a_n b_n\rangle + \gamma_n^s J_0^2(\sqrt{\gamma_n^s}R_0)\langle a_n b_n\rangle\right] w_n^2. \tag{8.78}$$

Thus we write equation (8.73) in compact form as

$$\frac{\mathrm{d}\alpha_m}{\mathrm{d}\tau} = -\frac{3C}{2R_0}\left[(1+\alpha_m)\langle\overline{B^2}\rangle - R_\alpha^{-1}\langle\overline{\mathbf{J}\cdot\mathbf{B}}\rangle\right] - \frac{3}{2R_0}(R_U + R_\kappa)\alpha_m. \tag{8.79}$$

As discussed in §8.2, the small-scale dynamo operation builds up a corona around the disc by releasing small-scale helicity flux across the boundary. The expression for coronal field (equation 8.48) along with the boundary condition given in equation (8.49) can be written as

$$\sum_{n=1}^{N} w_n r J_1\left(\sqrt{\gamma_n^s}r\right) a_n(1) = \sum_{n=1}^{N} e_n r J_1\left(\sqrt{\gamma_n^s}r\right)\exp\left(-\sqrt{\gamma_n^s - \mu^2}\right). \tag{8.80}$$

Comparing coefficients of $J_1\left(\sqrt{\gamma_n^s}r\right)$ on both sides, we get

$$e_n(t) = w_n(t)a_n(1)\exp\left(\sqrt{\gamma_n^s - \mu(t)^2}\right), \tag{8.81}$$

which gives the dynamical evolution of the coronal field with time. In order to compare the helicity of the coronal field, we use the prescription given in Low (2006, 2011) which gives the measure of helicity as (see Appendix 8.E for details)

$$\overline{H_c} = \int \frac{2\psi_c T_c}{r^2}\mathrm{d}V = \int \frac{2\mu\psi_c^2}{r^2}\mathrm{d}V. \tag{8.82}$$

Substituting equations (8.53) & (8.81) in equation (8.82), we obtain

$$\begin{aligned}\overline{H_c} \;=\; & \sum_{n,m=1}^{N} 4\pi\mu e_n e_m \int_0^{R_0} J_1(\sqrt{\gamma_n^s}r)J_1(\sqrt{\gamma_m^s}r)r\mathrm{d}r \\ & \int_1^{\infty} \exp(-\sqrt{\gamma_n^s - \mu^2}z)\exp(-\sqrt{\gamma_m^s - \mu^2}z)\mathrm{d}z \end{aligned} \tag{8.83}$$

Substituting Using the orthogonality property of Bessel functions given in equation (8.64), we can simplify equation (8.83) as

$$\overline{H_c} = \sum_{n=1}^{N} 2\pi\mu e_n^2 R_0^2 J_2^2(\sqrt{\gamma_n^s}R_0)\int_1^{\infty}\exp(-2\sqrt{\gamma_n^s - \mu^2}z)\mathrm{d}z. \tag{8.84}$$

The z integral in equation (8.84) can easily be solved as

$$\int_1^{\infty}\exp(-2\sqrt{\gamma_n^s - \mu^2}z)\mathrm{d}z = \left.\frac{\exp(-2\sqrt{\gamma_n^s - \mu^2}z)}{-2\sqrt{\gamma_n^s - \mu^2}}\right|_1^{\infty} = \frac{\exp(-2\sqrt{\gamma_n^s - \mu^2})}{2\sqrt{\gamma_n^s - \mu^2}} \tag{8.85}$$

Thus combining equations (8.84) & (8.85), we get

$$\overline{H_c}(t) = \sum_{n=1}^{N}\pi\mu(t)e_n^2(t)R_0^2 J_2^2(\sqrt{\gamma_n^s}R_0)\frac{\exp(-2\sqrt{\gamma_n^s - \mu^2(t)})}{\sqrt{\gamma_n^s - \mu^2(t)}}. \tag{8.86}$$

Combining equation (8.81) with equation (8.86), we get

$$\overline{H_c}(t) = \sum_{n=1}^{N}\pi\mu(t)w_n^2(t)a_n^2(1)R_0^2\frac{J_2^2(\sqrt{\gamma_n^s}R_0)}{\sqrt{\gamma_n^s - \mu^2(t)}}. \tag{8.87}$$

The equation for coronal helicity is given by equation (8.12) as

$$\frac{\mathrm{d}\overline{H_c}}{\mathrm{d}t} = \int \left(\frac{l_0^2 B_{eq}^2}{\eta_t} \nabla \cdot \mathcal{F} \right) \mathrm{d}V. \tag{8.88}$$

Combining equations (8.9), (8.66) & (8.69) with the above equation, and reducing the above equation in dimensionless form using the transformations given in equation (8.27), we get (see Appendix 8.F for details)

$$\frac{\mathrm{d}\overline{H_c}}{\mathrm{d}\tau} = \frac{2\pi R_0^2}{rC} R_\alpha (R_U - R_\kappa) \alpha_m. \tag{8.89}$$

Now volume averaging equation (8.89) and noting

$$\left\langle \frac{1}{r} \right\rangle = \frac{2}{R_0} \int_0^{R_0} \mathrm{d}r = 2, \tag{8.90}$$

we get the final equation as

$$\frac{\mathrm{d}\overline{H_c}}{\mathrm{d}\tau} = \frac{4\pi R_0^2}{C} \left(R_U R_\alpha + R_\kappa R_\alpha \right) \alpha_m \tag{8.91}$$

The above equation gives the dynamical evolution of the coronal helicity H_c.

We now list out equations (8.63), (8.79) and (8.91) together, which are to be solved simultaneously to study the non-linear time evolution of the dynamo:

$$\begin{aligned}
&\sum_{n=1}^{N} \langle J_m^s | r J_n^s \rangle \dot{w}_n + \langle J_m^s | J_n^s \rangle (\gamma_n^s - \gamma_n) w_n = 0 \\
&\frac{\mathrm{d}\alpha_m}{\mathrm{d}\tau} = -\frac{3C}{2R_0} \left[(1 + \alpha_m) \langle \overline{B^2} \rangle - R_\alpha^{-1} \langle \overline{\mathbf{J} \cdot \mathbf{B}} \rangle \right] - \frac{3}{2R_0} (R_U + R_\kappa) \alpha_m \\
&\frac{\mathrm{d}\overline{H_c}}{\mathrm{d}\tau} = \frac{4\pi R_0^2}{C} R_\alpha (R_U - R_\kappa) \alpha_m
\end{aligned} \tag{8.92}$$

8.6 Solutions of time-dependent dynamo equations

In this section, we present a summary of our simulations for the global nonlinear dynamo using the turbulence parameters are taken from the SNe driven

scenario presented in Table 8.1.

8.6.1 Evolution and saturation of the dynamo with time

To study the effect of advective and diffusive flux on the saturated field strength B_{sat}, we vary the vertical advection velocity, U_0 in the range 0-2 kms^{-1} and the diffusive flux R_κ is taken to be (= 0, 0.15 or 0.3). The quantities $B_{sat}, \alpha_{m,sat}$ presented here refer to their volume averaged values. The following are the key results:

1. We find that in all the cases, there is an initial brief phase of rapid growth (t =0-5, in units of t_d) when the magnetic field grows exponentially with time (see, Fig. 8.2a & 8.2a). This represents the kinematic regime of dynamo operation where $\alpha_m = 0$ (see, Fig. 8.2c & 8.2d). As α_m decreases rapidly from zero in the range t = 5-20 (as compared to the constant $\alpha_k = 1$), hence the total α effect also initially decreases with time. The dynamo starts getting quenched and reaches saturation around t=40, when the field strength is in equipartition with the turbulent kinetic energy ($\sim B_{eq}$). This is in agreement with the results from numerical simulations presented in Gressel, Bendre, and Elstner (2013) & Chamandy *et al.* (2014). The final saturation value of α_m is around -0.9 which corresponds to a net $\alpha = 0.1$ (10% of the initial value).

2. Due to the transport of the small-scale helicity from the disc to the corona, the helicity of the corona grows with time carrying the same sign as that of the small scale fields. As seen from Fig. 8.2e & 8.2f, in the kinematic phase, when $\alpha_m = 0$, there is no helicity flux and hence

helicity of the coronal field is zero. It then grows rapidly for non-zero α_m between $t = 5 - 20$. When α_m saturates (around $t \geq 20$), the helicity in the corona grows at a constant rate which is proportional to the net flux $(R_U + R_\kappa)$.

3. In the absence of the fluxes ($R_U = R_\kappa = 0$), we find that the field initially grows in the kinematic regime to a strength of $\sim 0.2 B_{eq}$ (Sur, Shukurov, and Subramanian, 2007), but once the α-quenching becomes operative, it catastrophically decays to nearly zero field strength (see Fig. 8.2a). As expected, the helicity in corona remains zero throughout for this case. In all other cases, the saturated value of the field proportional to the net flux, i.e. the saturated mean field strength is higher for higher values of R_U and R_κ (the field is assumed to be saturated at $t = t_{sat}$ when it reaches 95% of its values $t = 100$).

4. For the plausible case of $U_0 = 0.5 - 1$ kms^{-1} ($R_U = 0.3 - 0.6$), we obtain a saturated field strength of $\sim$ 1-1.6 B_{eq} depending upon of value of R_κ used (see Table 8.2 for details of saturated values of B and α_m for different parameters and the corresponding timescales). This is in good agreement with the field strengths reported in observations (Beck, 2012; Van Eck *et al.*, 2014) The timescale needed for saturation in this case is from a seed field of 10^{-3} μG to the equipartition field strength is about 1 Gyr.

5. The seed field taken here is $d_1 = d_2 = d_3 = d_4 = 10^{-3} B_{eq}$ at $t = 0$ (equation 8.55). We have also explored different choices of seed fields, like taking pure $n = 1$ and pure $n = 2$ field. The different choices of seed field do not affect the results as all cases show a similar behavior after the initial exponential growth phase. The relative field strengths

of the different modes for the case of $R_U = 0.3$ and $R_\kappa = 0$ are shown in Fig. 8.3. Here we find that the most contribution is coming from the second and third radial mode, while the highest mode ($n = 4$) contributes the least. We have also checked the solutions with higher values of n (till $n = 6$ for a smaller range in R_U and R_κ), and the results are qualitatively similar as the higher orders do not contribute much. Since we are computationally constrained, we have thus used solutions till $n = 4$ for most of the analysis.

6. We also find in Fig. 8.2a that the growth rate, γ of the magnetic field is directly proportional to R_U (for a given R_κ). This is true even in the kinematic regime. To illustrate the dependence of γ on the advective flux R_U, we use the kinematic solutions of the dynamo equation (obtained by solving only equations 8.33-8.35 with $\alpha_m = 0$) for a larger range of R_U (till R_U=20). This is shown in Fig. 8.4. We find that the growth rate increases with R_U for smaller values (R_U= 0-5) till a maximum value of $R_U = 5$ is reached and then it decreases monotonically for higher values of R_U. Since, we have used only low values of R_U between 0-1.2, we find that in our cases that the flux term helps the dynamo to operate faster. Brandenburg *et al.* (1992, 1993) have also reported similar results in their numerical simulations where the dynamo action is enhanced by the aid of galactic winds.

8.6.2 Distribution of the field across the disc

Here we discuss the structure of the saturated magnetic field and its distribution across the disc and the halo.

1. The distribution of the poloidal component of the field can be inferred

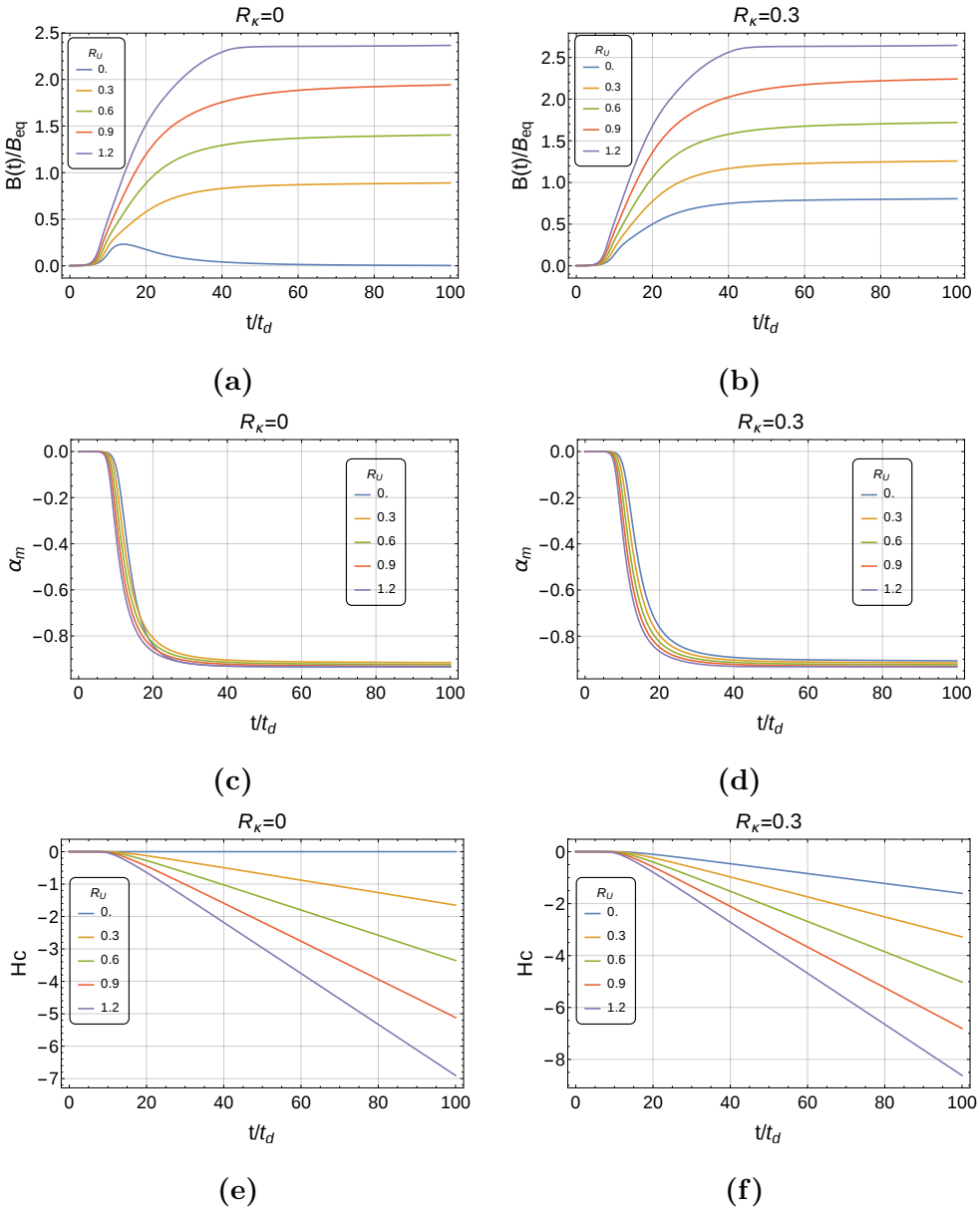

Figure 8.2: The evolution of the magnetic field (normalized with respect to the equipartition field strength), α_m and helicity of the corona H_c with time are shown in the first, second and third row respectively for different values of R_U. The left and the right panel are evaluated for $R_\kappa = 0$ and 0.3 respectively. The time t is in units of the diffusion timescale t_d (=23.5 Myr).

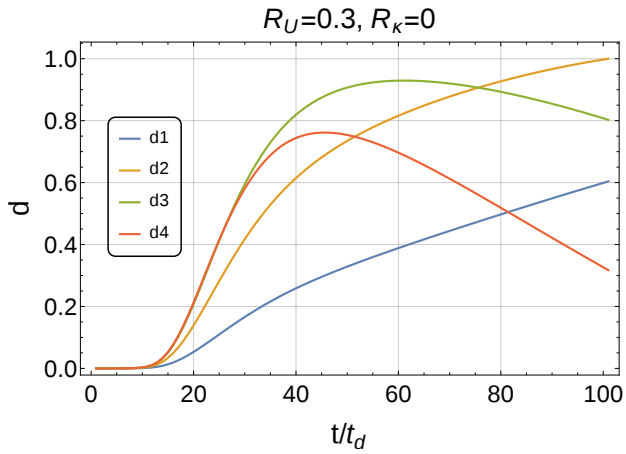

Figure 8.3: Relative strengths of the different expansion coefficients d in equation (8.55) for the case of $R_U = 0.3$ and $R_\kappa = 0$ are shown as a function of time. The initial condition for the simulation was taken as $d_1 = d_2 = d_3 = d_4 = 10^{-3} B_{eq}$ at $t = 0$

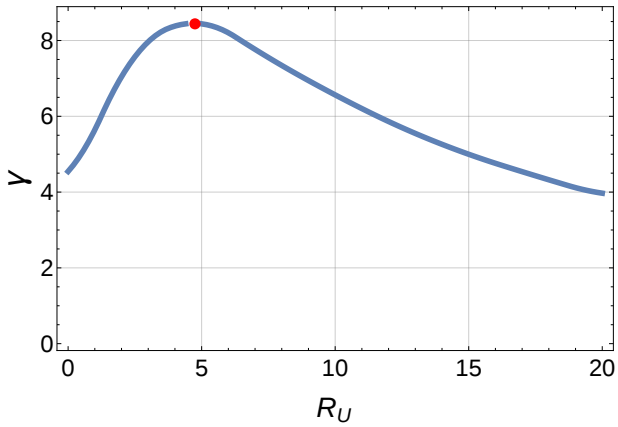

Figure 8.4: The variation of the local growth rate γ shown as a function of the advective flux R_U. The range for R_U in our simulations is 0-1.2, where γ increases linearly with R_U. However, after $R_U = 5$ (shown by the red dot), this behavior changes and γ decreases with increase in R_U.

R_U	R_κ	$t_{sat}(Gyr)$	$B_{sat}(B_{eq})$	$\alpha_{m,sat}(\alpha_0)$
0.00	0.00	2.347	0.00	-0.93
0.00	0.15	1.016	0.54	-0.90
0.00	0.30	1.052	0.76	-0.90
0.30	0.00	1.044	0.85	-0.91
0.30	0.15	1.058	1.03	-0.91
0.30	0.30	1.067	1.19	-0.91
0.60	0.00	1.112	1.33	-0.92
0.60	0.15	1.117	1.49	-0.92
0.60	0.30	1.121	1.63	-0.92
0.90	0.00	1.194	1.84	-0.93
0.90	0.15	1.197	1.99	-0.93
0.90	0.30	1.200	2.13	-0.93
1.20	0.00	.879	2.25	-0.93
1.20	0.15	.881	2.38	-0.93
1.20	0.30	.883	2.51	-0.93

Table 8.2: The saturated timescales t_{sat} with corresponding values of B^2 and α listed for different input values for R_U and R_κ. The quantities mentioned in the table refer to their global averages over the volume of the disc.

from the plots of the magnetic stream function ψ, as shown in Fig. 8.5. Here, we discuss first discuss the one dimensional (1-D) cross-section for comparison with results presented in previous 1-D calculations and also present the complete 3-D axisymmetric solutions using contour plots. In Fig. 8.5a & 8.5b we show the dependence of ψ on z for different values of R_U and R_κ at r=4 kpc. The continuity of the field lines across the boundary is clearly seen. We find that the strength of ψ increases with advection and diffusion. The complete variation of ψ for

two cases $R_U = 0.3, R_\kappa = 0$ and $R_U = 1.2, R_\kappa = 0.3$ are shown in Fig. 8.5c & 8.5d. These plots can be inferred as the shape of the poloidal component of the magnetic field. We also see oscillations in the radial field as contributions from higher values of n in equation (8.55). The effect of advection is also clearly evident in the stretching of field line in the vertical direction.

2. The variation of poloidal current, T with disc height z at a radius of 4 kpc is shown in Fig. 8.6a & 8.6b. The poloidal current decreases in strength as we move away from the disc center. The poloidal current becomes negligibly small outside disc ($z > 1$). The radial variation of T within the disc can be seen from the contour plots in Fig. 8.6c & 8.6d. The contour plots are shown only till $z = 1$, since the fields outside the disc are negligibly small. We again find oscillations in the field due to contribution from higher modes in the radial function (as seen in case of ψ). We also find that the contribution from higher modes is more pronounced in Fig. 8.6d where the fluxes are greater as compared to Fig. 8.6c.

3. The variation of all three components of the magnetic field, B_r, B_ϕ and B_z with disc height z is explicitly shown in Fig. 8.7 for different values of advective and diffusive fluxes. Fig. 8.7a & 8.7b depict the radial component of the field. The radial component of the field changes sign near the disc, which is necessary condition for the dynamo to operate (Ruzmaikin, Sokolov, and Shukurov, 1988), so that the sign of the flux leaving through the surface is opposite to that of the flux in the mid plane. The strength of B_r increases with the amount of flux leaving the surface, but the height at which B_r changes sign is almost same

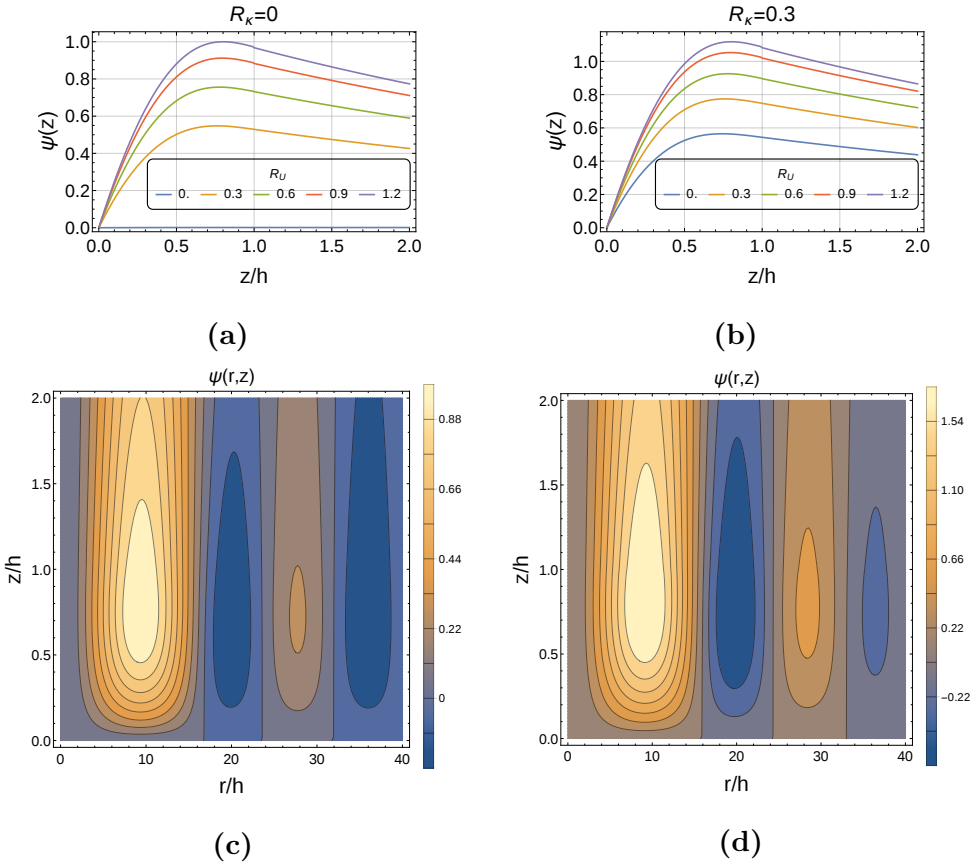

Figure 8.5: Vertical cross sections of the magnetic stream function ψ for different values of the advective flux R_U and diffusive flux R_κ at a radius of 4 kpc are shown in panel (a) and (b). $z = 1$ represents the height of the disc. Panel (a) and (b) have been scaled with respect to the maximum value of ψ for $R_U = 1.2$, $R_\kappa = 0$. Panel (c) and (d) represent the meridional contour plots of ψ for different advective fluxes; panel (c) corresponds to $R_U = 0.3$ and $R_\kappa = 0$ where as panel (d) corresponds to $R_U = 1.2$ and $R_\kappa = 0$. The contour plots are normalized with respect to the maximum value of the field in panel (c) so as to compare their relative strengths.

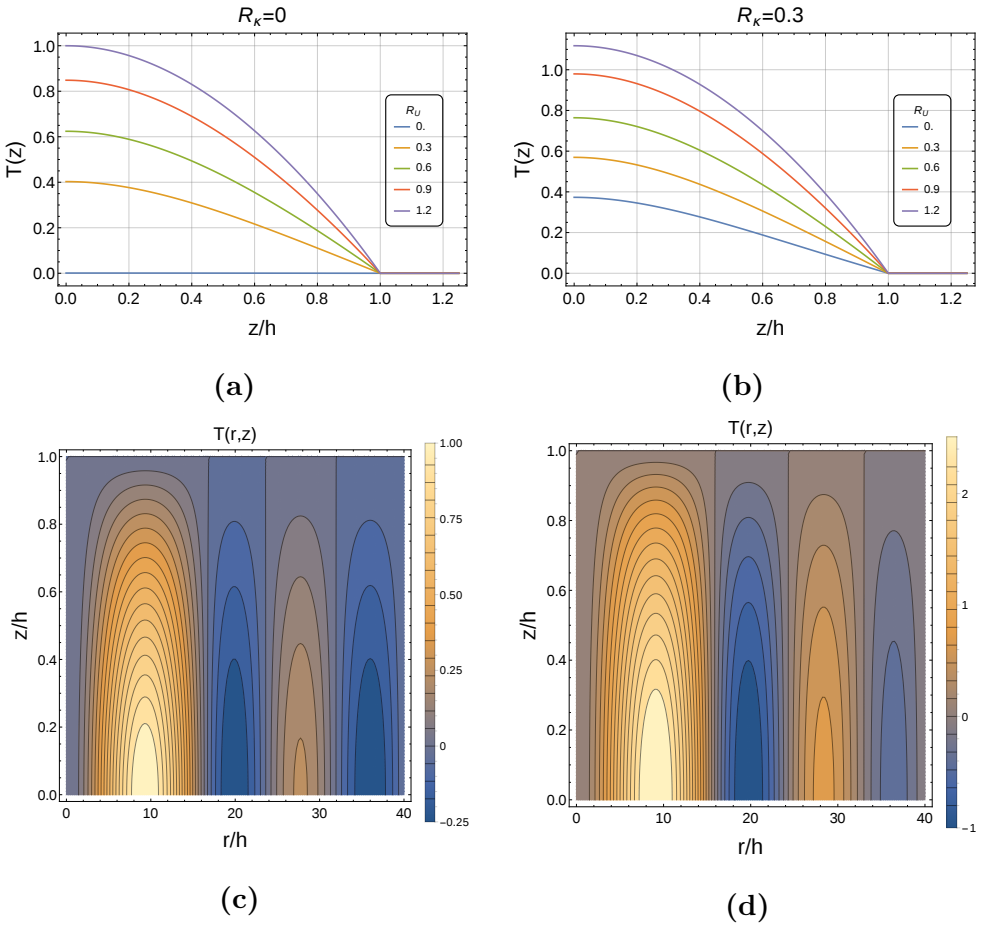

Figure 8.6: Vertical cross sections of the stream function T for different values of the advective flux R_U and diffusive flux R_κ at a radius of 4 kpc are shown in panel (a) and (b). The height of the disc is represented by $z = 1$. Panel (a) and (b) have been scaled with respect to the maximum value of ψ for $R_U = 1.2$, $R_\kappa = 0$. Panel (c) and (d) represent the meridional contour plots of T for different advective fluxes; panel (c) corresponds to $R_U = 0.3$ and $R_\kappa = 0$ where as panel (d) corresponds to $R_U = 1.2$ and $R_\kappa = 0$. The contour plots are normalized with respect to the maximum value of the field in panel (c) so as to compare their relative strengths.

in all the cases. The azimuthal component is depicted is Fig. 8.7c & 8.7d. The ratio of strength of the azimuthal and the radial component is in general of the order $\sim [R_\omega/R_\alpha(1+\alpha_m)]^{1/2}$ (as seen in the plots). The strength of the azimuthal field decreases with height and tends to zero near the disc surface (as also inferred from Fig. 8.6). Finally, the vertical component of the magnetic field is shown in Fig. 8.7e & 8.7f. The strength of B_z component is found to be much weaker compared to B_r and B_ϕ.

4. The magnetic pitch angle, defined as

$$p = \tan^{-1}(B_r/B_\phi) = \frac{-\sum_{n=1}^{4} w_n(t) Q_n^s(r) a_n'(z)}{\sum_{n=1}^{4} w_n(t) Q_n^s(r) b_n(z)}, \tag{8.93}$$

and the variation with height for different values of R_U and R_κ are shown in Fig. 8.8a & 8.8b. The pitch angle is found to be around -7° at the mid plane where as the observed values are close to -20° (Fletcher, 2010). It might be possible to obtain higher values for the pitch angle by incorporating mean radial flows (Moss, Shukurov, and Sokoloff, 2000) or by invoking spiral shocks (Van Eck *et al.*, 2014). We plan to investigate these effects in future attempts. Since B_r and B_ϕ have opposite sign at the mid plane (see Fig. 8.7), the pitch angle is negative at the mid plane, decreases in magnitude with height and becomes positive near the surface (when B_r changes sign). This means that the magnetic spiral which is trailing within the disc starts leading near the surface. This is in agreement with what has been previously reported in Chamandy *et al.* (2014) and is expected in a model with outflows and corona (Ruzmaikin *et al.*, 1979; Ji *et al.*, 2014).

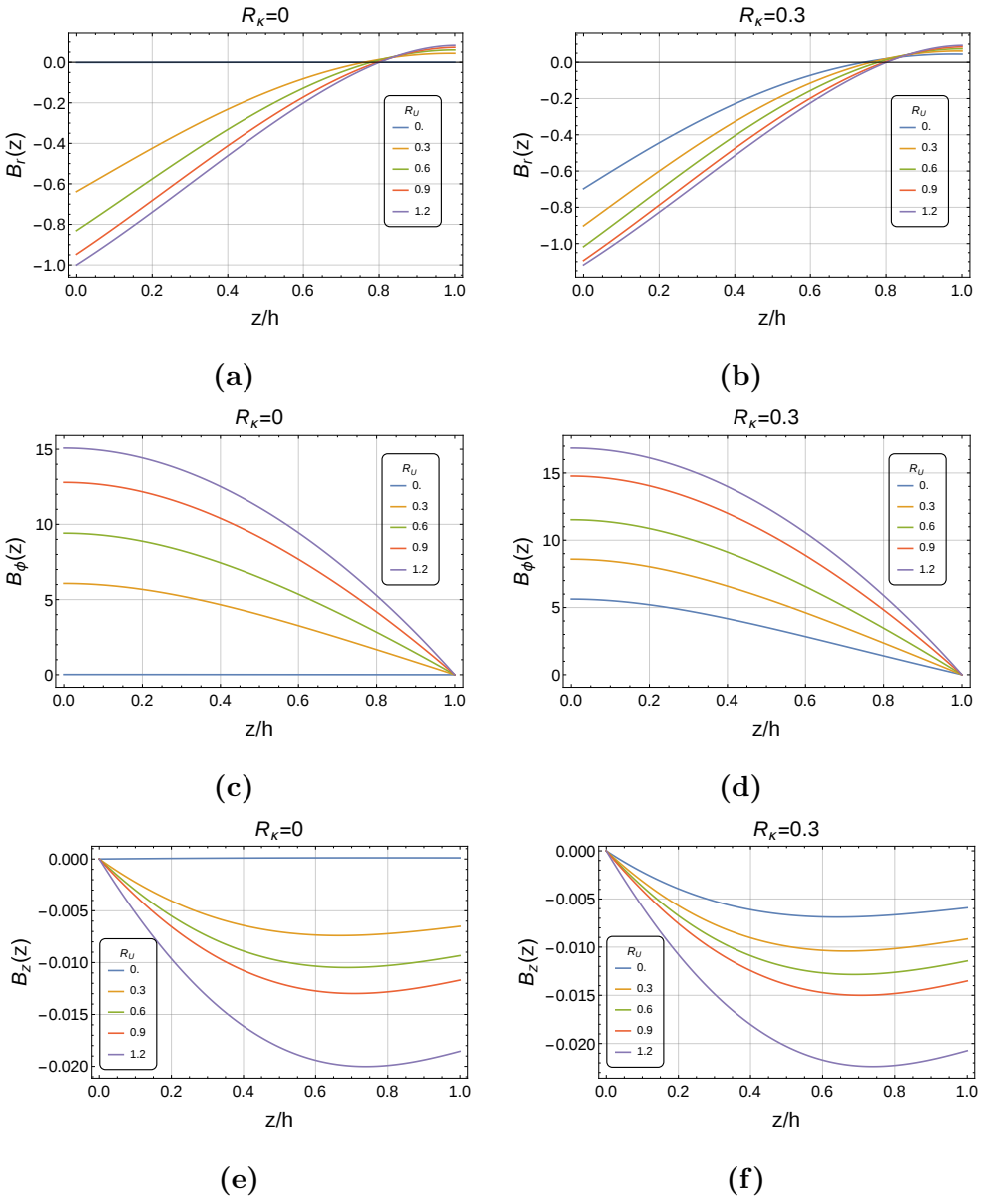

Figure 8.7: Magnetic field B_r, B_ϕ and B_z are shown as a function of z for different values of R_U and R_κ at a radius of 4 kpc. The values are normalized with respect to the maximum value of B_r for the case of $R_U = 1.2$, $R_\kappa = 0$. The sign of B_r, B_ϕ and B_z is arbitrary but their relatives sign are fixed in accordance with equations (8.28a) & (8.28b).

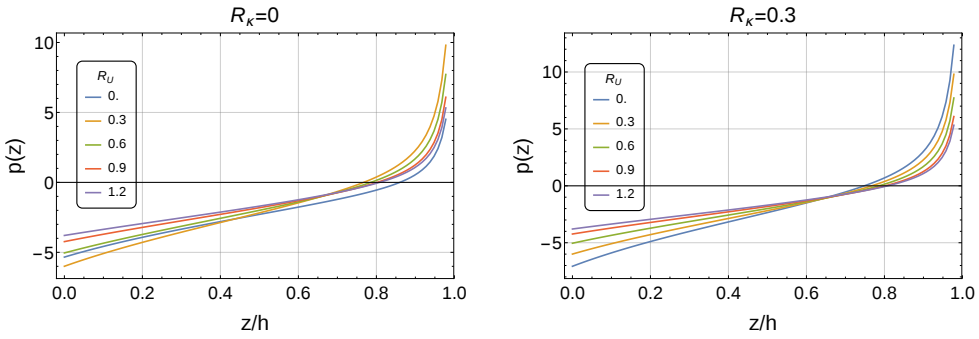

(a) **(b)**

Figure 8.8: The variation of the pitch angle, $p = \tan^{-1}(B_r/B_\phi)$ is shown as a function of disc height z at a radius of 4 kpc. The galactic mid plane and disc surface are given by $z = 0$ and $z = 1$ respectively. The left and the right panels represent $R_\kappa = 0$ & 0.3 respectively. The different values of the advective flux R_U are given in the figure legend.

8.7 Summary and conclusions

We have developed a global semi-analytic 3D model for the dynamo operation in a galaxy with a corona. The model includes small-scale (advective and diffusive) helicity fluxes that transfer magnetic helicity from the disc to the corona and prevent the catastrophic quenching of the dynamo. The effect of these helicity fluxes on the nonlinear saturation of the dynamo is also demonstrated from the strength and structure of the global saturated magnetic field. Here we summarize and highlight the novel features of this work

1. We have incorporated the radial dependence in the SNe (and MRI) driven turbulence parameters and have shown that all these parameters, α, Ω, η_t and U_z have similar radial variation ($\propto 1/r$). Thus the dynamo parameters R_α, R_ω and R_U defined in equation (8.26) are

nearly independent of r. This leads to a great simplification in our formulation and the dynamo equations (8.28a) & (8.28b) take the same dimensionless form for both SNe and MRI driven turbulence.

2. A comparison of the timescales of dynamo operation for SNe and MRI driven turbulence is presented in Table 8.1. We find that the SNe driven dynamo operates at a much faster rate than the MRI driven dynamo and hence the magnetic field generation in the disc is likely to be dominated by SNe driven turbulence. As the combined treatment of both SNe and MRI driven turbulence is beyond the scope of this treatment, we have used only the SNe driven turbulence parameters for our analysis.

3. We solve the dynamo equations in the disc for the global steady-state solutions which are matched to a linear force-free field in the corona (§8.4.1). These global analytic solutions allow us to calculate the global relative helicity for both the disc and the corona.

4. We have presented an analysis of the relative helicity flux terms in Appendix 8.A. We include the advective and diffusive fluxes for the work presented in this chapter and plan to explore the contribution from other terms in future.

5. We solve the full time-dependent problem in §8.4.2 by expanding the time-dependent magnetic field in a basis obtained from the steady-state solutions. We obtain quadrupolar solutions for the saturated magnetic field strength, $B(\sim B_{eq})$, which is proportional to the advective and diffusive fluxes leaving the surface, see Table 8.2. For the plausible values of vertical outflow U_z = 0.5-1 kms^{-1} at a radius of 4 kpc, we obtain a mean field strength of $B_{sat} = 5-7\mu$G, which is close to what is

reported in numerical simulations (Gressel, Bendre, and Elstner, 2013; Chamandy *et al.*, 2014) and in observations (Beck, 2012; Van Eck *et al.*, 2014). The timescale for the dynamo saturation is found to be around 1 Gyr, which is comparable to galactic lifetime.

6. Through the dynamo operates the small-scale helicity fluxes slowly build up the corona with a helicity that carries the same sign as that of the small-scale helicity fluxes, see Fig. 8.2e & 8.2f. In absence of the flux terms ($R_U = R_\kappa = 0$), we find that the mean field initially grows to a maximum value of $\sim 0.2 B_{eq}$ in the kinematic phase and then is catastrophically quenched (see Fig. 8.2a). This confirms the crucial role of the helicity fluxes for the dynamo operation (Sur, Shukurov, and Subramanian, 2007).

7. The radial and vertical distribution of the field across the disc are shows there is a reversal sign as we move radially outward from the disc center (Fig. 8.5 & 8.6). B_r changes sign with variation in z towards the surface (Fig. 8.7) which leads to the magnetic pitch angle also changing sign near the surface (starting from a value of -7° at the mid plane) as shown in Fig. 8.8. This feature was previously reported in Chamandy *et al.* (2014) and is expected in a model with outflows and corona (Ruzmaikin *et al.*, 1979; Ji *et al.*, 2014).

In future, we plan to work on a hybrid model for the dynamo with a simultaneous treatment of both SNe and MRI driven turbulence. We also plan to include a more realistic model for the coronal field that involves details of the helicity dissipation by reconnection in the corona. The contribution from the remaining small- and large- scale helicity flux terms (apart from advective and diffusive fluxes) in equations (8.3) and (8.4) need to be explored in order

to study its effect on the saturation of the dynamo.

Appendix

8.A Magnetic helicity dynamics

The induction equation is given by

$$\frac{\partial \mathbf{B}}{\partial t} = \nabla \times (\mathbf{U} \times \mathbf{B} - \eta \nabla \times \mathbf{B}) \,. \tag{8.94}$$

The mean-field component of the induction equation is given by:

$$\frac{\partial \overline{\mathbf{B}}}{\partial t} = \nabla \times \left(\overline{\mathbf{U}} \times \overline{\mathbf{B}} - \eta \nabla \times \overline{\mathbf{B}} + \boldsymbol{\mathcal{E}}\right) . \tag{8.95}$$

Uncurling equation (8.95), we get

$$\frac{\partial \overline{\mathbf{A}}}{\partial t} = \overline{\mathbf{U}} \times \overline{\mathbf{B}} - \eta \nabla \times \overline{\mathbf{B}} + \boldsymbol{\mathcal{E}} + \nabla \varphi_1 \tag{8.96}$$

where φ_1 is a scalar function. In order to calculate the temporal evolution of large-scale helicity $\overline{H} = \int \overline{\mathbf{A}} \cdot \overline{\mathbf{B}} \mathrm{d}V$, we first take the time-derivative of its density

$$\partial_t(\overline{\mathbf{A}} \cdot \overline{\mathbf{B}}) = 2\partial_t \overline{\mathbf{A}} \cdot \overline{\mathbf{B}} + \nabla \cdot (\partial_t \overline{\mathbf{A}} \times \overline{\mathbf{A}}) = 2\boldsymbol{\mathcal{E}} \cdot \overline{\mathbf{B}} - 2\eta \overline{\mathbf{J}} \cdot \overline{\mathbf{B}} + 2\nabla \cdot (\varphi_1 \overline{\mathbf{B}}) + \nabla \cdot (\partial_t \overline{\mathbf{A}} \times \overline{\mathbf{A}}) \tag{8.97}$$

where $\partial_t \overline{\mathbf{A}} \times \overline{\mathbf{A}} = \left(\overline{\mathbf{U}} \times \overline{\mathbf{B}} - \eta \overline{\mathbf{J}} + \boldsymbol{\mathcal{E}} + \nabla \varphi_1\right) \times \overline{\mathbf{A}}$. The volume average of equation (8.97) now gives the equation for the evolution of large scale helicity, $\overline{H}$ (Mangalam, 2008)

$$\frac{\mathrm{d}\overline{H}}{\mathrm{d}t} = 2 \int \boldsymbol{\mathcal{E}} \cdot \overline{\mathbf{B}} \mathrm{d}V - 2 \int \eta \overline{\mathbf{J}} \cdot \overline{\mathbf{B}} \mathrm{d}V - \oint \mathbf{F} \cdot \hat{n} \mathrm{d}S, \tag{8.98}$$

where $\hat{n}$ represents the normal to the surface S enclosing volume V and

$$\mathbf{F} = (\eta\overline{\mathbf{J}} - \overline{\mathbf{U}} \times \overline{\mathbf{B}} - \boldsymbol{\mathcal{E}} - \nabla\varphi_1) \times \overline{\mathbf{A}} - 2\varphi_1\overline{\mathbf{B}}, \tag{8.99}$$

is the large-scale helicity flux. Similarly, for the evolution of the mean small-scale helicity $H' = \int \overline{\mathbf{a} \cdot \mathbf{b}} \mathrm{d}V$, we first note that the time derivative of small-scale magnetic field obtained from subtracting equation (8.95) from equation (8.94) is given by

$$\partial_t \mathbf{b} = \nabla \times (\mathbf{u} \times \overline{\mathbf{B}} + \overline{\mathbf{U}} \times \mathbf{b} + \mathbf{u} \times \mathbf{b} - \boldsymbol{\mathcal{E}} - \eta\mathbf{j}) \tag{8.100}$$

Uncurling equation (8.100), we get

$$\partial_t \mathbf{a} = \mathbf{u} \times \overline{\mathbf{B}} + \overline{\mathbf{U}} \times \mathbf{b} + \mathbf{u} \times \mathbf{b} - \boldsymbol{\mathcal{E}} - \eta\mathbf{j} + \nabla\varphi_{\mathbf{2}}. \tag{8.101}$$

The time derivative of the small-scale helicity density $\chi = \overline{\mathbf{a} \cdot \mathbf{b}}$ is then given by

$$\partial_t(\overline{\mathbf{a} \cdot \mathbf{b}}) = 2\overline{\partial_t \mathbf{a} \cdot \mathbf{b}} + \nabla \cdot \overline{\partial_t \mathbf{a} \times \mathbf{a}}. \tag{8.102}$$

Using equation (8.101), we get

$$\partial_t(\overline{\mathbf{a} \cdot \mathbf{b}}) = -2\boldsymbol{\mathcal{E}} \cdot \overline{\mathbf{B}} - 2\eta\overline{\mathbf{j} \cdot \mathbf{b}} + 2\nabla \cdot \overline{(\varphi_2 \mathbf{b})} + \nabla \cdot (\overline{\partial_t \mathbf{a} \times \mathbf{a}}). \tag{8.103}$$

The volume average of equation (8.103), now gives us the equation for the evolution of the mean small scale helicity, H' as

$$\frac{\mathrm{d}H'}{\mathrm{d}t} = -2\int \boldsymbol{\mathcal{E}} \cdot \overline{\mathbf{B}} \mathrm{d}V - 2\int \eta\overline{\mathbf{j} \cdot \mathbf{b}} \mathrm{d}V - \oint \mathbf{f} \cdot \hat{n} \mathrm{d}S, \tag{8.104}$$

where the $\mathbf{f} = -\overline{\partial_t \mathbf{a} \times \mathbf{a}} - 2\overline{\varphi_2 \mathbf{b}}$ represents the surface flux terms which can be expanded in detail as

$$\begin{aligned} \mathbf{f} \;=\; & \overline{(\mathbf{a} \cdot \overline{\mathbf{B}})\mathbf{u}} - \overline{(\mathbf{a} \cdot \mathbf{u})\overline{\mathbf{B}}} - \overline{(\mathbf{a} \cdot \overline{\mathbf{U}})\mathbf{b}} + \overline{(\mathbf{a} \cdot \mathbf{b})\overline{\mathbf{U}}} - \overline{(\mathbf{a} \cdot \mathbf{u})\mathbf{b}} + \overline{(\mathbf{a} \cdot \mathbf{b})\mathbf{u}} \\ & + \overline{\boldsymbol{\mathcal{E}} \times \mathbf{a}} + \eta\overline{\mathbf{j} \times \mathbf{a}} - \overline{\nabla\varphi_2 \times \mathbf{a}} - 2\overline{\varphi_2 \mathbf{b}}. \end{aligned} \tag{8.105}$$

8.B Derivation of equation (8.26)

We start with equation (8.19) given by

$$\left(\frac{\partial}{\partial t}+\overline{U}_z\frac{\partial}{\partial z}-\eta_t(r)\Lambda\right)\overline{\psi}=\alpha\overline{T} \tag{8.106}$$

where we have explicitly mentioned the r dependence of η_t. Now substituting the variables using the transformations given in equation (8.27), we get

$$\left(\frac{r_0\eta_t(r_0)}{h^3}\frac{\partial}{\partial\tau}+\frac{\overline{U}_z}{h}\frac{\partial}{\partial\tilde{z}}-\frac{\eta_t(r)}{h^2}\tilde{\Lambda}\right)\psi_0\tilde{\psi}=\tilde{\alpha}\alpha_0\frac{\psi_0\tilde{T}}{h}, \tag{8.107}$$

where we have used $t_d=h^2/\eta_t(r_0)$. Dividing the above equation throughout with $\dfrac{\psi_0\eta_t(r)}{h^2}$, we get

$$\left[\frac{r_0}{h}\left(\frac{\eta_t(r_0)}{\eta_t(r)}\right)\frac{\partial}{\partial\tau}+\left(\frac{\overline{U}_z h}{\eta_t(r)}\right)\frac{\partial}{\partial\tilde{z}}-\tilde{\Lambda}\right]\tilde{\psi}=\left(\frac{\alpha_0 h}{\eta_t(r)}\right)\tilde{\alpha}\tilde{T}. \tag{8.108}$$

Since $\eta_t(r)\propto 1/r$ (from equations 8.22 & 8.23), we can write

$$\left(\frac{\eta_t(r_0)}{\eta_t(r)}\right)=\frac{r}{r_0}. \tag{8.109}$$

Using definitions of R_U and R_α from equation (8.26) and $\tilde{r}=r/h$, we write equation (8.108) as

$$\left(\tilde{r}\frac{\partial}{\partial\tau}+R_U\frac{\partial}{\partial\tilde{z}}-\tilde{\Lambda}\right)\tilde{\psi}=R_\alpha\tilde{\alpha}\tilde{T}. \tag{8.110}$$

Similarly, we rewrite equation (8.20) as

$$\left(\frac{\partial}{\partial t}+\overline{U}_z\frac{\partial}{\partial z}-\eta_t\Lambda\right)\overline{T}=\Omega\frac{\partial\overline{\psi}}{\partial z} \tag{8.111}$$

where we have used $\Omega(r)=\dfrac{r_0\Omega_0}{r}$. Substituting the dimensionless variables from equation (8.27) in the above equation, we get

$$\left(\frac{r_0\eta_t(r_0)}{h^3}\frac{\partial}{\partial\tau}+\frac{\overline{U}_z}{h}\frac{\partial}{\partial\tilde{z}}-\frac{\eta_t(r)}{h^2}\tilde{\Lambda}\right)\frac{\psi_0\tilde{T}}{h}=\frac{\Omega\psi_0}{h}\frac{\partial\tilde{\psi}}{\partial\tilde{z}}. \tag{8.112}$$

Following the same steps as taken after equation (8.107), we get the final form as

$$\left(\tilde{r}\frac{\partial}{\partial\tau}+R_U\frac{\partial}{\partial\tilde{z}}-\tilde{\Lambda}\right)\tilde{T}=R_\omega\frac{\partial\tilde{\psi}}{\partial\tilde{z}}. \tag{8.113}$$

8.C Derivation of quadrupolar boundary conditions given in equation (8.54)

The functions ψ and T have the same radial dependence both outside and inside the disc, given by equation (8.37). Thus in writing the boundary conditions for quadrupolar symmetry (equations 8.49-8.51), the radial part cancels out and we obtain a set of four equations relating the eigenvalues and eigenfunctions of a_n^s. Substituting equation (8.40) and the z part of ψ_c from equation (8.53) in equations (8.49a) & (8.49b), we get

$$\sum_{j=1}^{4} c_{nj} \exp(\lambda_{nj}) = e_n \exp(-\sqrt{\gamma_n^s - \mu^2}) \tag{8.114}$$

$$\sum_{j=1}^{4} c_{nj} \lambda_{nj} \exp(\lambda_{nj}) = e_n (-\sqrt{\gamma_n^s - \mu^2}) \exp(-\sqrt{\gamma_n^s - \mu^2}) \tag{8.115}$$

Multiplying equation (8.123) with $\sqrt{\gamma_n^s - \mu^2}$ and adding with equation (8.124), we obtain

$$\sum_{j=1}^{4} \left(\lambda_j + \sqrt{\gamma_n^s - \mu^2}\right) c_{nj} \exp(\lambda_{nj}) = 0. \tag{8.116}$$

We rewrite equation (8.34) as

$$b_n^s = \frac{1}{R_\alpha(1+\alpha_m)} \left(\gamma_n^s a_n^s + R_U \frac{\mathrm{d}a_n^s}{\mathrm{d}z} - \frac{\mathrm{d}a_n^s}{\mathrm{d}z^2}\right) \tag{8.117}$$

Combining equations (8.40), (8.117) & (8.50), we get

$$\sum_{j=1}^{4} \left[\gamma_n^s + R_U \lambda_{nj} - \lambda_{nj}^2\right] c_{nj} \exp(\lambda_{nj}) = \sum_{j=1}^{4} \mu R_\alpha (1+\alpha_m) c_{nj} \exp(\lambda_{nj}). \tag{8.118}$$

Rearranging terms in the above equation, we get

$$\sum_{j=1}^{4} \left[\mu R_\alpha (1+\alpha_m) + \lambda_{nj}^2 - R_U \lambda_{nj} - \gamma_n^s\right] c_{nj} \exp(\lambda_{nj}) = 0. \tag{8.119}$$

For quadrupolar boundary conditions, we substitute equation (8.40) in equation (8.51a) to get

$$\sum_{j=1}^{4} c_{nj} = 0. \tag{8.120}$$

Differentiating equation (8.117) with respect to z, we get

$$\frac{\mathrm{d}b_n^s}{\mathrm{d}z} = \frac{1}{R_\alpha(1+\alpha_m)}\left(\gamma_n^s \frac{\mathrm{d}a_n^s}{\mathrm{d}z} + 2R_U \frac{\mathrm{d}^2 a_n^s}{\mathrm{d}z^2} - \frac{\mathrm{d}^3 a_n^s}{\mathrm{d}z^3}\right). \tag{8.121}$$

Substituting equation (8.121) in equation (8.51b), we get

$$\sum_{j=1}^{4} \left(\gamma_n^s \lambda_{nj} + R_U \lambda_{nj}^2 - \lambda_{nj}^3\right) c_{nj} = 0. \tag{8.122}$$

8.D Derivation of $\langle\overline{B^2}\rangle$ and $\langle\overline{\mathbf{J}\cdot\mathbf{B}}\rangle$

Using equations (8.13) & (8.14), we can write

$$\overline{\mathbf{B}} = \overline{\mathbf{B}}_P + \overline{\mathbf{B}}_\phi = \hat{P}\overline{\psi}; \quad \overline{\mathbf{B}}_\phi = \frac{\overline{T}}{r}\hat{\phi}. \tag{8.123}$$

The expression for the energy of the mean field can be written as

$$\overline{B^2} = \frac{1}{r^2}\left[(\partial_z\psi)^2 + (\partial_r\psi)^2 + T^2\right] \tag{8.124}$$

where $\partial_z = \dfrac{\partial}{\partial z}$, $\partial_r = \dfrac{\partial}{\partial r}$. From equation (8.55), we can write

$$\partial_z\psi = \sum_{n=1}^{N} Q_n a_n' w_n; \quad \partial_r\psi = \sum_{n=1}^{N} Q_n' a_n w_n \tag{8.125}$$

where $a_n' = \dfrac{\mathrm{d}a_n}{\mathrm{d}z}$ and $Q_n' = \dfrac{\mathrm{d}Q_n}{\mathrm{d}r}$. Thus substituting equation (8.125) in (8.124), we obtain

$$\overline{B^2} = \sum_{n,m=1}^{N} \frac{1}{r^2}\left[Q_n Q_m\left(a_n' a_m' + b_n b_m\right) + Q_n' Q_m' a_n a_m\right] w_n w_m. \tag{8.126}$$

For the current density, we can write

$$\overline{\mathbf{J}} = \nabla \times \overline{\mathbf{B}} = \nabla \times \hat{P}\psi + \nabla\left(\frac{1}{r}T\right) = -\left(\frac{1}{r}\Lambda\psi\right)\hat{\phi} + \hat{P}T. \tag{8.127}$$

Combining equations (8.123) & (8.127), we get

$$\overline{\mathbf{J}\cdot\mathbf{B}} = \hat{P}T\cdot\hat{P}\psi - \frac{1}{r^2}(\Lambda\psi)T. \tag{8.128}$$

The first term in the right-hand side (RHS) of equation (8.128) is given by

$$\hat{P}T\cdot\hat{P}\psi = \frac{1}{r^2}\left(\partial_z T\partial_z\psi + \partial_r T\partial_r\psi\right) = \sum_{n,m=1}^{N}\frac{1}{r^2}\left(Q_nQ_m a_n' a_m' + Q_n' Q_m' a_n a_m\right) w_n w_m \tag{8.129}$$

The second term in the RHS of equation (8.128) is given by

$$-\frac{1}{r^2}(\Lambda\psi)T = \frac{1}{r^2}\left[r\partial_r\left(\frac{1}{r}\partial_r Q_n\right) + \partial_z^2\psi\right]T. \tag{8.130}$$

The first term in the RHS of equation (8.130) can be written as

$$r\partial_r\left(\frac{1}{r}\partial_r\psi\right) = \sum_{n=1}^{N} r\partial_r\left(\frac{1}{r}\partial_r Q_n\right)a_n w_n = \sum_{n=1}^{N} -\gamma_n^s Q_n a_n w_n, \tag{8.131}$$

where we have used equation (8.33). Noting that $\partial_z^2\psi = \sum_{n=1}^{N} Q_n a_n'' w_n$ and substituting equation (8.131) in equation (8.130), we get

$$-\frac{1}{r^2}(\Lambda\psi)T = \sum_{n,m=1}^{N}\frac{1}{r^2}\left[Q_nQ_m w_n w_m b_m(a_n'' - \gamma_n^s a_n)\right]. \tag{8.132}$$

Substituting equations (8.129) & (8.132) in equation (8.128), we obtain

$$\overline{\mathbf{J}\cdot\mathbf{B}} = \frac{1}{r^2}\left[Q_nQ_m\left(a_n' b_m' + a_n'' b_m - \gamma_n^s a_n b_m\right) + Q_n' Q_m' a_n b_m\right] w_n w_m. \tag{8.133}$$

In order to obtain the volume averaged quantities $\langle\overline{B^2}\rangle$ and $\langle\overline{\mathbf{J}\cdot\mathbf{B}}\rangle$, we note that, since the quantities in equations (8.126) & (8.133) are separable in variables r and z, we can split the volume average as radial averages on

functions related to Q_n multiplied by vertical averages on functions of a_n and b_n. Using the above relations, we can write the volume averaged quantities as

$$\begin{aligned}\langle\overline{B^2}\rangle &= \sum_{n=1}^{N}\left[\left\langle\frac{1}{r^2}Q_n^2\right\rangle\langle a_n'^2+b_n^2\rangle+\left\langle\frac{1}{r^2}Q_n'^2\right\rangle\langle a_n^2\rangle\right]w_n^2 \\ &= \left[J_2^2(\sqrt{\gamma_n^s}R_0)\langle a_n'^2+b_n^2\rangle+\gamma_n^s J_0^2(\sqrt{\gamma_n^s}R_0)\langle a_n^2\rangle\right]w_n^2 \quad (8.134)\end{aligned}$$

$$\begin{aligned}\langle\overline{\mathbf{J}\cdot\mathbf{B}}\rangle &= \sum_{n=1}^{N}\left[\left\langle\frac{1}{r^2}Q_n^2\right\rangle\langle a_n'b_n'+a_n''b_n-\gamma_n^s a_n b_n\rangle+\left\langle\frac{1}{r^2}Q_n'^2\right\rangle\langle a_n b_n\rangle\right]w_n^2 \\ &= \left[J_2^2(\sqrt{\gamma_n^s}R_0)\langle a_n'b_n'+a_n''b_n-\gamma_n^s a_n b_n\rangle+\gamma_n^s J_0^2(\sqrt{\gamma_n^s}R_0)\langle a_n b_n\rangle\right]w_n^2 \quad (8.135)\end{aligned}$$

where we have used the properties of Bessel functions and equation (8.37) to write

$$\left\langle\frac{1}{r^2}Q_n^2\right\rangle = \frac{2}{R_0^2}\int_0^{R_0}\frac{Q_nQ_m}{r^2}r\mathrm{d}r=\delta_{n,m}J_2^2(\sqrt{\gamma_n^s}R_0) \quad (8.136)$$

$$\left\langle\frac{1}{r^2}Q_n'^2\right\rangle = \frac{2}{R_0^2}\int_0^{R_0}\frac{Q_n'Q_m'}{r^2}r\mathrm{d}r=\delta_{n,m}\gamma_n^s J_0^2(\sqrt{\gamma_n^s}R_0). \quad (8.137)$$

8.E A gauge invariant description of helicity in cylindrical geometry

The Chandrasekhar-Kendall representation of magnetic fields in cylindrical geometry is given by (Low, 2006, 2011)

$$\mathbf{B} = \mathbf{B}_\psi+\mathbf{B}_\phi \quad (8.138)$$

$$\mathbf{B}_\phi = \nabla\times\phi\hat{z};\quad \mathbf{B}_\psi=\nabla\times(\nabla\times\psi\hat{z}). \quad (8.139)$$

Then the absolute magnetic helicity density, defined as

$$h_{abs}(\psi,\phi)=(\nabla\times\psi\hat{z})\cdot[\nabla\times(\nabla\times\psi\hat{z})+2(\nabla\times\phi\hat{z})] \quad (8.140)$$

is a gauge invariant measure of helicity density. The magnetic vector potential given as $\overline{\mathbf{A}} = \nabla \times \psi\hat{z} + \phi\hat{z}$ is also well defined. For the case of axisymmetry, $\nabla \times \psi\hat{z} = -\dfrac{\partial\psi}{\partial r}\hat{\phi}$. Thus, we can write

$$\overline{\mathbf{A}}_{\phi} = \nabla \times \psi\hat{z} \tag{8.141}$$

and rewrite equation (8.140) as

$$h_{abs} = \overline{\mathbf{A}}_{\phi} \cdot \left(\overline{\mathbf{B}}_{\psi} + 2\overline{\mathbf{B}}_{\phi}\right). \tag{8.142}$$

Also under axisymmetry, equation (8.139) can be rewritten as

$$\overline{\mathbf{B}}_{\phi} = -\frac{\partial\phi}{\partial r}\hat{\phi}, \quad \overline{\mathbf{B}}_{\psi} = \frac{\partial^2\psi}{\partial r\partial z}\hat{r} - \frac{1}{r}\frac{\partial}{\partial r}\left(r\frac{\partial\psi}{\partial r}\right)\hat{z}. \tag{8.143}$$

Thus combining equations (8.141), (8.142) & (8.143), we get

$$\overline{\mathbf{A}}_{\phi} \cdot \overline{\mathbf{B}}_{\psi} = 0; \quad \overline{\mathbf{A}}_{\phi} \cdot \overline{\mathbf{B}}_{\phi} = A_{\phi}B_{\phi}. \tag{8.144}$$

So, we get the final expression for absolute helicity density for axisymmetric field in cylindrical geometry as

$$h_{abs} = 2A_{\phi}B_{\phi}. \tag{8.145}$$

Comparing the definition for the field in equation (8.139) with our definition in equations (8.13) & (8.14), we get $A_{\phi} = \dfrac{\psi}{r}\hat{\phi}$ and $B_{\phi} = \dfrac{T}{r}\hat{\phi}$. Thus equation (8.145) in our notation takes the following form

$$h_{abs} = \frac{2\psi T}{r^2}. \tag{8.146}$$

The mean magnetic helicity of the corona can then be defined as

$$\overline{H_c} \int \frac{2\psi_c T_c}{r^2} \mathrm{d}V. \tag{8.147}$$

8.F Equation for evolution of coronal helicity

The rate of change of the mean magnetic helicity in the corona is given by equation (8.12)

$$\frac{\mathrm{d}\overline{H_c}}{\mathrm{d}t} = \int \left(\frac{l_0^2 B_{eq}^2}{\eta_t} \nabla \cdot \mathcal{F} \right) \mathrm{d}V. \tag{8.148}$$

Now we can write

$$\frac{1}{\eta_t} \nabla \cdot \mathcal{F} = \nabla \cdot \left(\frac{\mathcal{F}}{\eta_t} \right) - \mathcal{F} \cdot \nabla \left(\frac{1}{\eta_t} \right) = \nabla \cdot \left(\frac{\mathcal{F}}{\eta_t} \right) \tag{8.149}$$

where we have neglected the radial derivative of $1/\eta_t$. Now we can write equation (8.148) as

$$\frac{\mathrm{d}\overline{H_c}}{\mathrm{d}t} = l_0^2 B_{eq}^2 \int \nabla \cdot \left(\frac{\mathcal{F}}{\eta_t} \right) \mathrm{d}V = l_0^2 B_{eq}^2 \int \left(\frac{\mathcal{F}}{\eta_t} \right) \cdot \hat{z} \mathrm{d}S \tag{8.150}$$

where S represents the top surface of the disc. Using equations (8.9), (8.10) & (8.11), we can write

$$\mathcal{F} \cdot \hat{z} = U_z \alpha_m - \kappa \partial_z \alpha_m. \tag{8.151}$$

Also under the no-z approximation, we write $\partial_z \alpha_m = \alpha_m / h$; (8.150) now becomes

$$\frac{\mathrm{d}\overline{H_c}}{\mathrm{d}t} = l_0^2 B_{eq}^2 \int \left(\frac{U_z \alpha_m}{\eta_t} - \frac{\kappa \partial_z \alpha_m}{\eta_t} \right) \mathrm{d}S = \frac{l_0^2 B_{eq}^2 \alpha_m}{h} \int \left[\left(\frac{U_z h}{\eta_t} \right) - \left(\frac{\kappa}{\eta_t} \right) \right] \mathrm{d}S \tag{8.152}$$

where we have used $\partial_z \alpha_m = \alpha_m / h$; (8.152) can now be rewritten using equations (8.26) & (8.74) as

$$\frac{\mathrm{d}\overline{H_c}}{\mathrm{d}t} = \frac{l_0^2 B_{eq}^2 \alpha_m}{h} \pi R_0^2 \tag{8.153}$$

since both R_U and R_κ are independent of radius. Rescaling equation (8.153), we write

$$\frac{r_0 \eta_t(r_0)}{h^3} B_{eq^2} h^4 \frac{\mathrm{d}\overline{\tilde{H}_c}}{\mathrm{d}\tau} = \frac{l_0^2 B_{eq}^2 \eta_t(r)}{h^2} \left(\frac{\alpha_0 h}{\eta_t} \right) \tilde{\alpha}_m (R_U - R_\kappa) \pi \tilde{R_0}^2 h^2 \tag{8.154}$$

Rearranging the terms in equation (8.154), we get the following equations

$$\begin{aligned}\frac{\mathrm{d}\overline{\tilde{H}_c}}{\mathrm{d}\tau} &= \frac{l_0^2}{h}\frac{\eta_t(r)}{\eta_t(r_0)r_0}R_\alpha(R_U - R_\kappa)\tilde{\alpha}_m\pi\tilde{R_0}^2 \\ &= \frac{l_0^2}{h}\left(\frac{r_0}{r_0}\right)\left(\frac{h}{r}\right)R_\alpha(R_U - R_\kappa)\tilde{\alpha}_m\pi\tilde{R_0}^2 \end{aligned} \tag{8.155}$$

Simplifying equation (8.155) using equation (8.74) and dropping the tilde for simplicity we get the final equation for large scale magnetic helicity in the corona as

$$\frac{\mathrm{d}\overline{H_c}}{\mathrm{d}\tau} = \frac{2\pi R_0^2}{rC}R_\alpha(R_U - R_\kappa)\alpha_m. \tag{8.156}$$

Chapter 9

Conclusions

9.1 Summary

In Chapters 1-5, the background material to understand the physics of the objects of study have been given, which include an overview of solar and galactic magnetic fields, basics of MHD and topological properties of magnetic fields, properties of force-free fields, overview of coronal heating mechanisms and an introduction to turbulent dynamos. In Chapter 2, we have calculated the relative helicity in an arbitrary geometry that can be described by the toroidal-poloidal representation and applied it to special case of spherical and planar geometry. This is a useful formulation which we plan to extend to other cases and provide a geometric construction and constraints for existence of gauge free helicity that does not involve a calculation over an external volume. In Chapter 6, we present a systematic study of the force-free field equation for simple axisymmetric configurations in spherical geometry and apply it to the solar active regions. The condition of separability of solutions in the radial and angular variables leads to two classes of solutions: linear and nonlinear force-free fields (NLFF). We have studied these linear solu-

tions and extended the nonlinear solutions for the radial power law index to the irreducible rational form $n = p/q$, which is allowed for all cases of odd p and cases of $q > p$ for even p, where the poloidal flux $\psi \propto 1/r^n$ and the field $\mathbf{B} \propto 1/r^{n+2}$. We apply these solutions to simulate photospheric vector magnetograms obtained using the spectro-polarimeter on board Hinode. The effectiveness of our search strategy is first demonstrated on test inputs of dipolar, axisymmetric, and non axisymmetric linear force-free fields. Using the best fit, we build three- dimensional axisymmetric field configurations and calculate the energy and relative helicity with two independent methods, which are in agreement. We have analyzed five magnetograms for AR 10930 spanning a period of three days during which two X-class flares occurred and found the free energy and relative helicity of the active region before and after the flare; our analysis indicates a peak in these quantities before the flare events, which is consistent with the other results. We also analyzed single-polarity regions AR 10923 and 10933, which showed very good fits to potential fields. This method provides useful reconstruction of NLFF and input fields for other numerical techniques.

In Chapter 7, we use the simple axisymmetric nonlinear force-free (NLFF) fields (derived in Chapter 6), and apply them to estimate the amount of braiding and free energy content in solar active regions using the concept of mean crossing number. We find that the estimates of free energy content in braiding obtained using crossing numbers is in good agreement with those obtained by exact calculations NLFF fields. We then apply the model of self-organized criticality (SOC) to these structures and calculate the distribution of coherent braid sequences and flare energies. We find find good agreement in the flare energy distributions obtained using SOC model and NLFFF extrapolation of AR 10930 (observed on 12-14 December 2006). These results

provide useful information on the coronal loop structure and also imply that the coronal heating can be supplied by the braiding in the case of the active sun.

In Chapter 8, we present a global semi-analytic axisymmetric model for a turbulent dynamo operating in a galaxy with a corona. We show that the supernovae (SNe) and magneto-rotational instability (MRI) driven turbulence parameters have nearly the same radial dependence and can be treated in a common formalism; however we assume the main contribution from SNe. The general toroidal-poloidal representation is used to calculate the global gauge invariant relative magnetic helicity in cylindrical geometry. We present the analytic steady-state solutions within the disc that are matched to force-free fields in the corona. A dynamical solution for the dynamo is then obtained by expanding the time-dependent field in the basis of the steady-state solutions. The non-linear quenching of the dynamo is alleviated by inclusion of small-scale advective and diffusive magnetic helicity fluxes, which allow the helicity to be transferred outside the disc and consequently build up a corona during the course of dynamo action. We find quadrupolar solutions for in the galactic disc that extend out into the corona and show oscillations radially. The mean field is found to reach saturation within a timescale of 1 Gyr with a strength which is of the order of equipartition magnetic energy ($\sim B_{eq}$). The magnetic pitch angle is -7° at mid plane and changes sign near the disc surface.

9.2 Novel aspects and their impact

The Thesis aimed at applying novel techniques and formulae for Helicity and NLFF field using a semi-analytic approach to two different astrophysical set-

tings. The solutions obtained in the solar case provide alternate and verifiable means to calculate the structure and energetics of active regions. Further the topological methods provide a deeper understanding of the sources of coronal heating. In the case of the galactic dynamo, our analytic treatment provided a transparent and powerful use of eigen functions that yielded a full global solution to the magnetic field and its route to saturation.

By complementing the solutions thus obtained with future numerical models can give further insight and drive us to better models in both cases. The theoretical attempt of new Helicity formulae for arbitrary geometry holds promise of utility in several applications.

The specific points are listed below.

1. We provide a new formulation for relative helicity in arbitrary geometries using the toroidal-poloidal representation of the magnetic field in §2.5 and discuss the special cases of planar and spherical geometry. In a general astrophysical application, the fields penetrate the generation region and extend to a surrounding corona. It is important to develop gauge-free form for Helicity that can be readily used in different geometries without involving integrals over external volumes. The further extension of the ideas here can be formalized through use of differential geometry.

2. For the case of coronal magnetic fields, we were able to extend the solution set of the nonlinear force-free field equation previously obtained in Low and Lou (1990), from $n = 1$ to the irreducible rational form $n = p/q$, which is allowed for all cases of odd p and to cases of $q > p$ for even p. While several papers have dealt with individual cases of odd n, we have provided solutions to arbitrary $n = p/q$ which can be realized through a precise choice of p and q.

3. We calculated the potential fields consistent with these force-free fields inside a shell and the corresponding vector potentials which allowed us to calculated the relative helicity in the region using the Finn-Antonsen formula (Finn and Antonsen, 1983) and the potential field independent Berger formula (Berger, 1985). This is the first published example of the confirmation of the equivalence of the two forms.

4. All the field configurations analyzed were found to be negatively twisted as seen from the α for the C modes and the helicity of the LL modes. The fits with non-linear LL modes seem to be better than the linear C modes. This is a first clear demonstration of the result.

5. This method provides good exact input fields for testing other numerical codes used in reconstruction on the non-linear force-free fields. The existing NLFF numerical reconstructions suffer from fundamental inconsistencies and limitations mentioned in Schrijver *et al.* (2006).

6. In the case of AR 10930, there was a X3.4 class flare on December 13, 2006 and we confirm in both models a substantial decrease in free energy and relative helicity after the flare. The relative helicity and free energy in the C mode increased and in the LL mode decreased marginally after the X1.5 class flare on December 14, 2006.

7. The two ARs 10923, 10933 with single polarity show very high correlation ($> 90\%$) with potential fields.

8. We use these solutions to evaluate the topology of the field lines using the crossing numbers as measures.

9. The crossing number of the braided field is used to estimate the free energy of AR 10930 which is in agreement to those obtained in Prasad,

Mangalam, and Ravindra (2014).

10. We have calculated the power-law distribution for flare energies for AR 10930. We find that our estimates using the nonlinear force-free fields are in good agreement with those obtained using self-organized criticality models (Berger and Asgari-Targhi, 2009).

11. We have incorporated the radial dependence in the SNe (and MRI) driven turbulence parameters and have shown that all these parameters, α, Ω, η_t and U_z have similar radial variation ($\propto 1/r$). Thus the dynamo parameters R_α, R_ω and R_U defined in equation (8.26) are nearly independent of r. This leads to a great simplification in our formulation and the dynamo equations (8.28a) & (8.28b) take the same dimensionless form for both SNe and MRI driven turbulence.

12. We solve the dynamo equations in the disc for the global steady-state solutions which are matched to a linear force-free field in the corona (§8.4.1). These global analytic solutions allow us to calculate the global relative helicity for both the disc and the corona.

13. We solve the full time-dependent problem in §8.4.2 by expanding the time-dependent magnetic field in a basis obtained from the steady-state solutions. We obtain quadrupolar solutions for the saturated magnetic field strength, $B(\sim B_{eq})$, which is proportional to the advective and diffusive fluxes leaving the surface. For the plausible values of vertical outflow U_z = 0.5-1 kms^{-1} at a radius of 4 kpc, we obtain a mean field strength of $B_{sat} = 5 - 7\mu$G, which is close to what is reported in numerical simulations (Gressel, Bendre, and Elstner, 2013; Chamandy *et al.*, 2014) and in observations (Beck, 2012; Van Eck *et al.*, 2014).

The timescale for the dynamo saturation is found to be around 1 Gyr, which is comparable to galactic lifetime.

14. Through the dynamo operates the small-scale helicity fluxes slowly build up the corona with a helicity that carries the same sign as that of the small-scale helicity fluxes. In absence of the flux terms ($R_U = R_\kappa = 0$), we find that the mean field initially grows to a maximum value of $\sim 0.2 B_{eq}$ in the kinematic phase and then is catastrophically quenched. This confirms the crucial role of the helicity fluxes for the dynamo operation.

15. The radial and vertical distribution of the field across the disc are shows there is a reversal sign as we move radially outward from the disc center. B_r changes sign with variation in z towards the surface which leads to the magnetic pitch angle also changing sign near the surface (starting from a value of -7° at the mid plane). This feature was previously reported in Chamandy *et al.* (2014) and is expected in a model with outflows and corona (Ruzmaikin *et al.*, 1979; Ji *et al.*, 2014).

9.3 Future directions

In each of the problems taken up, there are several promising avenues for future study. To improve upon the models it is planned to compare and complement the semi-analytics with more comprehensive numerical models. For the reconstruction of NLFF fields we plan to use the boundary integral methods developed by Yan (1995); Yan and Sakurai (2000). In the case of the Galactic dynamo we plan to supplement our calculations with the use of pencil code of Brandenburg *et al.* (1992); Brandenburg, Candelaresi, and Chatterjee (2009). These and other plans specifically include:

1. We were not able to explore the full parameter space for the simulations presented in Chapter 6 due to computational constraints. The runs took about 8 hrs to complete for each mode search of the solutions upon parallel computation on a 24 node cluster with Intel i7 processors. We plan to improve on these solutions and get more accurate results in future.

2. The NLFFF solutions in Chapter 6 suffer from the problem of singularity at the origin which render them unphysical. We are planning to come up next with more physically viable solutions.

3. In future, using the spherical solutions, we plan to get an semi-analytical expression of free energy for the force-free solutions obtained in Prasad, Mangalam, and Ravindra (2014), in terms of the crossing number and estimate the total energy released in the corona for the braided structures presented in Chapter 7.

4. To estimate the total energy released in the corona from these braided structures and their significance with regards to the energy budget for the active Sun.

5. Calculate the energy released through small scale reconnection events and correlate them to the energy content in the force-free fields.

6. We also plan to incorporate the semi analytic force-free model for the 3 braided magnetic field (Wilmot-Smith, Hornig, and Pontin, 2009) in the model for SOC presented in Chapter 7.

7. We plan to improve the galactic dynamo model presented in 8 by developing a theory that involves simultaneous treatment of both SNe and MRI driven turbulence.

8. We also plan to include a more realistic model for the galactic coronal field that involves details of the helicity dissipation by reconnection in the corona.

9. We plan to include the contribution from the remaining small- and large- scale helicity flux terms (apart from advective and diffusive fluxes) in equations (8.3) and (8.4) need to be explored in order to study its effect on the saturation of the galactic dynamo.

In conclusion, the essence of the findings of the Thesis are in agreement in spirit with the following words :

> "The argument in the past has frequently been a process of elimination. One observed a certain phenomena and one investigated what part could be explained; the unexplained part was taken to be the effect of the magnetic field. It is clear in this case that, the larger one's ignorance, the stronger the magnetic field."
>
> - L. Woltjer

Bibliography

Alfvén, H.: 1947, Magneto hydrodynamic waves, and the heating of the solar corona. *Mon. Not. Roy. Astron. Soc.* **107**, 211. 69

Altschuler, M.D., Newkirk, G.: 1969, Magnetic Fields and the Structure of the Solar Corona. I: Methods of Calculating Coronal Fields. *Solar Phys.* **9**, 131 – 149. doi:10.1007/BF00145734. 50

Amari, T., Boulmezaoud, T.Z., Aly, J.J.: 2006, Well posed reconstruction of the solar coronal magnetic field. *Astron. Astrophys.* **446**, 691 – 705. doi:10.1051/0004-6361:20054076. 63, 110

Amari, T., Boulmezaoud, T.Z., Mikic, Z.: 1999, An iterative method for the reconstructionbreak of the solar coronal magnetic field. I. Method for regular solutions. *Astron. Astrophys.* **350**, 1051 – 1059. 63

Amari, T., Aly, J.J., Luciani, J.F., Boulmezaoud, T.Z., Mikic, Z.: 1997, Reconstructing the Solar Coronal Magnetic Field as a Force-Free Magnetic Field. *Solar Phys.* **174**, 129 – 149. doi:10.1023/A:1004966830232. 63, 110

Arlt, R., Rüdiger, G.: 1999, Accretion-disk dynamo models with dynamo-induced alpha-effect. *Astron. Astrophys.* **349**, 334 – 338. 189

Aschwanden, M.J.: 2004, *Physics of the Solar Corona. An Introduction.* 12, 71, 73

Aschwanden, M.J., Parnell, C.E.: 2002, Nanoflare Statistics from First Principles: Fractal Geometry and Temperature Synthesis. *ApJ* **572**, 1048 – 1071. doi:10.1086/340385. 75

Aschwanden, M.J., Tarbell, T.D., Nightingale, R.W., Schrijver, C.J., Title, A., Kankelborg, C.C., Martens, P., Warren, H.P.: 2000, Time Variability of the "Quiet" Sun Observed with TRACE. II. Physical Parameters, Temperature Evolution, and Energetics of Extreme-Ultraviolet Nanoflares. *ApJ* **535**, 1047 – 1065. doi:10.1086/308867. 75, 76

Babcock, H.W.: 1947, Zeeman Effect in Stellar Spectra. *ApJ* **105**, 105. doi:10.1086/144887. 1

Balbus, S.A., Hawley, J.F.: 1991, A powerful local shear instability in weakly magnetized disks. I - Linear analysis. II - Nonlinear evolution. *ApJ* **376**, 214 – 233. doi:10.1086/170270. 189

Ballai, I., Erdelyi, R.: 1998, Resonant Absorption of Nonlinear Slow MHD Waves in Isotropic Steady Plasmas - I. Theory. *Solar Phys.* **180**, 65 – 79. doi:10.1023/A:1005068127935. 69

Baryshnikova, I., Shukurov, A., Ruzmaikin, A., Sokoloff, D.D.: 1987, Generation of large-scale magnetic fields in spiral galaxies. *Astron. Astrophys.* **177**, 27 – 41. 95

Beck, R.: 2002, Observations of galactic magnetic fields. *Highlights of Astronomy* **12**, 712 – 715. 14

Beck, R.: 2007, Magnetism in the spiral galaxy NGC 6946: magnetic arms, depolarization rings, dynamo modes, and helical fields. *Astron. Astrophys.* **470**, 539 – 556. doi:10.1051/0004-6361:20066988. 18

Beck, R.: 2012, Magnetic Fields in Galaxies. *Space Sci. Rev.* **166**, 215 – 230. doi:10.1007/s11214-011-9782-z. 181, 209, 221, 238

Beck, R., Hoernes, P.: 1996, Magnetic spiral arms in the galaxy NGC6946. *Nature* **379**, 47 – 49. doi:10.1038/379047a0. 18

Beck, R., Wielebinski, R.: 2013, In: Oswalt, T.D., Gilmore, G. (eds.) *Magnetic Fields in Galaxies*, 641. doi:10.1007/978-94-007-5612-0_13. 181

Beck, R., Brandenburg, A., Moss, D., Shukurov, A., Sokoloff, D.: 1996, Galactic Magnetism: Recent Developments and Perspectives. *Ann.Rev. Astron. Astrophys.* **34**, 155 – 206. doi:10.1146/annurev.astro.34.1.155. 16, 181

Beliën, A.J.C., Martens, P.C.H., Keppens, R.: 1999, Coronal Heating by Resonant Absorption: The Effects of Chromospheric Coupling. *ApJ* **526**, 478 – 493. doi:10.1086/307980. 69

Bellan, P.M.: 2013, *Magnetic Helicity and Relaxation: Theory*, 119 – 128. ISBN 9781118664476. doi:10.1029/GM111p0119. http://dx.doi.org/10.1029/GM111p0119. 36

Berger, M.A.: 1985, Structure and stability of constant-alpha force-free fields. *ApJ, Suppl.* **59**, 433 – 444. doi:10.1086/191079. 41, 42, 43, 113, 153, 237

Berger, M.A.: 1988, An energy formula for nonlinear force-free magnetic fields. *Astron. Astrophys.* **201**, 355 – 361. 38

Berger, M.A.: 1991, Generation of coronal magnetic fields by random surface motions. I - Mean square twist and current density. *Astron. Astrophys.* **252**, 369 – 376. 71

Berger, M.A.: 1993, Energy-crossing number relations for braided magnetic fields. *Physical Review Letters* **70**, 705 – 708. doi:10.1103/PhysRevLett.70.705. 79, 80, 81, 179

Berger, M.A.: 1994, Coronal heating by dissipation of magnetic structure. *Space Sci. Rev.* **68**, 3 – 14. doi:10.1007/BF00749112. 72, 73, 79, 81, 82

Berger, M.A.: 1999, Introduction to magnetic helicity. *Plasma Physics and Controlled Fusion* **41**, 167. doi:10.1088/0741-3335/41/12B/312. 34

Berger, M.A., Asgari-Targhi, M.: 2009, Self-organized Braiding and the Structure of Coronal Loops. *ApJ* **705**, 347 – 355. doi:10.1088/0004-637X/705/1/347. 77, 170, 176, 177, 179, 238

Berger, M.A., Field, G.B.: 1984, The topological properties of magnetic helicity. *Journal of Fluid Mechanics* **147**, 133 – 148. doi:10.1017/S0022112084002019. 35, 112, 182, 195

Berger, M.A.: 2013, *Magnetic Helicity in Space Physics*, 1 – 9. ISBN 9781118664476. doi:10.1029/GM111p0001. http://dx.doi.org/10.1029/GM111p0001. 34

Berkhuijsen, E.M., Horellou, C., Krause, M., Neininger, N., Poezd, A.D., Shukurov, A., Sokoloff, D.D.: 1997, Magnetic fields in the disk and halo of M 51. *Astron. Astrophys.* **318**, 700 – 720. 16

Blackman, E.G., Field, G.B.: 2000, Coronal activity from dynamos in astrophysical rotators. *Mon. Not. Roy. Astron. Soc.* **318**, 724 – 732. doi:10.1046/j.1365-8711.2000.03830.x. 182

Blackman, E.G., Field, G.B.: 2001, How astrophysical mean field dynamos can circumvent existing quenching constraints. *Physics of Plasmas* **8**, 2407 – 2414. doi:10.1063/1.1351830. 182

Blackman, E.G., Field, G.B.: 2002, New Dynamical Mean-Field Dynamo Theory and Closure Approach. *Physical Review Letters* **89**(26), 265007. doi:10.1103/PhysRevLett.89.265007. 89, 90, 106, 181, 184

Boulmezaoud, T.Z., Amari, T.: 2000, On the existence of non-linear force-free fields in three-dimensional domains. *Zeitschrift Angewandte Mathematik und Physik* **51**, 942 – 967. 63

Brandenburg, A., Subramanian, K.: 2005a, Astrophysical magnetic fields and nonlinear dynamo theory. *Physics Reports* **417**, 1 – 209. doi:10.1016/j.physrep.2005.06.005. 2, 87, 181, 184

Brandenburg, A., Subramanian, K.: 2005b, Minimal tau approximation and simulations of the alpha effect. *Astron. Astrophys.* **439**, 835 – 843. doi:10.1051/0004-6361:20053221. 184

Brandenburg, A., Candelaresi, S., Chatterjee, P.: 2009, Small-scale magnetic helicity losses from a mean-field dynamo. *Mon. Not. Roy. Astron. Soc.* **398**, 1414 – 1422. doi:10.1111/j.1365-2966.2009.15188.x. 182, 185, 186, 239

Brandenburg, A., Donner, K.J., Moss, D., Shukurov, A., Sokolov, D.D., Tuominen, I.: 1992, Dynamos in discs and halos of galaxies. *Astron. Astrophys.* **259**, 453 – 461. 210, 239

Brandenburg, A., Donner, K.J., Moss, D., Shukurov, A., Sokoloff, D.D., Tuominen, I.: 1993, Vertical Magnetic Fields above the Discs of Spiral Galaxies. *Astron. Astrophys.* **271**, 36. 210

Candelaresi, S., Hubbard, A., Brandenburg, A., Mitra, D.: 2011, Magnetic helicity transport in the advective gauge family. *Physics of Plasmas* **18**(1), 012903. doi:10.1063/1.3533656. 185

Chamandy, L., Shukurov, A., Subramanian, K., Stoker, K.: 2014, Non-linear galactic dynamos: a toolbox. *Mon. Not. Roy. Astron. Soc.* **443**, 1867 – 1880. doi:10.1093/mnras/stu1274. 107, 182, 185, 186, 204, 208, 217, 221, 238, 239

Chandrasekhar, S.: 1956, On Force-Free Magnetic Fields. *Proceedings of the National Academy of Science* **42**, 1 – 5. doi:10.1073/pnas.42.1.1. 55, 56, 111, 116

Chandrasekhar, S.: 1960, The Stability of Non-Dissipative Couette Flow in Hydromagnetics. *Proceedings of the National Academy of Science* **46**, 253 – 257. doi:10.1073/pnas.46.2.253. 189

Chandrasekhar, S.: 1961, *Hydrodynamic and hydromagnetic stability.* 52, 158

Chandrasekhar, S., Kendall, P.C.: 1957, On Force-Free Magnetic Fields. *ApJ* **126**, 457. doi:10.1086/146413. 57, 136

Charbonneau, P., McIntosh, S.W., Liu, H.-L., Bogdan, T.J.: 2001, Avalanche models for solar flares (Invited Review). *Solar Phys.* **203**, 321 – 353. doi:10.1023/A:1013301521745. 74, 75

Cirtain, J.W., Golub, L., Winebarger, A.R., de Pontieu, B., Kobayashi, K., Moore, R.L., Walsh, R.W., Korreck, K.E., Weber, M., McCauley, P., Title, A., Kuzin, S., Deforest, C.E.: 2013, Energy release in the solar corona from spatially resolved magnetic braids. *Nature* **493**, 501 – 503. doi:10.1038/nature11772. 77

Cowie, L.L.: 1981, Cloud fluid compression and softening in spiral arms and the formation of giant molecular cloud complexes. *ApJ* **245**, 66 – 71. doi:10.1086/158786. 190

Cowling, T.G.: 1933, The magnetic field of sunspots. *Mon. Not. Roy. Astron. Soc.* **94**, 39 – 48. 1

Cowling, T.G.: 1976, *Magnetohydrodynamics*. 24

Cox, D.P.: 1990, The diffuse interstellar medium. In: Thronson, H.A. Jr., Shull, J.M. (eds.) *The Interstellar Medium in Galaxies*, *Astrophysics and Space Science Library* **161**, 181 – 200. 190

Crosby, N.B., Aschwanden, M.J., Dennis, B.R.: 1993, Frequency distributions and correlations of solar X-ray flare parameters. *Solar Phys.* **143**, 275 – 299. doi:10.1007/BF00646488. 75

Davila, J.M.: 1987, Heating of the solar corona by the resonant absorption of Alfven waves. *ApJ* **317**, 514 – 521. doi:10.1086/165295. 69

Demoulin, P., Priest, E.R.: 1992, The properties of sources and sinks of a linear force-free field. *Astron. Astrophys.* **258**, 535 – 541. 63

Ebrahimi, F., Bhattacharjee, A.: 2014, Helicity-Flux-Driven α Effect in Laboratory and Astrophysical Plasmas. *Physical Review Letters* **112**(12), 125003. doi:10.1103/PhysRevLett.112.125003. 185

Edlén, B.: 1943, Die Deutung der Emissionslinien im Spektrum der Sonnenkorona. Mit 6 Abbildungen. *Zeitschrift fur Astrophysik* **22**, 30. 12

Erdélyi, R., Ballai, I., Goossens, M.: 2001, Nonlinear resonant absorption of fast magnetoacoustic waves due to coupling into slow continua in the

solar atmosphere. *Astron. Astrophys.* **368**, 662 – 675. doi:10.1051/0004-6361:20010105. 69

Finn, J.M., Antonsen, T.M. Jr.: 1983, Turbulent relaxation of compressible plasmas with flow. *Physics of Fluids* **26**, 3540 – 3552. doi:10.1063/1.864115. 37, 38, 110, 113, 182, 195, 237

Fletcher, A.: 2010, Magnetic Fields in Nearby Galaxies. In: Kothes, R., Landecker, T.L., Willis, A.G. (eds.) *The Dynamic Interstellar Medium: A Celebration of the Canadian Galactic Plane Survey*, *Astronomical Society of the Pacific Conference Series* **438**, 197. 181, 217

Flyer, N., Fornberg, B., Thomas, S., Low, B.C.: 2004, Magnetic Field Confinement in the Solar Corona. I. Force-free Magnetic Fields. *ApJ* **606**, 1210 – 1222. doi:10.1086/383025. 153

Fontenla, J.M., Avrett, E.H., Loeser, R.: 1990, Energy balance in the solar transition region. I - Hydrostatic thermal models with ambipolar diffusion. *ApJ* **355**, 700 – 718. doi:10.1086/168803. 12

Gabriel, A.H.: 1976, A magnetic model of the solar transition region. *Royal Society of London Philosophical Transactions Series A* **281**, 339 – 352. doi:10.1098/rsta.1976.0031. 12

Gent, F.A., Shukurov, A., Sarson, G.R., Fletcher, A., Mantere, M.J.: 2013, The supernova-regulated ISM - II. The mean magnetic field. *Mon. Not. Roy. Astron. Soc.* **430**, L40 – L44. doi:10.1093/mnrasl/sls042. 14, 183

Germano, M.: 1992, Turbulence - The filtering approach. *Journal of Fluid Mechanics* **238**, 325 – 336. doi:10.1017/S0022112092001733. 14, 183

Gourgouliatos, K.N.: 2008, Self-similar magnetic arcades. *Mon. Not. Roy. Astron. Soc.* **385**, 875 – 882. doi:10.1111/j.1365-2966.2008.12858.x. 61

Grad, H., Rubin, H.: 1958, Hydromagnetic equilibria and force-free fields. *2nd International Conference on Peaceful Uses of Atomic Energy, Int. At. Energy Agency, Geneva.*. 63

Gressel, O., Bendre, A., Elstner, D.: 2013, On the magnetic quenching of mean-field effects in supersonic interstellar turbulence. *Mon. Not. Roy. Astron. Soc.* **429**, 967 – 972. doi:10.1093/mnras/sts356. 208, 221, 238

Grotrian, W.: 1934, Über das Fraunhofersche Spektrum der Sonnenkorona. Mit 10 Abbildungen. *Zeitschrift fur Astrophysik* **8**, 124. 12

Gruzinov, A.V., Diamond, P.H.: 1994, Self-consistent theory of mean-field electrodynamics. *Physical Review Letters* **72**, 1651 – 1653. doi:10.1103/PhysRevLett.72.1651. 2, 106, 181, 184

Hale, G.E.: 1908, On the Probable Existence of a Magnetic Field in Sun-Spots. *ApJ* **28**, 315. doi:10.1086/141602. 1

He, H., Wang, H., Yan, Y., Chen, P.F., Fang, C.: 2014, Variations of the 3-D coronal magnetic field associated with the X3.4-class solar flare event of AR 10930. *Journal of Geophysical Research (Space Physics)* **119**, 3286 – 3315. doi:10.1002/2013JA019157. 175

Heald, G.H.: 2012, Magnetic Field Transport from Disk to Halo via the Galactic Chimney Process in NGC 6946. *Astrophys. J. Lett.* **754**, L35. doi:10.1088/2041-8205/754/2/L35. 186

Heyvaerts, J., Priest, E.R.: 1983, Coronal heating by phase-mixed shear Alfven waves. *Astron. Astrophys.* **117**, 220 – 234. 69

Hollweg, J.V.: 1984, Resonances of coronal loops. *ApJ* **277**, 392 – 403. doi:10.1086/161706. 69

Hubbard, A., Rheinhardt, M., Brandenburg, A.: 2011, The fratricide of $\alpha\Omega$ dynamos by their α^2 siblings. *Astron. Astrophys.* **535**, A48. doi:10.1051/0004-6361/201116705. 185

Ichimoto, K., Lites, B., Elmore, D., Suematsu, Y., Tsuneta, S., Katsukawa, Y., Shimizu, T., Shine, R., Tarbell, T., Title, A., Kiyohara, J., Shinoda, K., Card, G., Lecinski, A., Streander, K., Nakagiri, M., Miyashita, M., Noguchi, M., Hoffmann, C., Cruz, T.: 2008, Polarization Calibration of the Solar Optical Telescope onboard Hinode. *Solar Phys.* **249**, 233 – 261. doi:10.1007/s11207-008-9169-9. 138

Inhester, B., Wiegelmann, T.: 2006, Nonlinear Force-Free Magnetic Field Extrapolations: Comparison of the Grad Rubin and Wheatland Sturrock Roumeliotis Algorithm. *Solar Phys.* **235**, 201 – 221. doi:10.1007/s11207-006-0065-x. 63

Ionson, J.A.: 1978, Resonant absorption of Alfvenic surface waves and the heating of solar coronal loops. *ApJ* **226**, 650 – 673. doi:10.1086/156648. 69

Jensen, T.H., Chu, M.S.: 1984, Current drive and helicity injection. *Physics of Fluids* **27**, 2881 – 2885. doi:10.1063/1.864602. 38

Ji, Y., Cole, L., Bushby, P., Shukurov, A.: 2014, Asymptotic solutions for mean-field slab dynamos. *Geophysical and Astrophysical Fluid Dynamics* **108**, 568 – 583. doi:10.1080/03091929.2014.898757. 217, 221, 239

Karpen, J.T., Antiochos, S.K., Dahlburg, R.B., Spicer, D.S.: 1993, The Kelvin-Helmholtz instability in photospheric flows - Effects of coronal heating and structure. *ApJ* **403**, 769 – 779. doi:10.1086/172248. 71

Kennicutt, R.C. Jr.: 1989, The star formation law in galactic disks. *ApJ* **344**, 685 – 703. doi:10.1086/167834. 190

Kleeorin, N., Moss, D., Rogachevskii, I., Sokoloff, D.: 2000, Helicity balance and steady-state strength of the dynamo generated galactic magnetic field. *Astron. Astrophys.* **361**, L5 – L8. 182

Kleeorin, N., Moss, D., Rogachevskii, I., Sokoloff, D.: 2002, The role of magnetic helicity transport in nonlinear galactic dynamos. *Astron. Astrophys.* **387**, 453 – 462. doi:10.1051/0004-6361:20020383. 182, 185, 186

Klimchuk, J.A.: 2015, Key Aspects of Coronal Heating. In: *AAS/AGU Triennial Earth-Sun Summit*, *AAS/AGU Triennial Earth-Sun Summit* **1**, 20308. 67

Klimchuk, J.A., Canfield, R.C., Rhoads, J.E.: 1992, The practical application of the magnetic virial theorem. *ApJ* **385**, 327 – 343. doi:10.1086/170942. 53

Krause, F., Beck, R.: 1998, Symmetry and direction of seed magnetic fields in galaxies. *Astron. Astrophys.* **335**, 789 – 796. 16

Krause, F., Rädler, K.H.: 1980, *Mean-field magnetohydrodynamics and dynamo theory*. 84, 183

Kulsrud, R.M., Zweibel, E.G.: 2008, On the origin of cosmic magnetic fields. *Reports on Progress in Physics* **71**(4), 046901. doi:10.1088/0034-4885/71/4/046901. 181

Larmor, J.: 1919, How could a rotating body such as the sun become a magnet? *Reports of the British Association* **87**, 159 – 160. 1

Leka, K.D., Barnes, G., Crouch, A.: 2009, An Automated Ambiguity-Resolution Code for Hinode/SP Vector Magnetic Field Data. In: Lites, B., Cheung, M., Magara, T., Mariska, J., Reeves, K. (eds.) *The Second Hinode Science Meeting: Beyond Discovery-Toward Understanding*, *Astronomical Society of the Pacific Conference Series* **415**, 365. 138

Linker, J.A., Lionello, R., Mikić, Z., Titov, V.S., Antiochos, S.K.: 2011, The Evolution of Open Magnetic Flux Driven by Photospheric Dynamics. *ApJ* **731**, 110. doi:10.1088/0004-637X/731/2/110. 51

Lites, B.W., Skumanich, A.: 1990, Stokes profile analysis and vector magnetic fields. V - The magnetic field structure of large sunspots observed with Stokes II. *ApJ* **348**, 747 – 760. doi:10.1086/168284. 138

Lites, B.W., Elmore, D.F., Seagraves, P., Skumanich, A.P.: 1993, Stokes Profile Analysis and Vector Magnetic Fields. VI. Fine Scale Structure of a Sunspot. *ApJ* **418**, 928. doi:10.1086/173450. 138

Low, B.C.: 1996, Solar Activity and the Corona. *Solar Phys.* **167**, 217 – 265. doi:10.1007/BF00146338. 133

Low, B.C.: 2006, Magnetic Helicity in a Two-Flux Partitioning of an Ideal Hydromagnetic Fluid. *ApJ* **646**, 1288 – 1302. doi:10.1086/504074. 44, 114, 182, 206, 229

Low, B.C.: 2011, Absolute magnetic helicity and the cylindrical magnetic field. *Physics of Plasmas* **18**(5), 052901. doi:10.1063/1.3587083. 44, 45, 182, 206, 229

Low, B.C., Lou, Y.Q.: 1990, Modeling solar force-free magnetic fields. *ApJ* **352**, 343 – 352. doi:10.1086/168541. 61, 62, 111, 114, 119, 120, 122, 149, 153, 236

Lu, E.T., Hamilton, R.J.: 1991, Avalanches and the distribution of solar flares. *Astrophys. J. Lett.* **380**, L89 – L92. doi:10.1086/186180. 74

Lynden-Bell, D., Boily, C.: 1994, Self-Similar Solutions up to Flashpoint in Highly Wound Magnetostatics. *Mon. Not. Roy. Astron. Soc.* **267**, 146. 61

Mangalam, A.: 2008, Constraints on Dynamo Action. In: *Turbulence, Dynamos, Accretion Disks, Pulsars and Collective Plasma Processes*, 69. doi:10.1007/978-1-4020-8868-1_5. 33, 38, 184, 223

Mangalam, A., Krishan, V.: 2000, Models of Flux Tubes from Constrained Relaxation. *Journal of Astrophysics and Astronomy* **21**, 299. doi:10.1007/BF02702413. 55, 110, 182, 195

Mangalam, A.V., Subramanian, K.: 1994, Dynamo generation of magnetic fields in accretion disks. *ApJ* **434**, 509 – 517. doi:10.1086/174752. 57, 58, 101, 186, 188, 189, 194, 195, 196, 198

Marsh, G.: 2006, Force-free magnetic fields: Solutions, topology and applications. 111

McClymont, A.N., Mikic, Z.: 1994, Thickness variations along coronal loops inferred from vector magnetograph data. *ApJ* **422**, 899 – 905. doi:10.1086/173781. 110

McClymont, A.N., Jiao, L., Mikic, Z.: 1997, Problems and Progress in Computing Three-Dimensional Coronal Active Region Magnetic Fields from

Boundary Data. *Solar Phys.* **174**, 191 – 218. doi:10.1023/A:1004976720919. 110

McKee, C.F., Ostriker, J.P.: 1977, A theory of the interstellar medium - Three components regulated by supernova explosions in an inhomogeneous substrate. *ApJ* **218**, 148 – 169. doi:10.1086/155667. 190

Metcalf, T.R.: 1994, Resolving the 180-degree ambiguity in vector magnetic field measurements: The 'minimum' energy solution. *Solar Phys.* **155**, 235 – 242. doi:10.1007/BF00680593. 138

Metcalf, T.R., Leka, K.D., Barnes, G., Lites, B.W., Georgoulis, M.K., Pevtsov, A.A., Balasubramaniam, K.S., Gary, G.A., Jing, J., Li, J., Liu, Y., Wang, H.N., Abramenko, V., Yurchyshyn, V., Moon, Y.-J.: 2006, An Overview of Existing Algorithms for Resolving the 180° Ambiguity in Vector Magnetic Fields: Quantitative Tests with Synthetic Data. *Solar Phys.* **237**, 267 – 296. doi:10.1007/s11207-006-0170-x. 138

Metcalf, T.R., De Rosa, M.L., Schrijver, C.J., Barnes, G., van Ballegooijen, A.A., Wiegelmann, T., Wheatland, M.S., Valori, G., McTtiernan, J.M.: 2008, Nonlinear Force-Free Modeling of Coronal Magnetic Fields. II. Modeling a Filament Arcade and Simulated Chromospheric and Photospheric Vector Fields. *Solar Phys.* **247**, 269 – 299. doi:10.1007/s11207-007-9110-7. 64, 110

Mikic, Z., McClymont, A.N.: 1994, Deducing Coronal Magnetic Fields from Vector Magnetograms. In: Balasubramaniam, K.S., Simon, G.W. (eds.) *Solar Active Region Evolution: Comparing Models with Observations*, *Astronomical Society of the Pacific Conference Series* **68**, 225. 64

Mikić, Z., Linker, J.A., Lionello, R., Riley, P., Titov, V.: 2007, Predicting the Structure of the Solar Corona for the Total Solar Eclipse of March 29, 2006. In: Demircan, O., Selam, S.O., Albayrak, B. (eds.) *Solar and Stellar Physics Through Eclipses*, *Astronomical Society of the Pacific Conference Series* **370**, 299. 51

Mitra, D., Candelaresi, S., Chatterjee, P., Tavakol, R., Brandenburg, A.: 2010, Equatorial magnetic helicity flux in simulations with different gauges. *Astronomische Nachrichten* **331**, 130. doi:10.1002/asna.200911308. 182, 185

Moffatt, H.K.: 1969, The degree of knottedness of tangled vortex lines. *Journal of Fluid Mechanics* **35**, 117 – 129. doi:10.1017/S0022112069000991. 2

Moffatt, H.K.: 1978, *Magnetic field generation in electrically conducting fluids*. 32, 84, 87, 183

Moss, D.: 1995, On the generation of bisymmetric magnetic field structures in spiral galaxies by tidal interactions. *Mon. Not. Roy. Astron. Soc.* **275**, 191 – 194. 204

Moss, D., Shukurov, A., Sokoloff, D.: 2000, Accretion and galactic dynamos. *Astron. Astrophys.* **358**, 1142 – 1150. 217

Nakagawa, Y.: 1974, Dynamics of the Solar Magnetic Field. I. Method of Examination of Force-Free Magnetic Fields. *ApJ* **190**, 437 – 440. doi:10.1086/152895. 63

Orszag, S.A.: 1970, Analytical theories of turbulence. *Journal of Fluid Mechanics* **41**, 363 – 386. doi:10.1017/S0022112070000642. 89

Parker, E.N.: 1955, Hydromagnetic Dynamo Models. *ApJ* **122**, 293. doi:10.1086/146087. 2, 83

Parker, E.N.: 1972, Topological Dissipation and the Small-Scale Fields in Turbulent Gases. *ApJ* **174**, 499. doi:10.1086/151512. 70, 73

Parker, E.N.: 1983, Magnetic Neutral Sheets in Evolving Fields - Part Two - Formation of the Solar Corona. *ApJ* **264**, 642. doi:10.1086/160637. 71, 73

Parker, E.N.: 1988, Nanoflares and the solar X-ray corona. *ApJ* **330**, 474–479. doi:10.1086/166485. 73, 77

Parnell, C.E., De Moortel, I.: 2012, A contemporary view of coronal heating. *Royal Society of London Philosophical Transactions Series A* **370**, 3217–3240. doi:10.1098/rsta.2012.0113. 75

Parnell, C.E., Jupp, P.E.: 2000, Statistical Analysis of the Energy Distribution of Nanoflares in the Quiet Sun. *ApJ* **529**, 554–569. doi:10.1086/308271. 75

Pevtsov, A.A., Berger, M.A., Nindos, A., Norton, A.A., van Driel-Gesztelyi, L.: 2014, Magnetic Helicity, Tilt, and Twist. *Space Sci. Rev.* **186**, 285–324. doi:10.1007/s11214-014-0082-2. 36

Poedts, S.: 2002, MHD waves and heating of the solar corona. In: Sawaya-Lacoste, H. (ed.) *SOLMAG 2002. Proceedings of the Magnetic Coupling of the Solar Atmosphere Euroconference*, *ESA Special Publication* **505**, 273–280. 69

Poedts, S., Toth, G., Belien, A.J.C., Goedbloed, J.P.: 1997, Nonlinear MHD Simulations of Wave Dissipation in Flux Tubes. *Solar Phys.* **172**, 45 – 52. doi:10.1023/A:1004924017304. 69

Pouquet, A., Frisch, U., Leorat, J.: 1976, Strong MHD helical turbulence and the nonlinear dynamo effect. *Journal of Fluid Mechanics* **77**, 321 – 354. doi:10.1017/S0022112076002140. 89, 91, 106, 181, 184

Prasad, A., Mangalam, A., Ravindra, B.: 2014, Separable Solutions of Force-Free Spheres and Applications to Solar Active Regions. *ApJ* **786**, 81. doi:10.1088/0004-637X/786/2/81. 175, 176, 178, 179, 237, 240

Priest, E.: 2014, *Magnetohydrodynamics of the Sun.* 48, 50, 60, 61, 63

Pudritz, R.E.: 1981, Dynamo Action in Turbulent Accretion Discs around Black Holes - Part Two - the Mean Magnetic Field. *Mon. Not. Roy. Astron. Soc.* **195**, 897. 189

Rädler, K.-H., Kleeorin, N., Rogachevskii, I.: 2003, The Mean Electromotive Force for MHD Turbulence: The Case of a Weak Mean Magnetic Field and Slow Rotation. *Geophysical and Astrophysical Fluid Dynamics* **97**, 249 – 274. doi:10.1080/0309192031000151212. 184

Ravindra, B., Howard, T.A.: 2010, Comparison of energies between eruptive phenomena and magnetic field in AR 10930. *Bulletin of the Astronomical Society of India* **38**, 147 – 163. 148

Ravindra, B., Yoshimura, K., Dasso, S.: 2011, Evolution of Spinning and Braiding Helicity Fluxes in Solar Active Region NOAA 10930. *ApJ* **743**, 33. doi:10.1088/0004-637X/743/1/33. 148

Régnier, S., Amari, T., Kersalé, E.: 2002, 3D Coronal magnetic field from vector magnetograms: non-constant-alpha force-free configuration of the active region NOAA 8151. *Astron. Astrophys.* **392**, 1119 – 1127. doi:10.1051/0004-6361:20020993. 63

Riley, P., Linker, J.A., Mikič, Z.: 2013, Ensemble modeling of the ambient solar wind. In: Zank, G.P., Borovsky, J., Bruno, R., Cirtain, J., Cranmer, S., Elliott, H., Giacalone, J., Gonzalez, W., Li, G., Marsch, E., Moebius, E., Pogorelov, N., Spann, J., Verkhoglyadova, O. (eds.) *American Institute of Physics Conference Series*, *American Institute of Physics Conference Series* **1539**, 259 – 262. doi:10.1063/1.4811037. 51

Rodrigues, L.F.S., Shukurov, A., Fletcher, A., Baugh, C.: 2015, Galactic magnetic fields and hierarchical galaxy formation. *ArXiv e-prints*. 190, 191

Roumeliotis, G.: 1996, The "Stress-and-Relax" Method for Reconstructing the Coronal Magnetic Field from Vector Magnetograph Data. *ApJ* **473**, 1095. doi:10.1086/178219. 64, 110

Rüdiger, G., Hollerbach, R.: 2004, *The magnetic universe : geophysical and astrophysical dynamo theory*. 16

Ruzmaikin, A.A., Sokolov, D.D., Shukurov, A.M. (eds.): 1988, *Magnetic fields of galaxies*, *Astrophysics and Space Science Library* **133**. 84, 93, 94, 95, 181, 214

Ruzmaikin, A.A., Turchaninov, V.I., Zeldovich, I.B., Sokoloff, D.D.: 1979, The disk dynamo. *Astrophys. Spa. Sci.* **66**, 369 – 384. doi:10.1007/BF00650011. 217, 221, 239

Sakurai, T.: 1979, A New Approach to the Force-Free Field and Its Application to the Magnetic Field of Solar Active Regions. *Pub. Astron. Soc. Japan* **31**, 209 – 230. 64

Sakurai, T.: 1981, Calculation of force-free magnetic field with non-constant α. *Solar Phys.* **69**, 343 – 359. doi:10.1007/BF00149999. 63

Sakurai, T.: 1982, Green's Function Methods for Potential Magnetic Fields. *Solar Phys.* **76**, 301 – 321. doi:10.1007/BF00170988. 50

Schmidt, H.U.: 1964, On the Observable Effects of Magnetic Energy Storage and Release Connected With Solar Flares. *NASA Special Publication* **50**, 107. 50

Schmidt, M.: 1959, The Rate of Star Formation. *ApJ* **129**, 243. doi:10.1086/146614. 190

Schrijver, C.J., De Rosa, M.L., Metcalf, T.R., Liu, Y., McTiernan, J., Régnier, S., Valori, G., Wheatland, M.S., Wiegelmann, T.: 2006, Nonlinear Force-Free Modeling of Coronal Magnetic Fields Part I: A Quantitative Comparison of Methods. *Solar Phys.* **235**, 161 – 190. doi:10.1007/s11207-006-0068-7. 64, 110, 237

Sellwood, J.A., Balbus, S.A.: 1999, Differential Rotation and Turbulence in Extended H I Disks. *ApJ* **511**, 660 – 665. doi:10.1086/306728. 189

Shapiro, P.R., Field, G.B.: 1976, Consequences of a New Hot Component of the Interstellar Medium. *ApJ* **205**, 762 – 765. doi:10.1086/154332. 191

Shukurov, A.: 2004, Introduction to galactic dynamos. *ArXiv Astrophysics e-prints*. 15, 190, 191

Shukurov, A.: 2005, Mesoscale Magnetic Structures in Spiral Galaxies. In: Wielebinski, R., Beck, R. (eds.) *Cosmic Magnetic Fields*, *Lecture Notes in Physics, Berlin Springer Verlag* **664**, 113. doi:10.1007/11369875_6. 84

Shukurov, A.: 2007, Galactic dynamos. In: Dormy, E., Soward, M. A. (eds.) *Mathematical aspects of natural dynamos*, *The fluid mechanics of astrophysics and geophysics, CRC Press/Taylor & Francis*. 92

Shukurov, A., Sokoloff, D., Subramanian, K., Brandenburg, A.: 2006, Galactic dynamo and helicity losses through fountain flow. *Astron. Astrophys.* **448**, L33 – L36. doi:10.1051/0004-6361:200600011. 182, 185, 186

Skumanich, A., Lites, B.W.: 1987, Stokes profile analysis and vector magnetic fields. I - Inversion of photospheric lines. *ApJ* **322**, 473 – 482. doi:10.1086/165743. 138

Sokoloff, D.D., Bykov, A.A., Shukurov, A., Berkhuijsen, E.M., Beck, R., Poezd, A.D.: 1998, Depolarization and Faraday effects in galaxies. *Mon. Not. Roy. Astron. Soc.* **299**, 189 – 206. doi:10.1046/j.1365-8711.1998.01782.x. 16

Steenbeck, M., Krause, F., Rädler, K.-H.: 1966, Berechnung der mittleren LORENTZ-Feldstärke $\mathbf{v} \times \mathbf{B}$ für ein elektrisch leitendes Medium in turbulenter, durch CORIOLIS-Kräfte beeinflußter Bewegung. *Zeitschrift Naturforschung Teil A* **21**, 369. 1

Sturrock, P.A.: 1994, *Plasma Physics*. 53

Sturrock, P.A., Uchida, Y.: 1981, Coronal heating by stochastic magnetic pumping. *ApJ* **246**, 331 – 336. doi:10.1086/158926. 71

Subramanian, K., Brandenburg, A.: 2004, Nonlinear Current Helicity Fluxes in Turbulent Dynamos and Alpha Quenching. *Physical Review Letters* **93**(20), 205001. doi:10.1103/PhysRevLett.93.205001. 182

Subramanian, K., Brandenburg, A.: 2006, Magnetic Helicity Density and Its Flux in Weakly Inhomogeneous Turbulence. *Astrophys. J. Lett.* **648**, L71 – L74. doi:10.1086/507828. 182, 185

Subramanian, K., Mestel, L.: 1993, Galactic Dynamos and Density Wave Theory - Part Two - an Alternative Treatment for Strong Non-Axisymmetry. *Mon. Not. Roy. Astron. Soc.* **265**, 649. 204

Sur, S., Shukurov, A., Subramanian, K.: 2007, Galactic dynamos supported by magnetic helicity fluxes. *Mon. Not. Roy. Astron. Soc.* **377**, 874 – 882. doi:10.1111/j.1365-2966.2007.11662.x. 106, 182, 185, 186, 205, 209, 221

Sur, S., Subramanian, K., Brandenburg, A.: 2007, Kinetic and magnetic α-effects in non-linear dynamo theory. *Mon. Not. Roy. Astron. Soc.* **376**, 1238 – 1250. doi:10.1111/j.1365-2966.2007.11511.x. 105

Taylor, J.B.: 1974, Relaxation of Toroidal Plasma and Generation of Reverse Magnetic Fields. *Physical Review Letters* **33**, 1139 – 1141. doi:10.1103/PhysRevLett.33.1139. 55, 109, 182, 186, 195

Taylor, J.B.: 1976, Relaxation of toroidal discharges. In: Evans, D.E. (ed.) *Pulsed High Beta Plasmas*, 59 – 67. 55

Tenorio-Tagle, G., Bodenheimer, P., Franco, J.: 1988, Supernova explosions inside pre-existing wind-driven cavities - Spherically symmetric models. In: Boerner, G. (ed.) *Supernovae, Remnants, Active Galaxies, Cosmology*, 77 – 87. 190

Thalmann, J.K., Tiwari, S.K., Wiegelmann, T.: 2014, Force-free Field Modeling of Twist and Braiding-induced Magnetic Energy in an Active-region Corona. *ApJ* **780**, 102. doi:10.1088/0004-637X/780/1/102. 77, 78

Toomre, A.: 1964, On the gravitational stability of a disk of stars. *ApJ* **139**, 1217 – 1238. doi:10.1086/147861. 190

Tüllmann, R., Dettmar, R.-J., Soida, M., Urbanik, M., Rossa, J.: 2000, The thermal and non-thermal gaseous halo of NGC 5775. *Astron. Astrophys.* **364**, L36 – L41. 17

van Ballegooijen, A.A.: 1985, Electric currents in the solar corona and the existence of magnetostatic equilibrium. *ApJ* **298**, 421 – 430. doi:10.1086/163626. 81

Van Eck, C., Brown, J.-A., Shukurov, A., Fletcher, A.: 2014, Magnetic Fields in a Sample of Nearby Spiral Galaxies. *ArXiv e-prints*. 181, 209, 217, 221, 238

Velikhov, E.P.: 1959, Stability of an ideally conducting liquid flowing between cylinders rotating in a magnetic field. *Sov. Phys. - JETP Lett.* **36**, 1398 – 1404. 189

Venkatakrishnan, P., Hagyard, M.J., Hathaway, D.H.: 1988, Elimination of projection effects from vector magnetograms - The pre-flare configuration of active region AR 4474. *Solar Phys.* **115**, 125 – 131. doi:10.1007/BF00146234. 138

Vishniac, E.T., Cho, J.: 2001, Magnetic Helicity Conservation and Astrophysical Dynamos. *ApJ* **550**, 752 – 760. doi:10.1086/319817. 182, 185

Vishniac, E.T., Shapovalov, D.: 2014, Properties of Magnetic Helicity Flux in Turbulent Dynamos. *ApJ* **780**, 144. doi:10.1088/0004-637X/780/2/144. 182, 185

Wheatland, M.S.: 2007, Calculating and Testing Nonlinear Force-Free Fields. *Solar Phys.* **245**, 251 – 262. doi:10.1007/s11207-007-9054-y. 110

Wheatland, M.S., Leka, K.D.: 2011, Achieving Self-consistent Nonlinear Force-free Modeling of Solar Active Regions. *ApJ* **728**, 112. doi:10.1088/0004-637X/728/2/112. 110

Wheatland, M.S., Régnier, S.: 2009, A Self-Consistent Nonlinear Force-Free Solution for a Solar Active Region Magnetic Field. *Astrophys. J. Lett.* **700**, L88 – L91. doi:10.1088/0004-637X/700/2/L88. 110

Wheatland, M.S., Sturrock, P.A., Roumeliotis, G.: 2000, An Optimization Approach to Reconstructing Force-free Fields. *ApJ* **540**, 1150 – 1155. doi:10.1086/309355. 64, 110

Wiegelmann, T.: 2004, Optimization code with weighting function for the reconstruction of coronal magnetic fields. *Solar Phys.* **219**, 87 – 108. doi:10.1023/B:SOLA.0000021799.39465.36. 64, 110

Wiegelmann, T.: 2008, Nonlinear force-free modeling of the solar coronal magnetic field. *Journal of Geophysical Research (Space Physics)* **113**, 3. doi:10.1029/2007JA012432. 63, 65

Wiegelmann, T., Inhester, B.: 2010, How to deal with measurement errors and lacking data in nonlinear force-free coronal magnetic field modelling? *Astron. Astrophys.* **516**, A107. doi:10.1051/0004-6361/201014391. 64

Wiegelmann, T., Inhester, B., Sakurai, T.: 2006, Preprocessing of Vector Magnetograph Data for a Nonlinear Force-Free Magnetic Field Reconstruction. *Solar Phys.* **233**, 215 – 232. doi:10.1007/s11207-006-2092-z. 64, 65, 110

Wilmot-Smith, A.L., Hornig, G., Pontin, D.I.: 2009, Magnetic Braiding and Parallel Electric Fields. *ApJ* **696**, 1339 – 1347. doi:10.1088/0004-637X/696/2/1339. 78, 180, 240

Withbroe, G.L.: 1988, The temperature structure, mass, and energy flow in the corona and inner solar wind. *ApJ* **325**, 442 – 467. doi:10.1086/166015. 82

Withbroe, G.L., Noyes, R.W.: 1977, Mass and energy flow in the solar chromosphere and corona. *Ann.Rev. Astron. Astrophys.* **15**, 363 – 387. doi:10.1146/annurev.aa.15.090177.002051. 67

Woltjer, L.: 1958, A Theorem on Force-Free Magnetic Fields. *Proceedings of the National Academy of Science* **44**, 489 – 491. doi:10.1073/pnas.44.6.489. 53

Woltjer, L.: 1960, On the Theory of Hydromagnetic Equilibrium. *Reviews of Modern Physics* **32**, 914 – 915. doi:10.1103/RevModPhys.32.914. 182, 195

Yan, Y.: 1995, The 3-D Boundary Element Formulation of Linear Force-Free Magnetic Fields with Finite Energy Content in Semi-Infinite Space. *Solar Phys.* **159**, 97 – 113. doi:10.1007/BF00733034. 64, 239

Yan, Y.: 2003, On the application of the boundary element method in coronal magnetic field reconstruction. *Space Sci. Rev.* **107**, 119 – 138. doi:10.1023/A:1025567521251. 64

Yan, Y., Sakurai, T.: 1997, Analysis of it YOHKOH SXT Coronal Loops and Calculated Force-Free Magnetic Field Lines from Vector Magnetograms. *Solar Phys.* **174**, 65 – 71. doi:10.1023/A:1004943409775. 110

Yan, Y., Sakurai, T.: 2000, New Boundary Integral Equation Representation for Finite Energy Force-Free Magnetic Fields in Open Space above the Sun. *Solar Phys.* **195**, 89 – 109. doi:10.1023/A:1005248128673. 64, 110, 239

Yang, W.H., Sturrock, P.A., Antiochos, S.K.: 1986, Force-free magnetic fields - The magneto-frictional method. *ApJ* **309**, 383 – 391. doi:10.1086/164610. 110

Zeldovich, I.B., Ruzmaikin, A.A., Sokolov, D.D. (eds.): 1983, *Magnetic fields in astrophysics* **3**. 2, 27

Zhang, M., Flyer, N., Chye Low, B.: 2012, Magnetic Helicity of Self-similar Axisymmetric Force-free Fields. *ApJ* **755**, 78. doi:10.1088/0004-637X/755/1/78. 121